Novel Methods for Modern NMR Spectroscopy

Optimized Pulses and New Experiments

Zur Erlangung des akademischen Grades eines

Doktors der Naturwissenschaften
(Dr. rer. nat.)

von der KIT-Fakultät für Chemie und Biowissenschaften
des Karlsruher Instituts für Technologie (KIT)
genehmigte

Dissertation

von

Dipl.-Chem. Martin R. M. Koos

aus
Karlsruhe

KIT-Dekan: Prof. Dr. Willem Klopper
Referent: Prof. Dr. Burkhard Luy
Korreferent: Prof. Dr. Jan Korvink
Tag der mündlichen Prüfung: 17. Oktober 2016

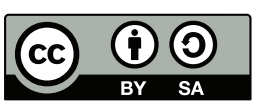

Publikationsliste

Teile dieser Arbeit wurden bereits veröffentlicht.

P. Trigo-Mouriño, C. Merle, M. R. M. Koos, B. Luy, and R. R. Gil, "Probing Spatial Distribution of Alignment by Deuterium NMR Imaging", *Chemistry – A European Journal*, vol. 19, no. 22, pp. 7013–7019, 2013.

M. R. M. Koos, H. Feyrer, and B. Luy, "Broadband excitation pulses with variable RF amplitude-dependent flip angle (RADFA)", *Magn. Reson. Chem.*, vol. 53, no. 11, pp. 886–893, 2015.

M. R. M. Koos, E. Danieli, F. Casanova, B. Blümich, and B. Luy, "Differentiation of enantiomers by 2D NMR spectroscopy at 1 T using residual dipolar couplings", *Magn. Reson. Chem.*, vol. 54, no. 6, pp. 527–530, 2016.

M. R. M. Koos, G. Kummerlöwe, L. Kaltschnee, C. M. Thiele, and B. Luy, "CLIP-COSY: A Clean In-Phase Experiment for the Rapid Acquisition of COSY-type Correlations", *Angew. Chem. Int. Ed.*, vol. 55, no. 27, pp. 7655–7659, 2016.

Weitere Veröffentlichungen nach Abschluss der Arbeit:

M. R. M. Koos, H. Feyrer, and B. Luy, "Broadband rf-amplitude-dependent flip angle pulses with linear phase slope", *Magn. Reson. Chem.*, vol. 55, no. 9, pp. 797–803, 2017, mrc.4593.

D. Schulze-Sünninghausen, J. Becker, M. R. Koos, and B. Luy, "Improvements, extensions, and practical aspects of rapid asap-hsqc and alsofast-hsqc pulse sequences for studying small molecules at natural abundance", *J. Magn. Reson.*, vol. 281, no. Supplement C, pp. 151–161, 2017.

M. Reller, S. Wesp, M. R. M. Koos, M. Reggelin, and B. Luy, "Biphasic liquid crystal and the simultaneous measurement of isotropic and anisotropic parameters by spatially resolved nmr spectroscopy", *Chemistry – A European Journal*, vol. 23, no. 54, pp. 13 351–13 359, 2017.

Hiermit versichere ich, dass ich die vorliegende Arbeit selbstständig verfasst habe; dass ich die Stellen der Arbeit, die anderen Werken im Wortlauf oder dem Sinn nach entnommen sind, entsprechend kenntlich gemacht habe; und dass die verwendeten Quellen und Hilfsmittel vollständig angegeben sind.

Karlsruhe, 30. September 2017

Martin R. M. Koos

Contents

Chapter 1

Motivation: NMR – It's Awesome

A modern nuclear magnetic resonance spectrometer basically consists of an expensive magnet made from coils of superconducting wire, cooled by liquid nitrogen and liquid helium, combined with a high quality radio transmit and receive circuit, tuned to the frequency of atoms' nuclear spins. The marvelous versatility of NMR arises from the multitude of ways the radio signals can be composed. High power pulses that spin spins around, mixed with rests*, delays of free evolution, constitute a question posed to the spins of the molecules. Their response is usually a faint echo in the same frequency range. It is measured and transformed into a spectrum, that contains the answer, provided the question was posed appropriately. The combination of pulse sequence question and guideline to interpret the answer is called NMR experiment.

Fortunately, most NMR spectroscopists require only little training in formulating questions, as many important NMR experiments have been devised and studied in depth. They are contained in pulse program libraries, shipped with the spectrometer software, and can be applied straightforwardly to all kinds of samples yielding highly reproducible results.

Still, in this work, I tried to understand the properties of widespread experiments to further improve existing ones, add to the libraries, and devise new *questions* to ask.

*An interval of silence in music; it is silent but still an active part of the music.

Chapter 2

Introduction

Nuclear magnetic resonance (NMR) spectroscopy surely is one of the most important and versatile analytical methods and is widely used in many fields of research. The versatility of NMR spectroscopy originates from the countless experiments that can be performed on a high number of NMR-active isotopes, available for most elements. When nuclei of different suitable isotopes are present in a sample, experiments can easily embrace all of them to show correlated spectra or measure interactions [1]. Depending on sample composition, a multitude of information can be obtained from such spectra, indicating electron density, bond situation and orientation, but also internuclear distances and evidence of molecular interactions at atomic resolution [2–4].

Today's method, pulse-Fourier transform NMR, relies on radio frequency (RF) pulses. Most common is the so-called *hard pulse*, an RF pulse with a square-shaped amplitude that is still used most widely in today's NMR applications [5]. The current high level of spectral quality achieved on modern high-field, high-resolution NMR spectrometers, however, reveals their limitations, and these pulses that were once considered good enough to do any thinkable task with sufficient quality are becoming a limiting factor. The demand for improved pulsing techniques is amplified by new developments like cryogenically cooled probe heads that reduce noise intensity, but create a less homogeneous RF field [6], or toroidal cavity probes which can be built to tolerate high RF power, high pressure, and high temperature, at the price of even less homogeneous RF fields [7]. Higher magnetic field strengths, while increasing the signal to noise ratio, also increase the chemical shift frequency range and therefore the frequency offset the RF pulse has to overcome. Most ^{1}H spectra extend over a spectral width of 10 ppm, which is equal to 6 kHz at a magnetic field of 14.1 T and easily handled by hard pulses. ^{13}C nuclei, on the other hand, are much more sensitive to the chemical environment, and their chemical shifts can often cover 200 ppm in a single molecule. With its lower nuclear magnetic moment compared to ^{1}H, these 200 ppm correspond to 30 kHz on a 14.1 T magnet, which is more than the available hard pulses on most modern high resolution NMR spectrometers can excite effectively, let alone manipulate with the precision required for complicated multipulse experiments. Other nuclei like ^{19}F or

^{195}Pt, covering 1300 ppm and 15 000 ppm, respectively, are completely beyond the capacity of conventional rectangular-shaped RF pulses.

One way out of the dilemma, is to advance the shape of the RF pulses from the basic form, to other, more complicated shapes with advantageous properties. Initially, simple mathematical functions like the sinc function or Gaussian function were translated into constant-phase pulse shapes with improved bandwidth profile [8, 9]. Phase or frequency modulated pulses were introduced for adiabatic state inversion and were found to compensate for effects such as RF field inhomogeneity [10, 11]. Composite pulses, series of pulse elements of different length and phase but with constant amplitude, are another early approach to overcome pulse imperfections [12]. In recent years, with sufficiently developed theory and increasing computational power, the optimization of arbitrary pulse shapes became possible. Algorithms derived from optimal control theory (OCT) nowadays are among the most efficient ways to develop new pulse shapes characterized by hundreds or thousands of parameters [13]. These OCT pulse shapes can not only increase the spectral quality when they replace rectangular pulses, they can also be optimized to achieve novel tasks. In Chapter 3 of this work, pulse shapes for several tasks are presented. One group of optimizations in this chapter even provided the knowledge and the pulse shapes necessary to create the CLIP-COSY experiment presented in Chapter 4.

At the same time, the ongoing pursuit of higher resolution is never satisfied. Especially in ^{1}H spectra, one can almost always find a group of signals with molecular positions too similar or internuclear couplings too strong to be separated. Increasing the magnetic field strength helps to reduce the spectral overlap, and the advancement from the first commercially available machines in the 1950s at 30 MHz to the 1 GHz instrument installed 2009 in Lyon was accompanied by many breakthroughs. At this very moment, a new class of superconducting materials is required to reach higher fields, but as rumor and pre-orders have it we might actually see such magnets within a few years from now. For most applications, however, the latest developments are not essential [14] as another solution has long been found: Resolution enhancement is achieved elegantly by the introduction of an additional dimension that is sampled indirectly within a pulse sequence. Correlating e. g., ^{1}H signals with the frequency of connected ^{13}C or ^{15}N nuclei, provides a 2D spectrum with excellent signal separation [1, 15]. Multidimensional experiments reveal the true power of NMR spectroscopy [16]. Such an indirect spectral dimension can even be used to probe quantum states that do not generate a measurable magnetic field and, therefore are invisible to the RF coil. Sample inhomogeneity, dreaded for the line broadening it causes, can also be addressed by multidimensional NMR experiments. Proper selection of the pulse sequence e. g., can compensate for magnetic field deviations. The spatial composition of samples, is the speciality of the closely related field of magnetic resonance imaging (MRI). Combining advances from MRI and NMR to develop new experiments is often fruitful. Sample inhomogeneities can

be characterized by acquiring spectra with spatial resolution, and inhomogeneities can even be resolved and additional information retrieved from them. Chapter 8 illustrates some of the challenges and possibilities presented by sample inhomogeneity.

The main drawback of all multidimensional NMR experiments is their increased duration. While a simple 1D spectrum can often be acquired within a second or two, 2D spectra commonly take minutes to hours, and spectra of higher dimensionality can even require days of measurement time. Spectrometer time however, often is scarce. Especially in routine NMR laboratories where a high number of samples has to be processed everyday this is a problem. Often the measurement time that is available per sample is barely enough for 2D experiments, so they have to be acquired with limited resolution, or not at all. When spectrometer time is is ample, spectrometer stability becomes crucial. NMR spectroscopy detects frequency shifts smaller than a millionth of the base frequency. Vibrations, air conditioning duty cycles, and differences between day and night can influence spectra. These perturbations are small but when a long series of FIDs is recorded for a multidimensional experiment, each FID contributes to the whole spectrum, and spectral resolution will be degraded.

Therefore a topic of current research is the reduction of these long experiment durations. This can be achieved by novel processing schemes that allow skipping a good portion of the points of indirect dimensions [17]. Furthermore, there exist pulse sequences that can acquire multidimensional datasets significantly faster. The CLIP-COSY experiment presented in Chapter 4 can be reduced in length compared to the conventional DQF-COSY [18]. In recent time, the ASAP-HSQC and related experiments that allow rapid acquisition have drawn attention [19, 20]. In Chapter 5, a set of ASAP-HSQC experiments with improved spectral quality is presented. To describe the expected signal intensity and explain the source of the increased intensity of some fast acquisition schemes, two simple mathematical models are developed and presented in Chapters 6 and 7.

The objective of this work was to extend the scope of NMR spectroscopy, simplify and accelerate its methods, and reveal the physical limits it is subject and subjected to.

Chapter 3

NMR Pulse Shape Optimization with Optimal Control Theory

The program Octopussi modified for this work was written by Sebastian F. Ehni. The RADFA pulses were optimized in cooperation with Hannes Feyrer. Parts of this chapter are published in [21].

3.1 The Role of Pulse Shapes in NMR

First measurements of nuclear magnetic resonance utilized a continuous RF irradiation, there was no place for shaped pulses. It was succeeded by pulse-Fourier transform NMR [5, 22], using constant-amplitude radio frequency (RF) pulses. When the frequency of such rectangular pulses is resonant with respect to a nuclear spin state transition, they create a superposition of the spin states. The composition of the superposition oscillates between the two states, a process called Rabi oscillation [23]. The frequency of that oscillation, the Rabi frequency, defines the RF amplitude, and is the reason why this amplitude is often expressed in the unit Hertz or kHz. Upon deactivation of the RF pulse the spins will initially remain in their state. An RF pulse of the right length can therefore create any desired mix of the two states. The phase within the Rabi oscillation is called flip angle. Equal contribution of both spin states is obtained after 1/4 of the Rabi period, a 90° pulse, creating the maximum transverse magnetization and measurable signal. A pulse with length equal to half of the Rabi period, a 180° pulse, causes inversion of the population of the two states.

When the Larmor frequency is not equal to the frequency of the RF pulse, the frequency offset disturbs the oscillation between states. The apparent frequency of the oscillation is different, and not all superpositions can be reached. In NMR experiments, one important consequence is reduced signal intensity and increased phase errors of 90° pulses, when the frequency offset is larger than the RF amplitude which can happen at the edges of the spectrum. Another consequence is the impossibility of off-resonance state inversion with constant-phase pulses. This means, 180° pulses will only work well for a very small range of offset frequencies, e. g., at

5 kHz offset the apparent flip angle around the direction of the pulse of a 10 kHz 180° pulse is only 123° while an additional rotation around the z axis is observed.

RF amplitudes of liquid state NMR spectrometers nowadays reach 10 to 30 kHz. The offset frequency of a spin is proportional to its chemical shift difference from the center frequency and the magnetic field strength. Most ^{1}H spectra usually cover 10 ppm, corresponding to 6 kHz at the field strength of 14.1 T (600 MHz). The chemical shift dispersion of ^{13}C nuclei in organic molecules, on the other hand, easily reaches 220 ppm corresponding to 33 kHz, a range that cannot be covered with rectangular pulses alone. In the future, the wide adoption of spectrometers with higher magnetic field strength will make the problem even more severe.

In most parts of NMR, the theory is developed well enough that disagreement between theory and experiment implies spectrometer misalignment. While analytical solutions for pulse shapes are only known for rectangular and hyperbolic secant pulses [11], numerical calculation allows simulating the effect of any pulse shape at arbitrary precision [24]. From the numerical calculation, pulse quality can be assessed and shaped pulses can be optimized to perform simple tasks to replace rectangular pulses, but also tasks, that are impossible for rectangular pulses. They can be optimized for band selectivity, compensate certain hardware limitations, or have special rotation properties, as will be shown in the following.

3.2 The GRAPE Algorithm

3.2.1 Quantum Mechanical Spin Dynamics

A quantum mechanical system is defined by the operator corresponding to its total energy, the Hamiltonian $\mathcal{H}$. The eigenstates of that operator and their superpositions are the allowed states of the system. The subsystem of states that is important in NMR is to a high degree isolated from other molecular states, it is therefore often sufficient to consider isolated spins. For a spin 1/2 particle with gyromagnetic ratio γ in a magnetic field parallel to the z axis, but otherwise unperturbed, the Hamiltonian is

$$\mathcal{H}_{\text{evo}} = -\gamma \mathbf{I}_{\text{z}} B_0, \tag{3.1}$$

where $\mathbf{I}_{\text{z}}$ is the operator of angular momentum along the z axis. The relation between nuclear spin orientation and energy state is the Zeeman effect [25]. The Hamiltonian is also the basis for calculating the time evolution of a system, so the operator $\mathcal{H}_{\text{evo}}$ describes the free evolution of the system when no pulses are applied. The equation of motion in (non-relativistic) quantum

mechanics for a density operator state ρ is the von Neumann or Liouville-von Neumann equation

$$\frac{\partial \rho}{\partial t} = -\mathrm{i}\hbar \left[\mathcal{H}, \rho\right]. \tag{3.2}$$

It is the equivalent of the well-known Schrödinger equation for density operators. For a constant Hamiltonian, the solution of this equation is the time evolution operator

$$U(t) = e^{-\mathrm{i}\mathcal{H}t}, \tag{3.3}$$

a unitary operator that moves the state from $t = 0$ to any t by multiplication,

$$\rho(t) = U(t)\ \rho(0)\ U^{\dagger}(t). \tag{3.4}$$

The Hamiltonian of the same spin in an RF pulse field is

$$\mathcal{H}_{\mathrm{RF}}(t) = 2\pi \left(u_{\mathrm{x}}(t)\mathbf{I}_{\mathrm{x}} + u_{\mathrm{y}}(t)\mathbf{I}_{\mathrm{y}}\right), \tag{3.5}$$

with the RF amplitudes for x and y pulses, u_{x} and u_{y}, and the angular momentum operators $\mathbf{I}_{\mathrm{x}}$ and $\mathbf{I}_{\mathrm{y}}$. An NMR pulse shape is made up of these RF amplitudes. For the time evolution of a spin in an NMR experiment,

$$\mathcal{H}(t) = \mathcal{H}_{\mathrm{evo}} + \mathcal{H}_{\mathrm{RF}}(t) \tag{3.6}$$

in Equation (3.3) is clearly not constant in time. In most cases and for the shaped pulses in this work, however, the Hamiltonian can be split into N of piecewise constant parts and the time evolution described by

$$U_{\mathrm{pulse}} = U_N \cdots U_k \cdots U_3 U_2 U_1. \tag{3.7}$$

Pulse shape optimization is the task of improving the set of RF amplitudes, u_{x} and u_{y}, so they create the desired time evolution or target state.

3.2.2 A Very Short Introduction to Optimal Control Theory

Optimal control theory (OCT) is a mathematical optimization method that allows finding a set of input parameters, the controls or the control vector, for a given dynamic system such that a certain optimality criterion is fulfilled [26, 27]. It is an extension of the calculus of variations which allows including the equations of motion of said system as constraints. Some early applications of optimal control are illustrated in [28] and OCT can be applied to many fields and scientific disciplines from economics [29] over rocket science [30] to NMR [31], with of course, the latter being of highest interest for this work.

A set of n controls, u_1 to u_n, that stand for parameters that can be determined and changed at will, is arranged into a control vector

$$\mathbf{u} = \begin{pmatrix} u_1 \\ \vdots \\ u_n \end{pmatrix}. \tag{3.8}$$

The quality of a given control vector is assessed by calculating a cost functional $L(\mathbf{x}, \mathbf{u})$ that may in general depend on $\mathbf{u}$ as well as the state vector

$$\mathbf{x} = \begin{pmatrix} x_1 \\ \vdots \\ x_h \end{pmatrix}. \tag{3.9}$$

The evolution of the state vector and the influence of the controls are combined by n additional constraints

$$f_j(x_1, \ldots, x_h; u_1, \ldots, u_n) = 0 \tag{3.10}$$

that represent, e. g., the equations of motion in a physical system.

To minimize the cost functional while maintaining the constraints, a vector of n Lagrange multipliers

$$\lambda = \begin{pmatrix} \lambda_1 \\ \ldots \\ \lambda_n \end{pmatrix} \tag{3.11}$$

is used to join them to the cost functional L and obtain a new functional

$$H(\mathbf{x}, \mathbf{u}, \lambda) = L(\mathbf{x}, \mathbf{u}) + \sum_{j=1}^{m} \lambda_j f_j(\mathbf{x}, \mathbf{u}) \tag{3.12}$$

$$= L(\mathbf{x}, \mathbf{u}) + \lambda^T \mathbf{f}(\mathbf{x}, \mathbf{u}). \tag{3.13}$$

The Lagrange multipliers are undefined variables, that vanish from the cost functional as long as the constraint is fulfilled, i. e., the respective equation $f_j = 0$ in Equation (3.10) is true.

In a dynamic system that evolves from t_0 to t_f the cost functional can be divided into the final cost Φ and the running cost $\mathcal{J}$ by

$$L = \Phi[\mathbf{x}(t_\mathrm{f}), t_\mathrm{f}] + \int_{t_0}^{t_\mathrm{f}} \mathcal{J}[\mathbf{x}(t), \mathbf{u}(t), t] \, \mathrm{d}t. \tag{3.14}$$

For NMR pulse optimization, usually the final cost most important as it is directly related to the spectral quality or the purity of the state at the end of the pulse. However, $\mathcal{J}$ can still be used in the calculation and provides a way to estimate the pulse quality at each point in time. This allows, e. g., optimizations where a system should be kept close to a desired state over a certain time, as is important in some NMR applications [32, 33]. $\mathcal{J}$ also provides a method to penalize high amplitude of controls, which may correspond to overall physical cost like spent rocket fuel or RF power. The optimality criterion mentioned in the beginning is usually simply a threshold value of L or Φ, or tolerable minimal change of their values.

Early applications of OCT to pulse sequence optimizations come from MRI where effective selective pulses could be obtained [34, 35]. The most important application of OCT to NMR spectroscopy nowadays is the GRAPE algorithm [13, 31], next to the Krotov algorithm [36–38]. The two methods have been compared extensively, e. g. in [39–41]. In this work, the GRAPE algorithm was used with two classes of cost functionals, often simply called cost function for simplicity. The first cost functional is used to optimize transfer from defined initial state to defined target state, a *point-to-point* transfer. The second cost functional is used to optimize a rotation with defined axis and flip angle, a unitary rotation within the spin system. The second functional, when applied to a group of non-identical spins results in the same rotation for all spins, a *universal rotation*. In both cases only the final state or final cost is considered when assessing pulse quality.

3.2.3 Gradient Ascent Pulse Engineering

When optimizing a point-to-point transfer, the initial state ρ_{init} and the target state ρ_{T} have to be defined. The task of the optimization is to find the set of control amplitudes u to maximize the population of the target state after the pulse and the effect of uncontrollable terms in the Hamilton operator. The transfer created by a pulse is described by the propagator U_{pulse}, a unitary time evolution operator, by multiplying individual stepwise constant elements at time point k

$$U_k = \exp\left(-\mathrm{i}\left(\mathcal{H}_{\text{evo}} + \mathcal{H}_{\text{RF}}(k)\right)\right) \tag{3.15}$$

$$U_{\text{pulse}} = \prod_{k=1}^{n} U_k = U_n \cdots U_3 U_2 U_1. \tag{3.16}$$

and applying the pulse transformation to the state density matrix

$$\rho_{\text{F}} = U_{\text{pulse}} \rho_{\text{init}} U_{\text{pulse}}^{\dagger}. \tag{3.17}$$

The final state is then compared to the target state and the cost function for point-to-point pulses is defined as

$$\Phi_{\mathrm{PP}} = \mathrm{Re}\,\langle \rho_{\mathrm{T}} | \rho_{\mathrm{F}} \rangle = \mathrm{Re}\,\mathrm{Tr}(\rho_{\mathrm{T}}^{\dagger} \rho_{\mathrm{F}}). \tag{3.18}$$

Using Equations (3.16) and (3.17), ρ_k and λ_k are defined by

$$\Phi_{\mathrm{PP}} = \mathrm{Re}\,\langle \rho_{\mathrm{T}} | U_N \cdots U_k \cdots U_1 \rho_{\mathrm{init}} U_1^{\dagger} \cdots U_k^{\dagger} \cdots U_N^{\dagger} \rangle \tag{3.19}$$

$$= \mathrm{Re}\,\langle \underbrace{U_{(k+1)} \cdots U_N \rho_{\mathrm{T}} U_N^{\dagger} \cdots U_{(k+1)}^{\dagger}}_{\lambda_k} \,|\, \underbrace{U_k \cdots U_1 \rho_{\mathrm{init}} U_1^{\dagger} \cdots U_k^{\dagger}}_{\rho_k} \rangle\,. \tag{3.20}$$

$$\tag{3.21}$$

The state at time step 1 is ρ_{init}. With the current values of the control amplitudes in the pulse shape, at time step k, the state is ρ_k. Likewise, the desired state at time step N is the target state ρ_{T} and evolving backwards through time, λ_k describes the required state at time step k to reach the final state with the current pulse shape. As visualized in Figure 3.1, the difference between ρ and λ shows how the shape should be changed.

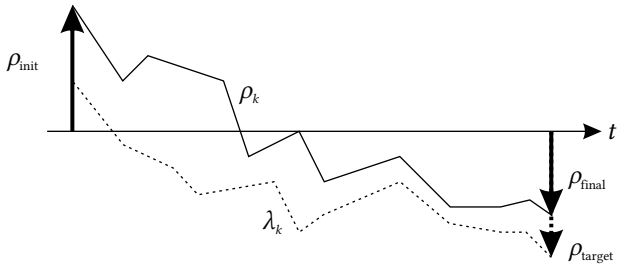

Figure 3.1: Forward and backward trajectory of a pulse propagation. The initial state ρ_{init} evolves to ρ_k, the target state is evolved from ρ_{T} backwards to λ_k. The gradient for step k is calculated from the difference in ρ_k and λ_k.

Consequently, the gradient is now calculated for each step k and for all control operators, independent from all other time steps, as is illustrated in Figure 3.2. Applying the gradient to the pulse shape, iteratively leads to a better shape. The first order approximation for the gradient of control amplitude u_j at time point k corresponding to control operator $\mathbf{I}_{\mathrm{j}}$ is

$$\frac{\mathrm{d}\Phi_{\mathrm{PP}}}{\mathrm{d}u_{j,k}} = -\langle \lambda_k | i\Delta t \left[I_j, \rho_k \right] \rangle \tag{3.22}$$

with $\left[I_j, \rho_k \right]$ denoting the commutator between the state and the control operator. There exist numerous methods to calculate the gradient at higher accuracy [42, 43]. The crucial step to

obtain exact gradients is the calculation of the derivatives of the pulse propagator U_{pulse} with respect to the control amplitudes u, which is nontrivial as the control operators and the drift Hamiltonian in general do not commute. In the program Octopussi by S. Ehni, that was used in this work, the calculation is performed in the eigenbasis of the Hamiltonian [44]. In recent years, improved methods to calculate gradients to higher orders, higher accuracy, as well as new ways to apply the gradient to the shape have been found [45, 46], but have not been implemented in Octopussi. It has to be noted that the optimization in the GRAPE algorithm is a gradient based iterative scheme. This means, global convergence is not guaranteed, the pulse shape may converge with only a locally optimal solution. This problem is partially reduced by the new methods in [45, 46], but usually it is necessary to run a multitude of optimizations with different initial pulse shapes to cover a larger part of the solution space.

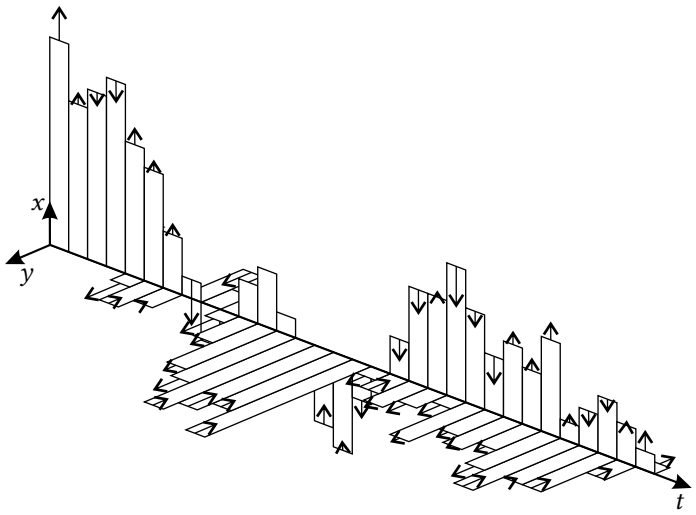

Figure 3.2: Pulse shape with x and y controls and gradient. Bars indicate the pulse amplitude while the gradient in x and y direction is indicated by arrows. The gradient represents the change required in each time step to improve the overall performance of the shape. Each arrow, i. e.gradient element, helps to minimize the difference between ρ and λ in Figure 3.1

The general layout of the gradient ascent pulse engineering (GRAPE) [13] algorithm is this:

1. An initial shape $\mathbf{u}^{(0)}$ with N steps is generated from pseudo random numbers.

2. The trajectory ρ_k of the magnetization affected by $\mathcal{H}_{\text{evo}}$ and $\mathcal{H}_{\text{RF}}$ is calculated from ρ_{init} to ρ_{F} for each step k.

3. The backwards trajectory λ_k is calculated from ρ_{T}.

4. The overall performance Φ and the gradient $\frac{\partial \Phi}{\partial u}$ pointing towards better performance for each point in time is calculated from ρ_k and λ_k.

5. The shape is improved by applying the gradient $\mathbf{u}^{(a+1)} \rightarrow \mathbf{u}^{(a)} + \epsilon \frac{\partial \Phi}{\partial u}$.

6. The Steps 2–5 are repeated until any convergence criterion is fulfilled.

The GRAPE algorithm requires only one complete calculation ofthe pulse propagators and two calculations of the trajectory to calculate the gradient and update the shape. Other methods like calculating the gradient from the difference quotient require N complete propagations for each control amplitude. Therefore the GRAPE algorithm can be applied to pulse shapes with large numbers of parameters and is not confined to basic shapes or mathematical functions.

When optimizing a universal rotation transformation, the aim is not to transfer from one state to another, $\rho_{\text{init}} \rightarrow \rho_{\text{F}}$, but to obtain a desired pulse operator U_{pulse} directly [47–51]. While the point-to-point transfer may be achieved by a multitude of different ways, i. e., different effective rotation axes and flip angles may reach the same state, the universal rotation pulse has a fixed rotation axis and angle. In theory, any universal rotation problem can be formulated as point-to-point transfer in a space of higher dimension [45, 50], an approach that was not chosen in this work. The straightforward way is direct optimization of the pulse propagator U_{pulse} as defined in Equation (3.16). The propagator is evaluated via comparison with a target propagator U_{T} that describes the desired rotation. The scalar product between the two operators, $\langle U_{\text{T}} | U_{\text{pulse}} \rangle$, is in general a complex number, therefore the difference is minimized by

$$\left\| U_{\text{T}} - U_{\text{pulse}} \right\|^2 = \| U_{\text{T}} \|^2 - 2 \operatorname{Re} \langle U_{\text{T}} | U_{\text{pulse}} \rangle - \left\| U_{\text{pulse}} \right\|^2 , \tag{3.23}$$

of which essentially only the middle term is changing, and the pulse quality is measured by

$$\Phi_{\text{UR}} = \operatorname{Re} \langle U_{\text{T}} | U_{\text{pulse}} \rangle . \tag{3.24}$$

The general GRAPE work flow is unchanged, and the trajectories of ρ_k and λ_k are replaced by the effective propagator of the pulse multiplied forward from 1 to the point k, or backward from the target operator.

3.2.4 Creating Pulse Shapes for NMR Applications

Up to this point, the control amplitudes are considered without limit, an assumption that will lead to problems when implementing the shapes on real hardware, spectrometers with electrical circuits, that usually do not take kindly to running them at unlimited current or power. Fortunately, the pulse shape optimization on the other hand, takes kindly the limiting of amplitudes by

a number of ways. Besides including an amplitude or power penalty in the cost funcional, the most simple way is a hard cut off value in Step 5 of the scheme shown above, where amplitude of the pulse is never allowed to exceed the cut off value [52].

The pulse shapes obtained from the optimization become interesting for real world applications, when not only a single Hamiltonian is considered, but the pulse shape is able to perform the desired transfer in the presence of a range of different Hamiltonians. In most cases, this means pulse shapes compensated to cover a wide range of offset frequencies in the drift Hamiltonian, i. e., broad band pulses or pulse shapes that are robust versus miscalibrated B_1 amplitude, which causes the control Hamiltonian to deviate. Using GRAPE, pulse shapes that are virtually calibration free and cover large bandwidths have been found [53].

The compensation is achieved simply by calculating the gradient for each Hamiltonian of the range of Hamiltonians that should be covered by the pulse, and applying the average gradient to the pulse shape. The resulting pulse is evaluated by calculating the average cost function.

1. An initial shape $\mathbf{u}^{(0)}$ with N steps is generated from pseudo random numbers.
2. The following steps are performed for each offset frequency, B_1 amplitude and other parameters that should be compensated.
   (a) The trajectory ρ_k of the magnetization affected by $\mathcal{H}_{\text{evo}}$ and $\mathcal{H}_{\text{RF}}$ is calculated from ρ_{init} to ρ_{F} for each step k.
   (b) The backwards trajectory λ_k is calculated from ρ_{T}.
   (c) The overall performance Φ and the gradient $\frac{\partial \Phi}{\partial u}$ pointing towards better performance for each point in time is calculated from ρ_k and λ_k.
3. The mean gradient is calculated from all parameter combinations.
4. The shape is improved by applying the mean gradient $\mathbf{u}^{(a+1)} \longrightarrow \mathbf{u}^{(a)} + \epsilon \overline{\frac{\partial \Phi}{\partial u}}$.
5. The Steps 2–4 are repeated until any convergence criterion is fulfilled.

The same principle can be used to introduce different target states or operators depending on offset frequency or B_1 amplitude, as will be utilized in the next sections.

As long as the optimization problem posed to the algorithm is physically feasible, the algorithm will provide a solution. The problem has to be formulated carefully or unexpected results will occur, however, fine tuning of the cost functional and the gradient allows remarkable feats, like reducing phase deviations in the xy plane by loosening the requirements towards the z axis [54] or compensation against detrimental effects like relaxation [55–57]. It is also

possible to find pulses with special phase behavior [58, 59]. Pulses can be optimized for two spins at the same time, yielding pulse sandwiches compensated against accidental Hartman-Hahn matching [60] and whole transfer elements including pulses and delays can be obtained [61, 62].

3.3 Creation of the Initial Pulse Shape

Initial pulse shapes are usually created deterministically from pseudo-random numbers. These random seed is specified in the input parameters file. When the shape is directly assembled from the random values, it assumes a highly oscillating profile, indistinguishable from noise. This profile is initially retained in the optimization, until a high number of iterations is reached. Pulse shapes from fully converged optimization runs, however, often feature a smooth profile, which may indicate, that the optimization is hindered by the noisy shape. To start the optimization run with a smooth but pseudo-random shape, spline interpolation was introduced in the program Octopussi. Depending on the length of the shape, a number of random values were obtained from the pseudo-random number generator and used as amplitude values at equidistant pulse steps. The shape was then completed by using cubic spline interpolation. In Figure 3.3, examples of initial shapes are shown.

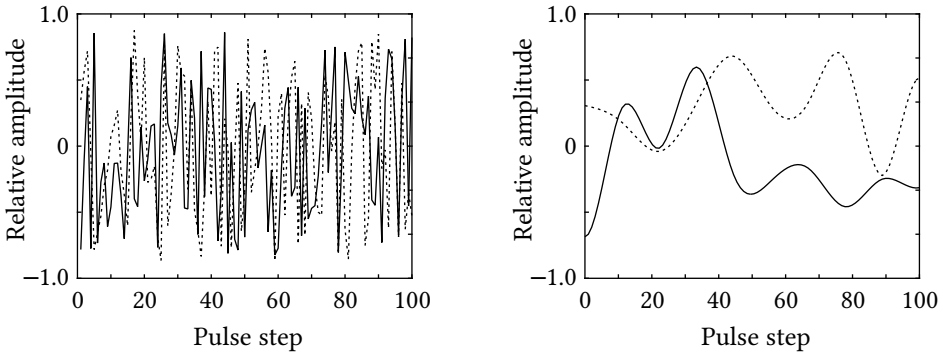

(a) Randomly generated values (b) Spline interpolated random values

Figure 3.3: Comparison of initial shapes generated from pseudo-random numbers; x amplitude drawn as solid line, y amplitude as dashed lines. a) Pseudo-random numbers directly assembled to a shape by assigning them to pulse step amplitudes. b) Pulse shape created by spline interpolation between 10 random values for x and y amplitude, each.

3.4 Energy Limited Excitation and Inversion Pulses

The high performance of OCT allows systematic studies by optimizing large numbers of pulses convering a wide parameter space. As shown before [51, 63, 64], this makes it possible to test the physical limits of RF pulses in NMR spectroscopy. One important limit is the energy requirement, a topic that was touched in [64], where RF power limits were used, but never fully explored. The RF energy transferred can heat the sample which will degrade shim quality, shift temperature-sensitive signals in the spectrum, and may even destroy fragile molecules. In medicinal applications, exposure to ionizing radiation, e. g. X-ray, that is mutagenic and can kill cells, must be limited. RF irradiation, in contrast, is not considered harmful, but prolonged exposure can still heat tissue and thereby damage it. So here the transferred energy should be monitored, too. Besides practical considerations, the energy requirement of pulses with different bandwidth is highly interesting from a theoretical point of view. It will provide insight into the cost associated with hardening pulse shapes.

The magnetic field strength of an RF pulse is proportional to the RF amplitude $u_{\mathrm{RF}} = \sqrt{u_{\mathrm{x}}^2 + u_{\mathrm{y}}^2}$. When permeating the sample, the magnetic field is usually slightly weakened by diamagnetic effects, but the internal field strength at the nucleus is approximately proportional to the external field strength. The power of an RF pulse is proportional to u_{RF}^2 and relative quantification of the energy is possible by introducing the RF energy ϵ_{RF}, free of all device- and sample-specific parameters,

$$\epsilon_{\mathrm{RF}} = u_{\mathrm{RF}}^2 \cdot \tau_P. \tag{3.25}$$

The B_1 energy of a rectangular pulse of 10 kHz amplitude and 100 µs duration is

$$\epsilon_{\mathrm{RF}} = (10\,000\,\mathrm{Hz})^2 \cdot 100\,\mu\mathrm{s} = 10\,000\,\mathrm{kHz}. \tag{3.26}$$

The GRAPE algorithm allows limiting the RF amplitude in a simple way as explained before in this chapter and in Reference [52]. From there it is only a small step to calculate the pulse energy or power from the pulse shape and cut off or scale the shape accordingly to optimize RF power and overall RF energy-limited pulses. Within the study, next to RF energy, the parameters bandwidth and RF field inhomogeneity (B_1 inhomogeneity) were sampled. The following evaluation is limited to pulses with varying bandwidth. For compensation of B_1 inhomogeneity, good pulse shapes with limited energy requirement were obtained, however, no deeper insight could be gained.

The RF energy for excitation pulses was sampled from 1 to 15 kHz, for inversion pulses it was 4 to 40 kHz. For each bandwidth and pulse length 10 starting shapes were created from pseudo-random numbers. The digitization pulse length Δt was generally chosen to be 0.5 µs with overall

lengths of the pulse shape starting at 10 µs. The optimization was run until local convergence was reached for all 10 pulse shapes. If the best pulse quality was below $\Phi_{\text{cutoff}} = 0.995$, pulse length was increased and a new set of 10 starting shapes was generated unless the maximum pulse length of 1 ms was reached. In the optimizations the energy limit was maintained by calculating the sum of squared amplitudes and downscaling all individual amplitudes whenever the value exceeded the allowed ϵ_{RF}.

Figure 3.4a shows the resulting time-optimality curves for excitation pulses with 20 kHz bandwidth and varying RF energy. The reachable pulse performance is highly dependent on the available energy. With increasing pulse length, a stepwise increase in pulse performance that has been reported previously is observed [63]. For longer pulses, however, the pulse performance for a certain RF energy seems to converge. In Figure 3.4b, the time-optimality curves for inversion pulses are shown. The behavior is very similar to the excitation pulses. Again the pulse quality depends on available energy, a stepwise increase can be seen and after about 300 us pulse length, the curve flattens and seems to converge. Looking at some excitation profiles in Figure 3.5, longer pulses have less effect on areas outside the desired bandwidth.

Figure 3.4 indicates, that the reachable pulse quality is bounded by energy and bandwidth even for arbitrarily long pulses. Figure 3.6a shows the quality of the longest pulse for each ϵ_{RF} and $\Delta\Omega$. The curve is almost linear in the exponential plot, an approximate upper bound is

$$\Phi_{\text{exc}}^{\tau_P \to \infty}(\epsilon_{\text{RF}}, \Delta\Omega) = 1 - 0.5 \exp\left(-2\pi^2 \cdot \frac{\epsilon_{\text{RF}}}{\Delta\Omega}\right) - 0.5 \exp\left(-10\pi^2 \cdot \frac{\epsilon_{\text{RF}}}{\Delta\Omega}\right). \tag{3.27}$$

In this equation the first subtrahend almost describes the full behavior and it is satisfying to see only numbers that are 2 or π. However, it deviates close to zero, where it should be complemented by a second subtrahend with higher exponent. The factor 10 has been chosen to fit the data, and is hard to justify from a theoretical direction.

Interestingly, the inversion data shown in Figure 3.6b can be approximated by a very similar formula,

$$\Phi_{\text{inv}}^{\tau_P \to \infty}(\epsilon_{\text{RF}}, \Delta\Omega) = 1 - 2 \exp\left(-\pi^2 \cdot \frac{\epsilon_{\text{RF}}}{\Delta\Omega}\right), \tag{3.28}$$

covering the whole range of positive and negative values of the cost function.

The behavior of very long pulses should, of course, reappear when looking at shorter pulses. For very short pulses that fail to create the desired transfer even for resonant spins, the pulse quality is approximated by

$$\Phi_{\text{exc}}(\epsilon_{\text{RF}}, \Delta\Omega, \tau_P) = \sin\left(2\pi\sqrt{\epsilon_{\text{RF}}\tau_P}\right) \cdot \operatorname{sinc}\left(0.5\,\Delta\Omega\tau_P\right) \cdot \tag{3.29}$$

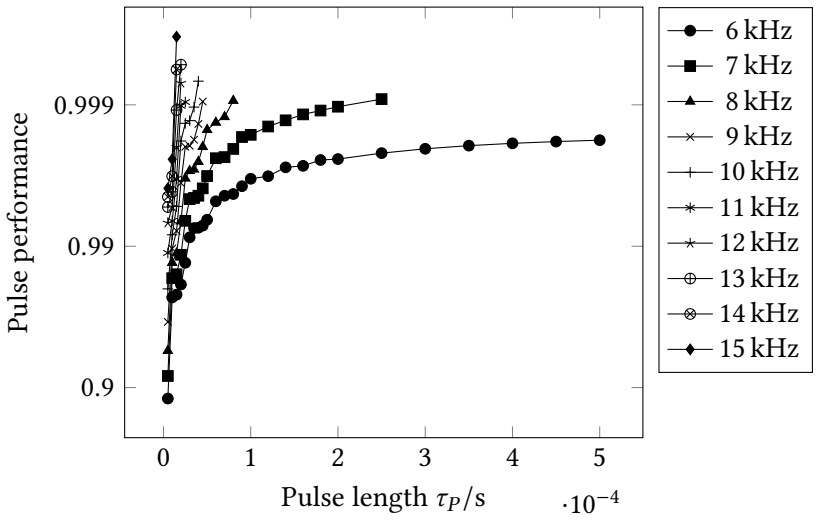

(a) Excitation pulses

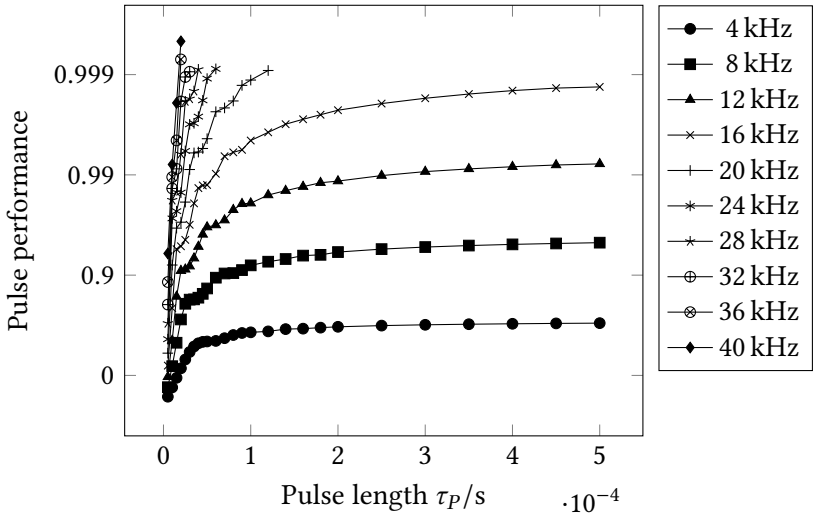

(b) Inversion pulses

Figure 3.4: Pulse quality of pulse shapes with varying RF energy limits and 20 kHz bandwidth versus pulse length; a) excitation pulses and b) inversion pulses.

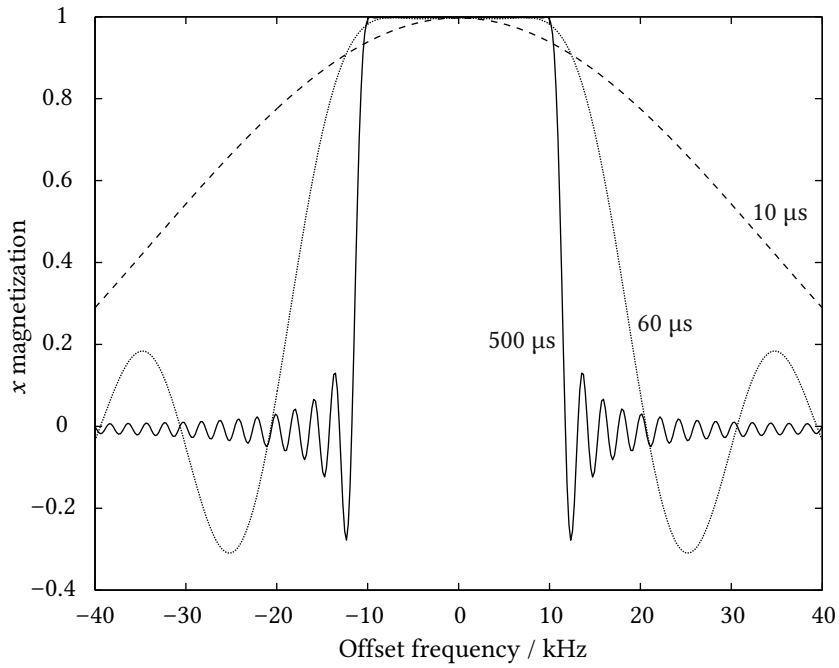

Figure 3.5: Excitation profile of a pulse with 10 µs (dashed line), a pulse with 60 µs (dotted line), and a pulse with 500 µs (solid line). All pulses have 20 kHz bandwidth, and 6 kHz available RF energy. Frequency band selectivity was not required in the optimization but emerged nontheless.

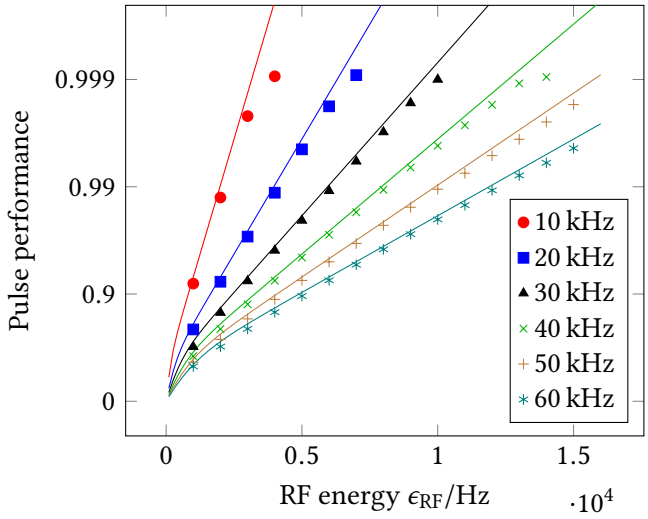

(a) Excitation pulses

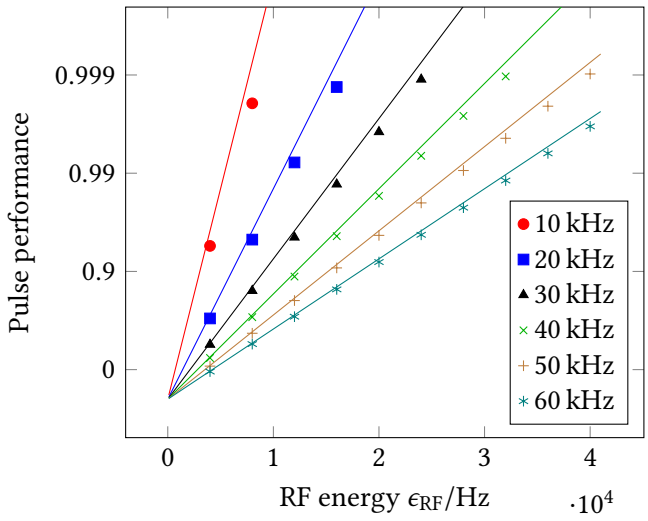

(b) Inversion pulses

Figure 3.6: Pulse quality versus overall ϵ_{RF} for different bandwidths. with the longest pulse length available for each ϵ_{RF}. a) Excitation pulses; the quality of obtained pulses is shown along with the approximation of Equation (3.27).
b) Inversion pulses; the quality of obtained pulses is shown along with the approximation of Equation (3.28).

for excitation pulses. Inversion pulses require an additional $\pi/2$ rotation, that can be included in the approximation

$$\Phi_{\mathrm{exc}}(\epsilon_{\mathrm{RF}}, \Delta\Omega, \tau_P) = \sin\left(-\frac{\pi}{2} + 2\pi\sqrt{\epsilon_{\mathrm{RF}}\tau_P}\right) \cdot \mathrm{sinc}\left(0.5\,\Delta\Omega\tau_P\right). \tag{3.30}$$

Longer pulses can reach higher on-resonance flip angles at the same overall RF energy, the additional time and energy enables the algorithm to create pulses with higher bandwidth. Unfortunately, no simple description could be found for the transition from very short to very long pulses. The function

$$\Phi(\tau_P) = \Phi_{\mathrm{exc}}^{\tau_P\to\infty}(\epsilon_{\mathrm{RF}}, \Delta\Omega) + b(\tanh(c \cdot \tau_P) - 1) \tag{3.31}$$

can be fitted to the longest 25 % of the pulses. With matched parameter b and c, Equation (3.31) descibes the behavior quantitatively but provides no deeper insight into the basic relations of RF energy, pulse length, rotations, and bandwith compensation.

While global optimality cannot be guaranteed, the smooth and monotonic trends observed, suggest that the pulses are actually close to the physical limit. Some facts could be established about energy requirement: The achievable bandwidth is limited by the available RF energy, and increasing pulse length seems to help guide the energy into the desired spectral region, but a certain minimum is required to cover the bandwidth. The relations that could be derived, however, are still not complete and need further refinement.

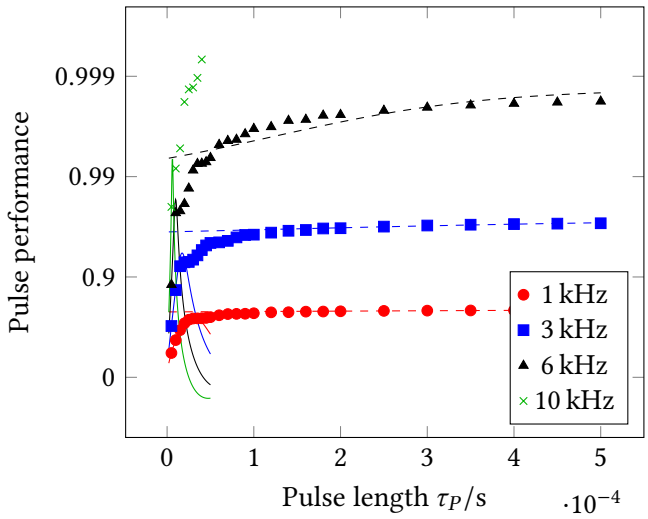

(a) Excitation pulses

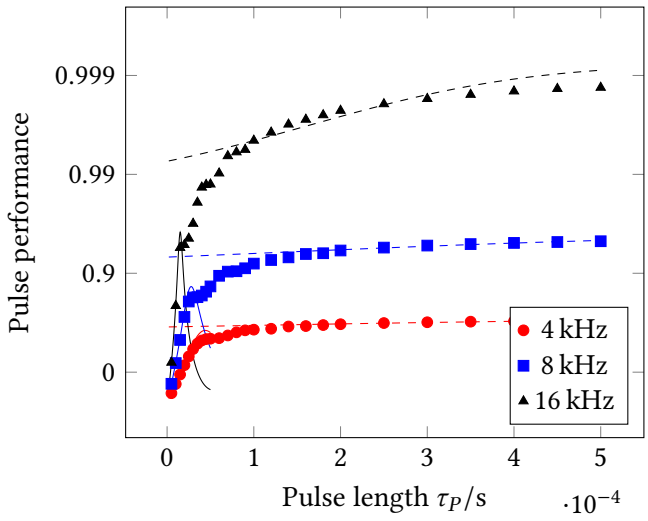

(b) Inversion pulses

Figure 3.7: Pulse quality with increasing pulse length for varying RF energies. a) Excitation pulses; the quality of obtained pulses is shown along with the approximation for short pulses of Equation (3.29), and a fit for the quality of long pulses of Equation (3.31). b) Inversion pulse; the quality of obtained pulses is shown along with the approximation for short pulses of Equation (3.30), and a fit for the quality of long pulses of Equation (3.31).

3.5 RF Amplitude Dependent Effective Flip Angle Pulses

3.5.1 Adjustable Flip Angle

Besides the common 90°, 180°, exciation, and inversion pulses, many experiments in modern high resolution NMR spectroscopy require the application of a pulse with adjustable effective flip angle, often called β-pulse, as an important element. Depending on the pulse sequence, the β-pulse is either used as a mixing pulse in correlation experiments or as an excitation pulse for effective usage of polarization. Typical experiments involving β-pulse mixing are the β-COSY [65, 66], zz-spectroscopy [67–69], the z-COSY [70–72], the P.E.COSY [73], or the P.E.HSQC [74] and variants thereof [75]. The classical example for a β-pulse application, however, is the Ernst angle excitation that is used today in practically every ^{13}C-1D experiment worldwide and which relies on a relaxation-matched flip angle [76] which is also used in two-dimensional correlation experiments like the SOFAST-HMQC [77–80]. Finally, pulses with variable effective flip angle are a central element in Chapter 7 of this work.

Commonly used β-pulses are rectangular-shaped hard pulses with well-known limitations. Especially in experiments using optimized flip angle pulse excitation involving nuclei with large bandwidths like ^{13}C, it would therefore be desirable to have broadband offset-compensated shaped pulses available that allow uniform excitation with an adjustable variable flip angle. While a multitude of broadband composite and shaped pulses with a specific effective flip angle have been reported, a systematic search for corresponding broadband pulse shapes with adjustable effective flip angle is not available. Besides very long, conctruction principle-derived adiabatic composite pulses, the only shaped pulse to be considered, is the polychromatic pulse shape [81] that was optimized for 90° excitation, but which features an RF amplitude dependent flip angle somewhat unintentionally. It has been our aim to use optimal control algorithms to optimize offset-compensated excitation pulses with RF amplitude dependent flip angles that are referred to as RADFA pulses in the following.

3.5.2 RADFA Implementation

The Hamiltonian of the system is rewritten to simplify integrating the RF amplitude dependence. During a shaped pulse consisting of N individual pulses of constant amplitude and phase, indexed by k and each of duration Δt, the resulting Hamiltonian during a pulse can be written as

$$\mathcal{H}_k\left(\Omega_i, \alpha_j\right) = \frac{2\alpha_j}{\pi}\left(u_{\mathrm{x},k} \cdot \mathbf{I}_\mathrm{x} + u_{\mathrm{y},k} \cdot \mathbf{I}_\mathrm{y}\right) + \Omega_i \cdot \mathbf{I}_\mathrm{z} \tag{3.32}$$

with the controls $u_{\mathrm{x},i}$ and $u_{\mathrm{y},k}$, the effective flip angle α_j, and the offset Ω_i. The values for the RF amplitude $u_{\mathrm{x},i}$ and $u_{\mathrm{y},k}$ are multiplied with the overall effective flip angle α_j, therefore

the scaling of the RF amplitude is directly correlated to the target flip angle. The flip angle dependency is now included in all of the following matrices. Via the flip angle-dependent propagators

$$U_{\text{pulse}}\left(\Omega_i, \alpha_j\right) = \prod_{k=1}^{n} exp\left(i\mathcal{H}_k\left(\Omega_i, \alpha_j\right)\Delta t\right), \tag{3.33}$$

the spin density operator ρ_{F} at the end of the pulse is easily calculated using

$$\rho_{\text{F}}\left(\Omega_i, \alpha_j\right) = U_{\text{pulse}}\left(\Omega_i, \alpha_j\right)^{\dagger} \cdot \rho_{\text{init}} \cdot U_{\text{pulse}}\left(\Omega_i, \alpha_j\right), \tag{3.34}$$

where the initial density matrix typically fulfills the equilibrium condition $\rho_{\text{init}} = \mathbf{I}_{\text{z}}$ for an excitation pulse. With the flip angle-dependent target density operator

$$\rho_{\text{T}}\left(\alpha_j\right) = \mathbf{I}_{\text{z}}\cos(\alpha_j) + \mathbf{I}_{\text{x}}\sin(\alpha_j) \tag{3.35}$$

in the xz plane, the final quality factor or cost function Φ_{RADFA} results in the sum

$$\Phi_{\text{RADFA}} = \frac{1}{n_\alpha, n_\Omega}\sum_{j=1}^{n_\alpha}\sum_{i=1}^{n_\Omega}\langle\rho_{\text{T}}\left(\alpha_j\right)|\rho_{\text{F}}\left(\Omega_i, \alpha_j\right)\rangle \tag{3.36}$$

over all n_α effective flip angles and n_Ω frequency offsets. This cost function is used in the GRAPE algorithm as explained in the beginning of this chapter. To limit the RF power, two restrictions were used. In one set of optimizations, the RF power was limited according to a maximum amplitude [63]

$$\sqrt{(u_{\text{x},k})^2 + (u_{\text{y},k})^2} \;\leq\; u_{\text{RF}}^{\text{max}} = 2\pi\nu_{\text{RF}}^{\text{max}}, \tag{3.37}$$

with $\nu_{\text{RF}}^{\text{max}} = 10\,\text{kHz}$. In another set, the RF power was restricted according to the maximum average RF power [64]

$$\frac{1}{n}\sum_{k=1}^{n}\{(u_{\text{x},k})^2 + (u_{\text{y},k})^2\} \;\leq\; (u_{\text{RF}}^{\text{max}})^2 = 4\pi^2(\nu_{\text{RF}}^{\text{max}})^2, \tag{3.38}$$

with again $\nu_{\text{RF}}^{\text{max}} = 10\,\text{kHz}$.

3.5.3 Proof of Principle

In initial tests, several ranges of flip angles typically covering a 30° bandwidth were optimized and simulated. Surprisingly it turned out that corresponding pulse shapes, when fulfilling the condition of a linear increase of the flip angle with the RF amplitude, will perform well for the

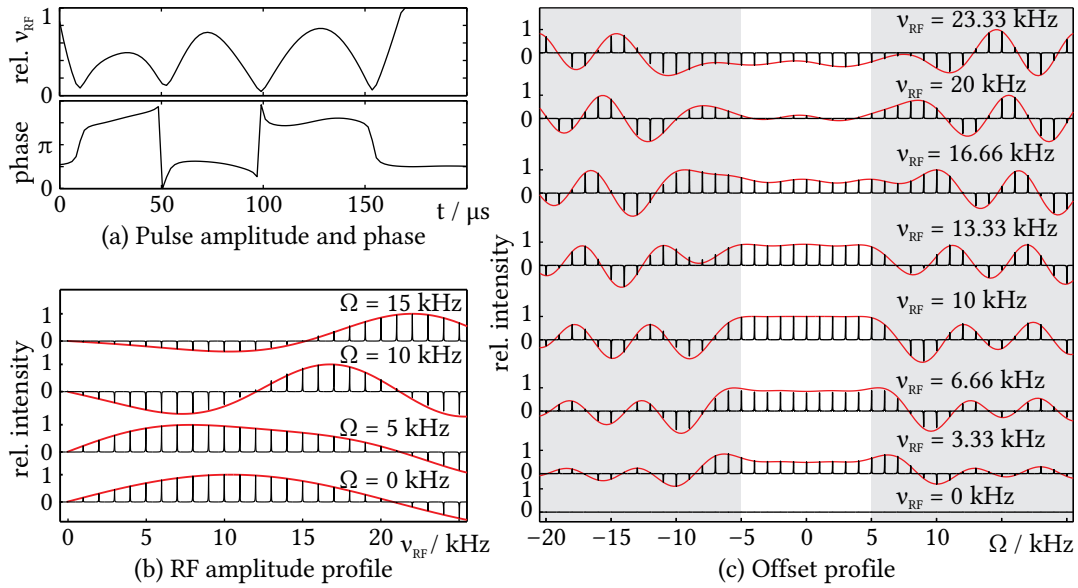

Figure 3.8: a) Pulse shape of a 200 µs RADFA pulse optimized for a bandwidth of 10 kHz using the optimal control-derived GRAPE algorithm with the quality factor derived in the theory section. b) Profile of the $\mathbf{I}_z \rightarrow \mathbf{I}_x$ transfer of the pulse with respect to RF amplitude at four different offsets from 0 to 15 kHz. Experimentally obtained spectra of residual HDO in doped D_2O in increments of 1 kHz are shown as well as the theoretical performance as a solid line on top of the spectra. c) Experimental and theoretical offset profiles of the pulse at various RF amplitudes corresponding to optimized effective flip angles that are multiples of 30°.

entire range of flip angles α of 0 to 180°. Further optimizations therefore were run over the full useful range up to 180°.

For evaluating the setup of the algorithm and for checking experimental feasibility, two broadband RADFA pulses of 200 µs and 300 µs duration were optimized for bandwidths of $\Delta\Omega = 10$ kHz and $\Delta\Omega = 25$ kHz, respectively. Flip angles in both cases were matched to fulfill the linear dependence starting with the trivial condition that $\alpha = 0°$ corresponding to a maximum RF amplitude $\nu_{\mathrm{RF}}^{\mathrm{max}} = 0$ kHz and the largest flip angle $\alpha = 180°$ to $\nu_{\mathrm{RF}}^{\mathrm{max}} = 20$ kHz. For the optimization the number of check points were chosen to $n_\alpha = 15$ and $n_\Omega = 40$ with a digitization of the pulse shape of $\Delta t = 2$ µs resulting in an overall calculation of 60 000 and 90 000 propagation steps per evaluation of the quality factor. Two Pulse shapes with $\Phi = 0.9995$ and $\Phi = 0.9655$, respectively, were obtained after optimizing over night on a dual core PC. They are shown in Figures 3.8a and 3.9a together with a PC53** pulse originally optimized for wideband 90° excitation [81] of 1.37 ms duration and an effective bandwidth of approximately $\Delta\Omega = 15$ kHz for comparison in Figure 3.10a.

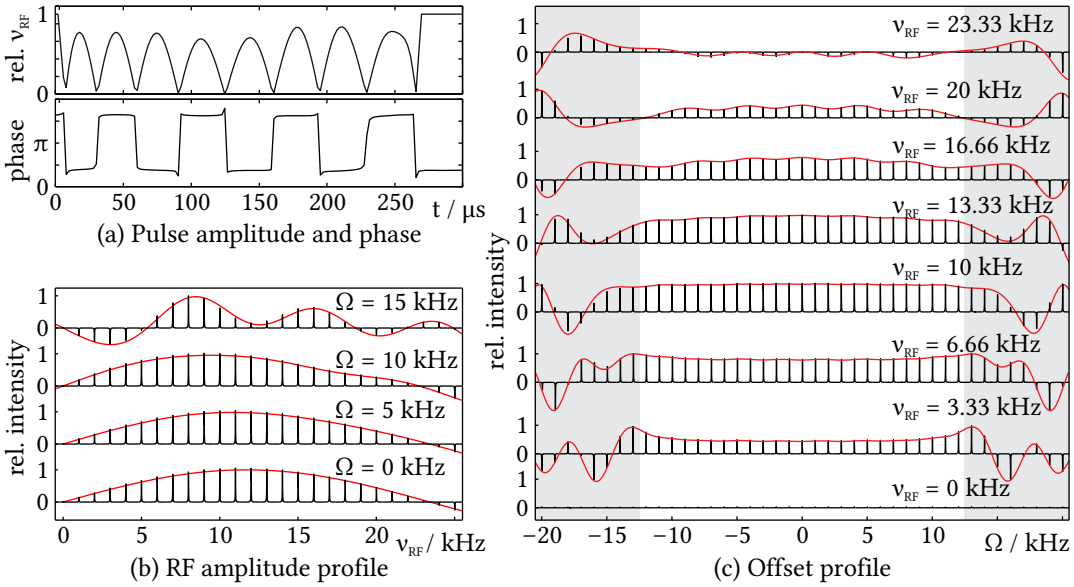

Figure 3.9: a) Pulse shape of a 300 µs RADFA pulse optimized for a bandwidth of 25 kHz using the optimal control-derived GRAPE algorithm with the quality factor derived in the theory section. b) Profile of the $\mathbf{I}_z \rightarrow \mathbf{I}_x$ transfer of the pulse with respect to RF amplitude at four different offsets 0 to 15 kHz. Experimentally obtained spectra of residual HDO in doped D_2O in increments of 1 kHz are shown as well as the theoretical performance as a solid line on top of the spectra. c) Experimental and theoretical offset profiles of the pulse at various RF amplitudes corresponding to optimized effective flip angles that are multiples of 30°.

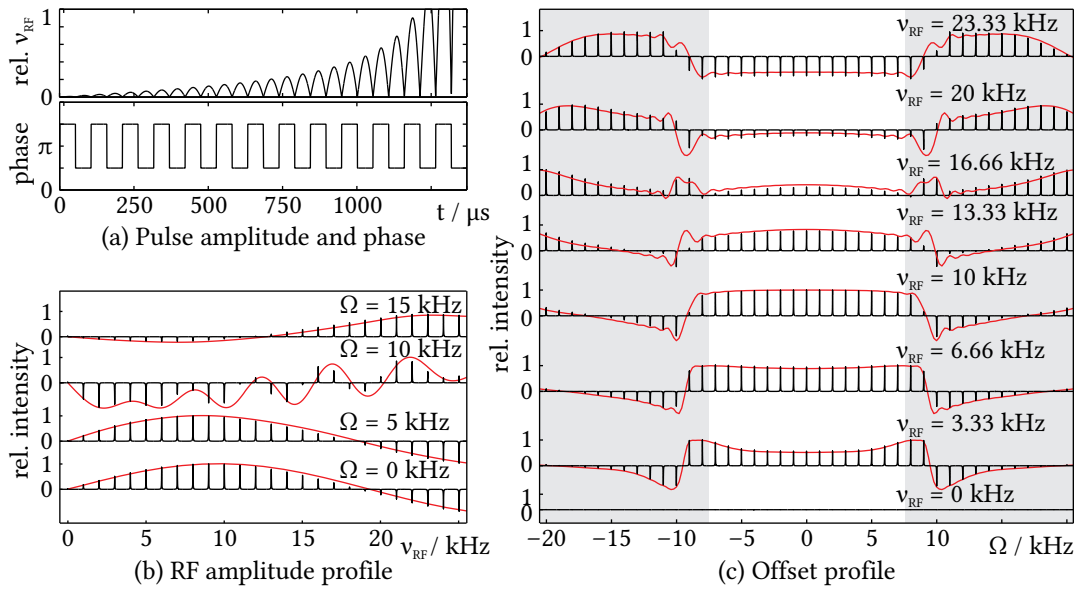

Figure 3.10: a) Pulse shape of a previously reported 1.37 ms PC53** polychromatic pulse [81] optimized for wideband excitation of approximately 15 kHz. b) Profile of the $\mathbf{I}_z \rightarrow \mathbf{I}_x$ transfer of the pulse with respect to RF amplitude at four different offsets from 0 to 15 kHz. Experimentally obtained spectra of residual HDO in doped D_2O in increments of 1 kHz are shown as well as the theoretical performance as a solid line on top of the spectra. c) Experimental and theoretical offset profiles of the pulse at various RF amplitudes corresponding to optimized effective flip angles that are multiples of 30°.

The two RADFA pulses and the PC53** pulse were then straightforwardly implemented on the spectrometer Ernst, a 600 MHz Avance III NMR Spectrometer equipped with a TCI Probehead and TopSpin 3.2. For evaluation of the excitation properties the transfer to the corresponding x axis was measured with respect to variations in RF amplitudes and offsets using a D_2O sample doped with $CuSO_4$ with an effective relaxation time of $T_1 = 210$ ms and the pulse sequence with purge gradients for removal of resulting magnetization along y and z axis shown in Figure 3.11.

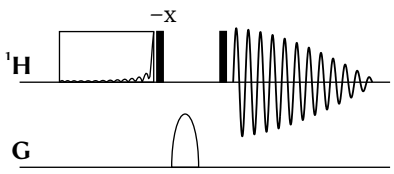

Figure 3.11: Pulse sequence used to measure the $\mathbf{I}_z \rightarrow \mathbf{I}_x$ transfer of shaped pulses. After application of the desired pulse shape at offset Ω, the resulting x magnetization is flipped along z via the first 90° pulse onresonant. After dephasing of all transverse magnetization using a purge gradient, remaining magnetization is flipped back along x before detection.

The pulse length of a rectangular pulse was calibrated experimentally by finding the power level for zero-crossing of a 360° pulse of 50 µs duration, corresponding to an RF amplitude of 20 kHz. After calculating corresponding power levels for RF amplitudes from 0 to 25 kHz, a list with 26 power level entries was incorporated into the pulse program to cover the effective range of flip angles from 0° to 225°. The series of experiments was measured for offsets of 0 kHz, 5 kHz, 10 kHz, and 15 kHz for all three pulse shapes. The resulting amplitude profiles are shown in Figures 3.8b, 3.9b and 3.10b.

Corresponding theoretical efficiencies for the $\mathbf{I}_z \rightarrow \mathbf{I}_x$ transfer were calculated by simulationof the pulse shapes with a self-written program and added in the figures for direct comparison. In addition, a bandwidth of 40 kHz was covered for maximum RF amplitudes ν_{RF} of 0 kHz, 3.33 kHz, 6.66 kHz, 10 kHz, 13.33 kHz, 16.66 kHz, 20 kHz, and 23.33 kHz; corresponding to theoretical effective flip angles of 0°, 30°, 60°, 90°, 120°, 150°, 180°, and 210°, by 41 offset increments using the `spoffs` parameter in TopSpin for defining the offset and setting `spoal` to 1.0 to ensure correct phase alignment for the excitation pulses. Corresponding experimental results together with the theoretical transfer efficiencies are given in Figures 3.8b, 3.9b and 3.10b. In all cases, the pulse shapes agree well with the theoretically predicted transfers and the desired quality criterion for RF amplitude-dependent excitation, which opens up the possibility for a systematic study of physical limits of broadband RADFA pulses.

3.5.4 Exploring the Limits I: RF Amplitude-Restricted RADFA Pulses

The optimizations from the previous section were repeated in a systematic study. Similar settings where used, n_α and n_Ω were set to 15 and 40, respectively, for varying bandwidths of 10 kHz, 15 kHz, 20 kHz, 25 kHz, and 30 kHz and maximum RF amplitudes of 0 to 20 kHz corresponding to effective flip angles α of 0 to 180°. For each bandwidth and pulse length, 100 starting shapes were created by spline interpolation of 10 randomly chosen points. The digitization pulse length Δt was generally chosen to be 2 µs with overall lengths of the pulse shape starting at 10 µs. The optimization was run until local convergence was reached for all 100 pulse shapes. If the best pulse quality was below $\Phi_{\text{cutoff}} = 0.995$, pulse length was increased and a new set of 100 starting shapes was generated unless the maximum pulse length of 1 ms was reached. For amplitude-limited optimizations of RADFA pulses, the RF amplitude was strictly cut off when nominal RF amplitude $\frac{2\alpha}{\pi}\nu_{\text{RF}}^{\max}$ with $\nu_{\text{RF}}^{\max} = 10\,\text{kHz}$ was reached. Overall about 15 000 RF amplitude-limited pulse shapes were optimized out of which the best 150 shapes were used for further analysis.

Figure 3.12 shows the resulting time optimality curves for the five different bandwidths. With increasing bandwidth, apparently the achievable pulse performance decreases significantly. While bandwidths of 10 kHz and 15 kHz have not yet reached a plateau within the optimization range, the other three bandwidths of 20 kHz, 25 kHz, and 30 kHz do not show significantly increased performance with longer pulse durations (longer than approximately 200 µs), which seems to indicate a physical limit for the given task. For pulse durations up to 200 µs clearly the previously reported stepwise increase in pulse performance [63] is observed. In Figure 3.13 four representative RF amplitude-restricted pulse shapes of different pulse durations τ_P and bandwidths $\Delta\Omega$ are shown together with their theoretical pulse performance. While very short pulses are remeniscent of composite pulses, longer pulse shapes show more and more wave-like oscillations with an approximately 35 µs long maximum amplitude pulse as the final element. This profile is very similar to previously reported relaxation-optimized excitation pulses [55] and polychromatic pulses [81]. Within the optimization limits the pulses generally perform very good. Best performance in all cases is reached for small effective flip angles α typically up to 90°. Also a kind of oscillatory behavior of the performance with respect to the offset and with decreasing frequency towards larger effective flip angles can be identified. At the edges of the optimized bandwidths corresponding pulse performances decrease noticably, but no abrupt decrease can be seen within the simulated range.

The maximum overall quality factors for the five different bandwidths is finally shown in Figure 3.14. While for a bandwidth of 10 kHz almost perfect excitations with $\Phi = 0.9995$ can be obtained, the performance quality reduces significantly for larger offsets, with the best

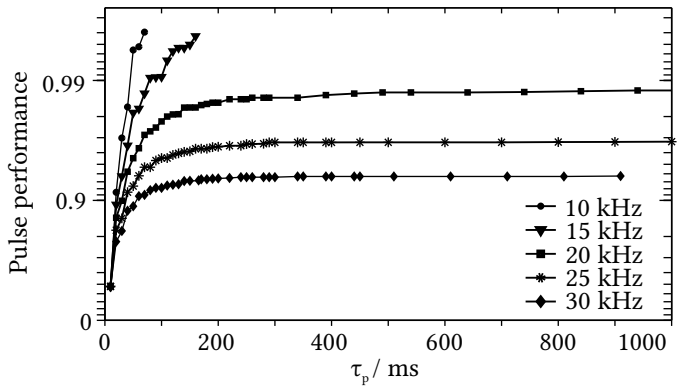

Figure 3.12: Time optimality curves for RF amplitude-limited broadband RADFA pulses for offset bandwidths of 10 kHz, 15 kHz, 20 kHz, 25 kHz, and 30 kHz. For each pulse length τ_P and bandwidth the best obtained quality factor Φ_{RADFA} out of 100 individual optimizations with restricted RF amplitude according to with $\nu_{\mathrm{RF}}^{\mathrm{max}} = 10\,\mathrm{kHz}$ is shown.

quality factor for 30 kHz bandwidth reaching $\Phi = 0.937$. The comparison with a rectangular hard pulse of 10 kHz RF amplitude, however, shows the significantly improved performance at all bandwidths. As many applications allow a phase correction after acquisition of spectra, we also allowed an ideal first order phase correction for the rectangular pulse, which shows a much improved performance of the hard pulse, but quality factors for RADFA pulses are still distinctly better in all cases. We also calculated the performance of a rectangular pulse when excitating into the xy plane without any phase restrictions, which lead to essentially identical results compared to the phase-corrected rectangular pulse (data not shown).

Not many shaped pulses have been optimized with comparable performances to the RADFA pulses introduced here. Closest are probably the polychromatic pulses with very similar looking overall pulse shapes with an oscillatory part in the beginning and a final element with maximum RF amplitude [81]. The performance of the so-called PC53** pulse is given in Figure 3.14 for comparison. Its performance resembles that of a phase-corrected hard pulse for bandwidths up to 15 kHz before the quality factor is significantly reduced for larger bandwidth. This can easily be understood as the PC53** pulse has been optimized as a selective pulse with a bandwidth corresponding to 12 kHz for an RF amplitude of 10 kHz and a pulse length of 1.37 ms. Another polychromatic pulse, known as PC9 [77], is optimized for an even smaller bandwidth so that we did not include it in the comparison.

3.5.5 Exploring the Limits II: RF Power-Restricted RADFA Pulses

While RF amplitude-restricted RADFA pulses are certainly very important for most practical applications, restrictions with respect to the applied RF power may equally apply, e. g.for re-

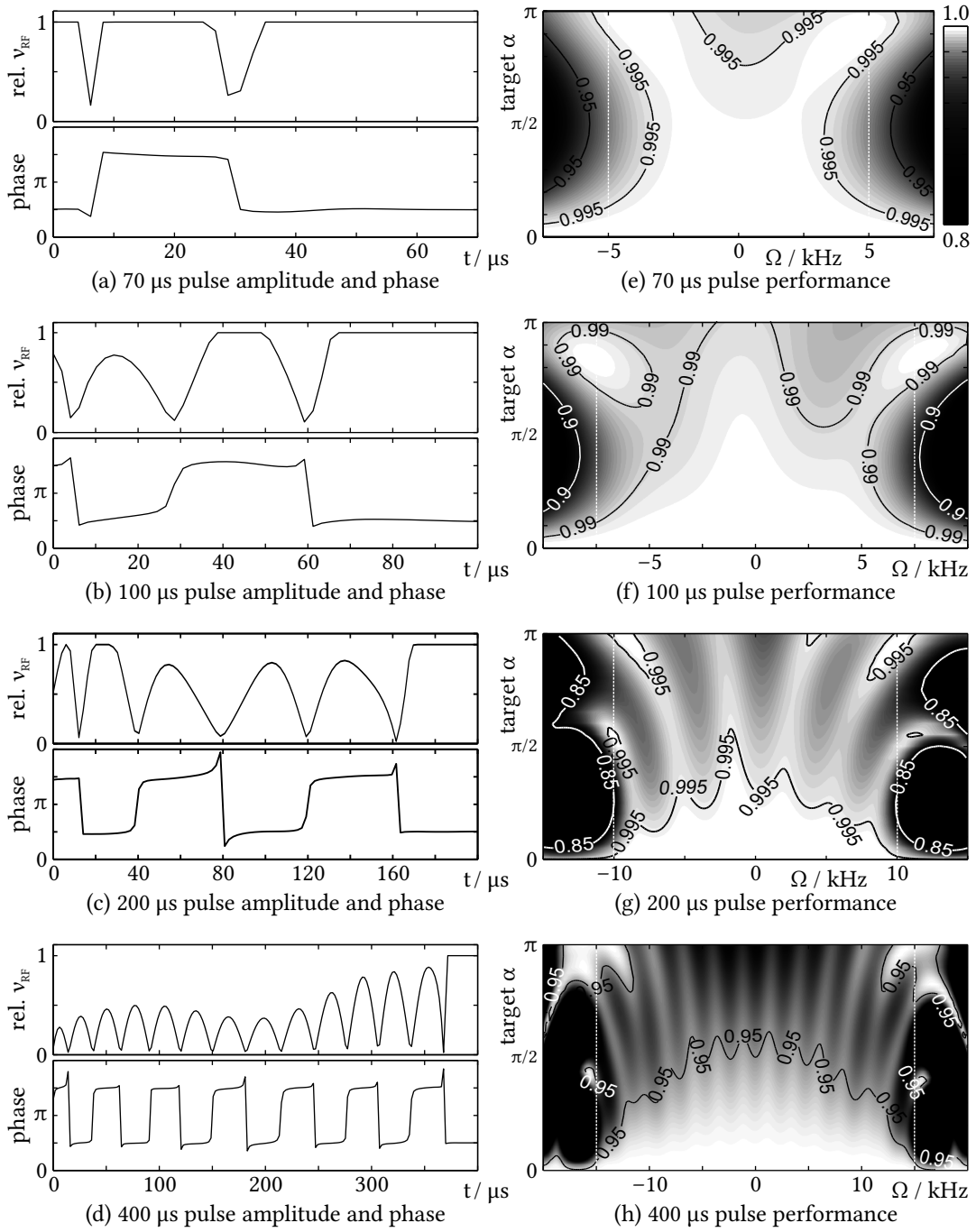

Figure 3.13: Selected time-optimal broadband RF amplitude-restricted RADFA pulse shapes (a–d) obtained from optimizations introduced in Figure 3.12 and their theoretical performances with respect to offset Ω and effective flip angle α (e–f). a, e) 70 µs pulse optimized for the bandwidth $\Delta\Omega = 10\,\text{kHz}$; b, f) 100 µs pulse optimized for $\Delta\Omega = 15\,\text{kHz}$; c, g) 200 micros pulse optimized for $\Delta\Omega = 20\,\text{kHz}$; d, h) 400 micros pulse optimized for $\Delta\Omega = 30\,\text{kHz}$;

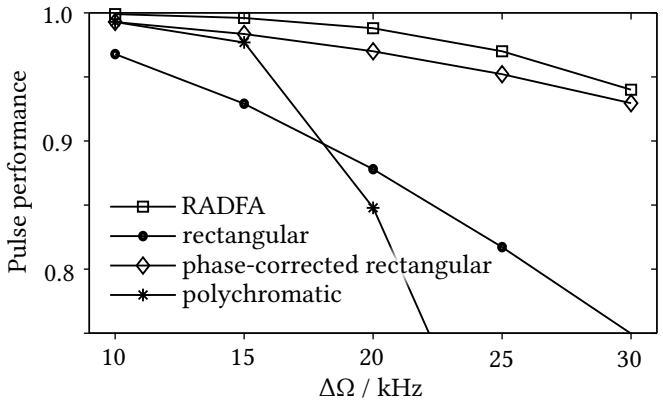

Figure 3.14: Comparison of best obtained quality factors for RADFA pulses with rectangular and polychromatic pulses. For rectangular pulses quality factors Φ_{RADFA} are shown for the plain pulse and after an additional ideal linear phase correction. As the polychromatic pulse [81] is defined as a selective excitation pulse, a fair comparison of the pulse with maximum RF amplitude of 10 kHz is only valid for bandwidths up to 12 kHz.

petitive pulse sequence elements or application in imaging. In addition, they are of interest from a theoretical point of view. In the presented study, RF power-limited RADFA pulses were optimized for bandwidths of 20 kHz, 40 kHz, 60 kHz, 80 kHz, and 100 kHz and pulse lengths from 10 to 250 µs while keeping all other parameters identical to optimizations performed for the RF amplitude-limited case introduced in the previous section. In the optimizations the limit was maintained by calculating the average of squared amplitudes for $\alpha = 90°$ and downscaling all individual amplitudes whenever the value exceeded with $\nu_{\mathrm{RF}}^{\mathrm{max}} = 10\,\mathrm{kHz}$ in Equation (3.38). The maximum allowed root mean square RF power therefore is equal to a rectangular pulse with constant RF amplitude of 10 kHz and same pulse duration. Altogether 7600 RF power-limited pulses were optimized out of which 76 pulse shapes were used for further analysis.

The obtained overall quality factors for the five different bandwidths are summarized in Figure 3.15 with respect to pulse duration τ_P. For any given bandwidth the performance increases almost exponentially with pulse duration, showing no inherent physical limit of the problem. When comparing the different bandwidths it seems on the other hand that there is also no limit with respect to the achievable bandwidth. Looking at a constant performance of $\Phi_{\mathrm{RADFA}} = 0.99$, for example, the pulse shape for $\Delta\Omega = 10\,\mathrm{kHz}$ has a duration of 50 µs and the pulse lengths of shapes with same performance increase by approximately 36 µs for every additional 20 kHz in bandwidth (see dotted guide to the eye in Figure 3.15).

Again, four representative pulse shapes are given with their amplitudes, phases, and theoretical performance with respect to offset and effective flip angle in Figure 3.17. Independent of the pulse length the same class of pulses can be observed. In general, oscillations with over time in-

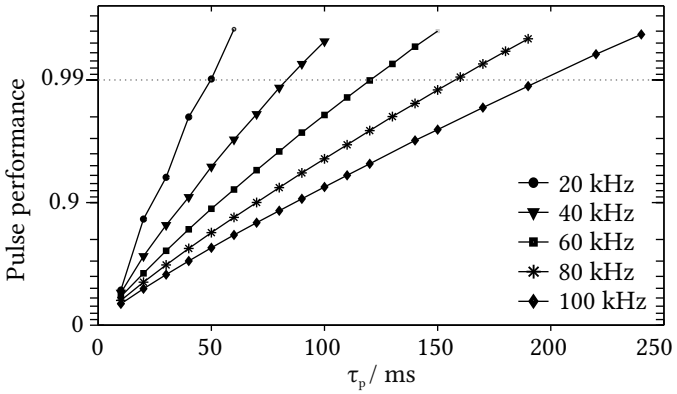

Figure 3.15: Time optimality curves for RF power-limited broadband RADFA pulses for offset bandwidths of 20 kHz, 40 kHz, 60 kHz, 80 kHz, and 100 kHz. For each pulse length τ_P and bandwidth the best obtained quality factor Φ_{RADFA} out of 100 individual optimizations with restricted RF power according to Equation (3.38) with $\nu_{\mathrm{RF}}^{\mathrm{max}} = 10\,\mathrm{kHz}$ is shown.

creasing RF amplitude are visible that culminate in a steep rise with the maximum RF amplitude always at the very end of the shape. It reminds to some extent on half a sinc-function and very similar pulse shapes have been found for RF power-restricted excitation pulses, so-called power-BEBOP pulses [64]. Apparently, within the pulse shapes RF energy is saved for a final burst. This behavior is also evident from Figure 3.16, where the maximum RF amplitudes of all shapes are drawn against the bandwidth $\Delta\Omega$. Clearly the addressable bandwidth is strongly correlated with the maximum RF amplitude at the end of the pulse shapes. The theoretical performance in Figure 3.17 indicates the same features that are already observed in the RF amplitude-restricted case. The best performance is achieved for small flip angles and a distinct oscillatory behavior with respect to offset can be seen, where the frequency of the oscillations increases with pulse duration and optimized bandwidth.

3.5.6 Discussion

Next to a viable cost function and an initial experimental proof of concept, the physical limits of broadband pulses with RF amplitude dependent effective flip angle (RADFA) have been explored considering both RF amplitude and RF power restrictions. Resulting pulse shapes are similar to previously reported shapes for relaxation-optimized [55] and polychromatic pulses [81] for the amplitude-restricted case and time-optimal power-BEBOP shapes [64] in the power-restricted case. Apparently maximum RF amplitudes are needed at the very end of pulse shapes for best results. It turns out that achievable performances are generally better than for corresponding hard pulses with the inherent advantage that no phase correction has to be

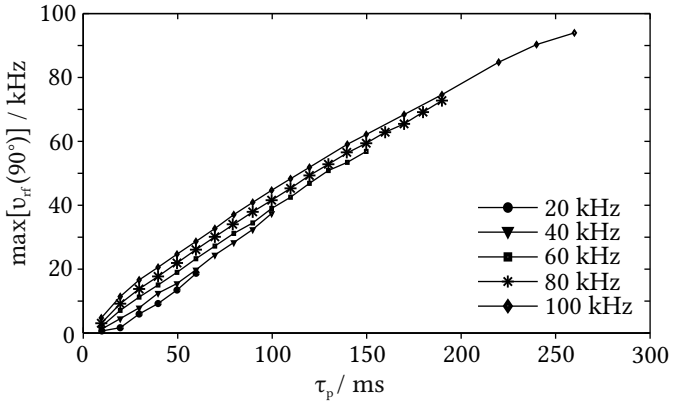

Figure 3.16: Maximum RF amplitudes of best obtained RADFA pulses from Figure 3.15 for the different offset bandwidths $\Delta\Omega$.

applied with the RADFA pulses. As the optimized pulses belong to the class of so-called point-to-point pulses [50] starting with $\mathbf{I}_z$ polarization, pulses are mainly designed for use as excitation pulses with variable effective flip angle, as for example routinely used in ^{13}C-1D experiments. In such cases the duration of corresponding pulse shapes is usually not critical, and best performing pulses should be used whatever their length.

When comparing RF amplitude-restricted and RF power-restricted pulses, it should be noted that minimum pulse lengths are much shorter and achievable bandwidths are by far larger for power-restricted pulses. The reason is obvious: apparently the maximum RF amplitude at the end of a pulse shape determines its performance; while the RF amplitude cannot exceed $\nu_{\mathrm{RF}}^{\mathrm{max}}$ in the first case, in power-restricted pulses the overall RF energy is saved for a final burst and resulting higher maximum RF amplitude – a behavior that has been observed previously for power-BEBOP pulses [64]. It should be noted that although relaxation has not been taken into account for the optimization, it can be expected that performance is good even for fast relaxing samples as most of the action during the pulse shape happens at the end similar to what has been observed for relaxation-optimized pulse shapes [55].

As with all RF pulses designed for a single spin-$\frac{1}{2}$ particle, corresponding pulse shapes can easily be scaled to desired properties. A RADFA pulse of twice the RF amplitude and half the duration τ_P, for example, will result in the same overall performance for twice the bandwidth. Equally, phase-modulation with a given frequency will result in a shifted offset dependence and shapes can be added in the conventional way to get the combined features of pulses. It should be further noted that for applications where a β pulse is used to create z magnetization for a z filter as is the case for example in the z-COSY experiment [70–72], the time-reversed pulse shape has to be used as with all excitation pulses.

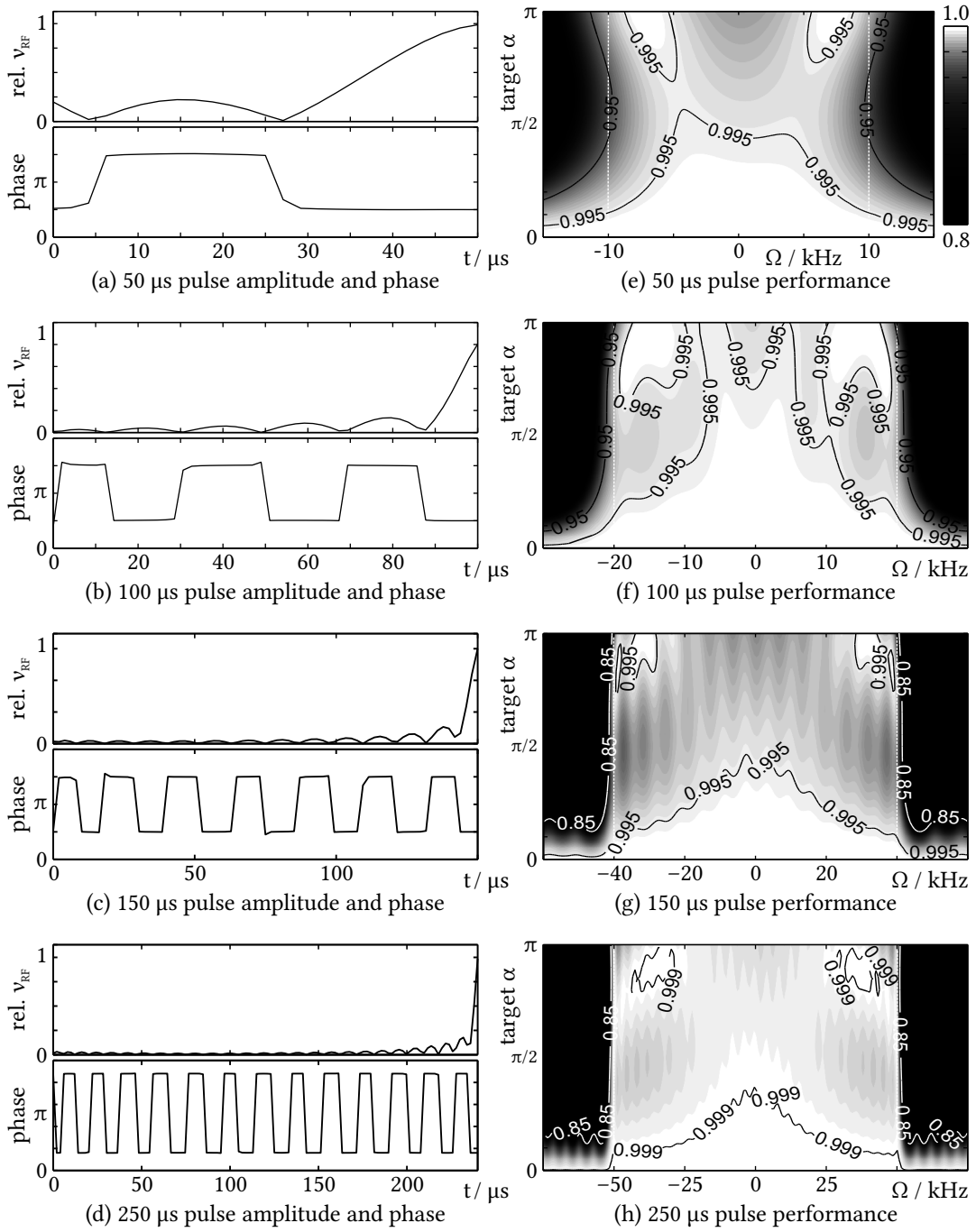

Figure 3.17: Selected time-optimal broadband RF power-restricted RADFA pulse shapes (a-d) obtained from optimizations introduced in Figure 3.15 and their theoretical performances with respect to offset Ω and effective flip angle α (e-f). a, e) 50 µs pulse optimized for the bandwidth $\Delta\Omega = 20$ kHz; b, f) 100 µs pulse optimized for $\Delta\Omega = 40$ kHz; c, g) 150 µs pulse optimized for $\Delta\Omega = 80$ kHz; d, h) 200 µs pulse optimized for $\Delta\Omega = 100$ kHz;

In summary, broadband pulses with RF amplitude dependent effective flip angles (RADFA) have been optimized and thoroughly characterized. Pulse performance is related to and generally better than hard pulses with equivalent maximum RF amplitudes. As resulting RADFA pulses are inherently phase compensated, their application is beneficial for use as an excitation pulse. Especially for fast pulsing experiments based on the so-called Ernst angle we foresee a number of advantages in the usage of corresponding pulse shapes.

3.6 Inversion pulses with Offset-Square Dependent Phase

3.6.1 Adiabatic Fast Passage and the Ideal Linear Frequency Sweep

Bloch first suggested adiabatic fast passage as a method of polarization inversion [22]. Pulse shapes like the hyperbolic secant [11] can approximate adiabatic inversion to a high degree, and one model to describe the inversion is a linear frequency sweep [10, 82]. An ideal linear frequency sweep is characterized by only two parameters; its sweep rate k and the pulse length τ_P. The frequency sweep at any point in time acts on a single frequency

$$\nu(t) = k\left(t - \frac{\tau_P}{2}\right) \tag{3.39}$$

that is inverted. Accordingly, the time of inversion of a spin with offset frequency ν_i is

$$t_i(\nu_i) = \frac{\nu_i}{k} + \frac{\tau_P}{2}. \tag{3.40}$$

The effect of the pulse is therefore, free evolution in the time up to t_i interrupted by a 180° rotation around a fixed axis, from now on called x axis, followed by free evolution until the end of the pulse at τ_P. Figure 3.18 illustrates the process.

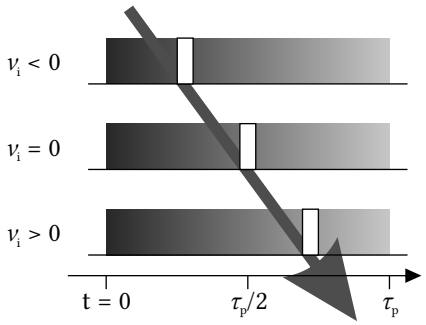

Figure 3.18: Model of the ideal linear frequency sweep. Spins are inverted consecutively within the pulse, at times depending on their offset frequency ν_i.

When an ideal frequency sweep is applied to transverse magnetization, the offset frequency will create a phase during the free evolution time. The 180° pulse inverts this phase. Spins at one end of the sweep width will be inverted at the beginning of the pulse and experience the whole pulse length of free evolution. Spins at the other end will undergo the free evolution first, but after the inversion at the end, the spins behave as if the free evolution time had negative duration. The effective time difference between the top and the bottom of the sample is therefore *twice* the length of the ideal linear frequency sweep.

Optimization of Linear Frequency Sweeps

An equivalent description is a 180° rotation around an axis that is rotated at the offset frequency. Since the time of inversion is also dependent on the frequency, the relative phase difference between the axis of rotation and the x axis is

$$\phi = \frac{2\pi}{k} \nu_i^2 \tag{3.41}$$

and the whole pulse can be written as an operator

$$U = \exp\left(-\mathrm{i}\pi\left(\mathbf{I}_\mathrm{x} \cdot \sin(\frac{2\pi}{k}\nu_i^2) + \mathbf{I}_\mathrm{y} \cdot \cos(\frac{2\pi}{k}\nu_i^2)\right)\right). \tag{3.42}$$

The optimization scheme is modified to obtain UR pulses and modified slightly further to create the special phase properties. While a broadband universal rotation pulse has the same target operator over the whole bandwidth, this optimization has a unique target for each offset point. Full calculation of a vector or matrix of target operators is possible, the memory requirement, however, is very high and calculation of this operator requires only a few operations. The target was therefore calculated on the fly for each iteration and offset point.

1. An initial shape $\mathbf{u}^{(0)}$ with N steps is generated from pseudo random numbers.
2. The following steps are performed for each offset frequency, B_1 amplitude and other parameters that should be compensated.
   (a) The target rotation $U_\mathrm{T}(\Omega)$ is calculated.
   (b) $U_\mathrm{pulse}(r)$, the pulse operator leading up to step r, including $\mathcal{H}_\mathrm{evo}$ and $\mathcal{H}_\mathrm{RF}$, is calculated by multiplying the time evolution operators U_k of each step k up to r.
   (c) The backwards pulse operator $\lambda(r)$ is calculated from the target operator U_T by multiplying with all the time evolution operators U_k from the last step N down to step r.

(d) The overall performance Φ and the gradient $\frac{\partial \Phi}{\partial u}$ pointing towards better performance for each point in time is calculated from $U_{\text{pulse}}(r)$ and $U_\lambda(r)$.

3. The mean gradient is calculated from U_{pulse} and U_{T} for all parameter combinations.

4. The shape is improved by applying the mean gradient $\mathbf{u}^{(a+1)} \longrightarrow \mathbf{u}^{(a)} + \epsilon \overline{\frac{\partial \Phi}{\partial u}}$.

5. The Steps 2–4 are repeated until any convergence criterion is fulfilled.

While quasi-adiabatic polarization inversion has been improved by moving towards non-linear frequency sweeps [83] and adiabatic inversion is usually outperformed by new, less restricted pulse shapes [13, 63, 84], some applications rely on the exact timing of a linear frequency sweep pulse or a pulse that mimics its behavior. One example is a single-scan 2D scheme [85, 86], in which different evolution times are introduced in different slices of the sample, and an acquisition method developed for MRI is used [87]. Corresponding experiments are called ultrafast experiments [88, 89]. Another important application is the suppression of so-called zero quantum coherence artifacts.

3.6.2 Suppression of Zero-Quantum Coherences

Polarization and Zero Quantum Coherence

Nowadays, NMR signals are usually processed to yield phase sensitive spectra, composed of a real and an imaginary part, whenever possible. A complex line shape consists of an absorptive and a dispersive contribution. As shown in Figure 3.19, the absorptive line features reduced linewidth, especially around the base of signals. While the change of sign in dispersive lines simplifies determination of the central frequency, it complicates spectra of overlapping peaks. EPR spectra conventionally use the dispersive representation but in NMR, in general, absorptive lines are highly desired, while the dispersive shape is sometimes unavoidable. The complex phase of spectra is therefore corrected in such a way, to include only the absorptive contribution in the real part of the spectrum and move the dispersive contribution to the imaginary part where it can be ignored. Superposition of both should be avoided, as the resulting peaks are distorted so that neither the maximum nor the zero crossing will indicate the central frequency, peak integrals will be affected, and lines will be broadened, reducing the effective resolution.

Internuclear coupling evolution is a common source of dispersive contribution that can often not be corrected by adjusting the global phase. Often this correlates with antiphase multiplet shape, giving rise to the multitude of effects shown in Figure 3.20. Absorptive in-phase multiplet shape is usually desired, while antiphase multiplets often contain additional information but also complexity. Further explanations of in-phase and antiphase multiplets are found in Chapter 4.

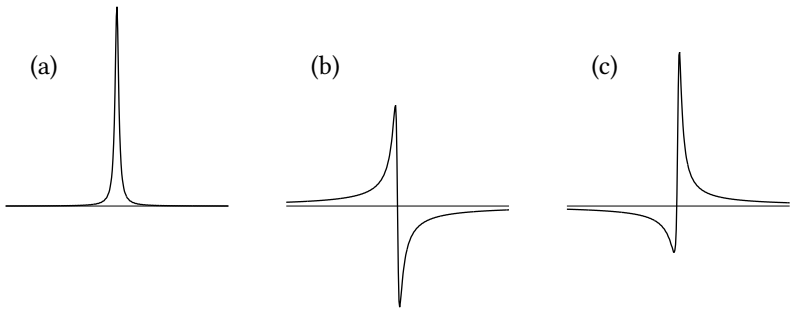

Figure 3.19: Examples of phases of a singlet. a) For an absorptive line the frequency evolution is cosine modulated; this corresponds to the real part of an ideally phased spectrum. b) For a dispersive line the frequency evolution is sine modulated; this corresponds to the imaginary part of an ideally phased spectrum. c) A mixed-phase lineshape contains sine and cosine contributions. This example was created by phase shifting the spectrum of a in the complex plane by approximately 60°.

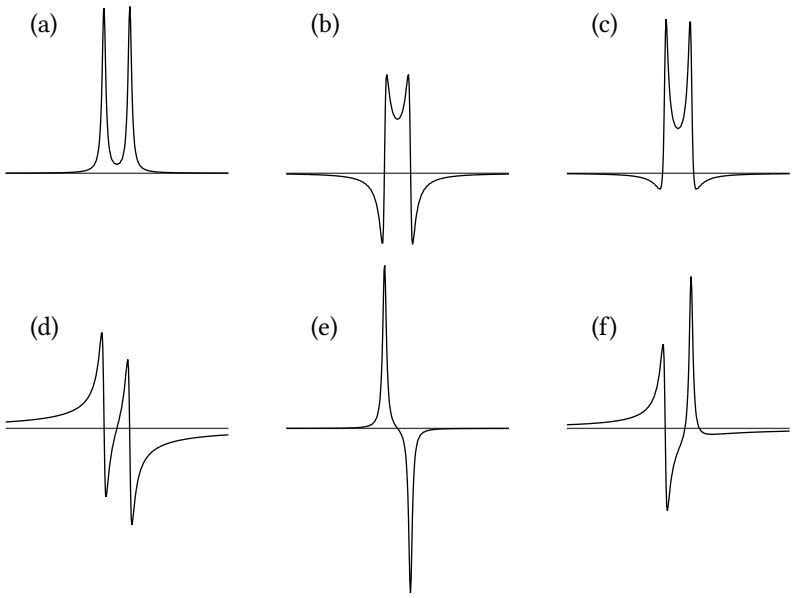

Figure 3.20: Examples of phases and lineshapes encountered in doublets. a) In an absorptive in-phase doublet all evolutions are cosine modulated. b) In a dispersive antiphase doublet the Larmor frequency evolution is cosine modulated while the coupling evolution is sine modulated. c) Combination of equal parts a and b. d) In a dispersive in-phase doublet the Larmor frequency evolution is sine modulated while the coupling evolution is cosine modulated. e) In an absorptive antiphase doublet all evolutions are sine modulated. f) Combination of equal parts a, b, d and e.

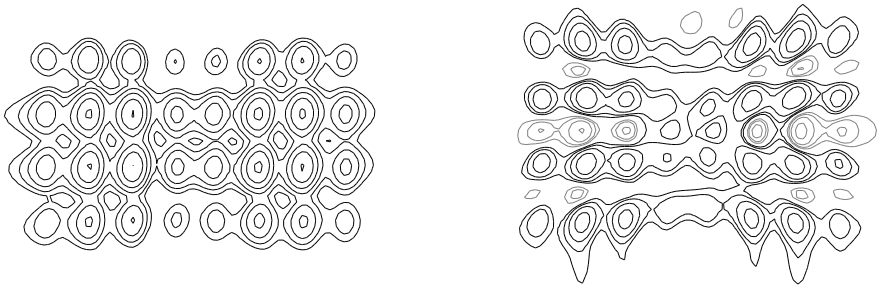

(a) Clean multiplet (b) Distorted multiplet

Figure 3.21: Multiplets obtained from a 2D CLIP-COSY experiment acquired on menthol. a) Sufficiently long z filter block results in a clean multiplet. b) Remaining ZQ contribution causes dispersive antiphase components, distorting the multiplet. Negative sign of intensity is indicated by gray contour lines.

In many experiments, magnetization giving rise to multiplets with combined dispersive antiphase and dispersive in-phase contributions cannot be separated from the desired magnetization by conventional methods of phase cycling or gradient selection. This happens when the desired and undesired magnetization have the same coherence order, like polarization, i. e. z magnetization, and zero quantum (ZQ) coherence.

Zero quantum coherence is a two-spin state in the transverse plane. In this entangled state, the two spins evolve with a zero quantum frequency Ω_{ZQ}, the difference of their Larmor frequencies. For homonuclear spins, the difference is only about a millionth of the Larmor frequency. While a pulsed magnetic field gradient quickly dephases and destroys regular transverse magnetization, ZQ terms experience only a millionth of the dephasing effect. An elegant way to still effectively suppress ZQ contributions was presented by Thrippleton and Keeler [90], using a z filter that is fundamentally based around the linear frequency sweep.

Like in the single-scan experiments mentioned in the last section, when a linear frequency sweep is applied during simultaneous application of a gradient, a position-dependent evolution time is introduced. The desired z magnetization is simply transformed into $-z$ magnetization, besides relaxation the varied evolution time has no effect. For the undesired ZQ coherences however, the varied evolution time introduces a ZQ phase shift over the sample, proportional to pulse length and ZQ frequency. When the signal is acquired subsequently, the individual artifact contributions from the sample slices cancel the macroscopic signal and a clean spectrum can be obtained. An example of a clean peak and a peak with remaining ZQ artifact contribution is shown in Figure 3.21.

Filter Duration and Artifact Intensity

The intensity of artifacts created by ZQ coherence is calculated by the integral over the whole volume. Assuming rectangular shape of the active volume, the intensity after a z filter of length τ_P is

$$S_{\mathrm{ZQ}} = \frac{\sin\left(f \cdot 2\pi\Omega_{\mathrm{ZQ}}\tau_P\right)}{f \cdot 2\pi\Omega_{\mathrm{ZQ}}\tau_P}. \tag{3.43}$$

The factor f is the evolution time difference between the top and the bottom part of the sample. $f = 2$ for an ideal linear frequency sweep, in reality, however, good pulses can only reach $f = 1$, corresponding to the full pulse length being active for dephasing. To ensure complete suppression of ZQ artifacts, filter elements have to be significantly longer than the lowest ZQ period $1/\Omega_{\mathrm{ZQ}}$ expected in the spectrum. Often this means durations of 20 to 100 ms. Such long delays, however, create new problems. For the duration of the z filter element, relaxation occurs, and transfer between spins takes place by NOE or strong coupling evolution. These effects cannot be prevented, and are best addressed by keeping the z filter elements as short as possible and select the pulses that create the linear frequency sweep carefully by their dephasing efficiency f.

Dephasing Efficiency of Pulse Classes

In the original publication, quasi-adiabatic linear frequency sweeps were used for the z filter elements [90]. When sufficiently long, i. e. 20 to 50 ms, these pulses are very close to the physical maximum of $f = 1$, and the actual choice of pulse shape plays no important role [91]. Shorter adiabatic pulses, however, lose a large part of that efficiency, since some time is required for the smooth amplitude ramp at the ends of the shape. An adiabatic chirp pulse of 2 ms length has $f \approx 0.65$, further reduction to 1 ms length lowers the dephasing efficiency to $f \approx 0.5$.

The OCT algorithm allows optimization towards arbitrary target phase separation and therefore arbitrary dephasing efficiency f. However, increasing f above the physical limit of 1 did not yield acceptable pulses. Instead, good pulses were obtained with 0.5 ms, 1 ms, and 2 ms pulse length and $f = 0.9$ with 20 kHz maximum RF amplitude and 40 kHz Bandwidth. In comparison with short adiabatic pulses, the OCT derived pulse shapes have up to twice the artifact suppression power. Figure 3.22 shows the expected artifact intensity versus frequency separation of ZQ terms. Using long filter elements, the difference between shapes vanishes, but the highest gains with respect to artifact reduction are achieved in the time of the first ZQ dephasing period, i. e. $\tau_P < 1/(f\Omega_{\mathrm{ZQ}})$.

Direct comparison of ZQ artifact suppression is not that easy. To prepare magnetization with high ZQ coherence content, the pulse sequence shown in Figure 3.23 was devised. The

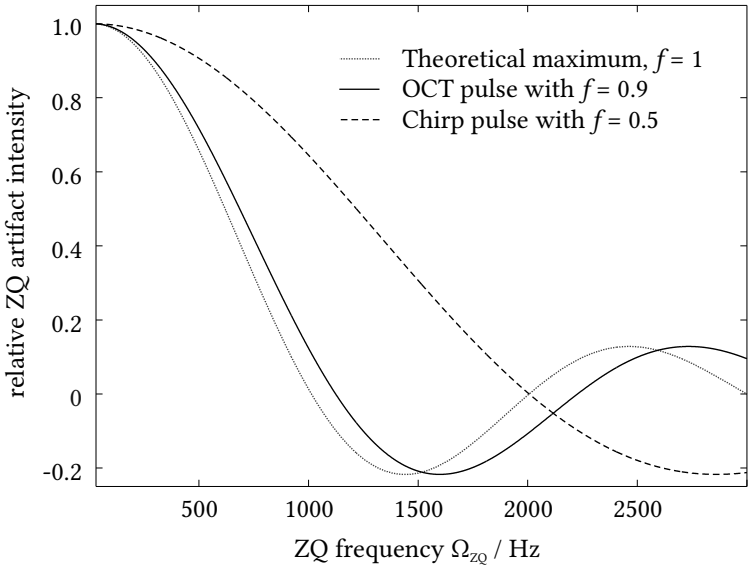

Figure 3.22: Simulation of zero quantum (ZQ) artifact intensity versus ZQ frequency Ω_{ZQ} for 1 ms long pulses of different dephasing efficiency f. This is an illustration of results of Equation (3.43). The theoretical limit is dotted in gray, an OCT pulse with $f = 0.9$ achieves the suppression drawn in solid black, and the intensity for a chirp pulse with $f = 0.5$ is dashed black. The largest part of the artifact intensity is removed in the first ZQ dephasing period, here the difference between shapes is most pronounced.

delay Δ was varied from 0 to $1/J_{HH}$, and highest ZQ contribution is obtained for $0.5 \cdot 1/J_{HH}$. The sequence was used with a 1 ms chirp pulse with $f \approx 0.5$ and an OCT pulse of equal length with $f = 0.9$. The effective evolution times of the pulses are 500 µs and 900 µs, respectively. The methyl doublet of L-Alanine in D_2O was used for the comparison, here $J_{HH} \approx 7$ Hz and $\Omega_{ZQ} \approx 1385$ Hz. The first zero crossing and sign inversion of artifact intensity expected around $1/\Omega_{ZQ} \approx 722$ ms. Figure 3.24 displays the signal shape obtained with the two pulses. The artifact is visible as dispersive contribution. The OCT pulse shows reduced artifact intensity. Additionally the sign of the artifact is inverted compared to the chirp pulse, confirming the theoretical concept. These OCT pulse shapes and longer chirp pulses are utilized as key elements in the CLIP-COSY experiment presented in Chapter 4.

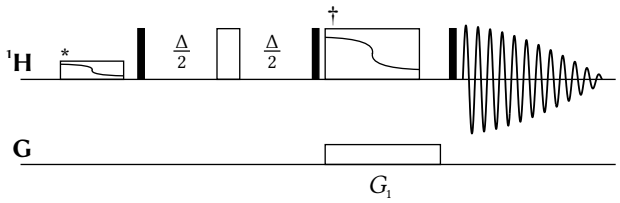

Figure 3.23: Pulse sequence for the controlled preparation of ZQ coherence in a two-spin system and subsequent elimination using a z filter block. The pulse labeled $*$ is a selective inversion pulse applied to one of the spins. The pulse labeled † is a linear-phase inversion pulse as described in this chapter. The gradient in combination with this pulse constitutes a z filter element as presented in [90]. The delay Δ is matched to $1/2J_{HH}$ for maximum ZQ contribution. Filled black rectangles stand for hard 90° pulses, unfilled rectangles for hard 180° pulses. All pulses are x pulses.

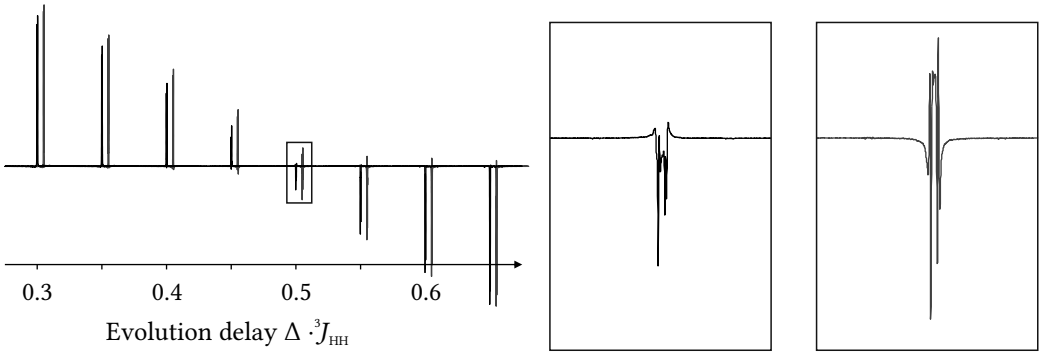

(a) Lineshape for increasing Δ (b) OCT pulse (c) Chirp pulse

Figure 3.24: Line shapes of doublets after application of a *z* filter element. The methyl doublet of L-Alanine in D_2O is shown with increasing Δ, acquired via the sequence shown in Figure 3.23. The spectrum acquired with a *z* filter block utilizing a 1 ms OCT pulse is drawn in black. The same spectrum acquired with a chirp pulse in drawn in gray. a) The peak shape changes with increasing *J* evolution delay Δ. Highest ZQ contribution is obtained for $\Delta = 0.5 \cdot 1/J$. The OCT and the chirp pulse remove a part of the antiphase contribution, thereby reducing the signal intesity. b) One peak obtained with the OCT pulse. c) One peak obtained with the chirp pulse. The sign of the absorptive signal component is negative in both cases, the sign of the dispersive artifact is different, the higher effective evolution time of the OCT pulse has allowed dephasing beyond the first intensity zero crossing.

3.7 RADFA Pulses with Linear Phase Evolution

An on-resonant, rectangular pulse is always the shortest pulse that can achieve a given rotation around an axis in the xy plane. Shaped pulses, with compensation towards certain perturbations or other special features included in the optimization, are significantly longer, often more than an order of magnitude. In multi pulse sequences that include delays, like 2D NMR experiments, the sum of delays usually exceeds the combined length of the pulses, so the difference is less pronounced. One way to reduce experiment duration at the pulse-length level, is to optimize a pulse shape that behaves like a shorter pulse followed by a delay, as illustrated in Figure 3.25. As pulses are followed by delays in many experiments, this is a promising approach.

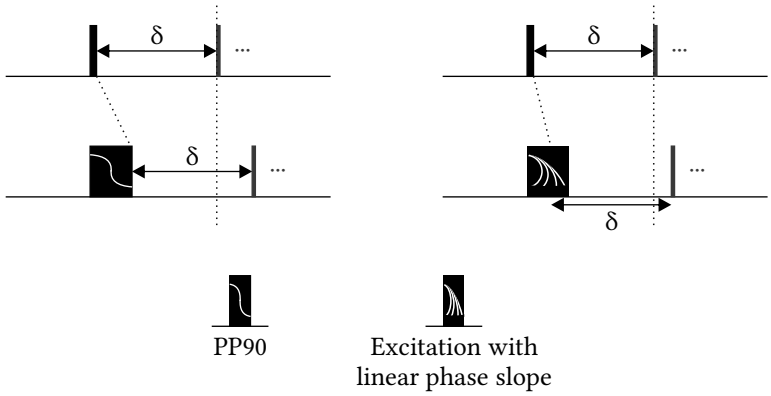

Figure 3.25: Explanation of the effective pulse length of pulses with linear phase slope. A rectangular pulse is the lower limit of pulse duration. Here, a 90° pulse is shown (top). On the left hand side, the 90° pulse is replaced by a shaped excitation pulse. This shaped pulse has longer duration in return for improved performance on the right hand side, linear phase slope pulse is used instead. The inclusion of an effective delay in the pulse shape final state reduces the overall experiment duration. At the end of the pulse, the spin state has already evolved chemical shifts and couplings equivalent to the state after a shorter pulse of $R \cdot \tau_P$ duration and a delay of $(1 - R) \cdot \tau_P$ length.

For excitation pulses it has been shown that part of the evolution period can be included in the pulse by defining a linear phase slope that resembles the resulting magnetization after the delay and the pulse [58]. A similar linear phase slope was also implemented for RADFA pulses. To define the target state the parameter R is introduced to describe the fraction of the pulse shape required for the desired effective flip angle, while $(1 - R)$ is the fraction of free evolution time. This results in a final state of a pulse of duration τ_P, that is equal to the state after a shorter pulse of duration $R \cdot \tau_P$ and a delay of length $(1 - R) \cdot \tau_P$. The effective pulse length is defined as the length of the imitated shorter pulse.

The target state used to assess pulse quality was modified, from the original RADFA target state of Equation (3.35) to

$$\rho_{\mathrm{T}}^{(R)}\left(\alpha_j, \nu_{\mathrm{off}}\right) = \mathbf{I}_{\mathrm{z}}\cos(\alpha_j) + \left(\mathbf{I}_{\mathrm{x}}\cos(2\pi(1-R)\nu_{\mathrm{off}}\tau_P) + \mathbf{I}_{\mathrm{y}}\sin(2\pi(1-R)\nu_{\mathrm{off}}\tau_P)\right)\cdot\sin(\alpha_j). \quad (3.44)$$

For $R = 1$ the effective pulse length is equal to the real pulse length, for $R = 0$, the pulse is required to recreate its full length as additional delay.

A systematic series of optimizations was conducted in a similar way to the original RADFA study. For the fractional effective pulse length R, values from 0 to 0.9 were examined. n_α and n_Ω were set to 15 and 40, respectively, for varying bandwidths of 10 kHz, 20 kHz, 30 kHz, 40 kHz, and 50 kHz and maximum RF amplitudes of 0 to 20 kHz corresponding to effective flip angles α of 0 to 180°. For each bandwidth and pulse length 100 starting shapes were created by spline interpolation of 10 randomly chosen points and optimized until convergence was reached. When the pulse quality was below $\Phi_{\mathrm{cutoff}} = 0.995$ and pulse length below 1 ms, the pulse length was increased and a new set of initial pulses created and optimized.

The quality of pulses optimized for 30 kHz bandwidth is shown in Figure 3.26 plotted versus the effective pulse length. For each overall pulse length, the graph shows, that for extreme values of R, corresponding pulse qualities are reduced in comparison to intermediate values. $R = 0$ corresponds to zero effective pulse length, i. e., the whole pulse length has to be used for the final phase layout, which is apparently not feasible. Interestingly, $R \approx 0.2$ yields the best pulse quality for pulses longer than 20 µs. Pulses with $R > 1$ are also possible in special cases [92], however no acceptable pulse quality could be reached in this domain for RADFA pulses.

Two shapes with $R = 0.7$ and $R = 0.3$ are shown in Figure 3.27. Within both shapes a plateau region approximately 18 µs wide can be seen, marking the main rotational part of the pulse shape that resembles to some point a hard pulse excitation corresponding to a 180° pulse at 10 kHz RF amplitude. Still the amplitude is not zero before and after that plateau, and imperfections of the pulse are corrected by low-power pulsing accompanying the effective evolution.

Pulses with negative phase slope could, in principle be used as a single-pulse spin echo. With RADFA conditions, however, no acceptable pulse quality could be reached. In [58], similarly, these optimizations could not fully reach the quality of positive phase slope pulses.

Using linear phase slope target states greatly improves the quality of RADFA pulses. Research on cooperative pulses, pairs or groups of pulse shapes that compensate each others errors, has also shown, that pulses optimized with phase slopes or free phase have significantly reduced pulse length [59, 93]. These pulse shapes, however, only work in combination with a

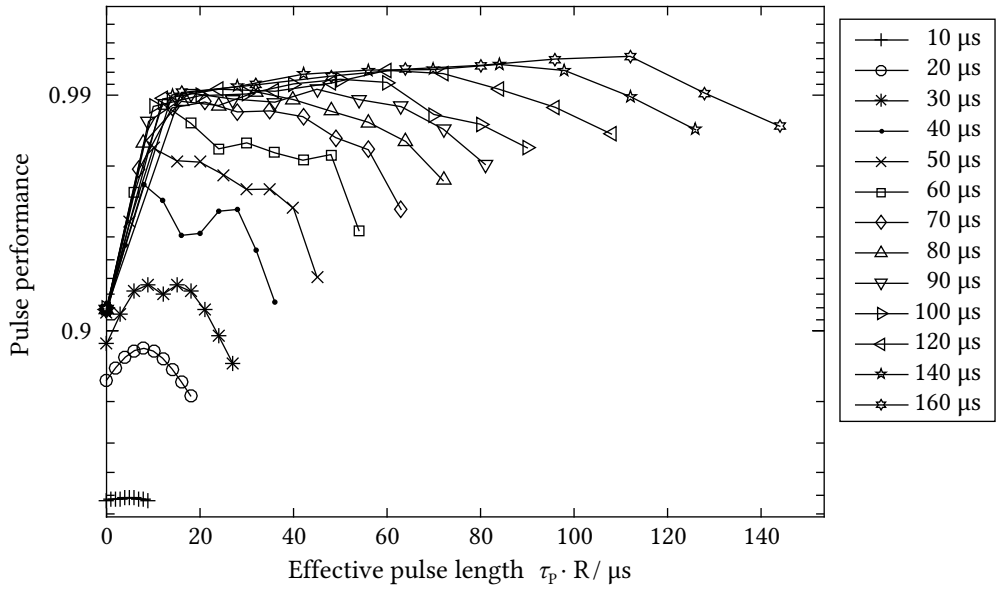

Figure 3.26: Pulse quality versus effective pulse length for pulses optimized for 30 kHz bandwidth with different overall pulse length. The effective pulse length is calculated by $R \cdot \tau_P$. For each overall pulse length, a set of pulses is connected by lines. Values of R range from $R = 0$, at the left of a set, where the effective pulse length is 0, to $R = 0.9$ on the right hand side.

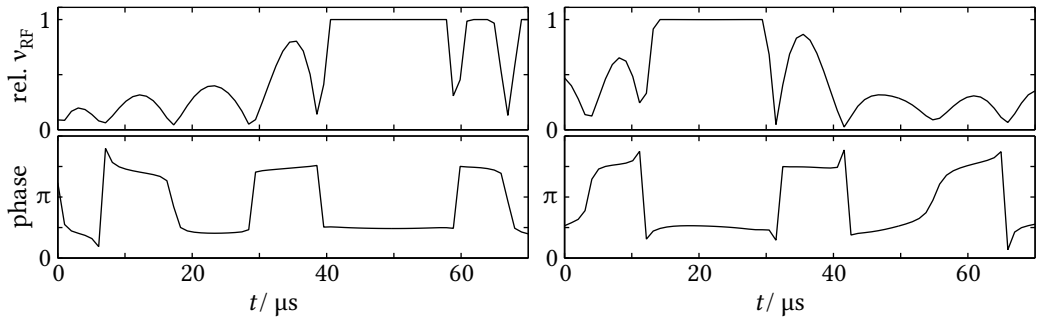

(a) $R = 0.7$ (b) $R = 0.3$

Figure 3.27: Two 70 us linear phase slope RADFA shapes with $R = 0.7$ and $R = 0.3$ obtained for 30 kHz bandwidth. Amplitude (top) and phase (bottom) of a) Pulse with $R = 0.7$, 70 % effective pulse length, 30 % internal evolution. b) Pulse with $R = 0.3$, 30 % effective pulse length, 70 % internal evolution.

each other. This fundamental limitation means, they can never replace pulses in a single-pulse 1D experiment and final pulses before the acquisition.

3.8 Conclusion

Pulse shape optimization provides access to pulses that achieve many tasks under different conditions. The increased duration of pulses, e. g., from 10 to 20 µs for simple transformations to 100 to 1000 µs, seems drastic, but the overall length of a modern pulse sequence using magnetic field gradients is in the range of 5 to 100 ms. So when all hard pulses are replaced by shaped pulses, the duration of the sequence is only slightly affected. If the additional pulse length still is prohibitive, the application of pulses with linear frequency slope poses an interesting alternative as long as such pulses are followed by a delay in the pulse sequence. Even when the sequence duration is not critical, their exceptionally good performance [93] makes them an attractive replacement whenever pulses are followed by delays and the pulse program can handle the complexity.

In return for the increased pulse length, the shaped pulses provide increased spectral intensity and quality where hard pulses fail. While the RADFA pulses aim to reproduce the relation between pulse power and flip angle naturally found in rectangular pulses, yet with broadband applicability, shaped pulses can also fulfill special roles, that are very different from rectangular pulse behavior. The pulses with offset-squared phase for example, are absolutely required in z filter elements and the experiments that utilize them [18, 90].

The multitude of available pulse shapes requires careful selection and metadata management. The simple inference of pulse bandwidth and pulse power or amplitude from pulse length is no longer possible. It is now the task of the pulse author to correctly name, label and tag pulse shapes, which has led to confusion in the past. A pulse shape file without the required information is close to useless and requires extensive simulations to be characterized. The difficulty of replacing rectangular pulses by shaped pulses is complicated further by the separation into point-to-point and universal rotation pulses. To explain their effect and differences, the trajectory of at least two initial states has to be visualized, which is not easily done without literal hand waving. Over a certain range of parameters, PP pulses may also perform like UR pulses, while they perform completely different in other regions.

A large part of the added complexity in experiment setup can easily mitigated by proper writing of modified pulse programs. In Bruker TopSpin 3, pulse programs can present required information about shapes to the user, and assist with most calculations. The author has not had the opportunity to try Varian/Agilent or JEOL pulse programming, but the use of the C programming language certainly gives hope. Together with robust, calibration-free broadband pulses [53], with sufficiently advanced hardware, shaped pulses can simplify routine NMR and increase the quality achieved even without optimal experiment setup.

The amplitudes and phases of pulses obtained by OCT are sometimes rapidly changing. With them the expectation values of observables like x or y magnetization often feature fast, complicated and hard-to-interpret time dynamics. Populations of carefully selected subspaces of states are much easier to analyze and interpret. The apparent "noisy" appearance of many OCT pulse shapes in NMR spectroscopy distracts from the fact that the underlying spin dynamics is smooth, orderly and very tightly controlled [94].

OCT is also readily used as a tool to explore the limits of shaped pulses. The pulse performance that is reached in a systematic search over a space of parameters, provides a lower bound of the physical limits. Even if one objects to the noise-like shapes often seen in OCT pulses, if a pulse can be obtained that achieves a given transfer within the physical model that is assumed, this transfer is demonstrated to be possible. The energy limited pulses shown in this work line up along similar investigations [51, 63, 64], and the relations derived are useful for all NMR applications. With the pulses with offset-squared phase, at the same time the physical limits of dephasing could be explored and usable short pulses that were unavailable before could be obtained.

Chapter 4

CLIP-COSY

The CLIP-relayed-COSY and PM-TOCSY sequences were examined in cooperation with Jens Haller. Parts of this chapter are published in [18].

4.1 Correlation Spectroscopy

4.1.1 The COSY Experiment

Correlation spectroscopy (COSY) was the first implementation of a 2D NMR experiment published [16]. To date it is still an essential homonuclear experiment for resonance assignment of small molecules as it allows the identification of adjacent protons in a covalent bonding network. The COSY experiment can be recorded in a phase-insensitive or phase-sensitive way, the latter offering higher resolution at the cost of increased experiment duration. The experiment duration forces many routine applications to use phase-insensitive COSY experiments. Therefore, it would be highly desirable to be able to acquire phase-sensitive COSY spectra within a few minutes for routine NMR spectroscopy of small molecules and metabolomics measurement series.

Over the past decades, many COSY variants emerged, featuring improved phase behavior [71, 72, 95–97], suitable signal shape for coupling measurements [66, 73, 98–100], constant time acquisition [101–104], or relayed transfer steps [105]. All of these experiments, including the widely used double quantum filtered COSY (DQF-COSY) [95], acquire so-called antiphase multiplets with severe disadvantages.

4.1.2 In-Phase and Antiphase Lineshape

While many NMR experiments create in-phase multiplets, i. e., the time-domain signal is cosine-modulated by the coupling constants, the FID of an antiphase multiplet is sine-modulated. Therefore, the FID starts at zero intensity and requires a minimum acquisition of data points to avoid a severe reduction in signal intensity as displayed in Figure 4.1a. Thus the acquisition time and the ensuing digital resolution must be high enough to resolve the active coupling to avoid

cancellation of the positive and negative multiplet components as has happened in Figure 4.1b. Assuming typical ^{1}H-^{1}H coupling constants of $J = 4$ to 10 Hz, a minimum of 1024 real points typically have to be acquired for t_1 on a 600 MHz spectrometer, leading to acquisition times of at least 30 minutes per sample, independent of the signal intensity. A COSY-type experiment featuring fully in-phase multiplets, therefore, is the first step to create a COSY that can be acquired in short duration.

A second drawback emerges in the case of inherently unresolved multiplet components: Passive couplings lead to the partial cancellation of positive and negative multiplet components, reducing the sensitivity. An example of a spin coupled to three other spins is shown in Figure 4.1c. Similarly, broad lines originating from field inhomogeneities, exchange broadening, or fast transverse relaxation lead to cancellation of antiphase signals as illustrated in Figure 4.1d, which cannot be alleviated by increased acquisition time. Therefore, for fast acquisition of spectra and to avoid cancellation artifacts, a COSY-type pulse sequence with in-phase multiplets is required

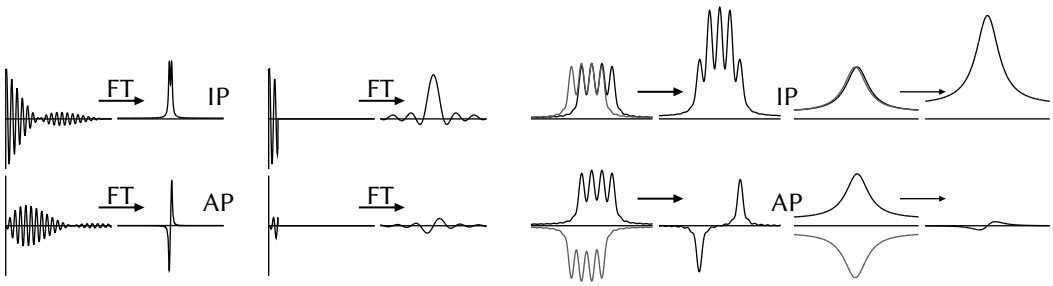

(a) Long acquisition (b) Short acquisition (c) Passive coupling (d) Broadened lines

Figure 4.1: Comparison of in-phase (IP, top) and antiphase (AP, bottom) multiplet patterns. a) Cosine- and sine-modulated FIDs lead to in-phase and antiphase multiplet patterns, respectively. When recorded with sufficiently long acquisition time, both lineshapes are resolved. b) Insufficient acquisition time causes a truncated FID which limits the signal intensity in the antiphase case. c) If a spin is coupled to more than one neighbour, overlapping multiplet components originating from passive couplings partially cancel antiphase signals. In this case a doublet of doublets, e. g., caused by a methyl group overlaps with another doublet. d) Broadened signals with linewidths larger than the underlying active coupling attenuate antiphase signals. The effect is similar to truncated FIDs.

Several in-phase variants of COSY have already been reported: SUPER-COSY [106] provides absorptive in-phase cross-peaks but leads to undesired dispersive antiphase diagonal peaks; ISECR-COSY [107] results in a similar behavior in the directly detected dimension; DQF-ISECR-COSY [107] finally provides the desired absorptive cross- and diagonal peaks, but requires a large number of scans per increment to be acquired, running contrary to the desired reduced

experiment duration. The IP-COSY experiment [108] also leads to the desired signal shapes, but employs a constant-time approach in the indirect dimension. This limits the accessible resolution and potentially distorts the peak intensities.

4.2 The CLIP-COSY Experiment

4.2.1 The Pulse Sequence

None of the published in-phase experiments enables the rapid acquisition of COSY-type correlations at any resolution. It was necessary to develop an in-phase sequence that enables acquisition with a single scan per increment. Therefore we designed a pulse sequence utilizing the general scheme introduced by Thrippleton and Keeler [90, 91]. The layout of the new experiment we call clean in-phase COSY (CLIP-COSY), is shown in Figure 4.2. It features in-phase to in-phase coherence transfer between directly coupled spins by using a perfect echo sequence [109–112] as mixing element. Antiphase and zero quantum contributions are removed by two single-scan z filter elements flanking the mixing period.

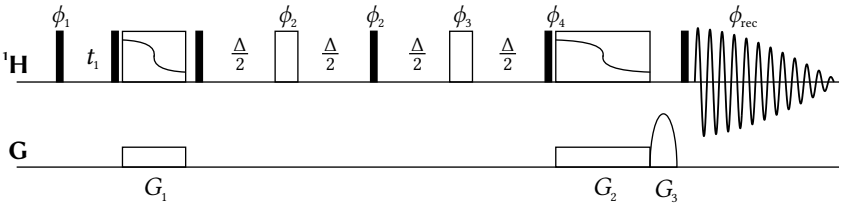

Figure 4.2: Pulse sequence of the CLIP-COSY experiment. The experiment can be acquired with a single scan per F_1 point; for additional scans, pulse phases are ϕ_1 = 4(x), 4(−x); ϕ_2 = y, −y, −y, y; ϕ_3 = −y, −x, −y, −x; ϕ_4 = x, x, −x, −x; ϕ_{rec} = x, −x, −x, x, −x, x, x, −x. When unspecified, pulse phase is x. Phase sensitivity in the indirect dimension is achieved via States-TPPI progression of ϕ_1. Filled rectangles represent 90° pulses, open rectangles 180° pulses, open rectangles with frequency sweep and simultaneous application of gradients indicate z filters.

The previously published IP-COSY [108] method can be seen as a nested constant-time variant of CLIP-COSY, optimized for systems where resolution is limited by the inherent line width. The CLIP-COSY pulse sequence can be applied using a single scan per increment and has full flexibility concerning the acquisition parameters in both dimensions. Water suppression may be applied either by presaturation during the recovery delay or by the addition of WATERGATE [113, 114], excitation sculpting [115], or PE WATERGATE [116] before acquisition.

The CLIP-COSY was straightforwardly implemented on a 600 MHz Avance III NMR Spectrometer equipped with a TCI Probehead and TopSpin 3.2. In Figure 4.3, a full CLIP-COSY spectrum acquired on hydroquinidine in $CDCl_3$ is shown. The spectrum was acquired without emphasis

on short experiment time and nicely shows the general look of CLIP-COSY spectra. All the peaks are positive, without antiphase contribution. All in all the spectrum resembles a TOCSY rather than a conventional COSY spectrum. In contrast to a TOCSY spectrum, however, only the directly coupled spins yield correlations. The assignment of hydroqiunidine is shown in Figure 4.8.

The overall experiment time can be reduced dramatically without a significant compromise in F_1 resolution. To get best results, CLIP-COSY can be easily combined with non-uniform sampling (NUS) methods [17, 117] such as compressed sensing. In the case of hydroquinidine, it is sufficient to acquire 76 data points for t_1, corresponding to 256 real data points with a NUS density of 30 %. Further extension to 512 points by linear prediction, results in a highly resolved and well-interpretable CLIP-COSY spectrum in three minutes that is shown in Figure 4.4.

4.2.2 Comparison of COSY-Type Experiments

In Figure 4.5, a conventional DQF-COSY, a variant of the IP-COSY with the Thrippleton-Keeler z filter, and a TOCSY experiment with a short mixing time are compared with CLIP-COSY. The DQF-COSY spectrum, although recorded with high resolution in the indirect dimension, has the lowest intensity. The spectrum had to be scaled by a factor of four to show the main cross-peaks, and some of the cross-peaks are still missing compared to the in-phase spectra. The IP-COSY achieves significantly better cross-peak intensities. It was acquired with an overall mixing period of $2(T_c + T_m) = 52$ ms as a good compromise between efficient coherence transfer and constant-time resolution. The CLIP-COSY spectra are of even higher intensity owing to the independently adjustable mixing period. Finally, the DIPSI-2 TOCSY experiment enables the acquisition of intense spectra with a short mixing time of 35 ms, but a number of cross-peaks from relayed correlations are visible, which are undesired in COSY-type applications. The pulse sequences of the various experiments are displayed in Figure 4.9.

From the spectra shown in Figure 4.5 and other spectra not shown acquired on hydroquinidine, F_2 traces were extracted and are displayed in Figure 4.6. The traces were extracted at 3.11 ppm, which is therefore also the frequency of the diagonal peak. Comparing the conventional DQF-COSY traces in Figures 4.7a and 4.7b, the strong dependence of intensity on F_1 acquisition time is visible. It causes causes severe reduction in signal strength. The constant-time evolution of the IP-COSY connects the F_1 resolution to the overall mixing time. Increasing resolution, therefore changes the cross peak intensity and may also affect the lineshape. In the CLIP-COSY the resolution is independent from the mixing time. Matching resolution and mixing time to the allowed parameters of a IP-COSY yields very similar spectra, shown in

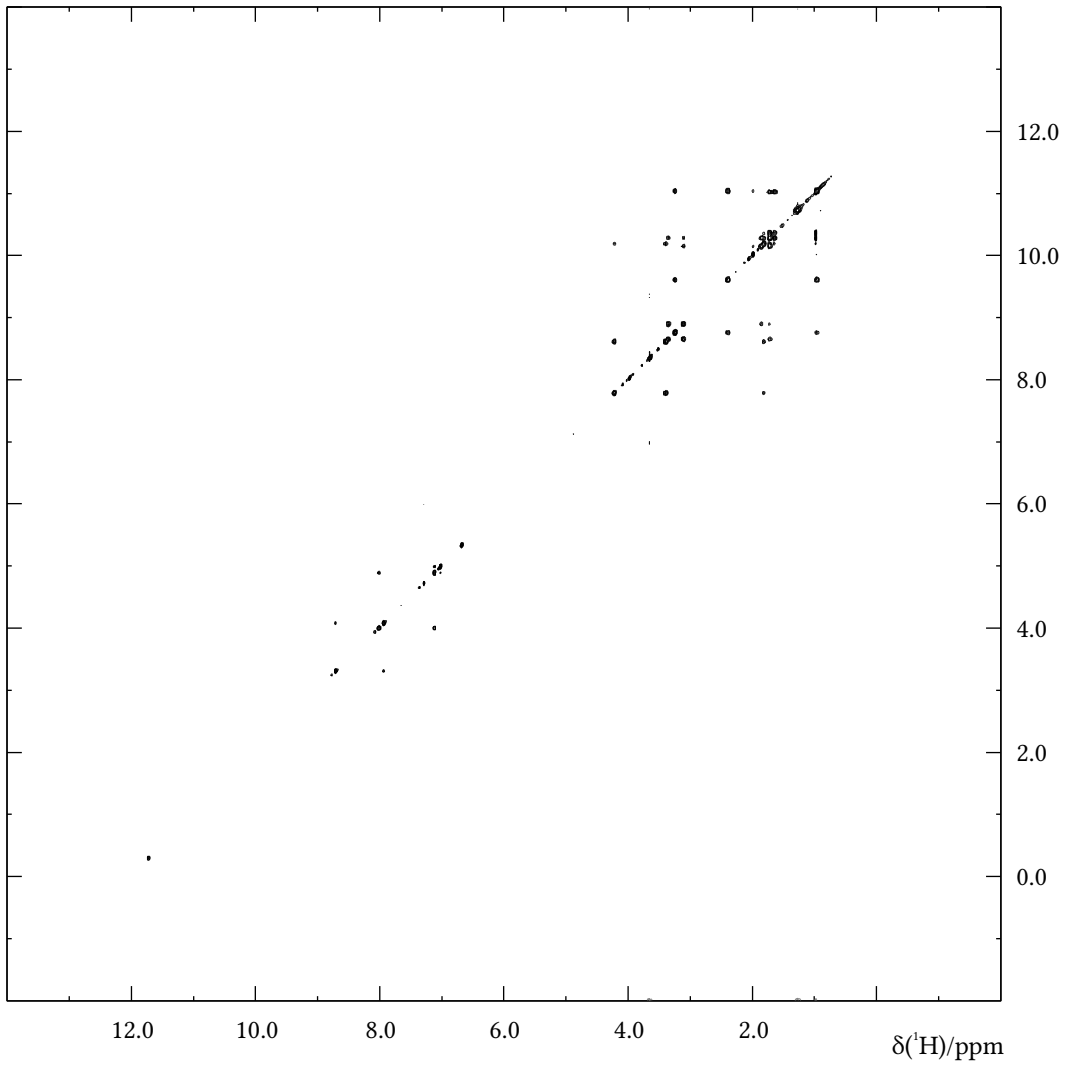

Figure 4.3: CLIP-COSY spectrum of 13.7 mM hydroquinidine in $CDCl_3$; 4096 × 1024 points recorded in 32 min 46 s with overall mixing time of $2\Delta = 33.33$ ms.

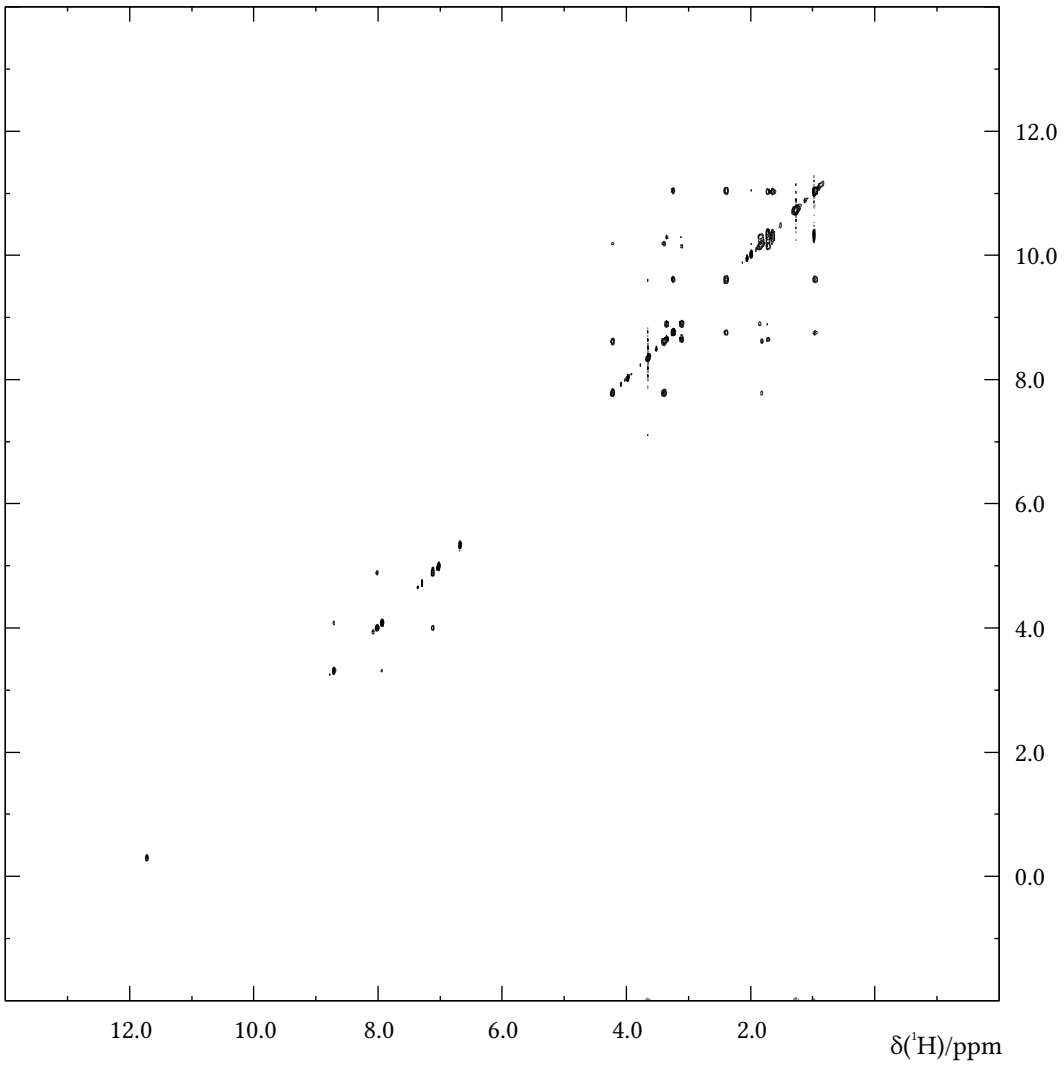

Figure 4.4: CLIP-COSY spectrum of 13.7 mM hydroquinidine in $CDCl_3$; 4096×76 non-uniformly sampled points (30 % NUS) recorded in 2 min 5 s, reconstructed to 4096×512 points using compressed sensing and linear prediction within TopSpin 3.2; The overall mixing time was $2\Delta = 33.33$ ms.

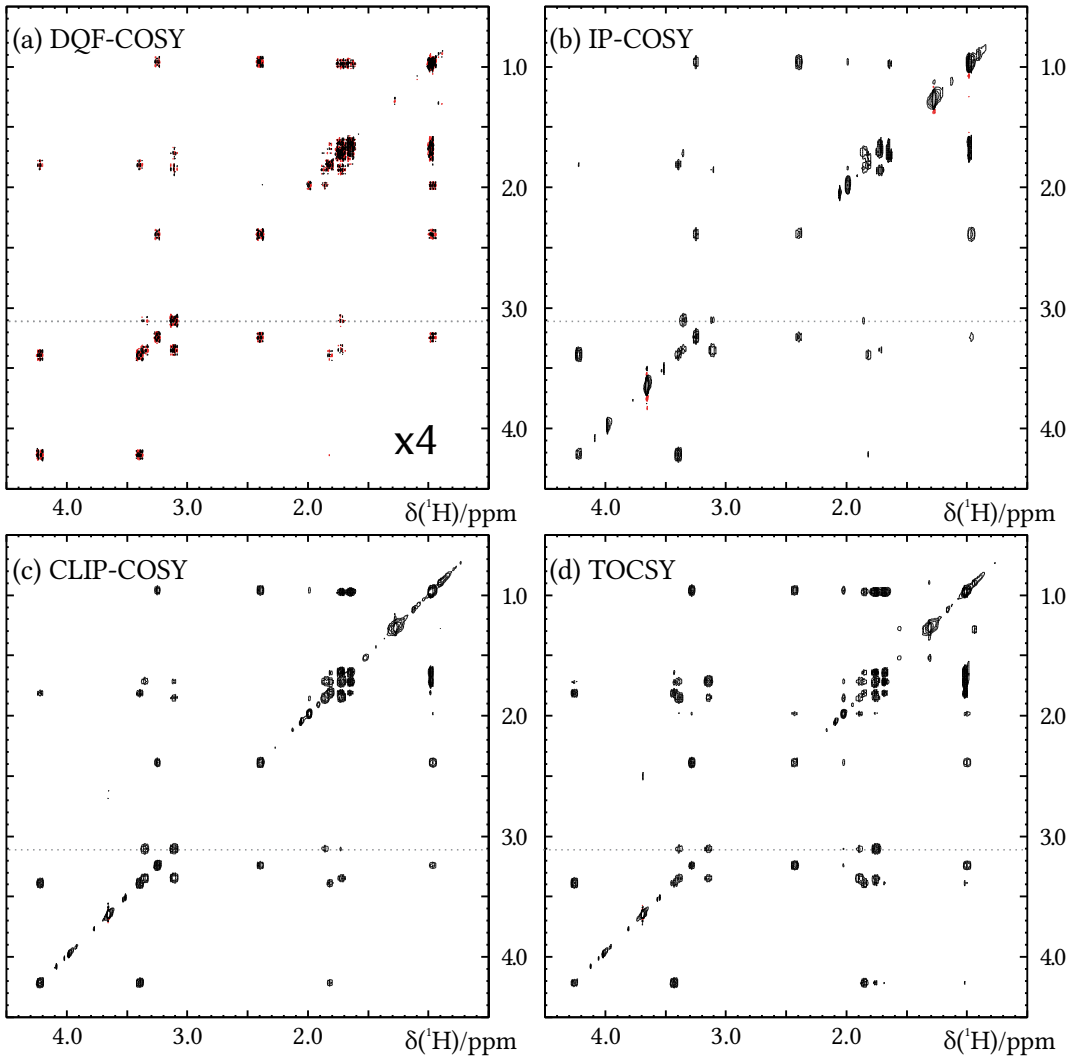

Figure 4.5: Aliphatic regions of different COSY-type spectra and a TOCSY spectrum, acquired on 13.7 mM hydroquinidine in $CDCl_3$. a) Conventional DQF-COSY, 4096 × 1024 points recorded in 32 min 4 s. The peak intensities were multiplied by a factor of four to show the main cross-peaks. b) IP-COSY with Thrippleton-Keeler z filter, 4096 × 384 points recorded in 13 min 3 s. The F_1 resolution is limited by the IP-COSY's constant time/overall mixing period of $2(T_c + T_m) = 52$ ms. c) CLIP-COSY, 4096 × 1024 points recorded in 34 min 18 s using an overall mixing period of $2\Delta = 33.33$ ms. d) TOCSY with Thrippleton-Keeler z filter, 4096×1024 points recorded in 34 min 24 s using DIPSI-2 with a mixing time of 34.5 ms. F_2 traces extracted from the spectra at 3.11 ppm as indicated by the dashed gray line are displayed in Figure 4.6. For the signal assignment see the Figure 4.8.

Figures 4.7c and 4.7e. In the TOCSY spectrum of Figure 4.7d, an additional correlation at 2 ppm is visible.

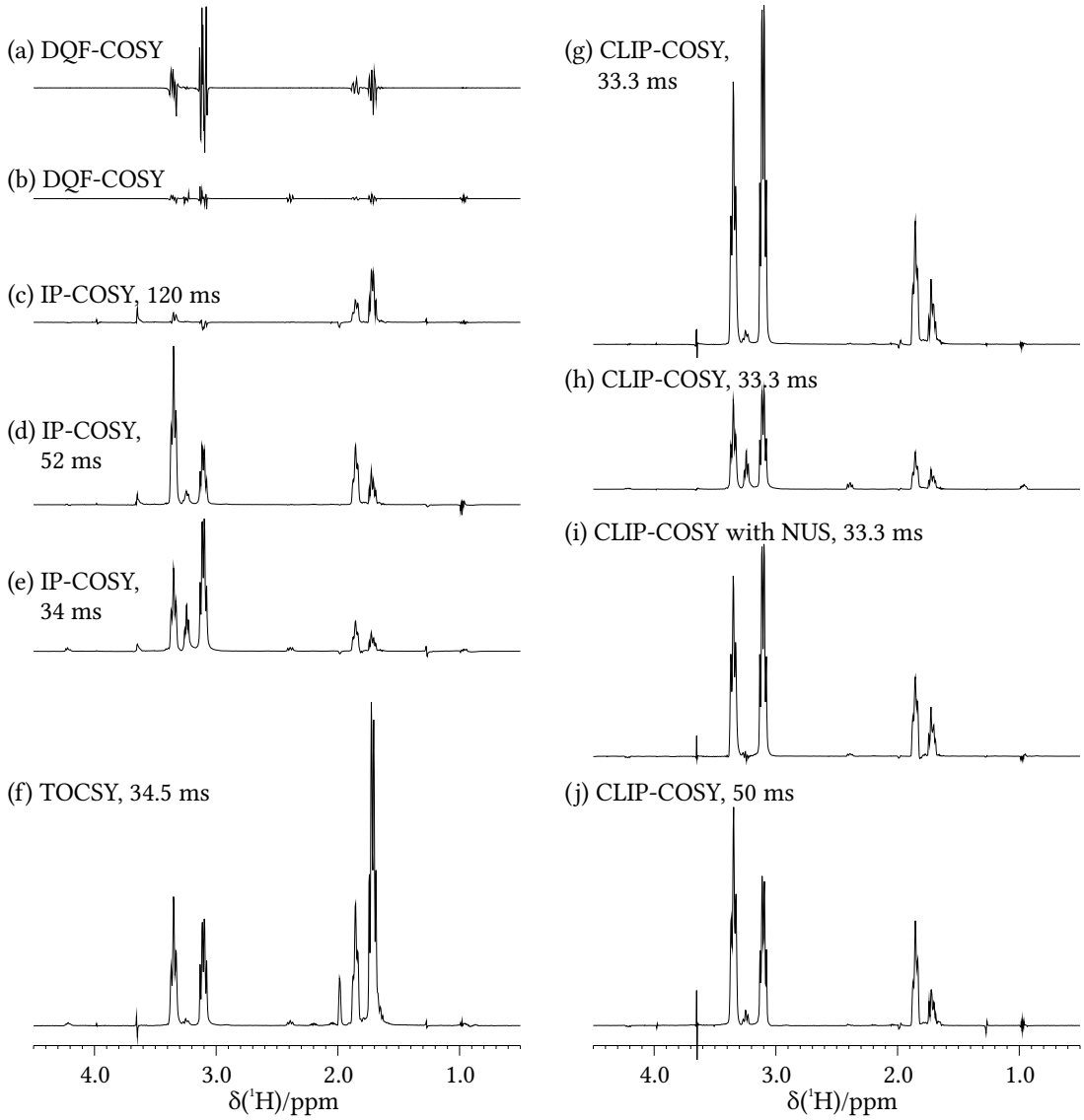

Figure 4.6: Unscaled F_2 traces of COSY-type spectra and TOCSY spectrum acquired on 13.7 mM hydroquinidine in $CDCl_3$. Traces were extracted at 3.11 ppm, as indicated by the dashed line in Figure 4.5. No peaks lie outside the region shown. Next to the experiment name, overall mixing times are stated where applicable. a) Conventional DQF-COSY with 4096 × 1024 points recorded in 32 min 46 s. b) Conventional DQF-COSY with 4096 × 192 points recorded in 6 min 29 s. c) IP-COSY with Thrippleton-Keeler z filter, $2(T_c + T_m) = 120$ ms overall mixing time and 4096 × 1024 points recorded in 35 min 9 s. d) IP-COSY with Thrippleton-Keeler z filter, $2(T_c + T_m) = 52$ ms overall mixing time and 4096 × 384 points recorded in 13 min 3 s. e) IP-COSY with Thrippleton-Keeler z filter, $2(T_c + T_m) = 33.3$ ms overall mixing time and 4096 × 192 points recorded in 6 min 34 s. f) TOCSY with Thrippleton-Keeler z filter using DIPSI-2 with 34.5 ms mixing time and 4096 × 1024 points recorded in 34 min 24 s. g) CLIP-COSY using an overall mixing period of $2\Delta = 33.33$ ms. 4096 × 1024 points were recorded in 34 min 18 s. h) CLIP-COSY using an overall mixing period of $2\Delta = 33.33$ ms. 4096 × 192 points were recorded in 6 min 47 s. i) CLIP-COSY with NUS; 4096 × 76 non-uniformly sampled points (30 % NUS) recorded in 2 min 59 s, reconstructed to 4096 × 512 points using compressed sensing and linear prediction within TopSpin 3.2; The overall mixing time was $2\Delta = 33.33$ ms. CLIP-COSY, 4096 × 76 non-uniformly sampled points recorded in 2 min 59 s using an overall mixing period of $2\Delta = 33.33$ ms. j) CLIP-COSY using an overall mixing period of $2\Delta = 50$ ms. 4096 × 1024 points were recorded in 34 min 18 s.

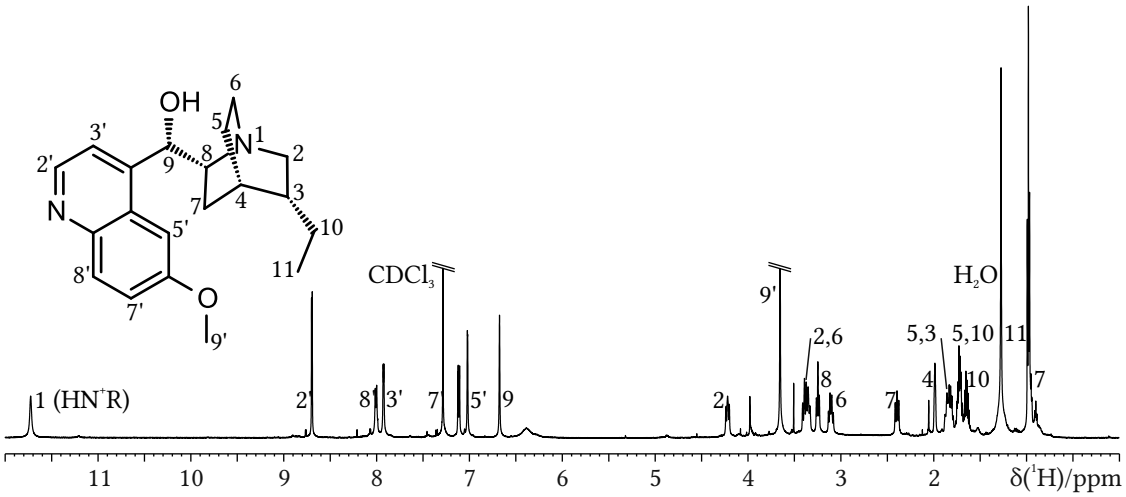

Figure 4.8: ^{1}H 1D NMR spectrum of 13.7 mM hydroquinidine in $CDCl_3$ with assignment. A single scan of 32768 points was acquired in 1.71 s. The same sample was used for all experiments on hydroquinidine.

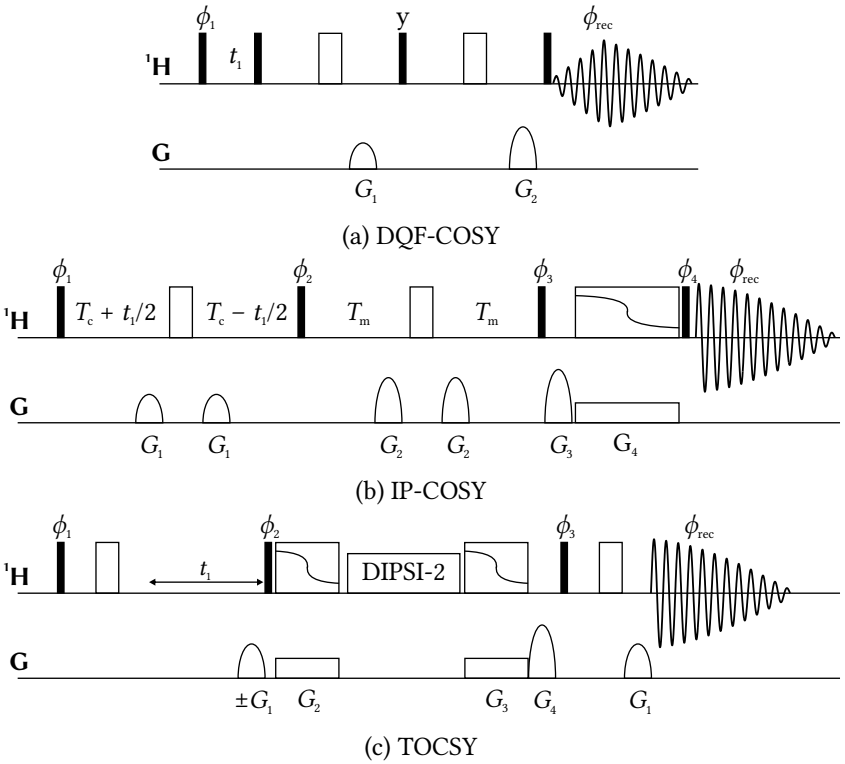

Figure 4.9: Experiments and pulse sequences used for comparison in Figure 4.5. a) DQF-COSY, the gradient selected pulse program `cosygpmfph` provided in the Bruker library was used without modifications. Pulse phases are $\phi_1 = \mathrm{y}, -\mathrm{y}$; $\phi_{\mathrm{rec}} = \mathrm{x}, -\mathrm{x}$; with States-TPPI progression of ϕ_1. b) IP-COSY [108], modified by adding a Thrippleton-Keeler z filter element. Pulse phases are $\phi_1 = 2(\mathrm{x}), 2(-\mathrm{x}), 2(\mathrm{y}), 2(-\mathrm{y})$; $\phi_2 = 4(\mathrm{y}), 4(\mathrm{x})$; $\phi_3 = 4(\mathrm{x}), 4(\mathrm{y})$; $\phi_4 = 4(\mathrm{x}, -\mathrm{x}), 4(\mathrm{y}, -\mathrm{y})$; $\phi_{\mathrm{rec}} = \mathrm{x}, -\mathrm{x}, -\mathrm{x}, \mathrm{x}, \mathrm{y}, -\mathrm{y}, -\mathrm{y}, \mathrm{y}$ with States-TPPI progression of ϕ_1. T_c is changed for each scan when multiple scans are acquired per FID; $T_{ci} = T_c + [i - 0.5 \cdot (ns + 1) \cdot \Delta T_c]$ with ns being the number of scans, $i = 1, 2, \ldots, ns$, and $\Delta T_c = 0.1\,\mathrm{ms} \cdot 16/ns$. c) TOCSY, the pulse program `dipsi2etgpsi` provided in the Bruker library was modified to include Thrippleton-Keeler z filters in the corresponding (empty) delays already included in the sequence. Pulse phases are $\phi_1 = 4(\mathrm{x}), 4(-\mathrm{x})$; $\phi_1 = \mathrm{x}, -\mathrm{x}$; $\phi_2 = 2(\mathrm{x}), 2(-\mathrm{x})$; $\phi_3 = 2(-\mathrm{x}), 2(\mathrm{x})$; $\phi_{\mathrm{rec}} = \mathrm{x}, -\mathrm{x}$. The first gradient is inverted together with ϕ_2 for the echo/antiecho detection, ϕ_1 is used for TPPI without states method. When unspecified, pulse phase is x. Filled rectangles represent 90° pulses, open rectangles 180° pulses, open rectangles with frequency sweep and simultaneous application of gradients indicate z filters [90].

4.3 Details and Theoretical Considerations

4.3.1 Pulse Sequence with Shaped Pulses

The CLIP-COSY performs well using only hard rectangular 90° and 180° pulses. A shaped pulse is only required for the Thrippleton-Keeler z filter, however, widely-used and well-implemented adiabatic pulses with linear frequency sweep can be applied. The theory of the z filter element is presented in Section 3.6, starting on Page 47, together with a way to assess the suppression capability of different pulse classes and best pulse shapes for a given z filter duration.

To boost performance, all rectangular pulses can be replaced by shaped pulses. As Figure 4.10 shows, different pulse classes are required: PP corresponds to point-to-point pulses which are optimized for efficient transfer of a single magnetization component, e. g., the transfer $z \rightarrow -y$ for a PP90 or excitation pulse, or $z \rightarrow -z$ for a PP180 or inversion pulse [63, 64]. UR pulses, instead, are optimized to transfer all three magnetization components according to a universal rotation [48, 51], i. e., create the same rotation independent of the offset frequency for all spins within the pulse bandwidth. Point-to-point pulses, e. g. PP90, can in principle be replaced by corresponding universal-rotation pulses, e. g. UR90, but not vice versa. The PP180 pulses required for the z filter in the CLIP-COSY, however, can only be replaced by pulses with z filter capabilities which UR180 or refocusing pulses cannot feature. The pulse classes and pulse nomenclature is introduced and discussed in more detail in Chapter 3 and Reference [51]. For the ^{1}H spectra the following shaped pulses were used:

PP90 BEBOP(10 kHz, 20 kHz, 550 us, ±20 %, 1100)
BEBOP $z \rightarrow -y$ point-to-point, 550 µs pulse length, 10 kHz bandwidth, 20 kHz B_1 amplitude, compensated for ±20 % B_1 deviation.

PP90 time reversed BEBOP^{TR}(10 kHz, 20 kHz, 550 us, ±20 %, 1100)
BEBOP $y \rightarrow -y$ point-to-point, shape of PP90 backwards.

UR90 BURBOP-90$_x$(10 kHz, 20 kHz, 200 us, ±20 %, 400)
BURBOP90°$_x$ universal rotation, 200 µs pulse length, 10 kHz bandwidth, 20 kHz B_1 amplitude, compensated for ±20 % B_1 deviation.

UR180 BURBOP-180$_x$(10 kHz, 20 kHz, 200 us, ±20 %, 400)
BURBOP180°$_x$ universal rotation, 200 µs pulse length, 10 kHz bandwidth, 20 kHz B_1 amplitude, compensated for ±20 % B_1 deviation.

PP180 z filter Either an adiabatic frequency-swept chirp pulse, or an optimal control derived pulse shape (OCT) with roughly the same rotation properties. The OCT pulse used for the

lysozyme spectrum was 500 µs long, optimized for 20 kHz maximum B_1 amplitude with compensation of ±20 % deviation of the nominal RF amplitude and 40 kHz bandwidth. Chirped pulses were generated as smoothed chirp using the shape tool `stdisp` of TopSpin 3.0 with 40 kHz total sweep width. The smoothed area was set to 10 % for the pulse of 5 ms pulse length and to 5 % for the longer pulses. The maximum B_1 amplitude was obtained from shape tool for $Q = 5$ in the middle of the shape. It is 2.6 kHz, 2 kHz, 1 kHz, and 1.3 kHz for corresponding 5 ms, 10 ms, 20 ms, and 50 ms pulse length, respectively.

For ^{13}C experiments of Section 4.4.3, pulses with higher bandwidth have to be used. On the available spectrometers, only 10 kHz RF amplitude could be used. Longer pulse shapes were required to accommodate both negative effects. For simplicity, all point-to-point pulses were replaced by universal rotation pulses.

UR90 BURBOP-90$_y$(37.5 kHz, 10 kHz, 750 us, ±5 %, 1500)
BURBOP90°$_y$ universal rotation, 750 µs pulse length, 37.5 kHz bandwidth, 10 kHz B_1 amplitude, compensated for ±5 % B_1 deviation.

UR180 BURBOP-180$_y$(37.5 kHz, 10 kHz, 1100 us, ±5 %, 2200)
BURBOP180°$_y$ universal rotation, 1100 µs pulse length, 37.5 kHz bandwidth, 10 kHz B_1 amplitude, compensated for ±5 % B_1 deviation.

For ^{19}F experiments, even higher bandwidth is required but 15 kHz RF amplitude can be used in Section 4.4.4. For simplicity and pulse shape availability, all point-to-point pulses were again replaced by universal rotation pulses.

UR90 BURBOP-90$_x$(75 kHz, 15 kHz, 433 us, 0 %, 1300)
BURBOP90°$_x$ universal rotation, 433 µs pulse length, 75 kHz bandwidth, 15 kHz B_1 amplitude, not compensated for B_1 deviation.

UR90 BURBOP-180$_x$(75 kHz, 15 kHz, 293 us, 0 %, 880)
BURBOP180°$_x$ universal rotation, 293 µs pulse length, 75 kHz bandwidth, 15 kHz B_1 amplitude, not compensated for B_1 deviation.

4.3.2 Product Operator Description

They CLIP-COSY pulse sequence is shown in Figure 4.2. A good approach to understand its properties, is to use the product operator formalism [118]. This description is equivalent to the full operator/density matrix description as long as all operators that are considered simultaneously do commute, i. e., infinitely short pulses and the weak coupling limit is assumed.

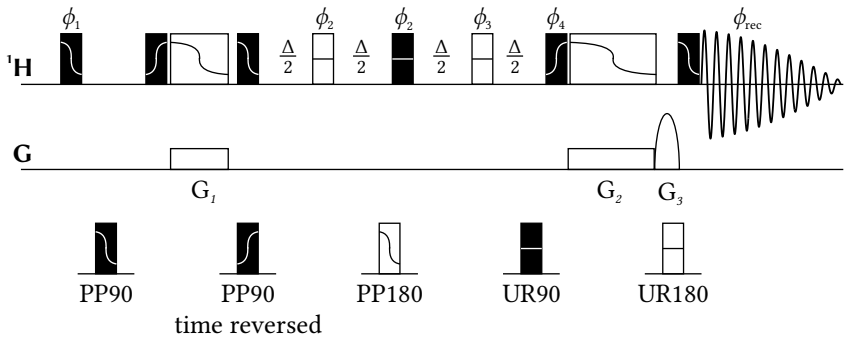

Figure 4.10: Pulse sequence of the CLIP-COSY experiment with explicit shaped pulses. The pulse sequence is obtained by replacing all rectangular pulses from Figure 4.2 by shaped pulses. Pulse phases are x when unspecified and $\phi_1 = 4(\mathrm{x}), 4(-\mathrm{x})$; $\phi_2 = \mathrm{y}, -\mathrm{y}, -\mathrm{y}, \mathrm{y}$; $\phi_3 = -\mathrm{y}, -\mathrm{x}, -\mathrm{y}, -\mathrm{x}$; $\phi_4 = \mathrm{x}, \mathrm{x}, -\mathrm{x}, -\mathrm{x}$; $\phi_{\mathrm{rec}} = \mathrm{x}, -\mathrm{x}, -\mathrm{x}, \mathrm{x}, -\mathrm{x}, \mathrm{x}, \mathrm{x}, -\mathrm{x}$. Phase sensitivity in the indirect dimension is achieved via States-TPPI progression of ϕ_1. PP corresponds to point-to-point pulses, UR to universal rotation pulses. Different pulse shape classes are specified by pictograms that are explained in the bottom of the figure.

The product operator description of the desired pathway is given for the first entry in the phase cycle wherever phases are cycled. The phase cycle is chosen not to attenuate the desired pathway, but remove contribution from other pathways, so no influence of phase cycling is to be expected in this description. The calculations are given for a coupled system of two spins, $\mathbf{I}_1$ and $\mathbf{I}_2$, with coupling constant J. One of the spins, $\mathbf{I}_1$, is used as the starting spin but all considerations are valid for the other spin as well as long as numbering of the two spins is interchanged. The offset frequency of spin $\mathbf{I}_1$ is ω and $\mathbf{I}_{1z}$ is assumed as initial magnetization.

$$\mathbf{I}_{1z} \xrightarrow{90^\circ_x} -\mathbf{I}_{1y} \xrightarrow{t_1} \begin{array}{c} -\mathbf{I}_{1y} \cdot \cos(\omega t_1) \cdot \cos(\pi J t_1) \\ +\mathbf{I}_{1x} \cdot \sin(\omega t_1) \cdot \sin(\pi J t_1) \\ +2\mathbf{I}_{1x}\mathbf{I}_{2z} \cdot \cos(\omega t_1) \cdot \sin(\pi J t_1) \\ +2\mathbf{I}_{1y}\mathbf{I}_{2z} \cdot \sin(\omega t_1) \cdot \sin(\pi J t_1) \end{array} \xrightarrow{90^\circ_x} \begin{array}{c} -\mathbf{I}_{1z} \cdot \cos(\omega t_1) \cdot \cos(\pi J t_1) \\ +\mathbf{I}_{1x} \cdot \sin(\omega t_1) \cdot \sin(\pi J t_1) \\ -2\mathbf{I}_{1x}\mathbf{I}_{2y} \cdot \cos(\omega t_1) \cdot \sin(\pi J t_1) \\ -2\mathbf{I}_{1z}\mathbf{I}_{2y} \cdot \sin(\omega t_1) \cdot \sin(\pi J t_1) \end{array}$$

The t_1 encoding is completed by the second 90° pulse, the abbreviation

$$c(t_1) = \cos(\omega t_1) \cdot \cos(\pi J t_1) = \tfrac{1}{2}\left(\cos(t_1(\omega + \pi J)) + \cos(t_1(\omega - \pi J))\right)$$

will be used in the following. At this point in the pulse sequence, a Thrippleton-Keeler z filter element is inserted to remove all product operator terms that are not fully parallel to the z-axis and the only remaining term is $\mathbf{I}_{1z}$.

$$\xrightarrow{z\text{ filter}} \mathbf{I}_{1z}\cdot c(t_1) \xrightarrow{90^\circ_x} \mathbf{I}_{1y}\cdot c(t_1) \xrightarrow{\frac{\Delta}{2},180^\circ_y,\frac{\Delta}{2}} \begin{matrix}-\mathbf{I}_{1y}\cdot c(t_1)\cos(\pi J\Delta)\\ 2\mathbf{I}_{1x}\mathbf{I}_{2z}\cdot c(t_1)\sin(\pi J\Delta)\end{matrix} \xrightarrow{90^\circ_y} \begin{matrix}-\mathbf{I}_{1y}\cdot c(t_1)\cos(\pi J\Delta)\\ -2\mathbf{I}_{1z}\mathbf{I}_{2x}\cdot c(t_1)\sin(\pi J\Delta)\end{matrix}$$

$$\xrightarrow{\frac{\Delta}{2},180^\circ_y,\frac{\Delta}{2}} \begin{matrix}-\mathbf{I}_{1y}\cdot c(t_1)\cos(\pi J\Delta)\cos(\pi J\Delta)\\ +2\mathbf{I}_{1x}\mathbf{I}_{2z}\cdot c(t_1)\sin(\pi J\Delta)\cos(\pi J\Delta)\\ -2\mathbf{I}_{1z}\mathbf{I}_{2x}\cdot c(t_1)\sin(\pi J\Delta)\cos(\pi J\Delta)\\ -\mathbf{I}_{2y}\cdot c(t_1)\sin(\pi J\Delta)\sin(\pi J\Delta)\end{matrix} \xrightarrow{90^\circ_x} \begin{matrix}-\mathbf{I}_{1z}\cdot c(t_1)\cos(\pi J\Delta)\cos(\pi J\Delta)\\ -2\mathbf{I}_{1x}\mathbf{I}_{2y}\cdot c(t_1)\sin(\pi J\Delta)\cos(\pi J\Delta)\\ +2\mathbf{I}_{1y}\mathbf{I}_{2x}\cdot c(t_1)\sin(\pi J\Delta)\cos(\pi J\Delta)\\ -\mathbf{I}_{2z}\cdot c(t_1)\sin(\pi J\Delta)\sin(\pi J\Delta)\end{matrix}$$

$$\xrightarrow{z\text{ filter}} \begin{matrix}\mathbf{I}_{1z}\cdot c(t_1)\cdot\cos^2(\pi J\Delta)\\ +\mathbf{I}_{2z}\cdot c(t_1)\cdot\sin^2(\pi J\Delta)\end{matrix} \xrightarrow{90^\circ_x} \begin{matrix}-\mathbf{I}_{1y}\cdot c(t_1)\cdot\cos^2(\pi J\Delta)\\ -\mathbf{I}_{2y}\cdot c(t_1)\cdot\sin^2(\pi J\Delta)\end{matrix}$$

The combination of J and the delay Δ determines the ratio between cross peak and diagonal peak intensities. With $\Delta = 16.7$ ms as used in most experiments, a signal with splitting $J = 7$ Hz has 87 % diagonal intensity and 13 % cross peak intensity, whereas a signal with $J = 15$ Hz has equal intensity for both and a signal with $J = 30$ Hz theoretically would show full cross peak and zero diagonal peak intensities. However, for larger spin systems with many coupling constants being active, the magnetization is distributed over all coupling partners, so that for practical applications mixing times of $\Delta = 16.7$ to 25 ms or overall mixing time of $2\Delta = 33$ to 50 ms give best results.

4.3.3 Optimal zFilter Length

The performance of the Thrippleton-Keeler z filters increases with their duration, but polarization transfer by nuclear Overhauser enhancement (NOE), chemical exchange, or conformational interconversion and TOCSY type transfer between strongly coupled spins may occur during this period, leading to artifacts. Therefore, a compromise between short duration and good performance has to be found. The essential element of the filter is the inversion pulse with effectively a frequency swept 180° rotation. The desired inversion can be achieved by the adiabatically swept CHIRP [119, 120] pulse, by BIP/BIBOP-type pulses [63, 64, 84] or by specific, optimal control (OCT) derived pulses. As explained in Section 3.6, quasi-adiabatic pulses are highly efficient down to a length of about 5 ms. For shorter pulses, OCT pulses have slightly

better artifact suppression efficiencies. In our experience, the best results for CLIP-COSY are obtained with z filters of 0.25 to 0.5 ms for large molecules such as proteins and with filters of 10 to 20 ms for small molecules with slow NOE build-up. The improvement of the signal shape with increasing filter length is shown in Figure 4.11, for menthol, a small molecule, while the NOE artifact build-up is visible at the same time.

As seen in Section 3.6, it should be mentioned again that the performance of the z filter inherently must break down close to the diagonal [90], and corresponding multiplets might get distorted. Such distortions, however, are inherent to all COSY-type experiments for strongly coupled spins.

4.3.4 Perfect Echo Transfer Element: Delay and Properties

For a critical evaluation of the CLIP-COSY method, the two potential drawbacks also have to be discussed in detail: Because of the central in-phase to in-phase coherence transfer step, in contrast to conventional COSY experiments, it is necessary to specify a mixing period of a certain duration. This implies that the coherence transfer will vary between different mixing delays Δ and will depend on the actual spin system. In the weak-coupling limit and neglecting relaxation, integrated cross-peak intensities in the CLIP-COSY are described by

$$I_{12} = \sin^2(\pi J_{12}\Delta) \prod_{i\neq 1,2}^{n} \cos(\pi J_{1i}\Delta) \prod_{j\neq 1,2}^{m} \cos(\pi J_{2j}\Delta) \tag{4.1}$$

with the active coupling J_{12} and the passive couplings J_{1i} and J_{2j} to the $(n-2)$ and $(m-2)$ neighboring spins of corresponding spin systems. The intensity is visualized in Figure 4.12. In theory, for a two-spin system, mixing times with Δ up to 50 ms should be practical. However, in our studies, we found that delays of $\Delta = 15$ to 25 ms are a better compromise for more complex coupling networks. In most applications with active coupling constants of $J > 3$ Hz, mixing times of around $\Delta = 15$ ms are advantageous whereas the detection of weaker couplings might require longer mixing times. In contrast to constant-time experiments such as IP-COSY, such short mixing periods do not limit F_1 resolution. Aside from variations in the signal intensities, the specified mixing period also potentially leads to relayed cross peaks if at least two spins of the spin system are strongly coupled. This effect has been discussed previously and is common to all in-phase COSY approaches [108], and one example is shown in Figure 4.13. The methyl group (11) at 0.98 ppm is directly coupled to the methylene group (10) at 1.65 to 1.72 ppm. A weak cross peak corresponding to the ^4J coupling between spins 3 and 11 is already visible in the conventional COSY. However, second order interactions of the spins 10 and 3 cause additional transfer and the coupling is exaggerated in the CLIP-COSY. Relayed cross peaks are created

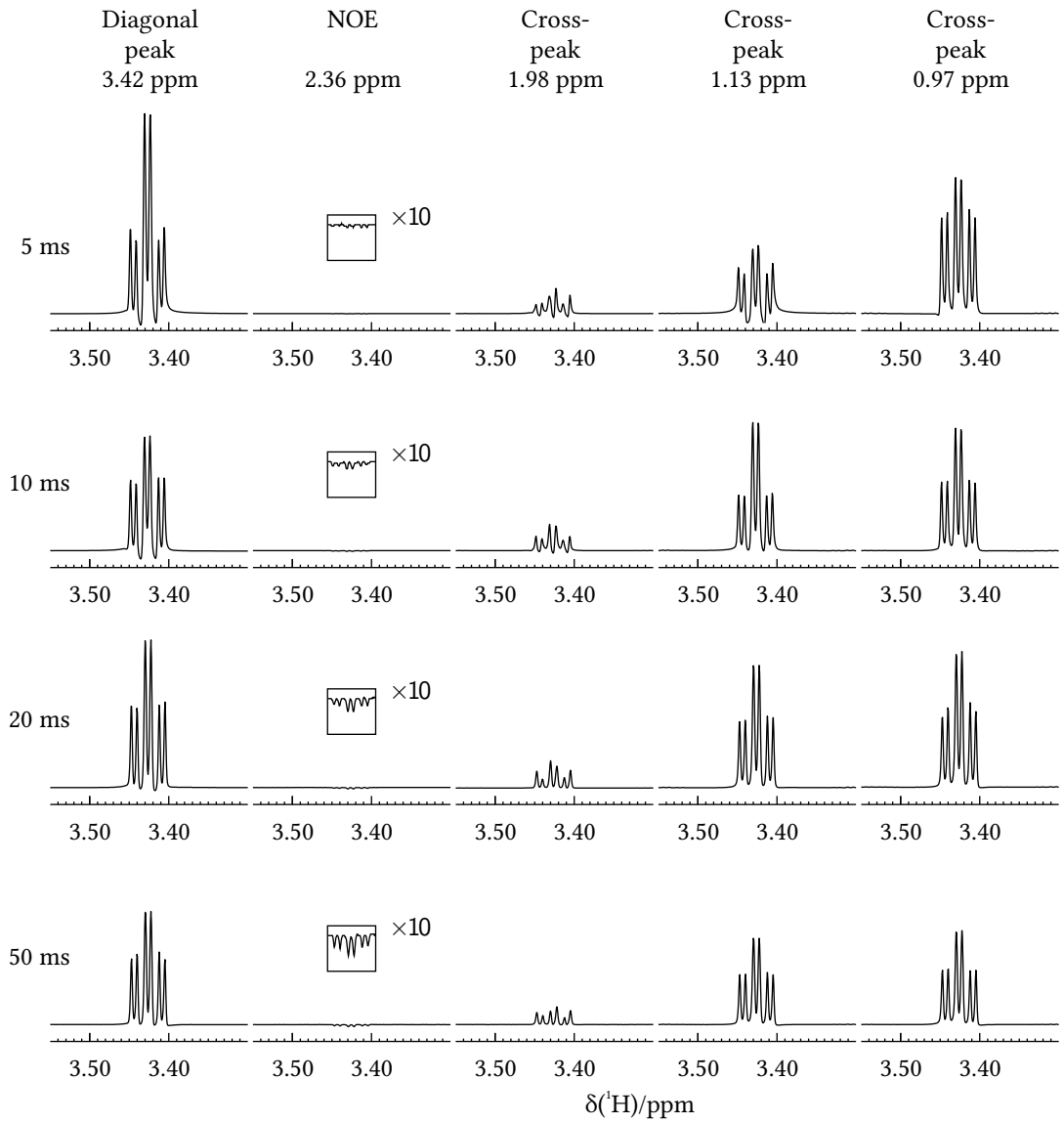

Figure 4.11: F_2 traces of peaks at 3.42 ppm in the directly detected dimension, extracted from CLIP-COSY experiments of 220 mM menthol with different lengths of z filter elements. The diagonal peak, an NOE artifact peak and three cross peaks are shown. The signal shape changes with increasing z filter length. The distortion of the in-phase pattern caused by zero quantum contribution is reduced with increasing length. At about 20 ms length, it becomes negligible. Simultaneously, NOE artifact buildup is observed for small molecules during z filter periods and its dependence on z filter lengths for the NOE contribution can be seen clearly. Here z filters of 10 to 20 ms duration give best overall results. For the full signal assignment of menthol see Figure 6.2.

when magnetization is transferred to one spin of a pair of strongly coupled spins. Transfer in the opposite direction, from one of the strongly coupled spins to a weakly coupled spin does not cause such artifacts. Consequently, the relayed cross peaks usually are asymmetric with respect to the diagonal.

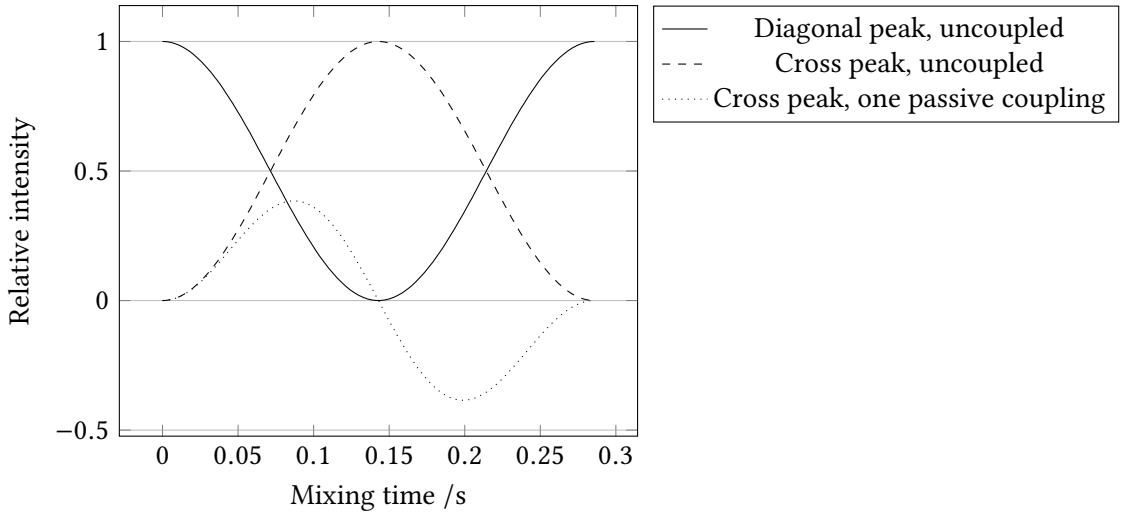

Figure 4.12: Transfer function of the CLIP-COSY transfer for isolated spins (solid and dashed) and with a single passive coupling (dotted). All coupling constants are 7 Hz. Two coupled but otherwise isolated spins can achieve complete transfer. Maximum intensity is reached after $2\Delta = 1/7\,\mathrm{Hz} = 0.14\,\mathrm{s}$. A single passive coupling to either of the two active spins prevents complete transfer and shift the maximum towards smaller overall mixing times.

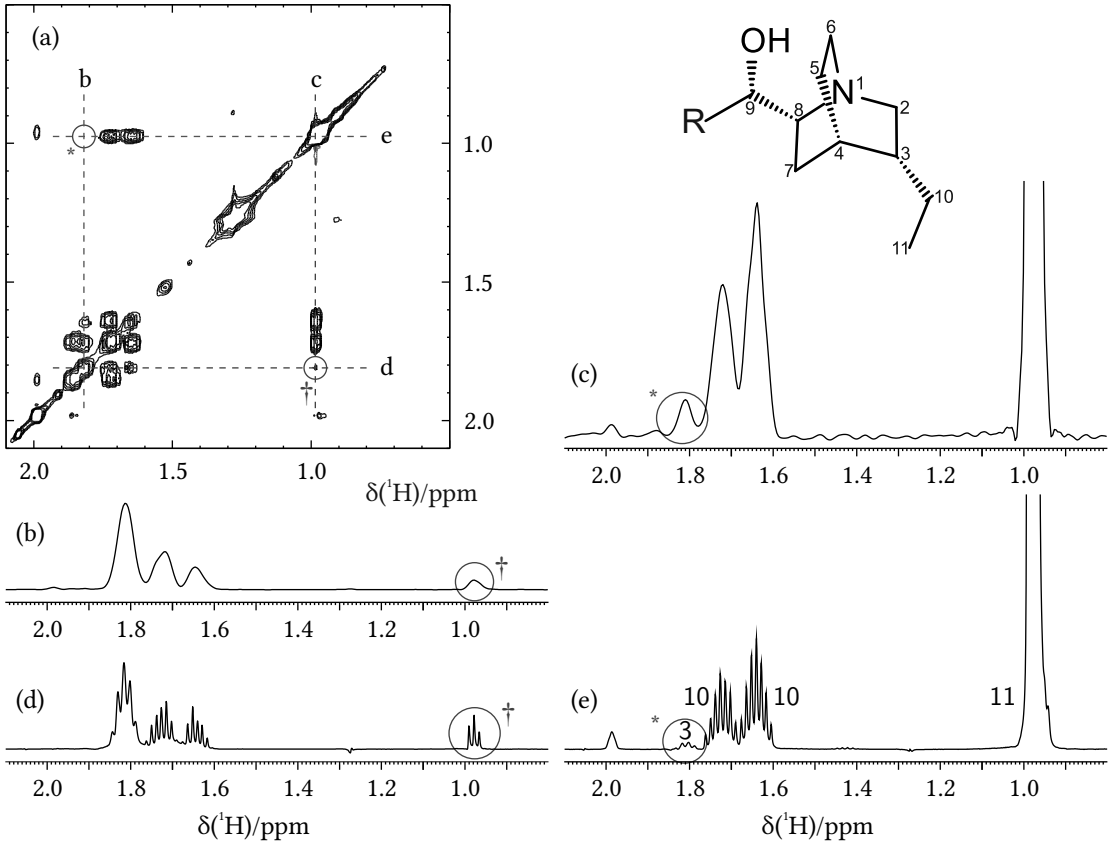

Figure 4.13: Relayed cross peak artifacts introduced by strong coupling. a) Region of CLIP-COSY of 13.7 mM hydroquinidine in $CDCl_3$, full spectrum shown in Figure 4.3. b, c) Traces extracted at 0.98 to 1.81 ppm in F_1 and d, e) Traces extracted at 0.98 to 1.81 ppm in F_2. The large diagonal peak at 0.98 ppm (11) is cut off at approximately 10 % of its height. The relayed cross peaks (encircled) at 0.98/1.81 ppm are visible next to the regular peaks.

4.4 Modified and Extended Sequences

4.4.1 CLIP-COSY Modified for Proteins and Solvent Suppression

The CLIP-COSY method can be conveniently applied to molecules dissolved in water using the mentioned water suppression schemes. For large molecules, like proteins, zero quantum artifacts are less of an issue. The second z filter was therefore omitted and replaced by an excitation sculpting element. The resulting pulse sequence is shown in Figure 4.14. It was tested on the protein hen egg-white lysozyme, which consists of 129 amino acids. The H^N-H^α fingerprint region of this spectrum is shown in Figure 4.15.

4.4.2 Homonuclear Decoupled CLIP-COSY

As CLIP-COSY spectra feature full in-phase multiplets, homonuclear decoupling methods for pure shift spectra [121–126] can directly be applied in both dimensions. The conventional COSY and other antiphase experiments are fundamentally incompatible to decoupling.

As a proof of principle, a CLIP-COSY spectrum with F_2 PSYCHE decoupling [122] was acquired on menthol and is shown in Figure 4.17b. The spectral quality is merely sufficient, as the decoupling sidebands of the high intensity methyl groups, do exceed weaker peaks and can be mistaken for cross peaks. However, the decoupling achieves reduction of the multiplets to singlets as desired.

4.4.3 The CLIP-relayed-COSY

The CLIP-COSY features a single transfer pulse within the transfer element. This ensures transfer between directly coupled spins only. When larger spin systems with partial overlap

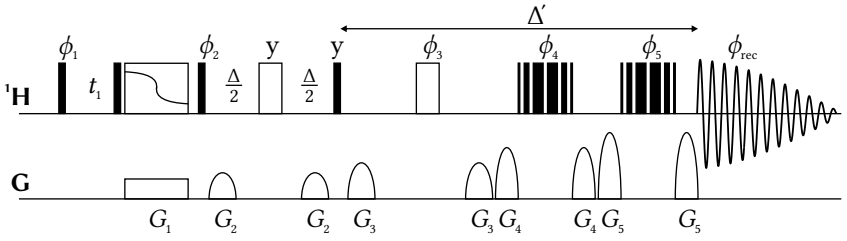

Figure 4.14: CLIP-COSY pulse sequence modified for solvent suppression and optimized for large molecules, e.g., proteins in H_2O. The second z filter element has been replaced by excitation sculpting [115] using a binomial 3-9-19 sequence [114]; pulse phases have been adapted to avoid $-z$ magnetization and are ϕ_1 = x; ϕ_2 = x, −x; ϕ_3 = y, −y; ϕ_4 = 4(x), 4(y), 4(−x), 4(−y); ϕ_5 = 2(x), 2(y), 2(−x), 2(−y); ϕ_{rec} = x, −x with States-TPPI progression of ϕ_1.

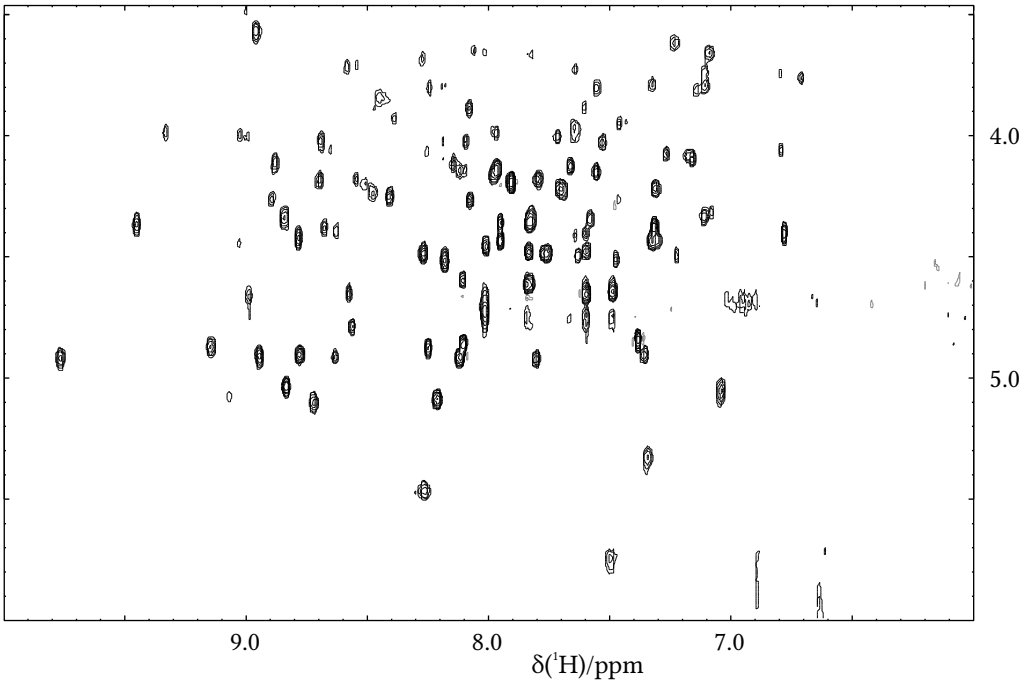

Figure 4.15: H^N-H^α fingerprint region of a CLIP-COSY spectrum of 1 mM lysozyme in 90 % H_2O / 10 % D_2O, using the pulse sequence shown in Figure 4.14. The transfer delays were set to $\Delta = 16.7$ ms and $\Delta' = 25$ ms; 4096×512 points were recorded in 1 h 27 min, with four transients per F_1 point.

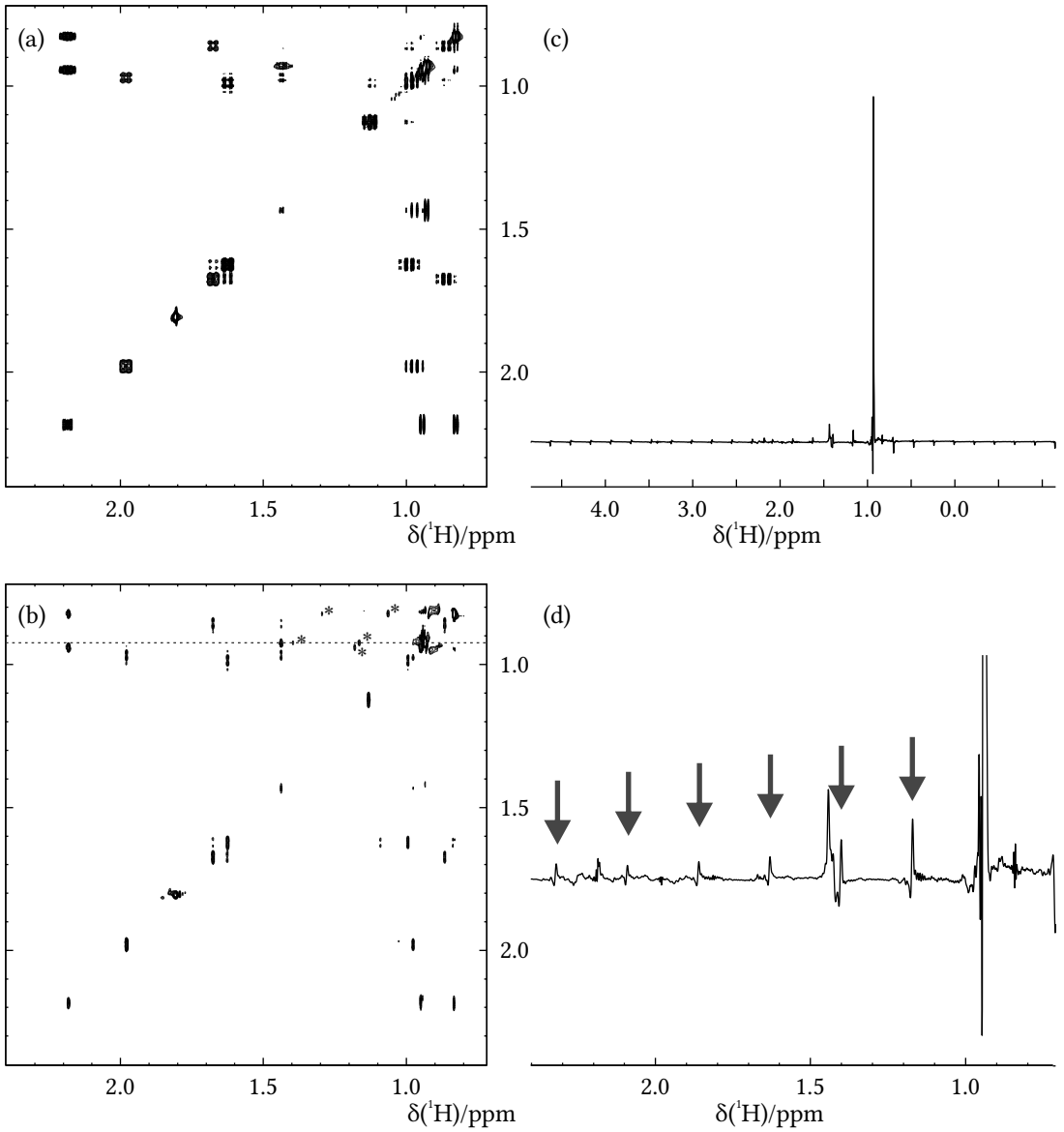

Figure 4.16: Spectra of 220 mM menthol in $CDCl_3$; a) CLIP-COSY, 8192 × 512 points were recorded in 36 min 33 s. b) CLIP-COSY with homonuclear decoupling during acquisition using PSYCHE [122]. 32 chunks of 7.143 ms were acquired in 10 h 38 min and rearranged to a 1728×512 points FID. Signals originating from methyl group decoupling sidebands are indicated by asterisks. Comparing a and b, as can be seen, the multiplets are reduced to singlets. c) F_2 trace from b at 1.2 ppm showing the corresponding methyl signal, corresponding cross peaks and decoupling sidebands. d) Region of c; the dark gray arrows mark decoupling side bands of which the largest two are visible in the spectrum d. The sidebands are equally spaced and roughly 140 Hz apart. Each acquisition chunk was 7.143 ms long and the side band spacing is inversely proportional to this length. Considering $1/7.143\,\text{ms} \approx 140\,\text{Hz}$, the position of the artifacts is explained.

are considered, it is often useful, to increase the range of the transfer and create additional cross peaks. This method has been demonstrated in the relayed-COSY [105], where it creates additional antiphase signals. It has also been added to the CLIP-COSY sequence, resulting in the CLIP-relayed-COSY sequence shown in Figure 4.18. Repeating the perfect echo transfer element leaves two 180° pulses in sequence only separated by delays. It is possible to replace these by a single 180° pulse placed in the center of the delay. Alternatively, with shaped pulses, it may be beneficial to retain two pulses and let one compensate the imperfections of the other [59], this then allows replacing universal rotation pulses by inversion pulses [50].

In cooperation with Jens Haller, the properties of CLIP-relayed-COSY were examined, and the experiment applied to several test samples. In Figure 4.19, a series of CLIP-relayed-COSY spectra on glucose is shown. The first experiment is a regular CLIP-COSY with cross peaks between directly coupled spins, constituting the first coupling sphere. The next experiment contains an additional transfer pulse, therefore cross peaks appear between not only a spin and directly coupled spins but also between this spin and all spins that are directly coupled to the spins from the first sphere. This scheme can be repeated until all spins in a spin system are included. Provided, one peak in the spectrum is properly identified and free from overlap, the series of relayed-experiments will not entangle the peak overlap, but will reveal the sequence of spins even beyond the overlapping peaks.

4.4.4 Planar-Mixing TOCSY

When the transfer element of the CLIP-relayed-COSY sequence in Figure 4.18 is repeated sufficient times, i. e., n is equal or larger than the number of spins in the spin system, the experiment contains TOCSY-like information. Since the perfect-echo transfer element approximates planar mixing conditions [127], the experiment is referred to as PM-TOCSY. Conventional TOCSY experiments create isotropic mixing conditions [128–133], so the experiments are not completely equivalent. The mixing sequences used for isotropic mixing, however, rely on continuous B_1 irradiation, either for the full length of the sequence as in the DIPSI-2 [131] or FLOPSY [132] experiments, or very closely spaced pulses separated only by short delays like in the MOCCA family [133]. The mixing efficiency in isotropic mixing is therefore limited by the allowed continuous power. In Figure 4.20a the transfer efficiency of the DIPSI-2 sequence is simulated. It shows the achievable transfer between two coupled spins at different chemical shift frequencies. The mixing time is matched to the coupling constant and the B_1 amplitude is set to 15 kHz, which is slightly above the safe limit. The transfer covers a region of about 15 kHz in both directions that is almost square-shaped but with reduced quality in the corners of maximum frequency separation.

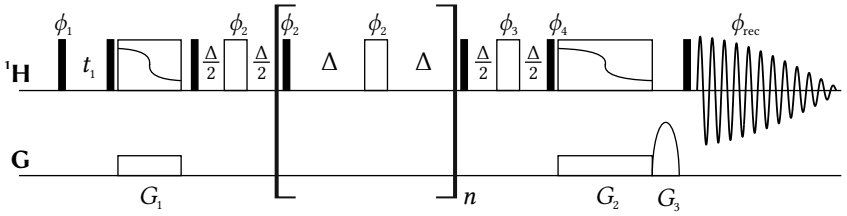

(a) Single 180° pulse

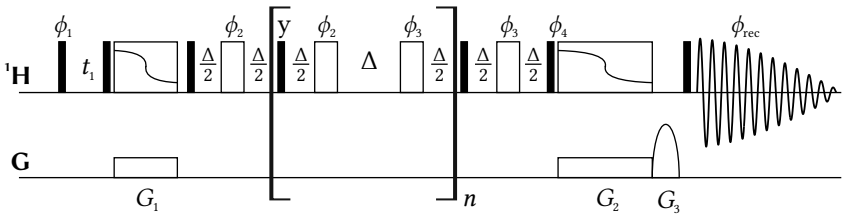

(b) Two 180° pulses

Figure 4.18: CLIP-relayed-COSY pulse sequence to include cross peaks between remotely coupled spins. The transfer element is repeated **n** times. Setting $n = 0$, the regular CLIP-COSY is acquired. Increasing n includes additional coupling spheres in the transfer. a) Principally, a single 180° pulse in the transfer element induce should less pulse errors and relaxation losses and therefore yield superior spectral quality. Unless specified otherwise, pulse phases are x; $\phi_1 = 4(\mathrm{x}), (-\mathrm{x})$; $\phi_2 = \mathrm{y}, -\mathrm{y}, -\mathrm{y}, \mathrm{y}$; $\phi_3 = -\mathrm{y}, -\mathrm{x}, -\mathrm{y}, -\mathrm{x}$; $\phi_4 = \mathrm{x}, \mathrm{x}, -\mathrm{x}, -\mathrm{x}$; $\phi_{\mathrm{rec}} = \mathrm{x}, -\mathrm{x}, -\mathrm{x}, \mathrm{x}, -\mathrm{x}, \mathrm{x}, \mathrm{x}, -\mathrm{x}$. b) However, simulations have shown in agreement with literature, in some cases when using shaped pulses, pulse imperfections can be compensated instead of accumulated by repeating the same shape with shifted phase, inverted phase, or time-reversed [50]. Unless specified otherwise, pulse phases are x; $\phi_1 = 4(\mathrm{x}), 4(-\mathrm{x})$; $\phi_2 = -\mathrm{y}, \mathrm{y}, -\mathrm{y}^{\mathrm{TR}}, \mathrm{y}^{\mathrm{TR}}$; $\phi_3 = \mathrm{y}, -\mathrm{y}, \mathrm{y}^{\mathrm{TR}}, -\mathrm{y}^{\mathrm{TR}}$; $\phi_4 = \mathrm{x}, \mathrm{x}, -\mathrm{x}, -\mathrm{x}$; $\phi_{\mathrm{rec}} = \mathrm{x}, -\mathrm{x}, -\mathrm{x}, \mathrm{x}, -\mathrm{x}, \mathrm{x}, \mathrm{x}, -\mathrm{x}$; with the superscript $^{\mathrm{TR}}$ indicating a time reversed shape, i. e., the shape is applied backwards. Phase sensitivity in the indirect dimension is achieved via States-TPPI progression of ϕ_1. Filled rectangles represent 90° pulses, open rectangles 180° pulses, open rectangles with frequency sweep and simultaneous application of gradients indicate z filters.

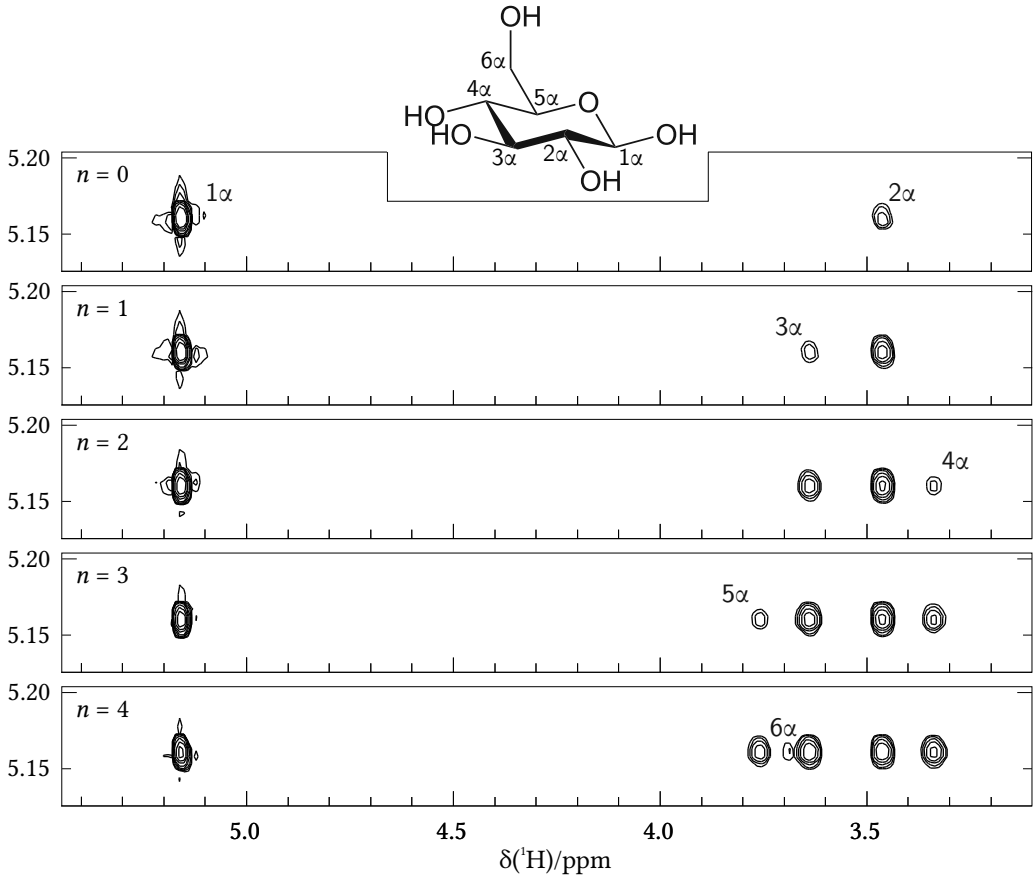

Figure 4.19: The F_1 stripe of the anomeric proton of α-glucose (1α) obtained in a series of CLIP-relayed-COSY experiments on 655 mM glucose in D_2O using the pulse sequence shown in Figure 4.18a. n was increased from a) $n = 0$ to e) $n = 4$. Each increase shows an additional cross peak. e) The $6\alpha'$ peak overlaps with 5α and is not visible. 8096×512 points were recorded in 17 min 59 s to 18 min 52 s, with transfer delay $\Delta = 16.7$ ms and a single scan per F_1 point.

The CLIP-COSY sequence, when extended to planar-mixing TOCSY, consists of short pulses separated by long delays. On the one hand, this allows pulsing at higher B_1 amplitude, on the other hand, all the individual pulses can be replaced by shaped pulses that can cover large bandwidths even at low amplitudes. Using the right shaped pulses [51] as described in Section 4.3.1, the PM-TOCSY can yield TOCSY-like transfer over enormous bandwidths. In Figure 4.20b the transfer efficiency of the PM-TOCSY sequence is simulated. It shows the achievable transfer between two coupled spins at different chemical shift frequencies. The mixing time is matched to the coupling constant and the B_1 amplitude is set to 15 kHz, which is a save power level for short pulses separated by delays. The transfer covers a region of about 75 kHz in both directions that is perfectly square-shaped and dwarfs the DIPSI-2 transfer region. It should be noted, that the pulse shapes are not ideal or optimized for repeated application. The dips in transfer efficiency are caused by imperfections in the pulse shapes and improved shapes will increase the transfer in these regions.

In Figure 4.21 a PM-TOCSY experiment on ^{19}F is shown. ^{19}F has a large chemical shift dispersion, and rectangular hard pulses fail to even excite the whole range, let alone create efficient mixing between spins at such large frequency distances. The fluorine spectrum was acquired on a 500 MHz Avance III HD NMR Spectrometer equipped with a cryogenically cooled BBO Probehead. In the spectrum the spin systems of the individual molecules are visible. Cross peaks exist between all spins in each spin system, even between spins separated by 140 ppm or 70 kHz. Strong coupling evolution between the atoms of the CF_2 groups created phase errors during the shaped pulses, the spectrum was therefore processed in magnitude mode. Still the spectrum is of very high quality, and even an impurity is detected.

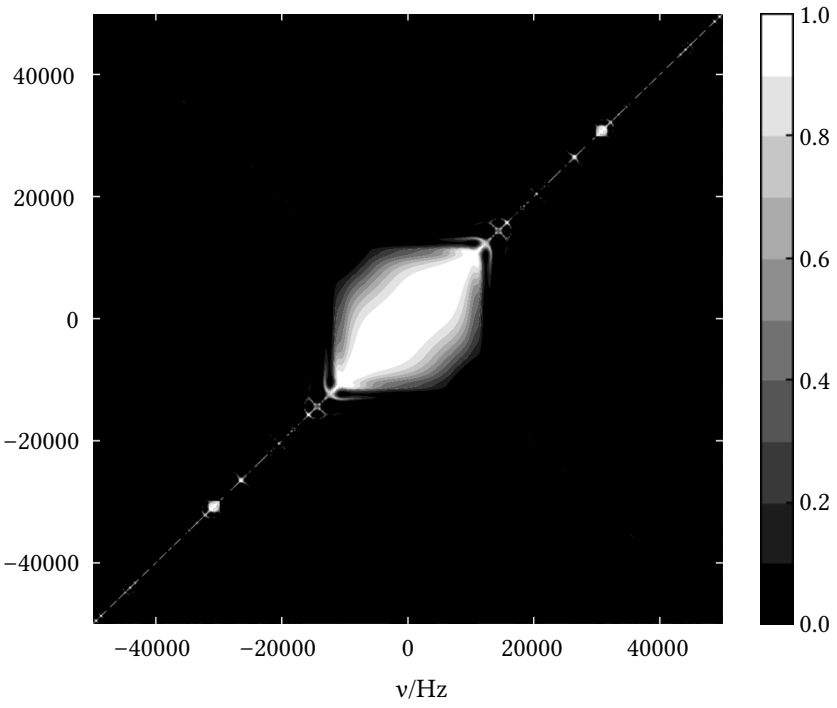

(a) DIPSI-2

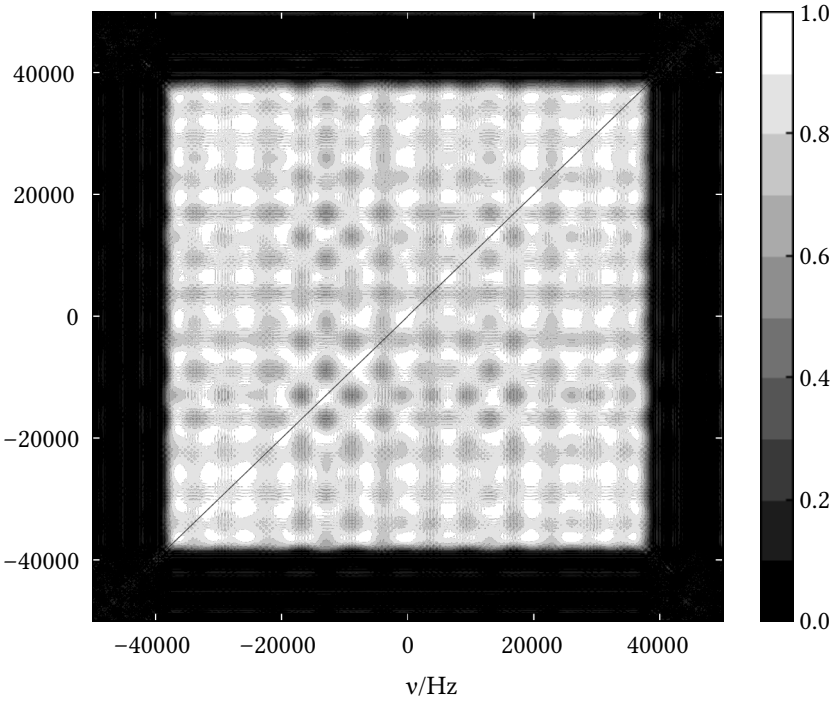

(b) PM-TOCSY

Figure 4.20: Transfer efficiency of DIPSI-2 and PM-TOCSY at 15 kHz B_1 amplitude and mixing time matched to $J = 7$ Hz. a) Transfer efficiency of the DIPSI-2 mixing sequence; b) Transfer efficiency of the PM-TOCSY; The CLIP-relayed-COSY sequence of Figure 4.18b was simulated with $\mathbf{n} = 2$ using shaped pulses as described in Section 4.3.1 on Page Page 74 and averaged over 4 phase cycle steps. At 600 MHz Larmor frequency, i. e., typical ^{1}H or ^{19}F frequencies, 75 kHz correspond to a chemical shift range of 125 ppm.

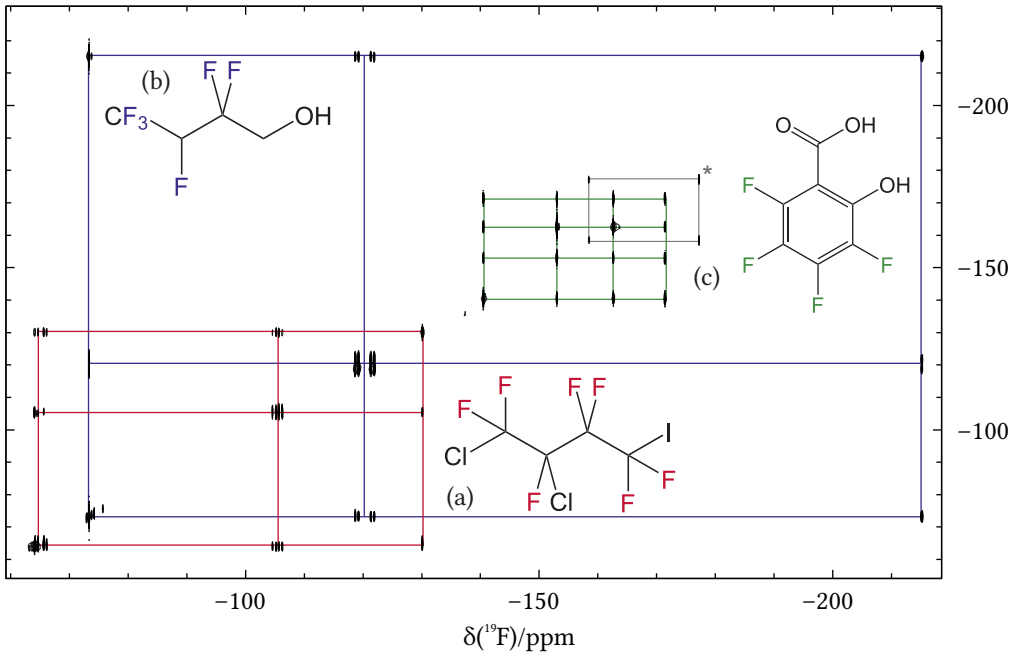

Figure 4.21: ^{19}F PM-TOCSY of a mixture of fluorinated compounds; a) 109 mM 2,3,4,5-Tetrafluoro-6-hydroxybenzoic acid (green), b) 134 mM 2,2,3,4,4,4-Hexafluoro-1-butanol (blue), c) 68 mM 1,2-Dichloro-4-iodo-heptafluoro-n-butane (red) in DMSO-d_6. The CLIP-relayed-COSY sequence in Figure 4.18a was used with $n = 2$, which is sufficient to mix all ^{19}F atoms in the sample. 65536×256 points were recorded in 1 h 56 min, with an overall mixing time of 60 ms and eight scans per F_1 point. The pulse shapes for ^{19}F from Section 4.3.1 on Page 74 were used at 15 kHz B_1 amplitude. An impurity is detected and marked by asterisk.

4.5 Conclusion

In summary, the CLIP-COSY method has been introduced as an easy-to-handle COSY experiment that provides high quality in-phase multiplet patterns. The main advantage of the CLIP-COSY experiment is the possibility to rapidly acquire spectra with fully absorptive lineshapes in a few minutes, especially when combined with non-uniform sampling methods. For signals with line broadening due to exchange, large improvements in sensitivity can be achieved compared to DQF-COSY experiments. The sequence does not limit the F_1 resolution and enables the combination of COSY with modern homodecoupled acquisition methods as for TOCSY/NOESY experiments [121, 134–137]. Owing to the strongly reduced experiment time, the acquisition of absorptive COSY-type correlation spectra will be amenable as a routine NMR method and might also find applications in metabolomics studies and quality control as a sensitive high-resolution 2D experiment. The CLIP-COSY pulse sequence also serves as the basis for extended sequences promising a new set of robust homonuclear correlation experiments.

Chapter 5

The ASAP-HSQC

The ASAP-HSQC experiment was examined in cooperation with Johanna Becker and David Schulze Sünninghausen.

5.1 Rapid Acquisition 2D NMR Experiments

In NMR spectroscopy, only the small difference in populations of the Zeeman energy levels contributes to the signal. For ^{1}H nuclei at room temperature and a magnetic field of 10 T only about one in 10 000 atoms is actually measured. In other spectroscopic methods, e. g. infrared (IR) spectroscopy, most molecules are in ground state and can contribute to the measured signal. Using modern cryogenically cooled probe heads, the lower limit of feasible sample concentration for high-resolution NMR studies is in the microgram or millimolar range [6]. Choosing the right solvent, samples containing much higher concentrations can be prepared. Provided that the sensitivity is no longer the limiting factor for the data collection, it becomes important to minimize the time needed for the data sampling process and NMR spectroscopy moves from sensitivity-limited to sampling-limited regime [6]. All indirect dimensions have to be sampled by running a series of 1D experiments and the overall experiment duration is multiplied by the number of points of each dimension. While a single 1D spectrum can typically be recorded on the order of 1 s, adding a second dimension with only 128 points resolution increases the overall time to 2 min and a third dimension of the same resolution brings it to 4.5 h.

The latest decades have brought a multitude of schemes to accelerate multidimensional NMR spectroscopy. On the processing side, non-uniform sampling or non-uniform undersampling (NUS) allows reduction of the number of FIDs that have to be acquired. The required number of FIDs for reconstruction scales only by a number proportinal to $\log_2$ of the desired number of points, providing significant speed-up especially in multidimensional experiments [17, 117].

The fastest experimental acquisition scheme so far reported is the ultrafast method (UF) that is able to acquire a 2D experiment in a single scan using gradient-encoding imaging-type schemes [85, 86, 88, 89], a method briefly mentioned in Section 3.6. It is even possible to acquire additional dimensions in the same scan using multi-directional gradient encoding [138]. The

2D ultrafast acquisition scheme, however, is severely limited in accessible resolution and sweep width due to diffusion, available gradient strengths, and gradient switching time. Additional dimensions accumulate the drawbacks of the 2D method, leading to a even tighter limits on sensitivity and resolution [139].

Promising, more conventional methods try to reduce the length of an individual scan in a multiscan acquisition scheme. A large part of such experiments is spent waiting for polarization to recover for the next scan via T_1 relaxation. In common heteronuclear experiments like the HMQC or the HSQC [1, 15, 140] of a small molecule this is a matter of 1 to 3 s. By using alternative methods to restore polarization, the delay between two scans can be lowered down to the acquisition time, either limited by the desired F_2 resolution or the allowed length of heteronuclear decoupling, usually 100 to 200 ms. This way, the overall experiment duration can be reduced by an order of magnitude.

When FIDs are recorded at a rate that is too fast for complete polarization recovery, signal intensity will be reduced. In many experiments, fortunately, incomplete excitation can be combined to balance the incomplete relaxation. The flip angle corresponding to the ideal amount of excitation is the famous Ernst angle [76]. While it is often approximated by 30° the Ernst angle actually depends on the experimental recovery delay per relaxation time. Not all NMR experiments can utilize this method, however, in many experiments the polarization that remains after initial Ernst angle excitation is destroyed by subsequent pulses.

The required alternative polarization recovery can also be achieved by exciting only an active subset of all the spins in the sample and using the remaining passive polarization to enhance the polarization recovery of the active spins. Band selective methods like the SOFAST-HMQC [77, 78] achieve this by band selectively exciting ^{15}N-bound protons, a method well suited for ^{15}N-labeled peptides and proteins. One method for broadband spectra and suited for molecules with natural isotope composition is the ALSOFAST-HMQC [141] where ^{12}C-bound magnetization is returned to its equilibrium orientation within the experiment sequence. The contribution of passive spins can be enhanced by actively sharing polarization between neighboring protons via a short homonuclear isotropic mixing period before the start of the next scan. The acceleration by sharing adjacent polarization (ASAP) was presented in the ASAP-HMQC [19] and a similar method is utilized in the IMPACT-HMBC [142].

The HSQC experiment provides superior spectral quality compared to the HMQC [143], however, the related ASAP-HSQC experiment was only presented quite recently [20]. The sequence is shown in Figure 5.1. It allows Ernst angle-like excitation by varying the first INEPT delay Δ' and by removing the mixing sequence, an ALSOFAST-HSQC corresponding to the ALSOFAST-HMQC is readily implemented. Figures 5.2a and 5.2b show the comparison

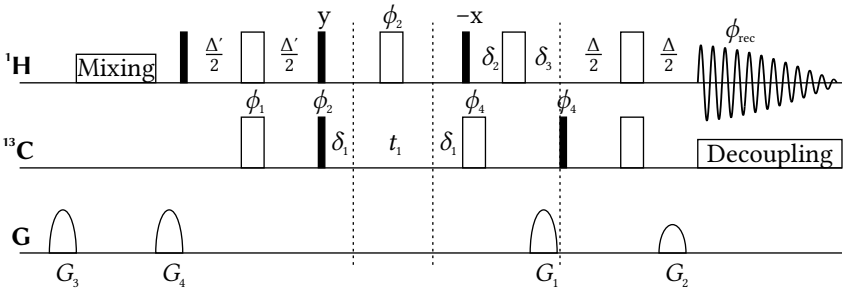

Figure 5.1: ASAP-HSQC sequence introduced by Schulze-Sünninghausen *et al.* [20]. The reservoir magnetization is returned to z before the first magnetic field gradient for the coherence order selection is applied. The selected ^{1}H magnetization is transformed to heteronuclear multiquantum coherence for a short time. When unspecified, pulse phases are x; ϕ_1 = x; ϕ_2 = x, −x; ϕ_3 = 2(x), 2(−x); ϕ_4 = 4(−x), 4(x); ϕ_{rec} = x, −x, x, −x, −x, x, −x, x. The phases ϕ_1 and ϕ_2 are incremented for TPPI. The delay $\Delta = 1/2^1 J_{CH}$ is matched to the average one bond coupling constant, usually 145 Hz, the delay Δ' is reduced for Ernst angle-like excitation. Chemical shift evolution during the delays and pulses is balanced by the small delays δ_1, δ_2, and δ_3. The gradients G_1 and G_2 are used for echo/antiecho coherence order selection. To select the multi-quantum coherence pathway, they have to be set to G_1 = (63.9 %, 80 %) and G_2 = (80 %, 59.9 %).

of an ASAP-HSQC with a conventional HSQC of menthol in $CDCl_3$. The signal intensity is significantly increased and a spectrum of good quality is obtained.

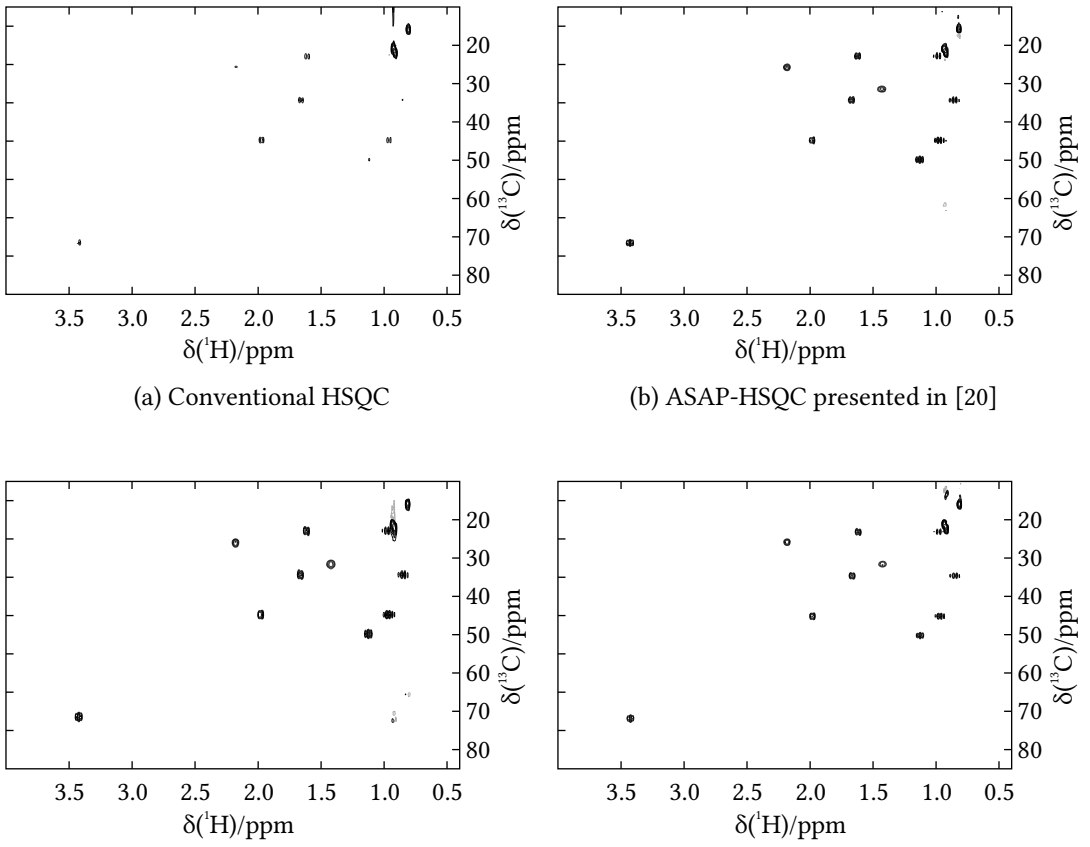

(a) Conventional HSQC

(b) ASAP-HSQC presented in [20]

(c) New symmetric ASAP-HSQC experiment

(d) New asymmetric ASAP-HSQC experiment

Figure 5.2: Short HSQC experiments of 220 mM menthol in $CDCl_3$. a) Conventional HSQC spectrum using the pulse program `hsqcetgp` from the Bruker library. b) ASAP-HSQC using the pulse sequence published in [20]. c) New symmetric pulse sequence presented in Section 5.2.1. d) New asymmetric pulse sequence presented in Section 5.2.2. The INEPT delay was $\Delta = \frac{1}{2 \cdot 145\,\mathrm{Hz}}$. In the ASAP experiments, the first INEPT delay was reduced to $\Delta' = 0.7 \cdot \Delta$. DIPSI-2 mixing was used with 34.5 ms mixing time to share polarization [131]. The recovery delay between two scans including the acquisition time and the mixing time was 0.15 s. 512×64 real points were recorded in 13 s with 16 dummy scans and 1 scan per increment. Phase sensitivity was achieved using echo/antiecho coherence order selection. GARP was used for heteronuclear decoupling [144]. All FIDs were extended to twice their length using forward linear prediction, multiplied with a $\cos^2$ window function, and Fourier transformed to 1024×128.

5.2 New ASAP-HSQC Sequences

5.2.1 Symmetric ASAP-HSQC Sequence

The ASAP-HSQC requires a way to selectively excite ^{13}C-bound protons while positioning all other protons along z, providing a reservoir of polarization. The reservoir contains magnetization of ^{1}H bound to ^{12}C or other non-^{13}C atoms, as well as the part of ^{13}C-bound proton magnetization that is not transferred in the INEPT step. For all periods when the reservoir is in the transverse plane, chemical shift evolution, and heteronuclear coupling needs to be refocused. In a conventional HSQC, however, the reservoir simply is dephased by the gradient pulses, never refocused, and therefore lost.

On these grounds, the central challenge in finding functional sequences for the ASAP-HSQC is the preservation of the reservoir in spite of the echo-antiecho coherence selection. In the original ASAP-HSQC sequence this is achieved by creating ^{1}H-^{13}C multiquantum terms for a short period before the second INEPT block. We found a novel, more general way of preserving the reservoir that is illustrated in Figure 5.3a [145]. Ernst angle-type excitation is achieved by optimizing the delay Δ' of the first INEPT step, as reported for the ASAP-HSQC and the ALSOFAST-HMQC [20, 141]. After the INEPT step the coherence order selection gradient is split into two gradient pulses, their dephasing effect on proton single quantum coherence, i. e. the reservoir, is canceled by the refocusing 180° pulse on the ^{1}H channel. At the beginning of the second INEPT step the reservoir is refocused on the x axis. The following 90° and 180° pulses with x phase return it to z where it remains until the start of the next scan. Overall, the sequence has a simple layout, gradients can be rearranged, should diffusion become a problem, and additional gradients can be introduced at several points to improve artifact and solvent suppression capabilities [146]. It is also highly symmetrical which helps reduce the effects of pulse errors. For the polarization sharing any homonuclear isotropic mixing sequence can be used. If the mixing sequence is omitted the sequence resembles an ALSOFAST-HSQC experiment.

The pulse sequence was implemented on a 600 MHz Avance III NMR Spectrometer equipped with a cryogenically cooled TCI Probehead and TopSpin 3.2. An ASAP-HSQC spectrum of menthol in $CDCl_3$ is shown in Figure 5.2c. Compared to the conventional spectrum, the symmetric sequence is clearly superior. The signal intensity is increased and artifacts are reduced. The spectrum of the original ASAP-HSQC sequence in Figure 5.2b is very similar. Using the symmetric version, the signal intensity is slightly reduced and the signal is further decreased, when the spectra with higher F_1 resolution are acquired. In return, the spectral quality is increased. The original sequence often creates mirroring artifacts in the indirect dimension that can be overcome by introducing OCT derived shaped pulses. In the symmetric version these artifacts

are already reduced without the use of shaped pulses. The intensity of t_1 noise is also reduced using the new sequence.

5.2.2 Asymmetric ASAP-HSQC Sequence

Another, less symmetric sequence is shown in Figure 5.3b. Again, the reservoir is refocused and returned to z in the second INEPT step. The lack of symmetry makes it slightly more prone to artifacts. However, it requires only a single 180° pulse on ^{13}C during the frequency encoding in the indirect dimension. This pulse is usually the most demanding transformation for broadband spectra and shaped pulses. It therefore should show less artifacts and loss of magnetization than the corresponding symmetric version. Compared to the original version, the intensity of artifact signals shifted by half spectral width is also reduced. An example spectrum is shown in Figure 5.2d. In addition, the pulse sequence can be extended to a ^{1}H,^{13}C-multiplicity-edited ASAP-HSQC without additional pulses. This experiment is presented in Section 5.3.

5.2.3 Implementation of Shaped Broadband Pulses

The two new sequences work well without the use of shaped broadband pulses, as long as the chemical shift dispersion, and therefore the spectral width, is below 1/5 of the RF amplitude of the 180° pulses [84]. Pulses with 20 kHz RF amplitude, corresponding to 25 µs pulse length of the 180° pulse, cover about 4 kHz, which is already less than a menthol spectrum on a 14.1 T magnet (600 MHz ^{1}H Larmor frequency) requires. For broadband applications, the sequence can easily be rewritten to use robust optimized shaped pulses. Figure 5.4 shows the two sequences with the different classes of pulses required, classified as follows:

PP90:^{1}H BEBOP(10 kHz, 20 kHz, 550 us, ±20 %, 1100)
BEBOP $z \rightarrow -y$ point-to-point, 550 µs pulse length, 10 kHz bandwidth, 20 kHz B_1 amplitude, compensated for ±20 % B_1 deviation.

UR180:^{1}H BURBOP-180$_x$(10 kHz, 20 kHz, 600 us, ±20 %, 1200)
BURBOP180°$_x$ universal rotation, 600 µs pulse length, 10 kHz bandwidth, 20 kHz B_1 amplitude, compensated for ±20 % B_1 deviation.

PP90:^{13}C BEBOP(37.5 kHz, 10 kHz, 550 us, ±5 %, 1100)
BEBOP $z \rightarrow y$ point-to-point, 550 µs pulse length, 37.5 kHz bandwidth, 10 kHz B_1 amplitude, compensated for ±5 % B_1 deviation.

PP90:^{13}C time reversed BEBOP^{TR}(37.5 kHz, 10 kHz, 550 us, ±5 %, 1100)
BEBOP $y \rightarrow z$ point-to-point, shape of PP90:^{13}C backwards.

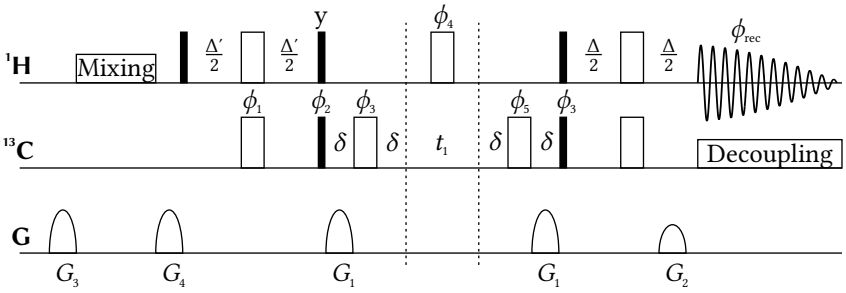

(a) New symmetric ASAP-HSQC sequence.

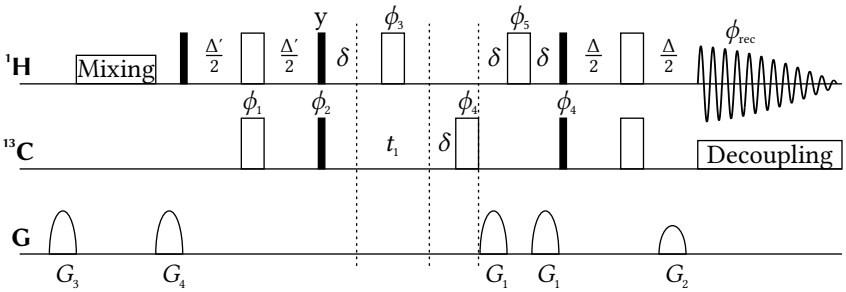

(b) New asymmetric ASAP-HSQC sequence.

Figure 5.3: New ASAP-HSQC pulse sequences in which the reservoir magnetization is dephased and refocused by the first pair of magnetic field gradients used for the coherence order selection. DIPSI-2 mixing is used with usually 20 to 40 ms mixing time to share polarization [131]. If the mixing sequence is removed the experiment becomes an ALSOFAST-HSQC experiment. Pulse phases are x unless specified otherwise. The phases ϕ_1 and ϕ_2 are incremented for TPPI. The delay $\Delta = 1/2^1 J_{CH}$ is matched to the average one bond coupling constant, usually 145 Hz, the delay Δ' is reduced for Ernst angle-like excitation. The gradients G_1 and G_2 are used for echo/antiecho coherence order selection at powers $G_1 = (40\,\%, -40\,\%)$ and $G_2 = (20.1\,\%, 20.1\,\%)$. The gradient pulse length is balanced by the small delay δ. Additional gradient pulses can be introduced during each δ to use asymmetric gradient ratios, as long as ^{1}H single quantum coherence is refocused at the end. a) Highly symmetric sequence with ϕ_1 = x; ϕ_2 = x, −x; ϕ_3 = 4(x), 4(−x); ϕ_4 = 2(x), 2(−x); ϕ_5 = 4(−x), 4(x); ϕ_{rec} = x, −x, x, −x, −x, x, −x, x. b) Asymmetric sequence with only a single 180° pulse on the ^{13}C channel during the frequency encoding of the indirect dimension. ϕ_1 = x; ϕ_2 = x, −x; ϕ_3 = 2(x), 2(−x); ϕ_4 = 4(x), 4(−x); ϕ_5 = 2(−x), 2(x); ϕ_{rec} = x, −x, x, −x, −x, x, −x, x.

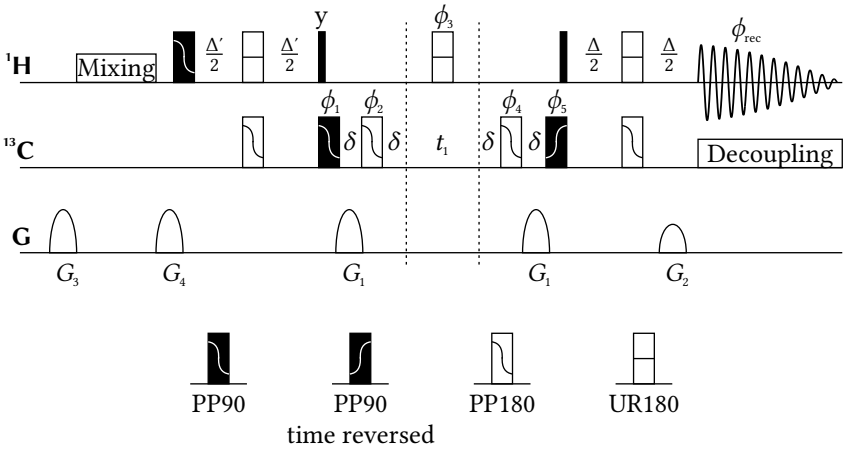

(a) New symmetric ASAP-HSQC sequence with shaped pulses.

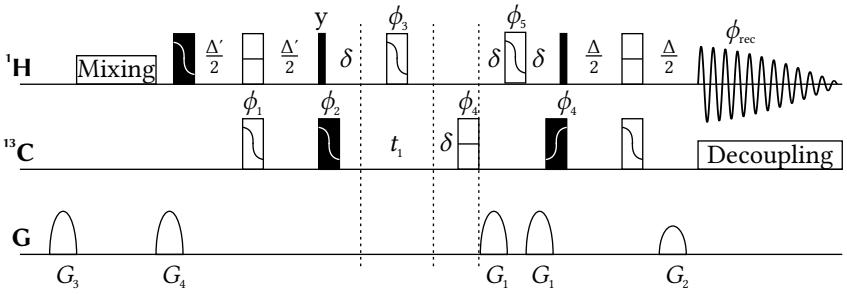

(b) New asymmetric ASAP-HSQC sequence with shaped pulses.

Figure 5.4: Improved versions of the ASAP-HSQC in an implementation using broadband shaped pulses. Pulse phases are x unless specified otherwise. Different pulse shape classes are specified by pictograms, PP corresponds to point-to-point pulses, UR to universal rotation pulses. a) Symmetric ASAP-HSQC sequence with shaped pulses. $\phi_1 = 4(\mathrm{x}), 4(-\mathrm{x})$; $\phi_2 = 4(\mathrm{y}), 4(-\mathrm{y})$; $\phi_3 = 2(\mathrm{x}), 2(-\mathrm{x})$; $\phi_4 = 4(-\mathrm{y}), 4(\mathrm{y})$; $\phi_5 = \mathrm{x}, -\mathrm{x}$; $\phi_6 = \mathrm{x}$; $\phi_{\mathrm{rec}} = \mathrm{x}, -\mathrm{x}, \mathrm{x}, -\mathrm{x}, -\mathrm{x}, \mathrm{x}, -\mathrm{x}, \mathrm{x}$. The phases ϕ_5 and ϕ_6 are incremented for TPPI. b) Asymmetric ASAP-HSQC with shaped pulses. $\phi_1 = \mathrm{x}$; $\phi_2 = \mathrm{x}, -\mathrm{x}$; $\phi_3 = 2(\mathrm{x}), 2(-\mathrm{x})$; $\phi_4 = 4(\mathrm{x}), 4(-\mathrm{x})$; $\phi_5 = 2(-\mathrm{x}), 2(\mathrm{x})$; $\phi_{\mathrm{rec}} = \mathrm{x}, -\mathrm{x}, \mathrm{x}, -\mathrm{x}, -\mathrm{x}, \mathrm{x}, -\mathrm{x}, \mathrm{x}$. The phases ϕ_1 and ϕ_2 are incremented for TPPI.

PP180:^{13}C BIBOP(37.5 kHz, 10 kHz, 600 us, ±5 %, 1200)

BIBOP $z \longrightarrow -z$ point-to-point, 600 µs pulse length, 37.5 kHz bandwidth, 10 kHz B_1 amplitude, compensated for ±5 % B_1 deviation.

UR180:^{13}C BURBOP(37.5 kHz, 10 kHz, 1100 us, ±5 %, 2200)

BURBOP180°$_x$ universal rotation, 1100 µs pulse length, 37.5 kHz bandwidth, 10 kHz B_1 amplitude, compensated for ±5 % B_1 deviation.

5.3 The Multiplicity-Edited ASAP-HSQC Experiment

Experiments that can edit NMR signals of heteronuclei by the number of attached protons, termed edited experiments, have been popular for a long time. Originally, experiments with heteronuclear detection were utilized, of which the DEPT ^{13}C NMR experiment [147] is still commonly encountered in routine NMR laboratories. The low gyromagnetic ratio of ^{13}C, however, strongly favors ^{1}H-detected experiments, providing significantly higher signal-to-noise ratio, making such experiments available even when the sample amount is limited. Among the first such experiments was the multiplicity-edited HMQC [148, 149] and shortly later the multiplicity-edited HSQC experiment [150]. Nowadays, gradient-assisted multiplicity-edited HSQC spectroscopy is a widely accepted important experiment [151], in advanced laboratories even used in routine NMR applications. It provides valuable information, useful for assignment and structure elucidation of small molecules and medium-sized molecules like peptides and has become indispensable in most NMR laboratories.

Several multiplicity-edited ASAP-HSQC sequences are possible and a number of them have been presented in [146]. One sequence based on the asymmetric new sequence is presented in Figure 5.5. The editing is achieved simply by increasing two of the delays δ to $\Delta + \delta$. It requires no additional pulses. The corresponding ^{1}H,^{13}C multiplicity-edited ASAP-HSQC spectrum of menthol is shown in Figure 5.6.

Unfortunately, the editing step introduces a severe problem with the ^{13}C-bound part of the reservoir magnetization. If the reservoir is in the transverse plane during the coupling delay, the ^{13}C-bound proton magnetization will also experience a change of sign and afterwards is phase shifted by 180° from the rest of the reservoir magnetization. In consequence, the experiment should either be run without Ernst angle-type excitation, as was done in the spectrum shown, or an additional change of sign has to be introduced by increasing the INEPT delay Δ' to $2 \cdot \Delta - \Delta'$, whereupon the ^{13}C-bound and all other ^{1}H reservoir magnetization end up with equal phase as desired.

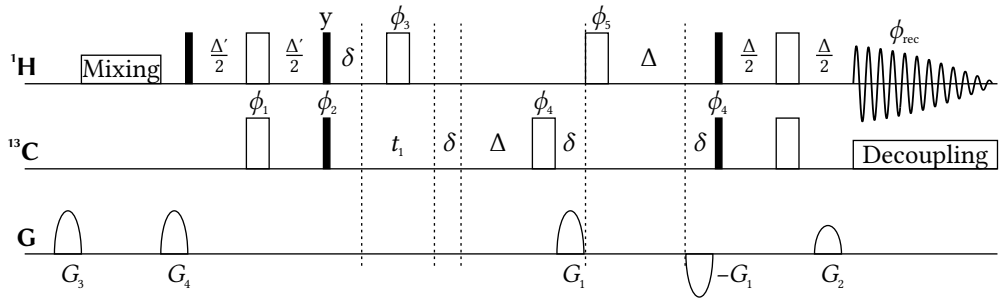

Figure 5.5: Asymmetric multiplicity-edited ASAP-HSQC sequence in which the reservoir magnetization is dephased and refocused by the first pair of magnetic field gradients used for the coherence order selection. Pulse phases are x unless specified otherwise, ϕ_1 = x; ϕ_2 = x, −x; ϕ_3 = 2(x), 2(−x); ϕ_4 = 4(x), 4(−x); ϕ_5 = 2(−x), 2(x); ϕ_{rec} = x, −x, x, −x, −x, x, −x, x. The phases ϕ_1 and ϕ_2 are incremented for TPPI. The delay $\Delta = 1/2^1J_{CH}$ is matched to the average one bond coupling constant, usually 145 Hz, the delay Δ' can be increased for Ernst angle excitation, as mentioned in the text. The gradients G_1 and G_2 are used for echo/antiecho coherence order selection at powers G_1 = (40 %, −40 %) and G_2 = (20.1 %, 20.1 %). The gradient pulse length is balanced by the small delay δ. Like in the other sequences, additional gradient pulses can be introduced during each δ to use asymmetric gradient ratios.

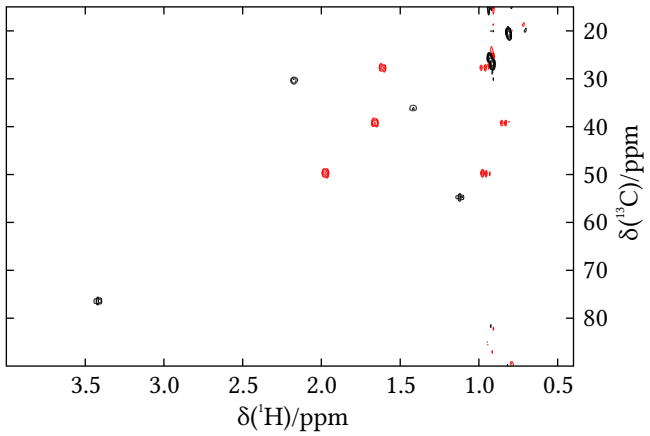

Figure 5.6: ^{13}C multiplicity-edited ASAP-HSQC experiment of 220 mM menthol in $CDCl_3$ acquired using the pulse sequence shown in Figure 5.5. CH and CH_3 groups are shown in black, CH_2 groups have opposite sign and are shown in red. A DIPSI-2 mixing was used with 34.5 ms mixing time to share polarization, the recovery delay between two scans including the acquisition time and the mixing time was 0.15 s. 512 × 64 real points recorded in 13 s with 16 dummy scans and 1 scan per increment. Phase sensitivity was achieved using echo/antiecho coherence order selection. The FID was extended to twice its length using forward linear prediction, multiplied with a $\cos^2$ window function, and Fourier transformed to 1024 × 128 points.

5.4 Conclusion

The ASAP-HSQC provides high quality spectra in very short time. The novel sequences presented can provide further increase in spectral quality compared to the original ASAP-HSQC. Especially without the use of shaped pulses, the reduced artifact intensty is visible. The disadvantage of the new sequences is the reduced signal intensity, for which several reasons are possible. The reservoir magnetization remains transverse approximately 4 ms longer in the new versions, compared to the original ASAP-HSQC. During this period it is subject to homonuclear coupling, that can reduce the available polarization for the mixing step. Diffusion is also a source of signal reduction; in the symmetric version the coherence order selection gradients are separated by a long time interval, that even increases with t_1 during the 2D experiment. When spins diffuse between the gradient pulses, the phases created by the additional magnetic field no longer cancel completely and signals are partially dephased. This dephasing and signal reduction is used as the source of information in diffusion-odered spectroscopy (DOSY). The diffusion effect affects active and passive spins alike, and careful modification of the gradient selection scheme of the sequence could in principle reduce the influence of diffusion without impairing artifact suppression.

Of course, the benefits of all ASAP- and ALSOFAST-HSQC experiments depend on the molecule in question. First of all, the ASAP-scheme depends on natural abundance of ^{13}C isotopes, ensuring a low number of active protons per molecule. The polarization sharing requires neighboring passive protons that have relevant coupling constants as reservoir magnetization. Menthol turned out to be an ideal candidate, featuring a high number of spins that are all connected by J couplings, while no problematic strong coupling artifacts were encountered. In a molecule without large spin systems, the mixing sequence will fail to increase the available polarization on the active protons. In fact, the saturation due to the additional pulses reduces the available polarization, and during the mixing sequence no polarization recovery via T_1 relaxation takes place further reducing the signal intensity compared to conventional other experiments. For a complete explanation, also the effect of the polarization sharing on the reservoir spins has to be considered. For a rough estimate see the models derived in the next chapter.

When the experiments presented in this chapter are used without the mixing sequence, the possible disadvantages are gone. The Ernst angle-type excitation available in the ALSOFAST-HSQC is a risk-free way to increase the signal-to-noise ratio in experimental setups where the delay between scans is too short to allow full relaxation. Without the active mixing, the contribution of passive spins is very small. In SOFAST experiments a positive influence could

be shown in proteins [77, 78]. For small molecules however, relaxation may actually be reduced as explained in the next chapter.

To understand the effects and properties of the different experiments, it is of great interest to examine the relaxation behavior and to find a simple theoretical model to describe processes that take place during the variety of fast experiments. In the next chapter corresponding models will be derived and discussed.

Chapter 6

Signal Recovery in Fast HSQC Experiments

6.1 T_1 Relaxation

6.1.1 Polarization and NMR Experiments

In an external static magnetic field, the spins of a sample are either aligned parallel or anti-parallel to the magnetic field. The two states have a small energy difference, and in thermal equilibrium, the state of lower energy will have slightly higher population. The population difference is primarily dependent on temperature, field strength and the magnitude of each spin's magnetic moment. Altogether, the spins contribute to a macroscopic sample magnetization, the sample is polarized by the external field. This *polarization* is not measured directly; NMR experiments transform it into measurable coherences using a pulse or pulse sequences, using up the polarization of relevant isotopes. Fortunately, the spins will always return to equilibrium and polarization will recover.

Increasing polarization above its thermal equilibrium is not readily achieved in a closed system. However, it is comparatively simple to transfer polarization from a spin with high thermal polarization to a spin with lower polarization, like in the INEPT experiment or the corresponding transfer element of many heteronuclear pulse sequences [**hmbc**, 1, 15, 147, 152]. Unfortunately, the spins will always return to equilibrium and polarization will be reduced to the original level.

The spins do not reach equilibrium instantaneously, but starting with initial polarization $P(0)$, follow a simple exponential law,

$$P(t) = P_{\mathrm{Eq}} - \left(P_{\mathrm{Eq}} - P(0)\right) \cdot e^{-t/T_1}. \tag{6.1}$$

The process of polarization returning to equilibrium is called T_1 relaxation or spin-lattice relaxation, and the characteristic time of the exponential law is called T_1 time or spin-lattice relaxation time. In general, its magnitude is determined by the kind of nucleus, its magnetic surroundings,

the B_0 strength, and the size of the molecule. Each spin within a molecule can have a different T_1 time, and even the precise state of the surrounding spins influences it [153].

As has been shown [154, 155], a process called *cross relaxation* occurs in a system of two spins in proximity and causes simultaneous spin flips of the two spins, which is a kind of polarization transfer. This effect can be used to record NOESY spectra, where the sign of cross signals compared to diagonal signals is dependent on the correlation time and therefore on the size of the molecule. If a single spin is considered, cross relaxation from surrounding spins can contribute to polarization recovery or impede it. It turns out, that in small molecules, the relaxation is impeded by surrounding positive polarization [153, 156] which leads, as will be shown in this chapter, to the seemingly counter intuitive behavior of longer relaxation time after selective excitation of single spins and many relaxation-optimized experiments that perform outstandingly on large molecules have fundamental problems when applied to small molecules.

6.1.2 Selective Recovery Experiments

Band-selective excitation data in different environment is obtained by using a modified inversion recovery sequence displayed in Figure 6.1. It consists of two pulses with variable flip angle, α and β, that were set to 0°, 90°, and 180° in all combinations. The spin at the center of the spectrum undergoes a rotation of $\alpha + \beta$, all other spins are only affected by β. This allows creating defined environments for the observed spin. In the recovery delay following the α and β pulses, the system will relax and the final polarization is measured by the readout 90° pulse. The recovery delay is varied from 1 ms to 10 s, the delay between two experiments is 30 s. When $\alpha = 0$, the experiment becomes a regular saturation or inversion recovery sequence. All spectra were acquired on a 600 MHz Avance III NMR Spectrometer equipped with a TCI Probehead and TopSpin 3.2.

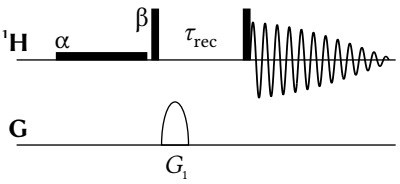

Figure 6.1: Pulse sequence used for the selective recovery experiment; The pulse labeled α is a 20 ms low-power rectangular pulse which is sufficiently selective to manipulate individual peaks. The flip angle α is adjusted by changing the power level. The pulse labeled β is a non-selective 29 kHz rectangular pulse. The flip angle β is adjusted by changing the pulse length. The recovery time τ_{rec} was varied from 35 ms to 10 s.

Menthol was the first molecule tested with the ASAP-HSQC. It is a good example of a system where the ASAP-method is advantageous. The regular 1D spectrum of menthol is quite crowded, but almost all peaks are separated. In the ^{13}C-filtered spectrum, some peaks cannot be interpreted individually, however, at least one proton signal per carbon position could be found. The assignment is shown in Figure 6.2.

The intensity obtained corresponds to the polarization after the variable delay. It is displayed for each spin in Figure 6.3 and as mean value for the whole molecule in Figure 6.4. The results are divided in the saturation recovery type curves starting around 0 and the inversion recovery curves starting close to -1. Working out the T_1 relaxation time by fitting an exponential function like Equation (6.1) reveals that the experiments with $\alpha = 0$ always have roughly the same relaxation time. These are non-selective experiments where the environment spins have the same polarization as the observed spins. Polarization transfer between them is negligible. This, of course, is in agreement with traditional experiments where one would not expect the relaxation time to be dependent on the pulse sequence.

The polarization curves and the T_1 times derived from them show faster relaxation when the environment is inverted compared to untouched environment. This is the effect of NOE in small molecules.

The second molecule that is measured in this series of experiments is the disaccharide maltose. The 1D spectrum of maltose shows many overlapping peaks. Some peak ranges can be assigned to individual positions, a large part corresponding to unspecified ring protons remains unassigned. The assignment is shown in Figure 6.5. Maltose is one of the few molecules where the ASAP-HSQC brings only a small advantage compared to the conventional HSQC. It was therefore chosen to show the limits of polarization recovery.

The intensity obtained from maltose which corresponds to the polarization after the variable delay is displayed for each spin in Figure 6.6 and as mean value for the whole molecule in Figure 6.7. Like with menthol, aligning the environment along $-z$ increases the relaxation rate. The reduced relaxation of $+z$ environment is even more pronounced here.

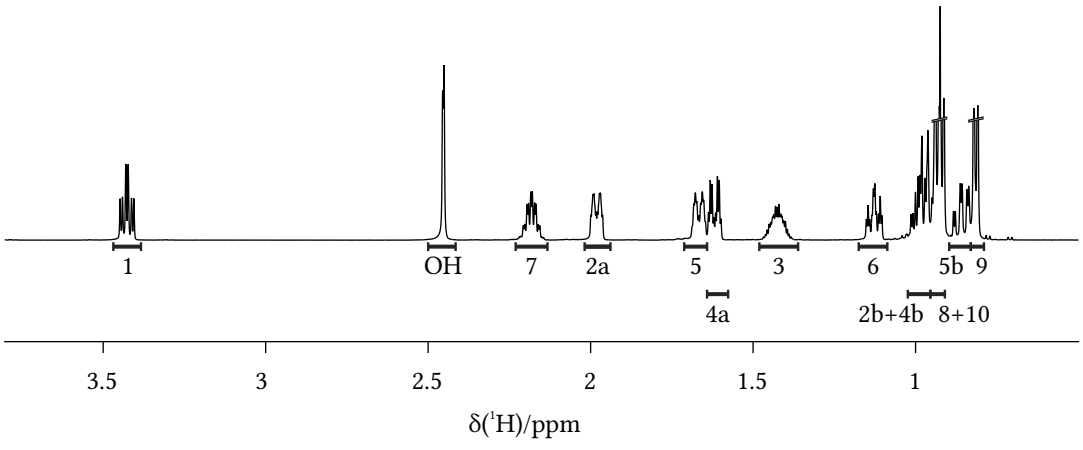

(a) ^{1}H 1D spectrum

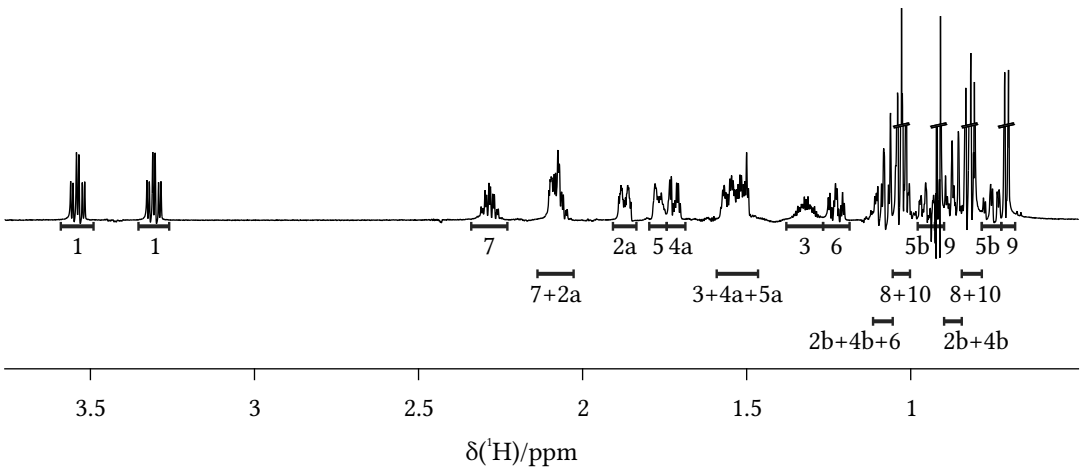

(b) ^{13}C-filtered spectrum

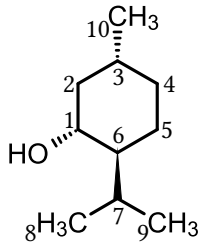

Figure 6.2: Assignment of spectral regions of menthol. a) Regular ^{1}H 1D spectrum. b) ^{13}C-filtered 1D spectrum obtained with the HSQC recovery experiment from Figure 6.8 with delay $\tau_{rec} = 10$ s without ^{13}C decoupling. The sample contains 0.5 M (−)-menthol in $CDCl_3$.

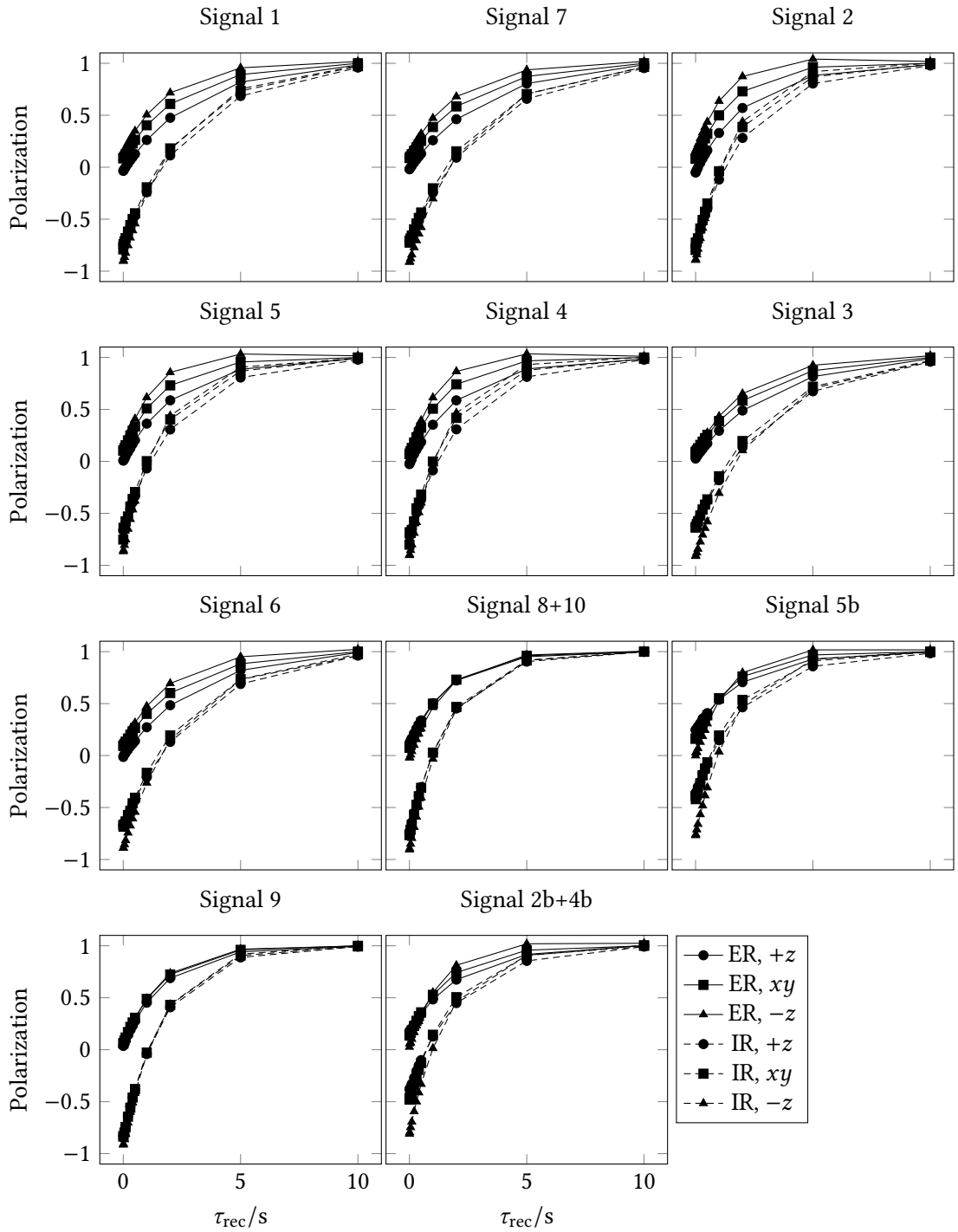

Figure 6.3: Individual menthol polarization versus recovery delay in a selective excitation recovery (ER) or inversion recovery (IR) experiment for different alignments of the reservoir, either along $+z$, dephased in the xy plane, or along $-z$.

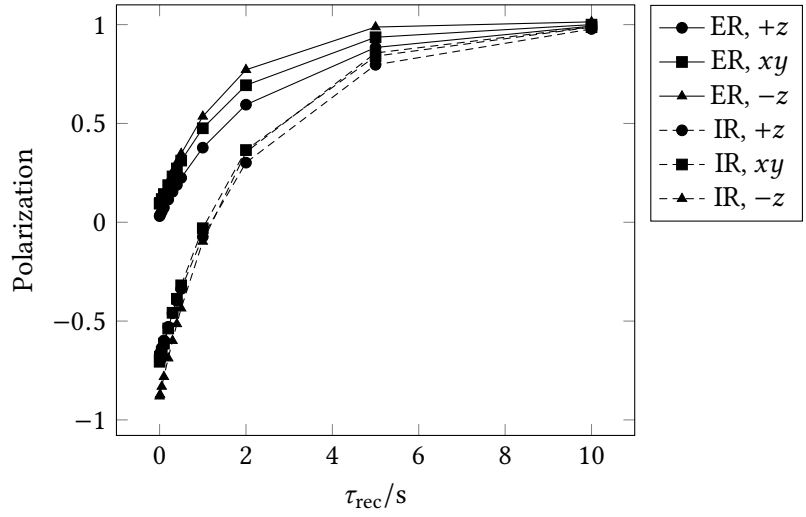

Figure 6.4: Mean menthol polarization versus recovery delay in a selective excitation recovery (ER) or inversion recovery (IR) experiment for different alignments of the reservoir, either along $+z$, dephased in the xy plane, or along $-z$.

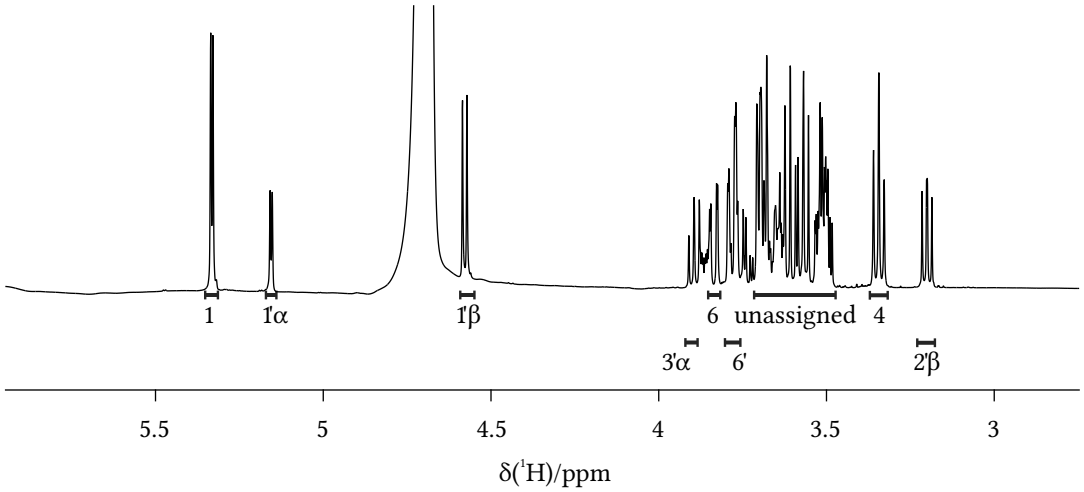

(a) ^{1}H 1D spectrum

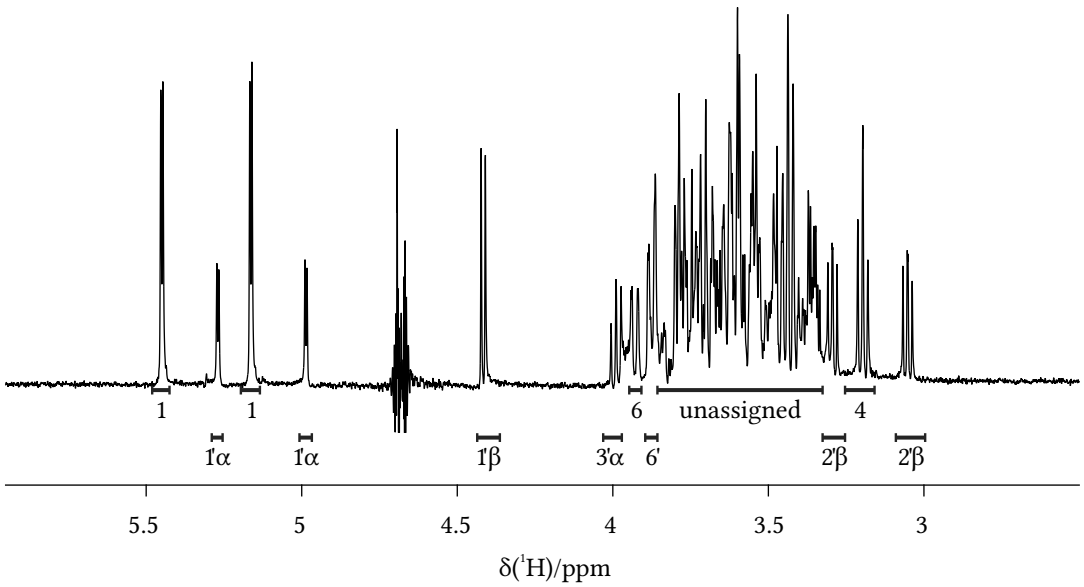

(b) ^{13}C-filtered spectrum

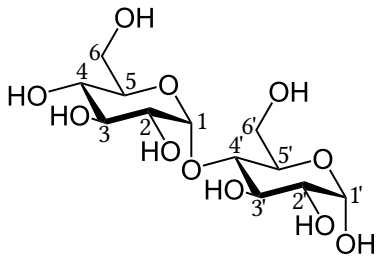

Figure 6.5: Assignment of spectral regions of α-maltose. a) Regular ^{1}H 1D spectrum. b) ^{13}C-filtered 1D spectrum obtained with the HSQC recovery experiment from Figure 6.8 with delay τ_{rec} = 10 s without ^{13}C decoupling. The crowded region of ring protons could not be assigned individually.

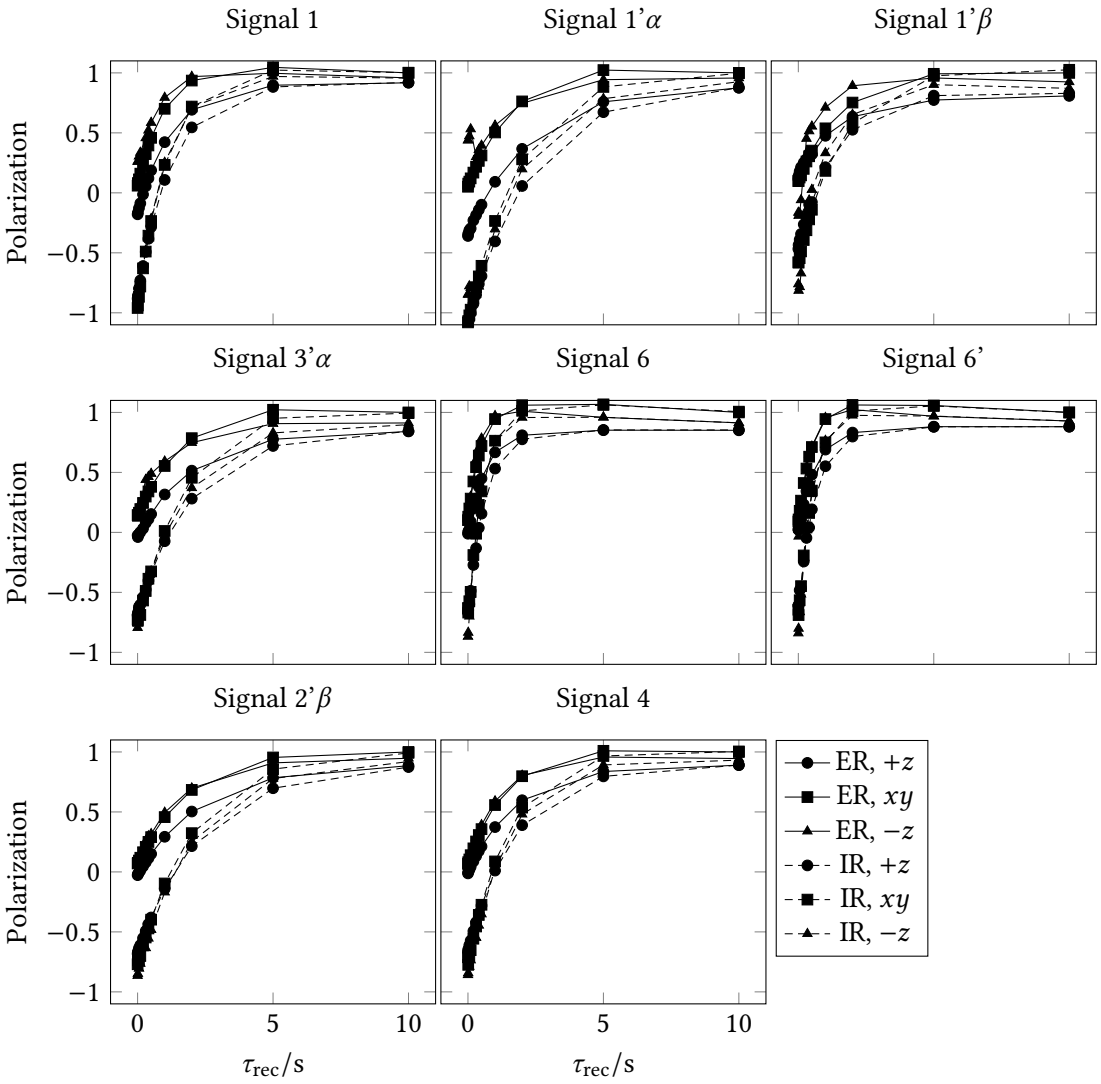

Figure 6.6: Individual maltose polarization versus recovery delay in a selective excitation recovery (ER) or inversion recovery (IR) experiment for different alignments of the reservoir, either along $+z$, dephased in the xy plane, or along $-z$.

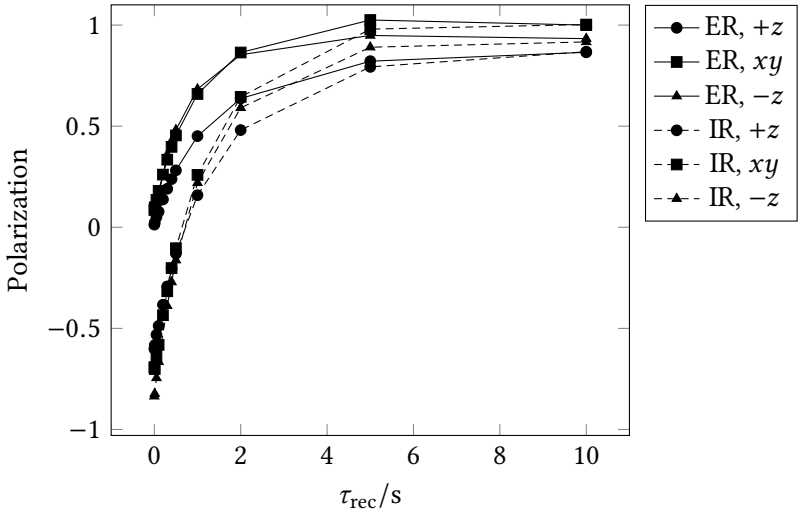

Figure 6.7: Mean maltose polarization versus recovery delay in a selective excitation recovery (ER) or inversion recovery (IR) experiment for different alignments of the reservoir, either along $+z$, dephased in the xy plane, or along $-z$.

6.1.3 Experimental Thermal Equilibrium State HSQC Recovery

The selective relaxation measurements confirmed the expectations of the influence, the environment has on local relaxation times. There is no reason to expect the available fast HSQC experiments to be exempt from the basic properties of relaxation. It is therefore of interest to obtain insight in the relaxation behavior of the ALSOFAST-HSQC and the ASAP-HSQC [20] that were introduced in the last chapter. The two experiments are similar except for the application of an isotropic mixing sequence. In an attempt to disentangle the different effects that influence the polarization and final signal intensity, the pulse sequence shown in Figure 6.8 was devised. It consists of the preparation phase where a 1D HSQC pulse sequence is either run once or repeated multiple times to saturate parts of the sample. Like in a real 2D HSQC, a part of initial polarization is transferred during the INEPT step and this part is not available for the next scan. The INEPT delay is matched to 145 Hz, so from ^{1}H bound to ^{13}C, most of the magnetization will be transferred. After the preparatory HSQC, the transferred magnetization is instantly dephased by a pulsed magnetic field gradient. The remaining small part that is not transferred can be preserved during the sequence. The $^{2}J_{\mathrm{CH}}$, $^{3}J_{\mathrm{CH}}$ and more distant couplings between ^{1}H and remote ^{13}C is small compared to $^{1}J_{\mathrm{CH}}$, so magnetization of these nuclei is only transferred to a very small part. All the untransferred magnetization makes up the reservoir. By changing pulse phases within the sequence, the final alignment of the reservoir can be controlled to be either parallel or antiparallel to the magnetic field or dephased together with the transferred magnetization. Following the HSQC element, the variable delay τ_{rec} allows relaxation which creates polarization. Here the influence of the environment, i. e. the orientation of the reservoir magnetization, will be revealed by a change in polarization recovery rate. Subsequently, a mixing element of variable length will show the relaxation behavior of the ASAP-HSQC and related experiments. The preparatory HSQC followed by the relaxation delay and optional mixing is either run once to create a well-defined state or repeated several times to reach the steady state of the system. Readout is accomplished by another 1D HSQC sequence with unmodified phases. The lack of F_1 frequency discrimination causes strong artifacts from ^{1}H bound to ^{12}C at the center frequency of the doublets. To keep these artifacts separated from the desired signals, therefore, no decoupling was used. To achieve some artifact suppression, two scans were recorded per experiment. The relaxation delay τ_{rec} was varied from 35 ms to 10 s. In a real 2D-HSQC, this delay must contain the experimental acquisition time as well as any additional delays in the pulse sequence until the start of the next scan, typically called `d1` or `d11` in Bruker pulse programs.

For mixing, the DIPSI-2 sequence was used and mixing time was varied from 0 to 58 ms. The whole preparation block was looped 1, 8, 16, or 64 times.

Out of the parameters covered, some combinations correspond to actual experiment conditions. To resemble a conventional HSQC, the reservoir is dephased in the xy plane, and no mixing is used. The ALSOFAST-HSQC case is created by retaining the reservoir along z. Finally, sharing proton polarization by aligning the polarization along $+z$ and including the mixing sequence with optimal mixing time resembles the conditions of the ASAP-HSQC.

Technical reasons prevented arbitrarily short relaxation delays. The subsequent fit of T_1 times, simultaneously yielded a value for polarization at $\tau_{\mathrm{rec}} = 0$ and $\tau_{\mathrm{rec}} = \infty$, which will be shown alongside the measured values where applicable.

Menthol

The intensities of the readout HSQC on menthol after a single preparatory HSQC are displayed in Figure 6.9. The measured intensity corresponds to the polarization right before the final part of the pulse sequence. All regions behave alike, therefore most results can be given as mean values as displayed in Figure 6.10. The initial magnetization depends on the sign of the reservoir and environment. The regeneration of polarization is roughly exponential, with respect to the length of the recovery delay. The initial values, however, deviate a lot, which is explained by the unmatched INEPT transfer delay. Fitting an exponential decay as described by Equation (6.1), yields the T_1 times shown in Figure 6.11, where the relaxation-reducing effect of the NOE is quite visible.

Application of the mixing sequence increases the impact of the sign of the reservoir. In the optimal case, i. e.DIPSI-2 mixing and positive reservoir, the mixing alone without recovery delay is sufficient to recover 25 to 75 % of the magnetization. Mixing with the wrong sign of the reservoir, consequently, greatly reduces intensity, in some cases even down to -1.

Figure 6.12 shows the course of initial polarization with increasing length of DIPSI-2 mixing. The mixing allows recovery of more than 50 % of magnetization without relaxation during the recovery delay. Unfortunately for the ASAP-HSQC, this fast polarization recovery depletes the reservoir and is not maintained over more than a few scans as we will see later.

Maltose

The polarization of maltose with increasing recovery delay after a single preparatory HSQC is displayed in Figure 6.13. The mean polarizations are displayed in Figure 6.14. The T_1 times obtained from the exponential fit as described by Equation (6.1) are shown in Figure 6.15.

Figure 6.12 shows the course of initial intensity with increasing length of DIPSI-2 mixing. Compared to menthol, the initial magnetization is much less dependent on the sign of the reservoir. Application of the mixing sequence causes positive contribution of the reservoir

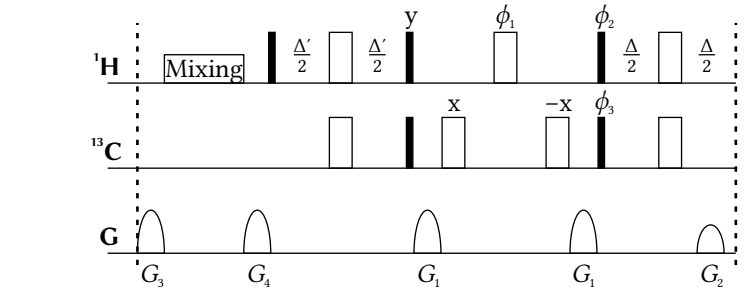

(a) Preparatory HSQC

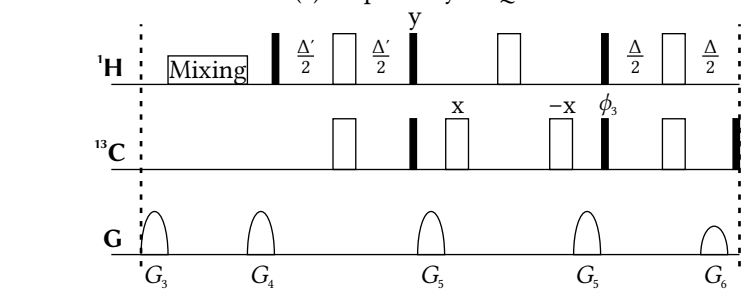

(b) Readout HSQC

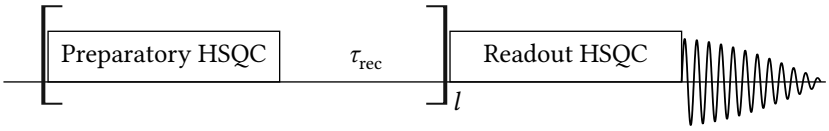

(c) Experiment outline

Figure 6.8: Pulse sequence used for the HSQC recovery experiments. The sequence consists of two sub-sequences, a) a preparatory HSQC and b) and a readout HSQC. c) In the experimental setup, the preparatory HSQC is followed by a delay, τ_{rec}, and then is run 1, 8, 16, or 64 times by changing the loopcounter l to show the difference between thermal equilibrium and steady state. The pulses are drawn as hard pulses for simplicity, however, shaped pulses as shown in Figure 5.4a were used. All pulses are x pulses, unless specified otherwise. ϕ_1 = x; ϕ_2 = y; ϕ_3 = x, −x; Switching the phase ϕ_1 from x to y, changes the reservoir alignment from z to $-z$. Switching the phase ϕ_2 from y to x, dephases the reservoir magnetization in the transverse plane. The transfer delay Δ' of the fist INEPT step can be adjusted to implement incomplete transfer and allow Ernst angle excitation.

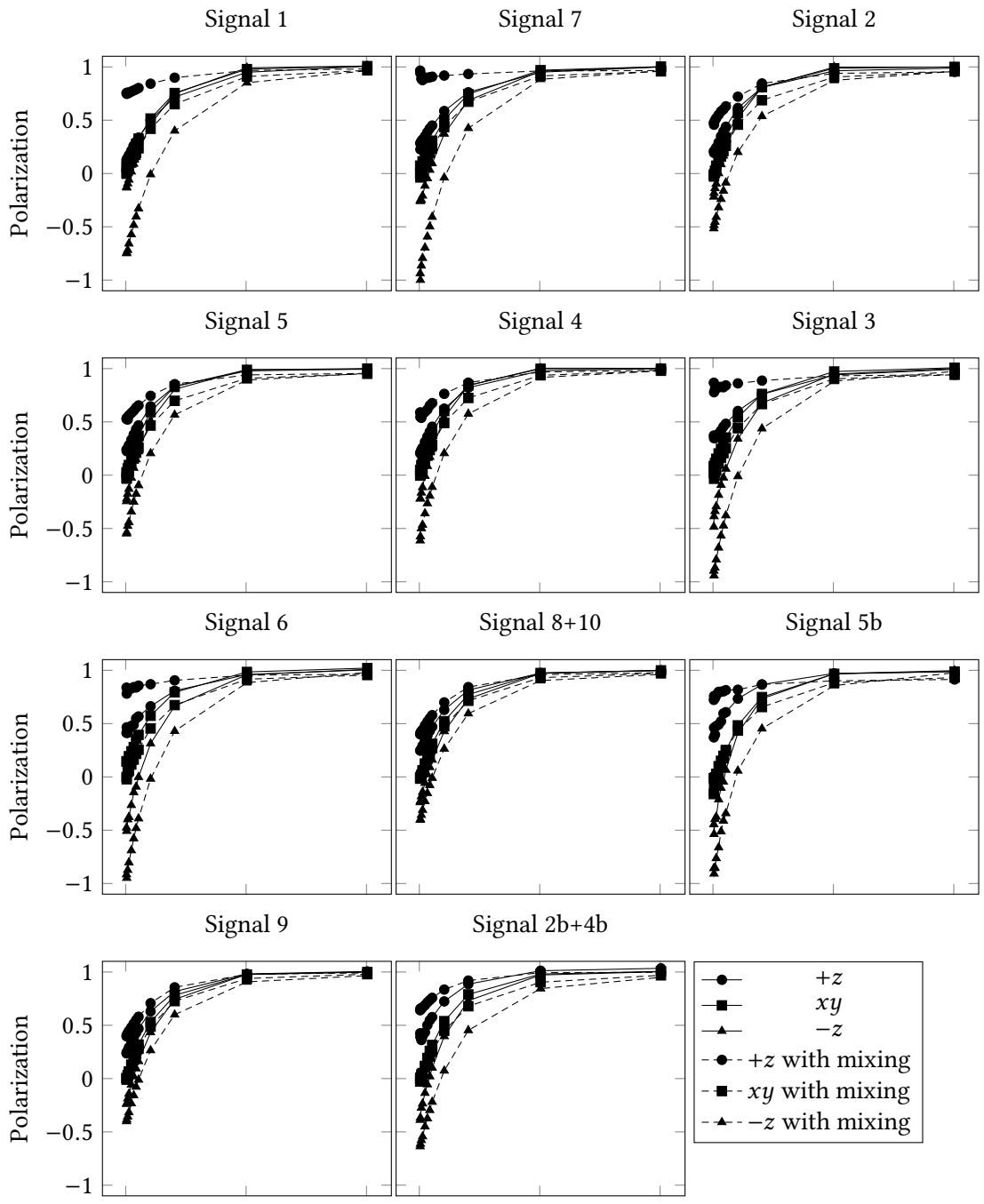

Figure 6.9: Individual experimental menthol polarization versus recovery delay from the HSQC-recovery experiment run in thermal equilibrium ($l = 1$). The reservoir is either aligned along $+z$, dephased in the xy plane or aligned along $-z$. DIPSI-2 mixing is either off or 34.5 ms.

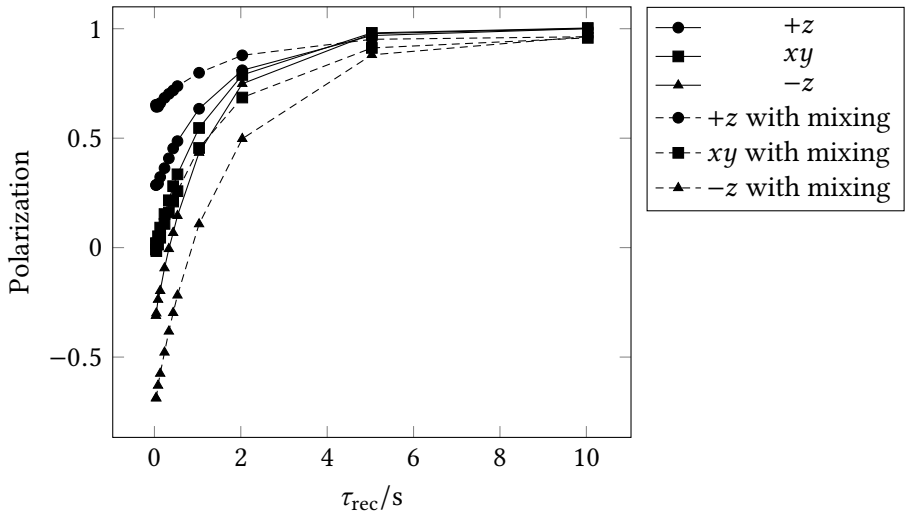

Figure 6.10: Mean menthol polarization versus recovery delay from the HSQC-recovery experiment run in thermal equilibrium ($l = 1$). The reservoir is either aligned along $+z$, dephased in the xy plane or aligned along $-z$. DIPSI-2 mixing is either off or 34.5 ms.

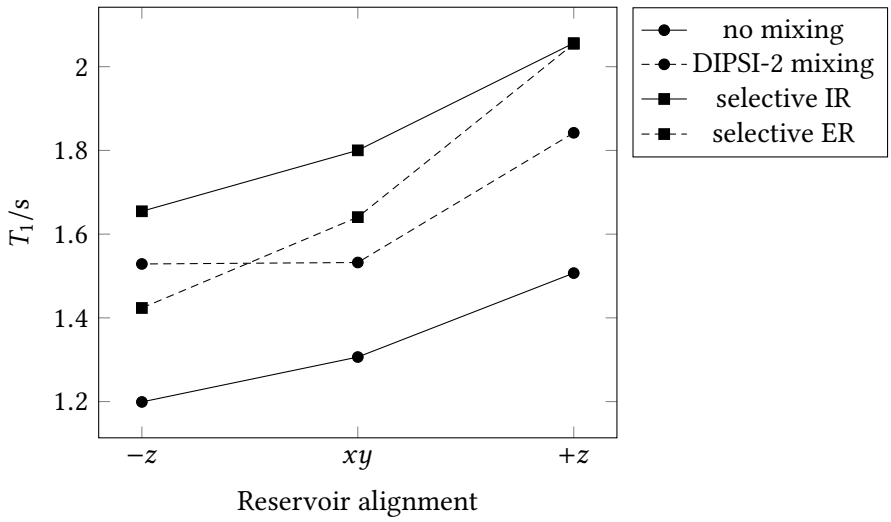

Figure 6.11: Mean T_1 time of menthol for different conditions obtained by fitting the polarization ($l = 1$) to the exponential function Equation (6.1). The conventional HSQC conditions are found without mixing and the reservoir dephased in the xy plane. The ALSOFAST-HSQC conditions are found without mixing and the reservoir aligned in $+z$. For the ASAP-HSQC, 34.5 ms DIPSI-2 mixing is used and the reservoir aligned along $+z$. The selective recovery data from excitation recovery (ER) and inversion recovery (IR) is shown for comparison.

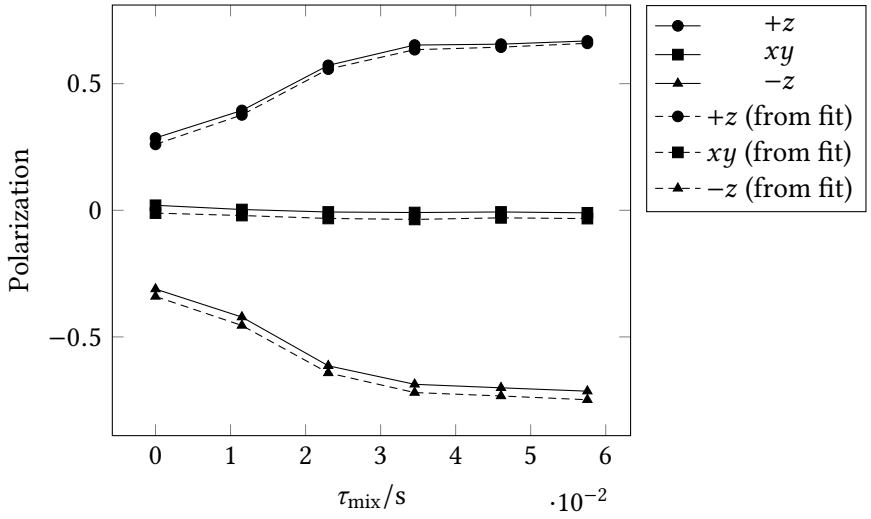

Figure 6.12: Mean experimental polarization of menthol after a single HSQC run ($l = 1$) and short recovery time versus mixing time. The measured intensity at minimum recovery delay, 35 ms, is shown (solid lines) alongside extrapolated polarization at $\tau_{\text{rec}} = 0$ from T_1 relaxation fit (dashed lines). The reservoir is either aligned along $+z$, dephased in the xy plane or aligned along $-z$. Given the right alignment, some polarization is recovered by the mixing sequence.

according to its alignment. In the optimal case, i. e.DIPSI-2 mixing and positive reservoir, the mixing alone is only able to recover less than 50 % of the magnetization. The discrepancy between measured value and fit parameter can be attributed to T_1 relaxation during the 35 ms minimum delay.

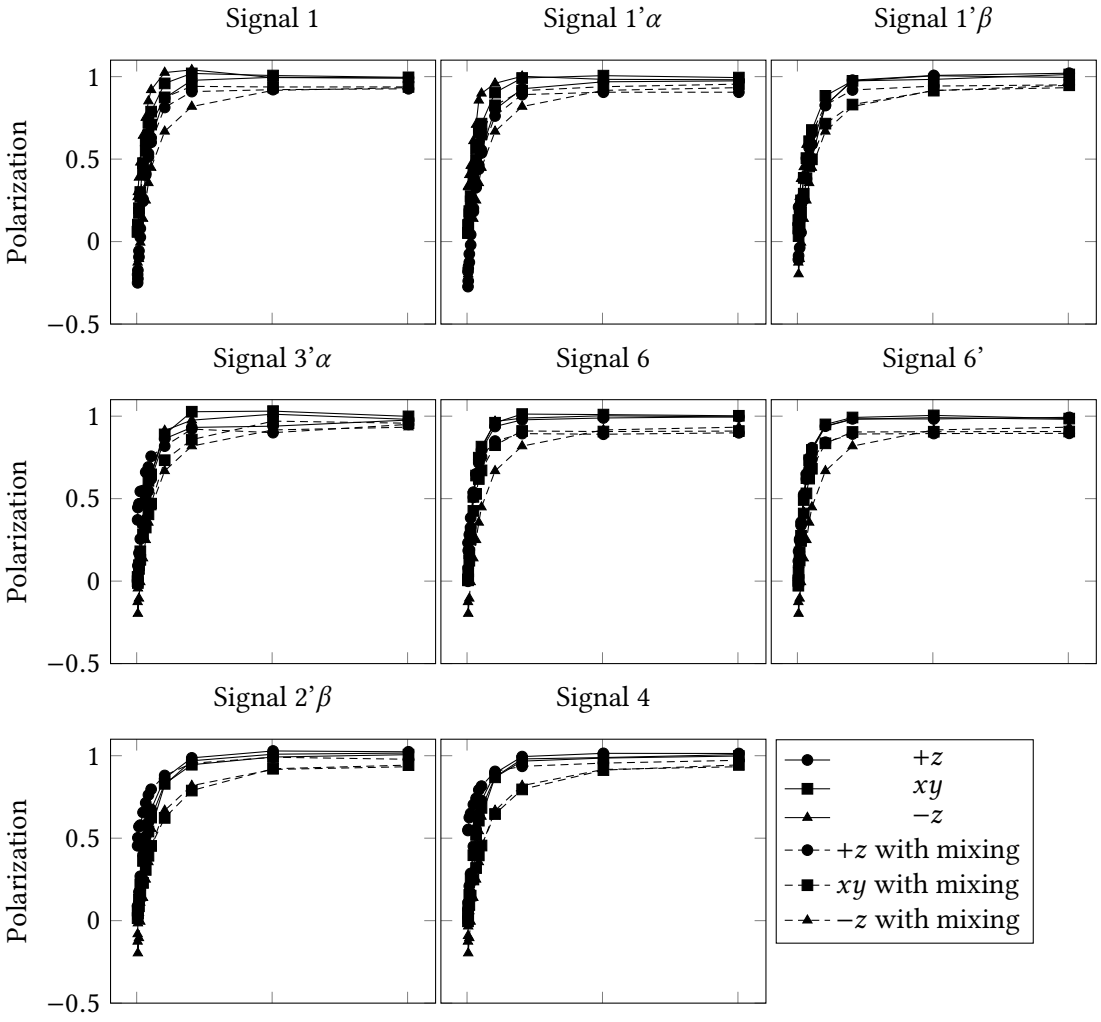

Figure 6.13: Individual maltose polarization versus recovery delay from the HSQC-recovery experiment run in thermal equilibrium ($l = 1$). The reservoir is either aligned along $+z$, dephased in the xy plane or aligned along $-z$. DIPSI-2 mixing is either off or 23 ms.

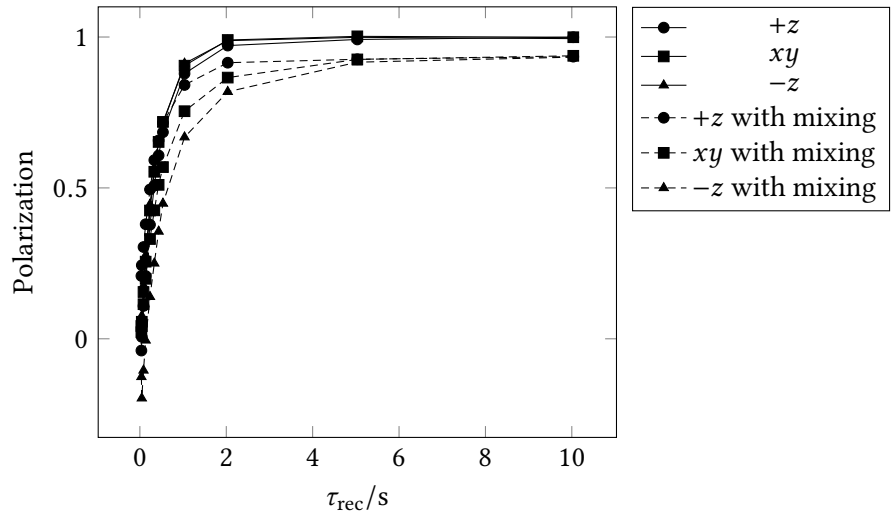

Figure 6.14: Mean experimental maltose polarization versus recovery delay from the HSQC-recovery experiment run in thermal equilibrium ($l = 1$). The reservoir is either aligned along $+z$, dephased in the xy plane or aligned along $-z$. DIPSI-2 mixing is either off or 23 ms.

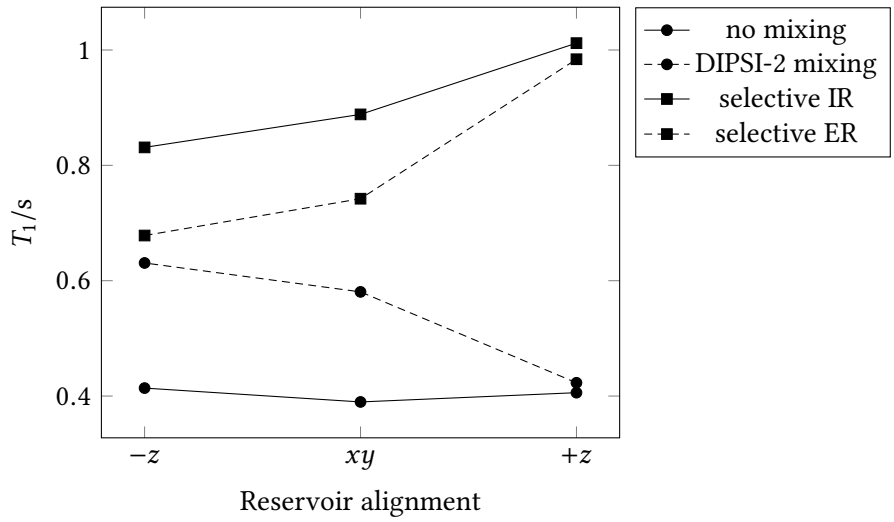

Figure 6.15: Mean T_1 time of maltose for different conditions obtained by fitting the polarization ($l = 1$) to the exponential function Equation (6.1). The conventional HSQC conditions are found without mixing and the reservoir dephased in the xy plane. The ALSOFAST-HSQC conditions are found without mixing and the reservoir aligned in $+z$. For the ASAP-HSQC, 23 ms DIPSI-2 mixing is used and the reservoir aligned along $+z$. The selective recovery data are shown for comparison.

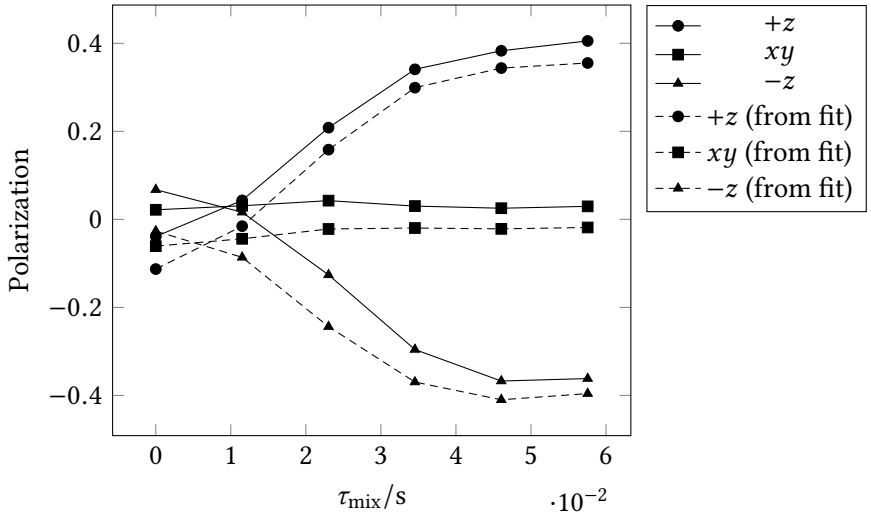

Figure 6.16: Mean experimental polarization of maltose after a single HSQC run ($l = 1$) and short recovery time versus mixing time. The measured intensity at minimum recovery delay, 35 ms, is shown (solid lines) alongside extrapolated polarization at $\tau_{\mathrm{rec}} = 0$ from T_1 relaxation fit (dashed lines). The reservoir is either aligned along $+z$, dephased in the xy plane or aligned along $-z$. Given the right alignment, some polarization is recovered by the mixing sequence.

6.2 Steady State Polarization

6.2.1 Transition from Equilibrium to Steady State

The first impression from the results of the HSQC recovery experiments gives mixed predictions for fast HSQC experiments. On the one hand, the reduced relaxation rate of small molecules caused by NOE after selective excitation is definitely a disadvantage. On the other hand, the mixing sequence in the ASAP-HSQC is very effective in restoring the polarization that is destroyed by a single scan. Real HSQC experiments, however, are rarely run as 1D spectra with a single scan. Usually a two dimensional spectrum is desired, often combined with multiple repetitions of the same point of the indirect dimension. Typically, the interscan delay is highly insufficient to reach the thermal equilibrium state, and after the first scans an unpredictable arrangement of decaying leftover coherences from past scans will arise. Yet, identical conditions and equal signal intensity for all scans are of high importance to achieve spectra of high quality.

Fortunately, there is a different way to create stable conditions. When excitation as well as relaxation is incomplete, leftover polarization from previous scans contributes to current polarization. After a small number of scans, the amount of polarization lost and recovered will be equal, and a so called *steady state* is reached. If excitation is exhaustive, i. e.equivalent to a 90° pulse, or the interscan relaxation delay is short, the polarization of this steady state will

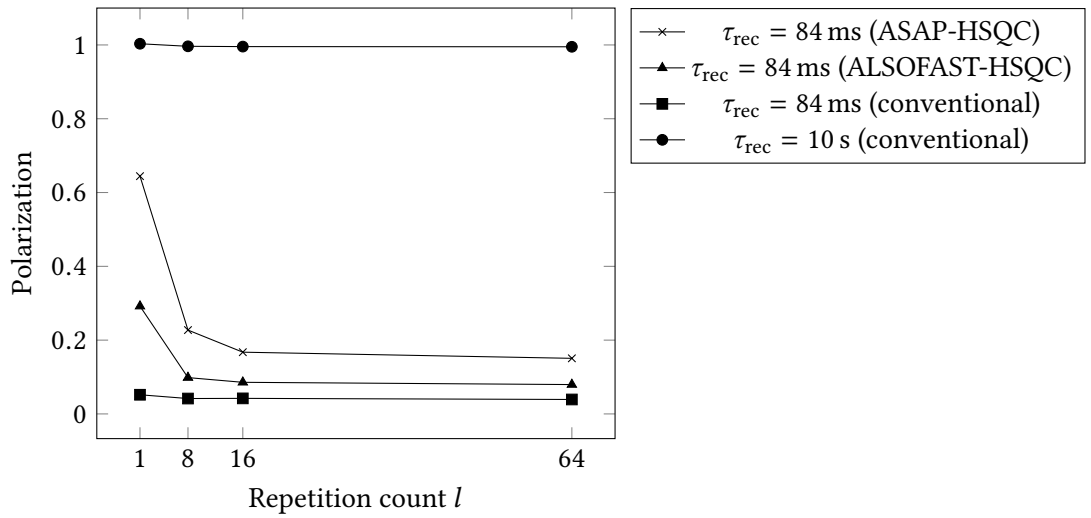

Figure 6.17: Mean experimental menthol polarization versus number of repetitions (l) of the preparatory loop: transition from thermal equilibrium to steady state. In the conventional setup, reservoir magnetization is dephased, the system is already saturated after the first step. In the ALSOFAST and ASAP case, the reservoir is conserved. DIPSI-2-mixing with 34.5 ms mixing time in the ASAP case increases the polarization even further.

be very low. Optimized partial excitation and adjusted delays, on the other hand, can create a steady state with high polarization.

Utilizing the HSQC recovery sequence, the transition can be visualized. The loop counter n in Figure 6.8 allows repeating the preparatory HSQC an arbitrary number of times before acquiring the signal with the readout HSQC. The change in polarization from thermal equilibrium that is increasingly disturbed by pulses, towards the steady state is shown in Figure 6.17. The polarization of the steady state and the signal intensity obtained at the same time is the central figure of merit for experiments featuring rapid acquisition. This steady state will now be explored theoretically as well as experimentally.

6.2.2 Theory of the Steady State

The model for the steady state polarization of HSQC experiments is based on the model for a single-pulse experiment that leads to the well-known Ernst angle used in many fast experiments and on samples with long relaxation times [76].

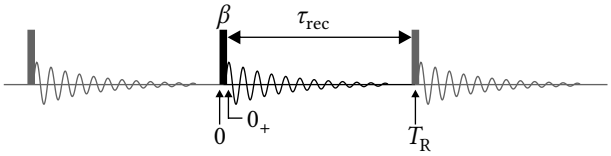

Figure 6.18: Simple pulse-acquire-experiment, basic concept for the Ernst angle. The experiment starts at $t = 0$ with a negligibly short pulse that ends at $t = 0_+$. In the following delay τ_{rec} the system recovers polarization until the next repetition starts at $t = T_{\mathrm{R}}$.

Single Pulse Model

The optimal flip angle with respect to signal intensity in a conventional 1D experiment as sketched in Figure 6.18, with many repetitions of repetition time T_{R} can be derived as shown in [76]. Starting from equilibrium polarization P_{Eq}, the resulting steady state polarization at time 0 directly before the β-pulse and after a sufficiently large number of scans may be described by $P(0)$. Following the pulse, the remaining polarization is

$$P(0_+) = P(0)\cos\beta. \tag{6.2}$$

Due to T_1 relaxation, the polarization grows as described in Equation (6.1). After the recovery delay $\tau_{\mathrm{rec}} \approx T_{\mathrm{R}}$, before the next pulse, the polarization has recovered to

$$P(\tau_{\mathrm{rec}}) = P(0_+)\,E_1 + P_{\mathrm{Eq}}(1 - E_1), \tag{6.3}$$

using the well-known abbreviation

$$E_1 = \exp(-\tau_{\mathrm{rec}}/T_1) \tag{6.4}$$

that was introduced in [76]. The steady state is then defined by $P(0) = P(T_{\mathrm{R}})$, which means that the polarization at the beginning of subsequent experiments is equal. This allows the calculation of the effective signal intensity of a single scan within the series of experiments by

$$S(0_+) = P_{\mathrm{Eq}}\frac{1 - E_1}{1 - E_1\cos\beta}\sin\beta. \tag{6.5}$$

Apparent relaxation time with respect to the recovery delay is enhanced if $\beta < 90°$ and the polarization is preserved by the pulse sequence. A mismatched 90° pulse can be enough, setting it to 80° in a system with $T_1 = 1\,\mathrm{s}$, changes the apparent relaxation time to $T_1^{\mathrm{SS}} = 0.84\,\mathrm{s}$.

ALSOFAST-HSQC Model

The ALSOFAST-HSQC as introduced as a variant of the ASAP-HSQC in Figure 5.3a of the last chapter retains unused magnetization along z. This is also implemented in the HSQC-recovery sequence shown in Figure 6.8. Conservation of the reservoir allows Ernst angle-type excitation to increase repetition rate and signal intensity. The excitation angle β has to be matched to the Ernst angle by varying the length of the initial INEPT delay Δ'. For determining optimal excitation, however, loss of magnetization due to relaxation, incomplete coherence transfer and pulse imperfections during the experiment need to be taken into account, which is most easily achieved by introducing an empirical factor $E_{\mathrm{HSQC}}\left(T_1, T_2, t_1, \nu_{\mathrm{off}}, {}^1J_{\mathrm{CH}}, J_{\mathrm{HH}}, \dots\right)$ that can be determined experimentally.

For simplification, a single factor E_{HSQC} is considered for the experiment in the following, which is clearly a rough approximation. Nevertheless, considering a small molecule with similar and long relaxation times for all nuclear species involved, E_{HSQC} will not vary significantly for increment times much shorter than the relaxation times of carbon spins and the $1/J_{\mathrm{HH}}$ coupling period. Equally, offset-dependent losses due to pulse imperfections are compensated by shaped broadband pulses and coherence transfer depends on $\cos(\pi {}^1J_{\mathrm{CH}}\Delta)$, which at least within the aliphatic or the aromatic region will not vary much in conventional samples.

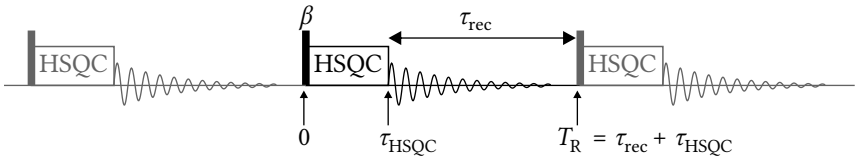

Figure 6.19: Outline of the Ernst angle HSQC or ALSOFAST-HSQC. The experiment starts at $t = 0$ with β excitation within a HSQC sequence. The HSQC ends at $t = \tau_{\mathrm{HSQC}}$, followed by a recovery delay τ_{rec}. The next scan starts at $t = T_{\mathrm{R}}$.

A layout of the acquisition scheme with contributing factors is shown in Figure 6.19. Compared to the simple pulse-acquire scheme, he excitation with the Ernst angle is combined with E_{HSQC} resulting in

$$P\left(\tau_{\mathrm{HSQC}}\right) = P\left(0\right)\cos\beta \cdot E_{\mathrm{HSQC}}. \tag{6.6}$$

Please note that conventional HSQC sequences, which do not store the unused polarization along z, would lead to $P\left(\tau_{\mathrm{HSQC}}\right) = 0$. After the pulse sequence, during acquisition and during the recovery delay, the polarization recovers, starting at $t = \tau_{\mathrm{HSQC}}$ until the start of the next scan at $T_{\mathrm{R}} = \tau_{\mathrm{HSQC}} + \tau_{\mathrm{rec}}$. The recovery due to T_1 relaxation,

$$P\left(T_{\mathrm{R}}\right) = P\left(\tau_{\mathrm{HSQC}}\right)E_1 + P_{\mathrm{Eq}}(1 - E_1), \tag{6.7}$$

with the steady-state condition

$$P(0) = P(T_R) \tag{6.8}$$

results in the steady state polarization

$$P(0) = \frac{P_{Eq}(1 - E_1)}{1 - E_{HSQC} E_1 \cos\beta}. \tag{6.9}$$

The corresponding signal intensity is given by

$$S(\tau_{HSQC}) = \frac{P_{Eq}(1 - E_1)}{1 - E_{HSQC} E_1 \cos\beta} \cdot E_{HSQC} \sin\beta. \tag{6.10}$$

ASAP-HSQC Model

In the case of the ASAP-HSQC, the situation is more complicated as additional contributions need to be taken into account. The ASAP-HSQC, as outlined in Figure 6.20, consists of several

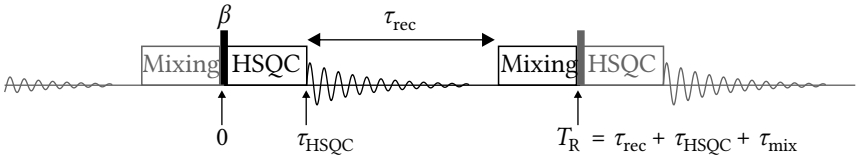

Figure 6.20: Outline of the ASAP-HSQC. The experiment starts at $t = 0$ with β excitation within a HSQC sequence. The HSQC ends at $t = \tau_{HSQC}$, followed by a recovery delay τ_{rec}. Before the next scan, a mixing block of length τ_{mix} is included, and the next scan starts at $t = T_R$.

sequential pulse sequence building blocks with different relaxation behavior and also requires separate, parallel treatment of magnetization that is transferred during INEPT as well as magnetization stored along z as a reservoir (denoted by the superscript $^{(r)}$ in the following).

Again, after a sufficiently large amount of scans, the polarization of k protons bound to ^{13}C directly before the excitation is described by $k \cdot P(0)$ and the resulting remaining polarization of a single ^{13}C-bound proton after the ASAP-HSQC experiment as well as the recovery due to T_1 relaxation is described by

$$P(\tau_{HSQC}) = P(0) \cos\beta \cdot E_{HSQC}, \tag{6.11}$$

$$P(\tau_{HSQC} + \tau_{rec}) = P(\tau_{HSQC}) E_1 + P_{Eq}(1 - E_1). \tag{6.12}$$

In addition, $(n-k)$ spins need to be considered that are part of the spin system consisting of altogether n protons that are not covalently bound to ^{13}C. For these remote spins the corresponding equations for the reservoir polarization $P^{(\mathrm{r})}$ are

$$P^{(\mathrm{r})}\left(\tau_{\mathrm{HSQC}}\right) = P^{(\mathrm{r})}(0)\, E^{(\mathrm{r})}_{\mathrm{HSQC}}, \tag{6.13}$$

$$P^{(\mathrm{r})}\left(\tau_{\mathrm{HSQC}} + \tau_{\mathrm{rec}}\right) = P^{(\mathrm{r})}\left(\tau_{\mathrm{HSQC}}\right) E^{(\mathrm{r})}_{1} + P^{(\mathrm{r})}_{\mathrm{Eq}}(1 - E^{(\mathrm{r})}_{1}). \tag{6.14}$$

with the equilibrium reservoir magnetization $P^{(\mathrm{r})}_{\mathrm{Eq}}$ and the corresponding loss constant $E^{(\mathrm{r})}_{\mathrm{HSQC}}$ during the HSQC and T_1 recovery according to $E^{(\mathrm{r})}_{1} = \exp(\tau_{\mathrm{rec}}/T^{(\mathrm{r})}_{1})$.

In the last remaining step of the ASAP-HSQC, the isotropic mixing period of duration τ_{mix}, ^{13}C-bound and reservoir proton polarization are mixed. In an ideal mixing situation, polarization is equally distributed among all n protons of the spin system. At the time $T_{\mathrm{R}} = \tau_{\mathrm{HSQC}} + \tau_{\mathrm{rec}} + \tau_{\mathrm{mix}}$, all spins, local and remote, have the polarization

$$\begin{aligned} P\left(T_{\mathrm{R}}\right) &= P^{(\mathrm{r})}(T_{\mathrm{R}}) = P\left(T_{\mathrm{R}}\right) \\ &= \left(P\left(\tau_{\mathrm{HSQC}} + \tau_{\mathrm{rec}}\right)\frac{k}{n} + P^{(\mathrm{r})}\left(\tau_{\mathrm{HSQC}} + \tau_{\mathrm{rec}}\right)\frac{n-k}{n}\right) E_{\mathrm{mix}}, \end{aligned} \tag{6.15}$$

assuming that all proton spins are affected equally by slight losses during the TOCSY period according to the empirically derived factor E_{mix}. Steady state conditions are again ensured by

$$P\left(0\right) = P\left(T_{\mathrm{R}}\right). \tag{6.16}$$

To solve this system of equations it is best to rearrange them into matrices. The pulse sequence affects the polarization according to

$$\mathbf{P}\left(\tau_{\mathrm{HSQC}}\right) = \underbrace{\begin{pmatrix} P\left(\tau_{\mathrm{HSQC}}\right) \\ P^{(\mathrm{r})}\left(\tau_{\mathrm{HSQC}}\right) \end{pmatrix}}_{\mathbf{P}\left(\tau_{\mathrm{HSQC}}\right)} = \underbrace{\begin{pmatrix} \cos\beta \cdot E_{\mathrm{HSQC}} & 0 \\ 0 & E^{(\mathrm{r})}_{\mathrm{HSQC}} \end{pmatrix}}_{\mathbf{P}} \underbrace{\begin{pmatrix} P\left(0\right) \\ P^{(\mathrm{r})}(0) \end{pmatrix}}_{\mathbf{P}(0)}, \tag{6.17}$$

while the subsequent recovery is described by

$$\mathbf{P}\left(\tau_{\mathrm{HSQC}} + \tau_{\mathrm{rec}}\right) = \underbrace{\begin{pmatrix} E_1 & 0 \\ 0 & E^{(\mathrm{r})}_{1} \end{pmatrix}}_{\mathbf{R}} \mathbf{P}\left(\tau_{\mathrm{HSQC}}\right) + \underbrace{\begin{pmatrix} P_{\mathrm{Eq}}(1 - E_1) \\ P^{(\mathrm{r})}_{\mathrm{Eq}}(1 - E^{(\mathrm{r})}_{1}) \end{pmatrix}}_{\mathbf{P}_{\mathrm{Eq}}} \tag{6.18}$$

and the idealized ASAP mixing period by

$$\mathbf{P}(T_\mathrm{R}) = \mathbf{P}(0) = \underbrace{\frac{1}{n}\begin{pmatrix} kE_\mathrm{mix} & (n-k)E_\mathrm{mix} \\ kE_\mathrm{mix}^{(\mathrm{r})} & (n-k)E_\mathrm{mix}^{(\mathrm{r})} \end{pmatrix}}_{\mathbf{T}} \mathbf{P}\left(\tau_\mathrm{HSQC} + \tau_\mathrm{rec}\right). \tag{6.19}$$

For the steady state condition the matrix equation

$$\mathbf{P}(0) = \mathbf{T}\left(\mathbf{RP}\cdot\mathbf{P}(0) + \mathbf{P}_\mathrm{Eq}\right), \tag{6.20}$$

has to be solved. The equation can be rearranged to

$$\mathbf{P}(0) = (1 - \mathbf{TRP})^{-1}\cdot\mathbf{TP}_\mathrm{Eq}, \tag{6.21}$$

which is then solved straightforwardly – albeit tediously – to obtain the steady state polarization of the active spins at time 0, right before the next excitation element,

$$P(0) = \frac{kP_\mathrm{Eq}(1-E_1) + (n-k)P_\mathrm{Eq}^{(\mathrm{r})}(1-E_1^{(\mathrm{r})})}{n - (n-k)E_\mathrm{mix}^{(\mathrm{r})}E_\mathrm{HSQC}^{(\mathrm{r})}E_1^{(\mathrm{r})} - kE_\mathrm{mix}E_\mathrm{HSQC}E_1\cos\beta}\cdot E_\mathrm{mix}, \tag{6.22}$$

and the resulting signal intensity after excitation,

$$S(0) = \frac{kP_\mathrm{Eq}(1-E_1) + (n-k)P_\mathrm{Eq}^{(\mathrm{r})}(1-E_1^{(\mathrm{r})})}{n - (n-k)E_\mathrm{mix}^{(\mathrm{r})}E_\mathrm{HSQC}^{(\mathrm{r})}E_1^{(\mathrm{r})} - kE_\mathrm{mix}E_\mathrm{HSQC}E_1\cos\beta}\cdot E_\mathrm{mix}E_\mathrm{HSQC}\sin\beta. \tag{6.23}$$

6.2.3 Exploring the Experimental HSQC Steady State

To visualize the changes and understand the relaxation of the system in a realistic steady state, the preparatory HSQC was looped 1, 8, 16, or 64 times before applying the readout HSQC. The change in polarization with respect to the number of loops was already shown in Figure 6.17.

It is important to understand that changing a parameter will, in general, change the resulting steady state, too. Increasing the recovery delay to measure the relaxation means changing in all preparatory HSQC blocks of the experiment, which will most likely increase the polarization of the reservoir. Provided, the reservoir has the correct alignment and mixing is enabled, this will increase value of T_1 obtained from the exponential fit. This apparent T_1 time, denoted by T_1^SS to distinguish, is not equivalent to the well defined longitudinal relaxation time, however, it is an attempt to describe the signal intensity of a real experiment. The steady state polarization of menthol is shown for each spin in Figure 6.21 and as mean value in Figure 6.23. In contrast to the

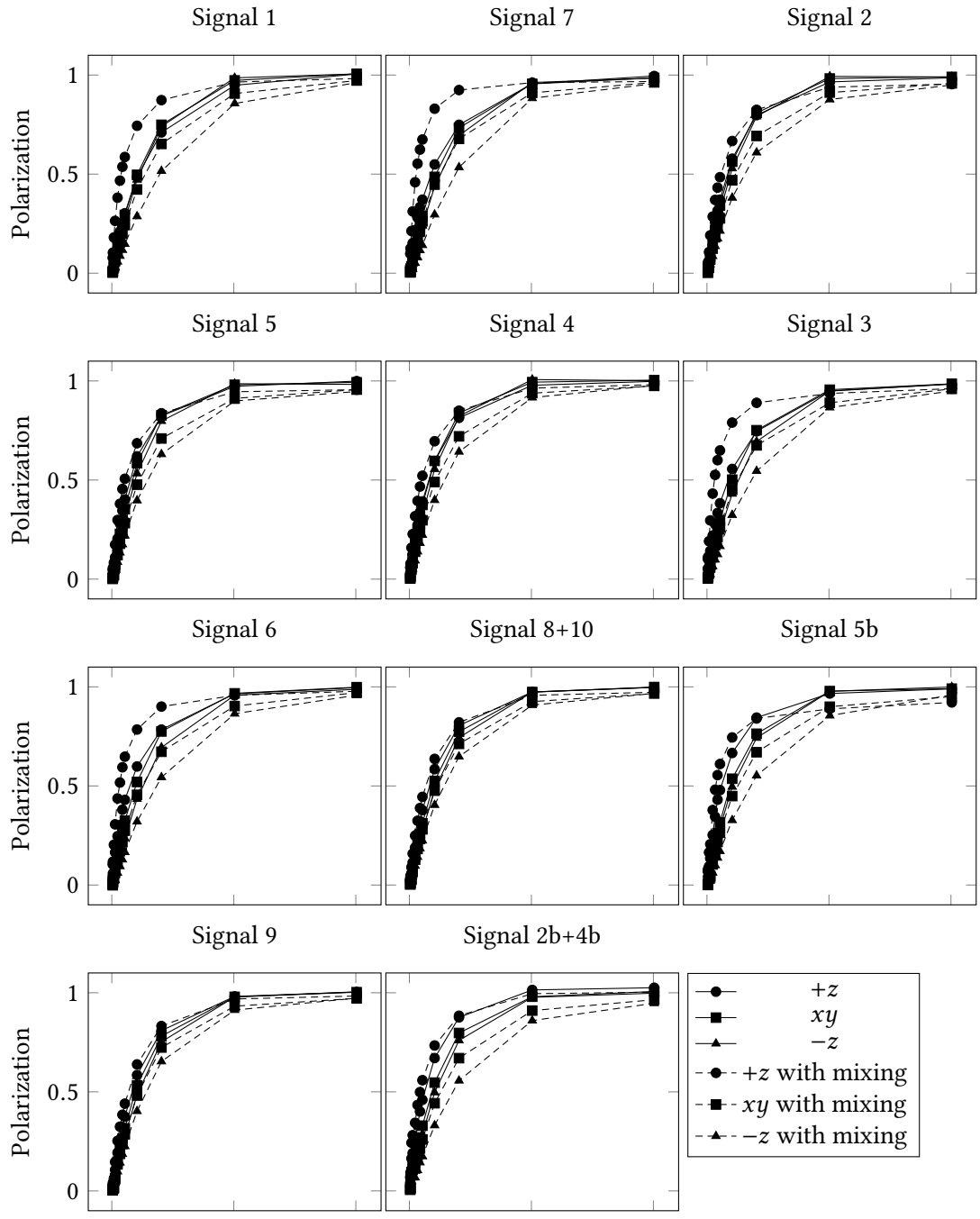

Figure 6.21: Individual experimental menthol steady state polarization ($l = 64$) versus recovery delay from the HSQC-recovery experiment. The reservoir is either aligned along $+z$, dephased in the xy plane or aligned along $-z$. DIPSI-2 mixing is either off or 34.5 ms.

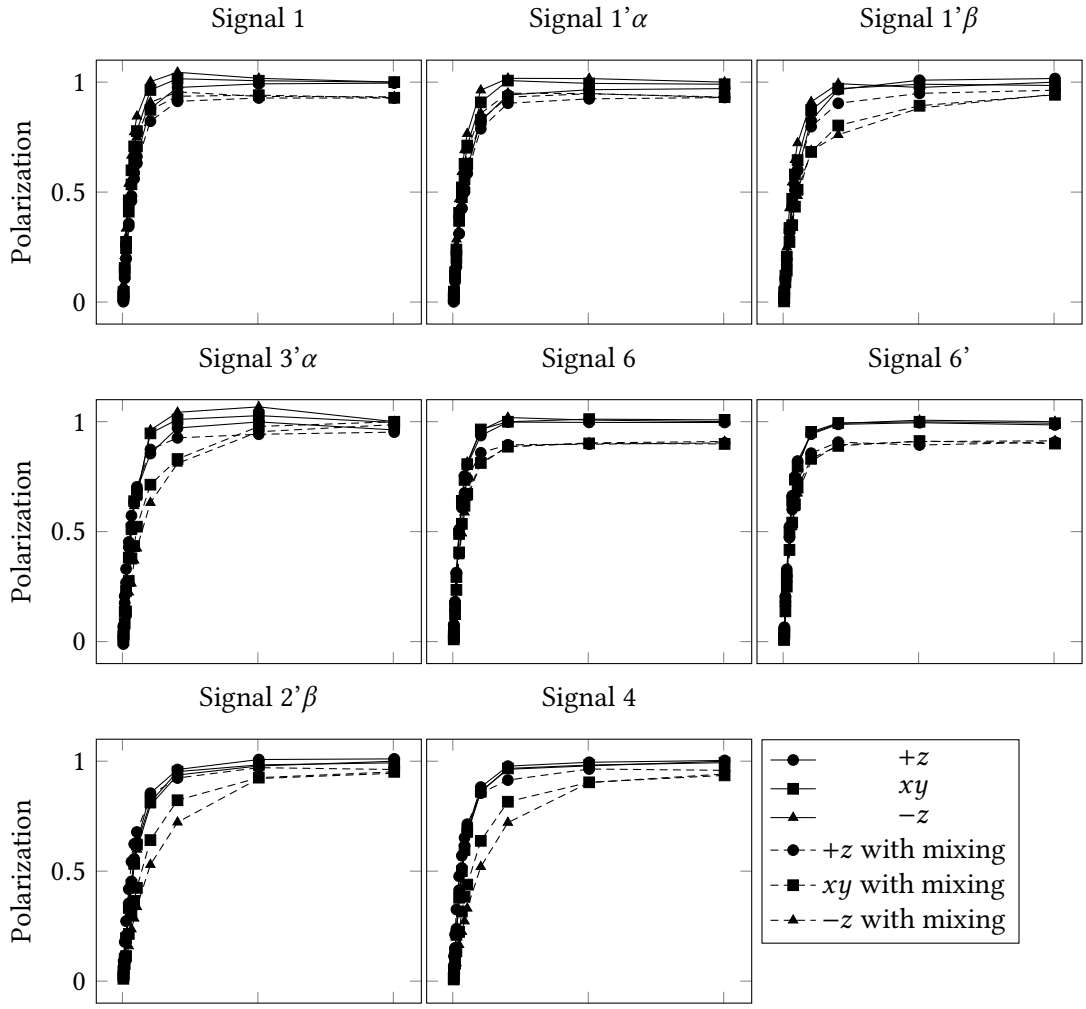

Figure 6.22: Individual experimental maltose steady state polarization ($l = 64$) versus recovery delay from the HSQC-recovery experiment. The reservoir is either aligned along $+z$, dephased in the xy plane or aligned along $-z$. DIPSI-2 mixing is either off or 23 ms.

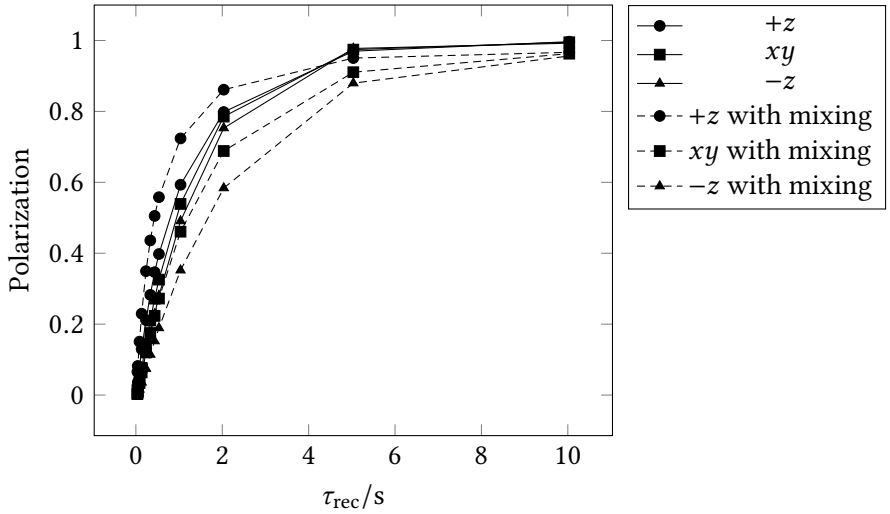

Figure 6.23: Mean experimental menthol steady state polarization ($l = 64$) versus recovery delay from the HSQC-recovery experiment. The reservoir is either aligned along $+z$, dephased in the xy plane or aligned along $-z$. DIPSI-2 mixing is either off or 34.5 ms.

results from the thermal equilibrium state experiments, all spins are effectively saturated after 64 loops. The influence of the reservoir is negligible, and even including the proton mixing does not increase the polarization. Obviously, in the steady state corresponding to short recovery delays, all magnetization – direct or reservoir – is depleted. Corresponding plots for maltose are shown in Figures 6.22 and 6.24.

Evaluating the relaxation data yields the values of T_1^{SS} shown in Figure 6.25. In contrast to the thermal equilibrium case, in the steady state after 64 sequence repetitions, the apparent T_1 relaxation, T_1^{SS}, is faster when untransferred magnetization is aligned along $+z$. This is mostly the effect of preserved polarization contributing to subsequent scans. The saturation of direct and remote spins alike will of course, also reduce the influence of reservoir ^{1}H on relaxation, negating the effect of isotope-selective excitation from the HSQC. The underlying T_1 relaxation time will be close to the non-selective T_1 time as long as short recovery delays τ_{rec} are considered.

Applying the mixing sequence is not without cost. Besides the increased experiment duration, that is relevant when the pulse sequence and acquisition time together are only about 200 ms long, the additional pulses are noticeable as well. In Figure 6.27, the polarization with long recovery delay $\tau_{rec} = 10$ s is shown. The loss of polarization with mixing time is clearly visible. Fortunately, for menthol, only some percent of polarization are lost, which is not severe. For maltose, on the other hand, 10 % of polarization are lost with typical mixing times of 20 to 35 ms. The value obtained for $\tau_{rec} = \infty$ from the T_1 fit is in agreement with the measured data

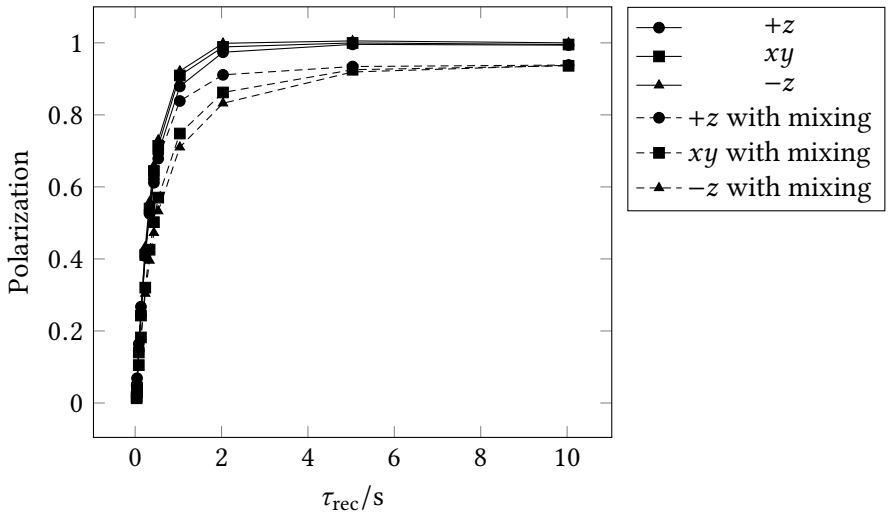

Figure 6.24: Mean experimental maltose steady state polarization ($l = 64$) versus recovery delay from the HSQC-recovery experiment. The reservoir is either aligned along $+z$, dephased in the xy plane or aligned along $-z$. DIPSI-2 mixing is either off or 23 ms.

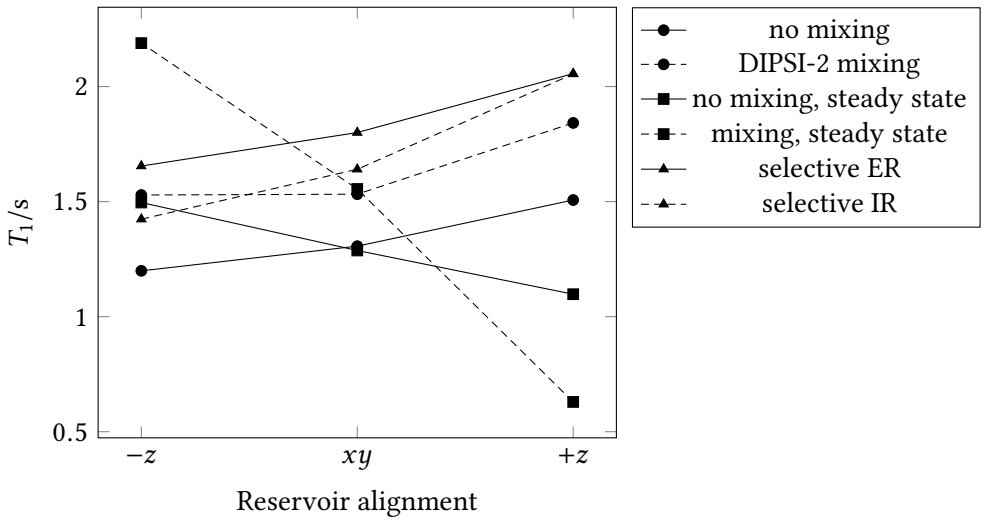

Figure 6.25: Mean menthol T_1 and apparent relaxation time T_1^{SS} time under different conditions. The conventional HSQC conditions are found without mixing and the reservoir dephased in the xy plane. The ALSOFAST-HSQC conditions are found without mixing and the reservoir aligned in $+z$. For the ASAP-HSQC, 34.5 ms DIPSI-2 mixing is used and the reservoir aligned along $+z$. The selective recovery data from excitation recovery (ER) and inversion recovery (IR) is shown for comparison.

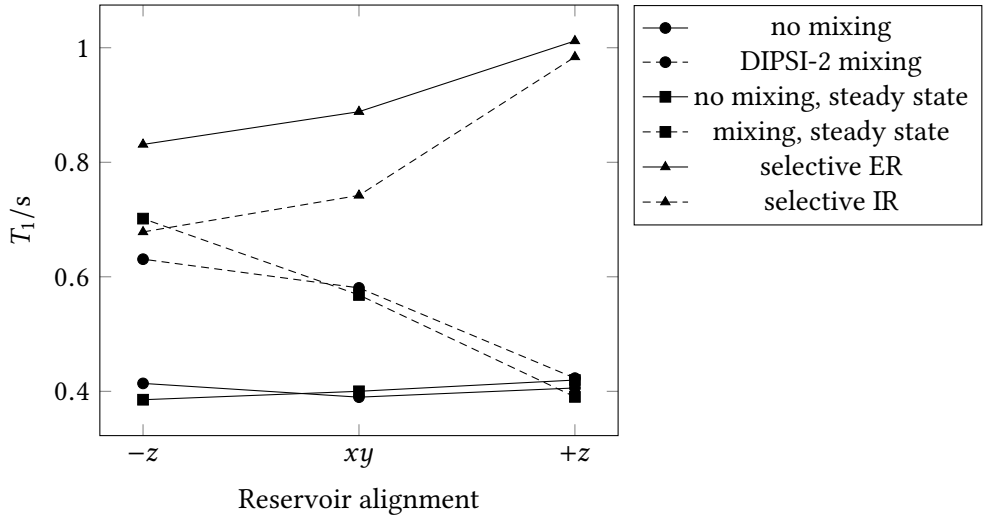

Figure 6.26: Mean maltose T_1 and apparent relaxation time T_1^{SS} time under different conditions. The conventional HSQC conditions are found without mixing and the reservoir dephased in the xy plane. The ALSOFAST-HSQC conditions are found without mixing and the reservoir aligned in $+z$. For the ASAP-HSQC, 23 ms DIPSI-2 mixing is used and the reservoir aligned along $+z$. The selective recovery data from excitation recovery (ER) and inversion recovery (IR) is shown for comparison.

and is shown as well. The long delay cancels the differences between reservoir alignments and other parameters, so only data for reservoir dephased in the xy plane is shown, where the T_1 fit is most accurate.

Figure 6.29 shows the steady state polarization of menthol when very short recovery delays are used. Compared to the single-scan data from Figure 6.12, there is almost no polarization left. The maltose steady state polarization for these recovery delays is shown in Figure 6.30. Here some positive contribution is visible as well. The faster T_1 relaxation of maltose creates a larger discrepancy between the measured value at $\tau_{rec} = 35$ ms and the fit parameter for $\tau_{rec} = 0$. In both molecules, in the steady state with short recovery delays, application of the mixing sequence hardly increases the available polarization. The fast pulsing saturates the whole spin system, so the remote protons cannot provide additional magnetization. As Figure 6.31 shows, when the recovery delay τ_{rec} is increased, however, the mixing sequence can actually increase the available polarization. This is not leftover initial reservoir polarization, but a contribution from relaxation of remote ^{1}H. All spins recover some polarization during τ_{rec}, but only the polarization on ^{1}H bound to ^{13}C is used for the next scan. If the spin system is large enough, this is only a small part of the overall polarization that was just recovered. Therefore the available polarization is increased by remote ^{1}H.

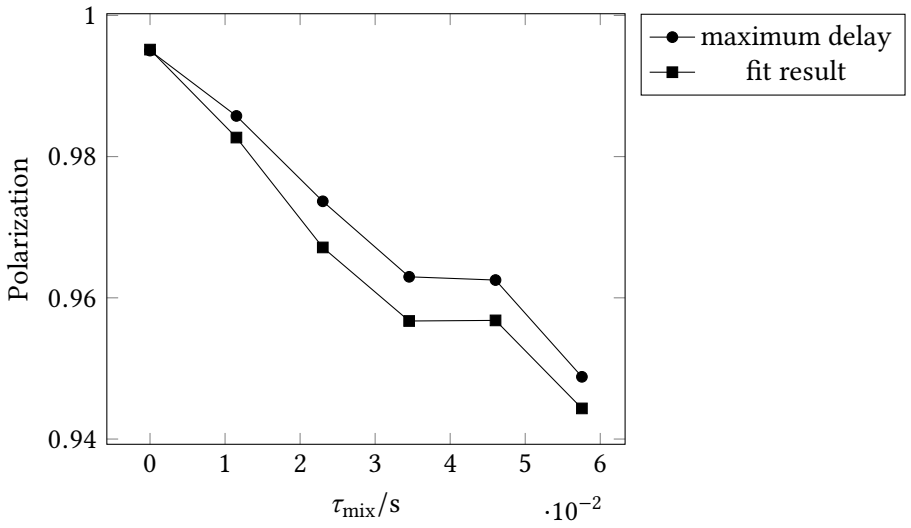

Figure 6.27: Mean experimental menthol steady state polarization ($l = 64$) after long recovery delay versus mixing time. The measured intensity at maximum recovery delay, 10 s, is shown (circles) alongside extrapolated polarization at $\tau_{rec} = \infty$ from T_1 relaxation fit (squares). Data for dephased reservoir are shown, however, after the long recovery delay, the differences between the alignments are negligible.

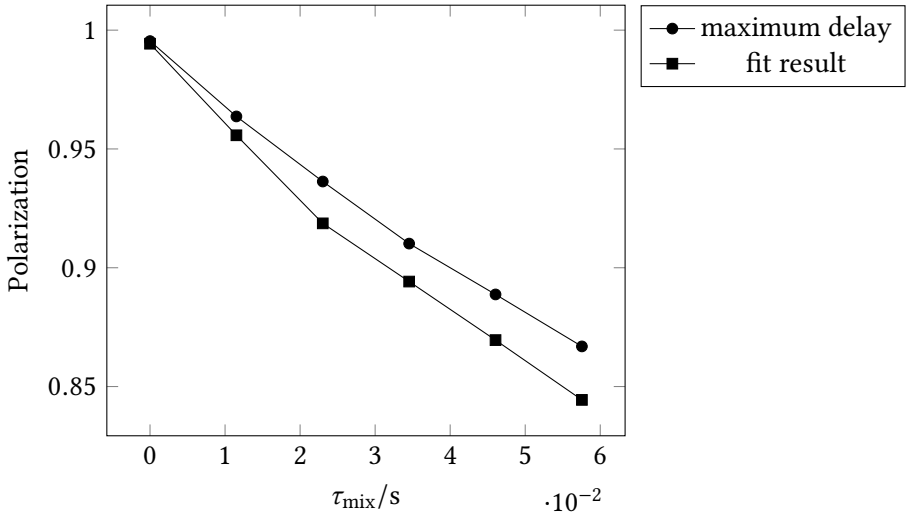

Figure 6.28: Mean experimental maltose steady state polarization ($l = 64$) after long recovery delay versus mixing time. The measured intensity at maximum recovery delay, 10 s, is shown (circles) alongside extrapolated polarization at $\tau_{rec} = \infty$ from T_1 relaxation fit (squares). Data for dephased reservoir are shown, however, after the long recovery delay, the differences between the alignments are negligible.

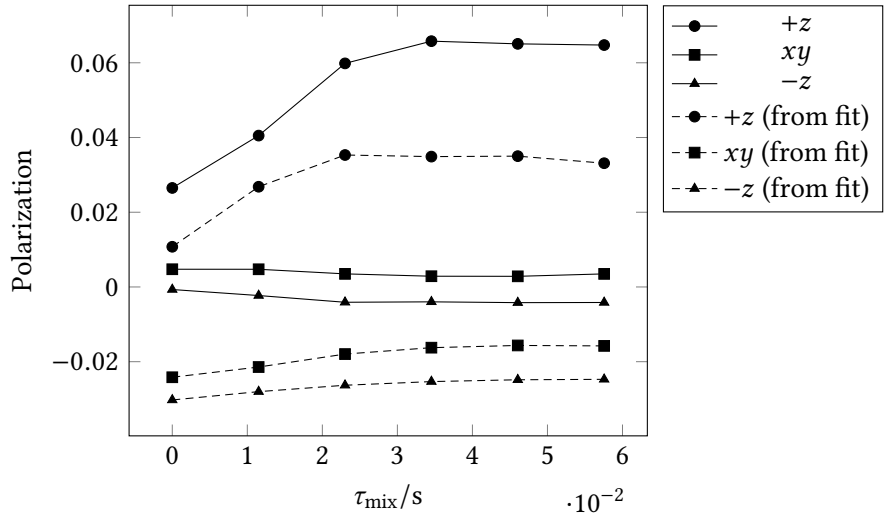

Figure 6.29: Mean experimental steady state polarization ($l = 64$) of menthol with short recovery time versus mixing time. The measured intensity at minimum recovery delay, 35 ms, is shown (solid lines) alongside extrapolated polarization at $\tau_{\mathrm{rec}} = 0$ from T_1 relaxation fit (dashed lines). The reservoir is either aligned along $+z$, dephased in the xy plane or aligned along $-z$. Given the right alignment, some polarization is recovered by the mixing sequence, however, the gain is much lower than after a single HSQC run as shown in Figure 6.12, where 25 to 75 % could be recovered.

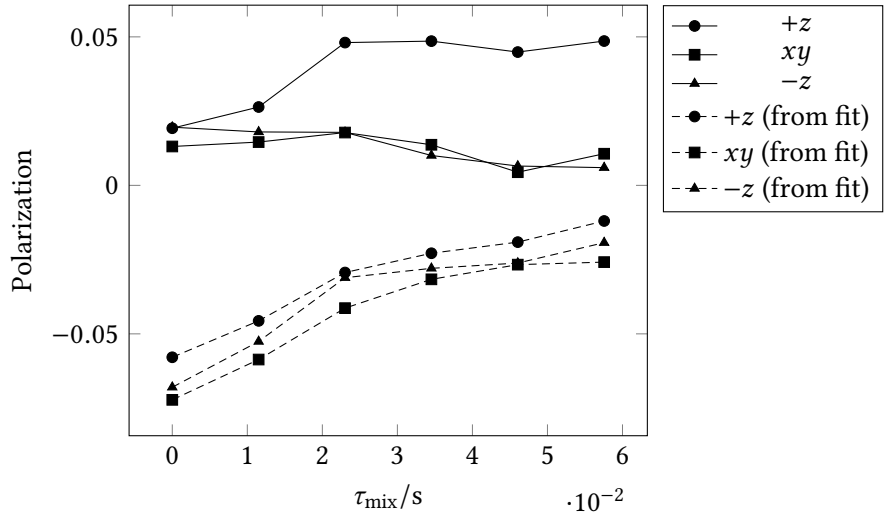

Figure 6.30: Mean experimental steady state polarization ($l = 64$) of maltose with short recovery time versus mixing time. The measured intensity at minimum recovery delay, 35 ms, is shown (solid lines) alongside extrapolated polarization at $\tau_{\mathrm{rec}} = 0$ from T_1 relaxation fit (dashed lines). The reservoir is either aligned along $+z$, dephased in the xy plane or aligned along $-z$. Almost no polarization is recovered by the mixing sequence.

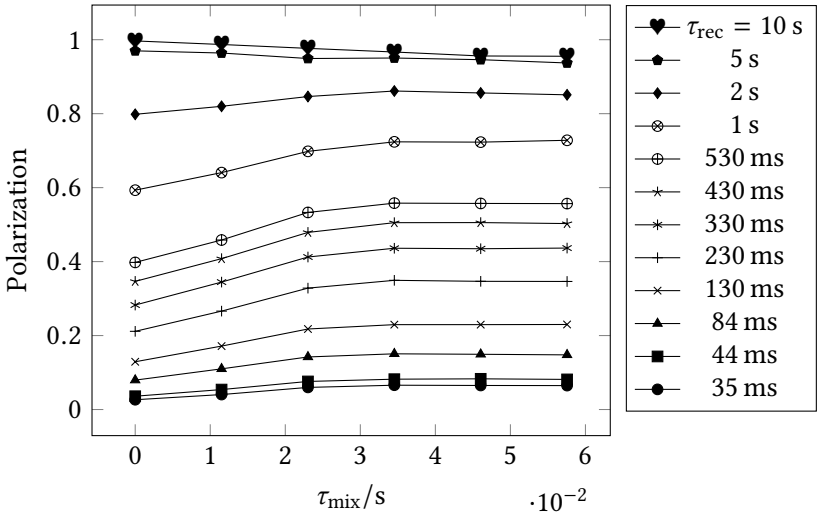

Figure 6.31: Mean experimental menthol steady state polarization ($l = 64$) versus DIPSI-2 mixing time with reservoir aligned along $+z$. All recovery delays τ_{rec} are shown.

To find the optimal the mixing time, the menthol polarization is plotted versus mixing time in Figure 6.31. In general, polarization is increased with mixing times up to 34.5 ms, whereupon a plateau is reached, so optimal mixing time for menthol was determined to be 34.5 ms. Shorter times do not allow full transfer of the available magnetization, while longer times show no gains but require time, better used for unperturbed polarization recovery. Saturation effects by the mixing sequence are also less severe when the mixing time is kept as short as possible. The influence of mixing is still visible with a long recovery delay of 2 s, but the best relative gains are achieved between 200 to 500 ms. Application of the mixing sequence with incorrect reservoir alignment decreases signal intensity significantly. The effect of the DIPSI-2 mixing in maltose is much less pronounced. A slight increase in available polarization is visible in the relevant τ_{rec} range from 100 to 300 ms with mixing times of 20 to 30 ms. Since the gains are minimal and the loss to saturation encountered in maltose is quite large, $\tau_{mix} = 23$ ms was found to be the best mixing time for maltose.

6.2.4 Joining the Model and Experimental Data

ALSOFAST-HSQC

The theoretical polarization can be compared to the experimental data. Since most parameters are known or derived from the data as well, the only unknown variable is, interestingly, the excitation flip angle β. In the HSQC experiment β does not correspond to an actual pulse flip angle, but to the length of the INEPT delay in relation to the heteronuclear $^1J_{CH}$ coupling. It

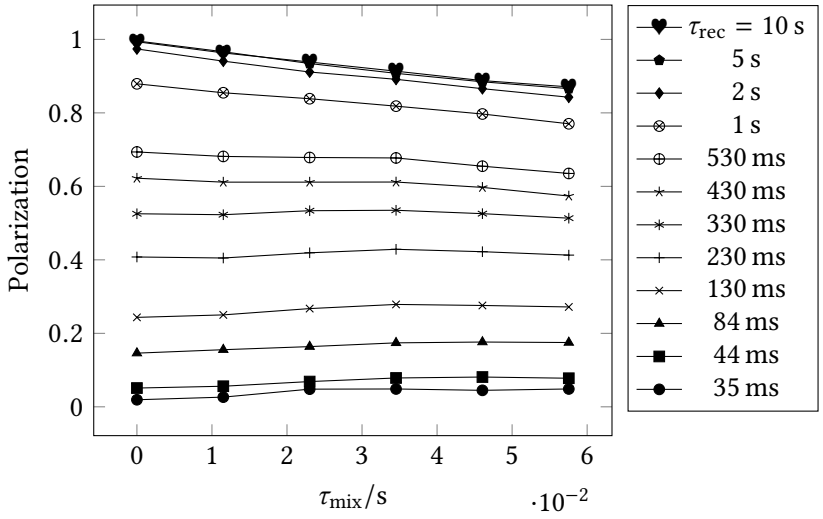

Figure 6.32: Mean experimental maltose steady state polarization ($l = 1$) versus mixing time with reservoir aligned along $+z$. All recovery delays τ_{rec} are shown.

is therefore different for each region and may be inaccurate when several peaks overlap. It was not possible to measure the coupling constants from the data acquired for this research. A CLIP-HSQC spectrum could provide the coupling constants to increase the accuracy of the model.

One example of the theoretical evaluation for menthol is shown in Figure 6.33 and for maltose in Figure 6.34. The values of β obtained from a simple fit are shown in Table 6.1 and Table 6.2.

In general, menthol has the lower excitation angle, leading to higher steady state polarization. For maltose, the default INEPT delay matched to $^1J_{CH} = 145$ Hz is actually too long. The reservoir ends up aligned at $-z$ and does not contribute constructively to the next scan but rather quickly relaxes towards saturation.

ASAP-HSQC

The theoretical ASAP-HSQC model allows predicting the steady state polarization in a given spin system. The parameter β as derived from the ALSOFAST-HSQC dataset is not changed. The loss during the mixing sequence, E_{mix}, is taken from experimental the intensity after 10 s recovery delay. Assuming equal efficiency coefficients for directly bound and remote ^{1}H, the only remaining uncertain parameter is the number of direct and remote spins. Fitting this parameter to the polarization measured in the HSQC-recovery experiments yields the effective number of neighboring spins that are reached by the mixing sequence per local spin. This is

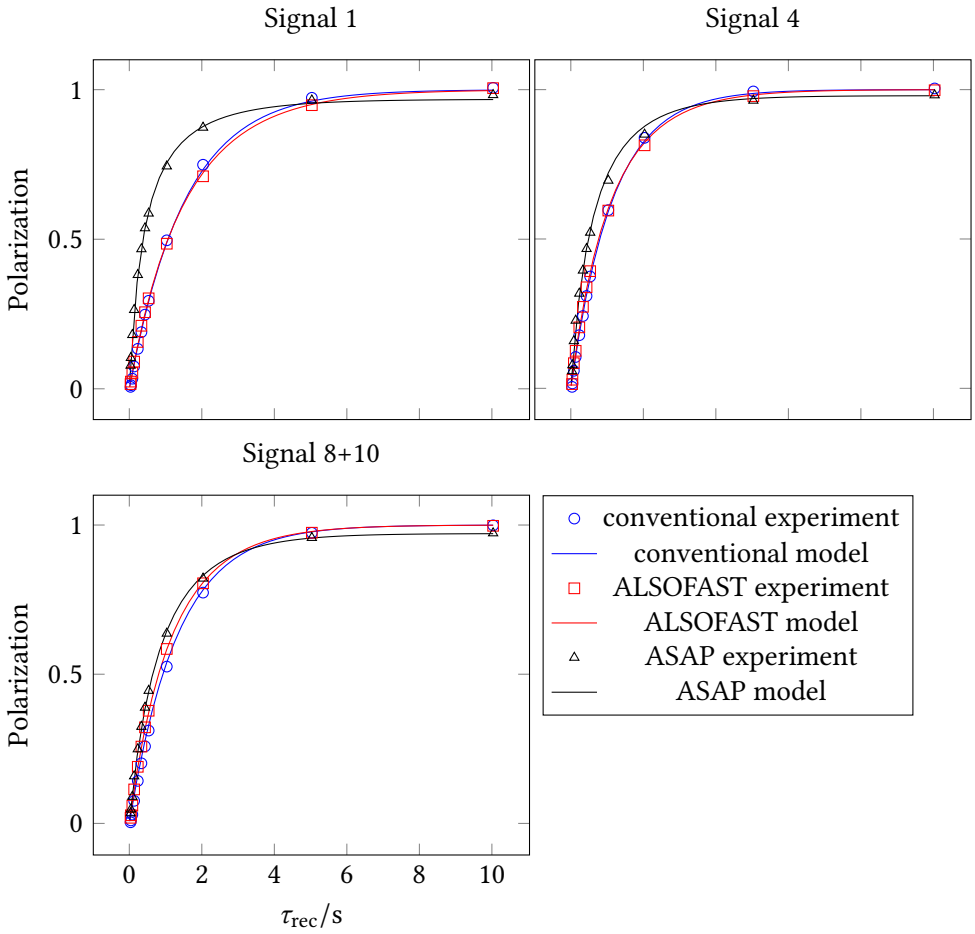

Figure 6.33: Menthol steady state polarization versus recovery delay from the HSQC-recovery experiment. Theoretical curve and experimental data points of some regions are shown.

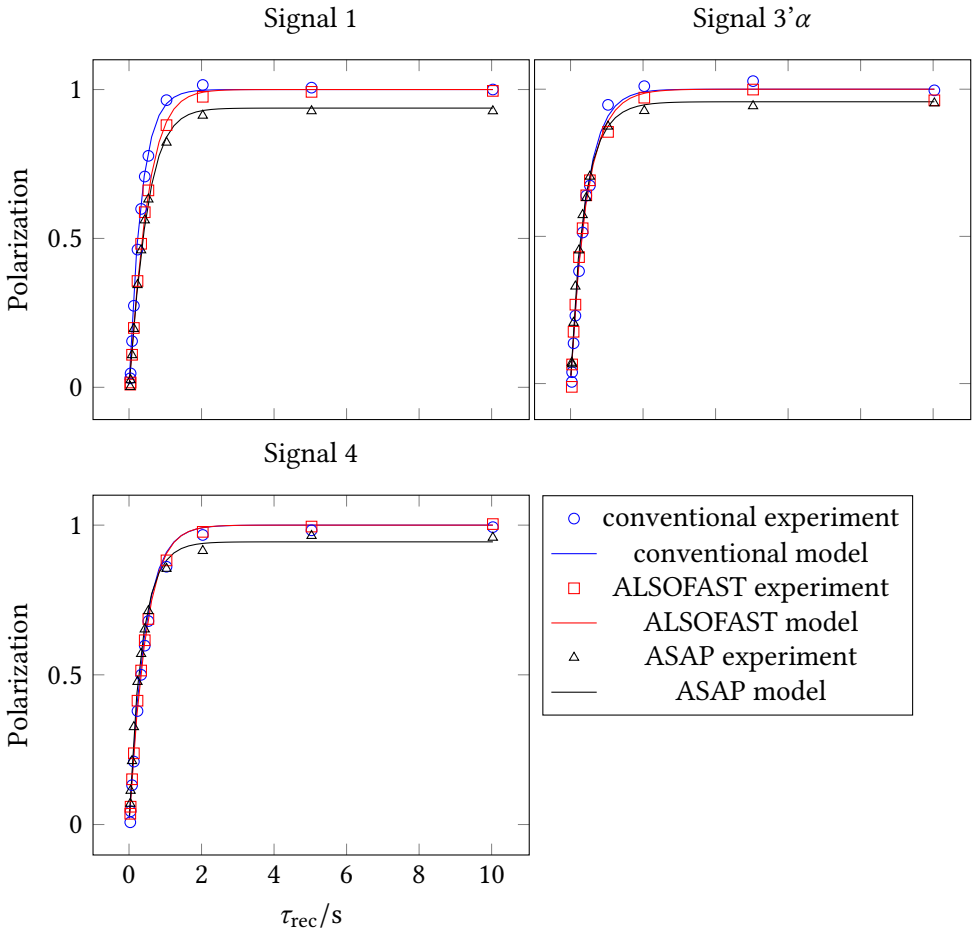

Figure 6.34: Maltose steady state polarization versus recovery delay from the HSQC-recovery experiment; Theoretical curve and experimental data points. some regions are shown.

Table 6.1: Effective flip angle β of menthol for the ALSOFAST-HSQC model; obtained by fitting the steady state polarization from the model to experimental data of menthol steady state polarization.

Assignment	$\beta/^\circ$
1	79.1
7	66.2
7+2	76.5
2	81.5
5	77.1
4	76.6
3+4+5	73.0
3	59.5
6	57.2
2b+4b+6	65.9
8+10	77.1
5b	69.6
9	77.5
2b+4b	57.7

Table 6.2: Effective flip angle β of maltose for the ALSOFAST-HSQC model; obtained by fitting the steady state polarization from the model to experimental data of maltose steady state polarization.

Assignment	$\beta/^\circ$
1	119.8
1 'α	123.8
1 'β	110.0
3 'α	83.7
6	107.6
6'	105.5
2'β	103.3
4	102.8

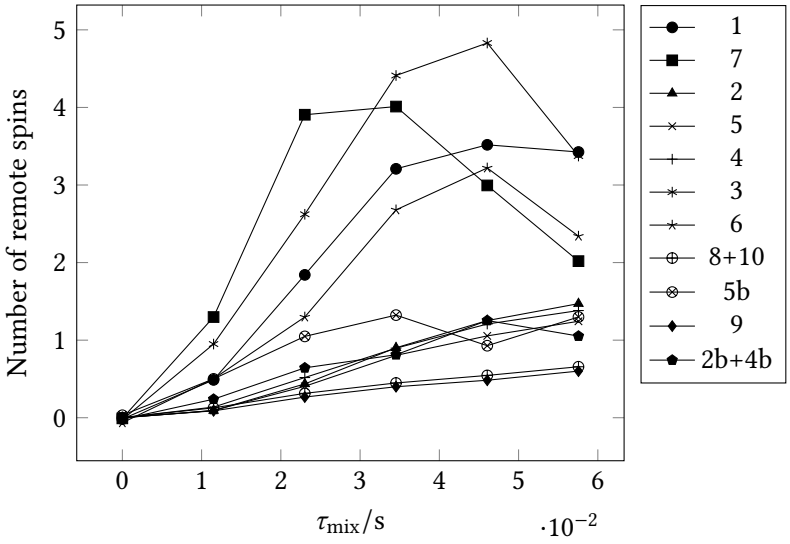

Figure 6.35: Theoretical number of remote spins per local spin of menthol reached by mixing versus mixing time in the ASAP-HSQC. Values obtained from the ASAP-HSQC model, using the number of spins as fitting parameter.

shown for menthol in Figure 6.35 and for maltose in Figure 6.36. An example of the comparison between theory and experiment is shown in Figures 6.33 and 6.34 for some spectral regions.

Menthol seems to have a huge number of reservoir spins available for most spins. Especially the positions 3 and 7 next to methyl groups are well-connected to other spins. The methyl groups, 8, 9 and 10, where the ratio of local to remote ^{1}H naturally is lower, gain only a little polarization by the contribution from adjacent protons but still benefit. For maltose, the values are smaller by an order of magnitude. There are almost no reachable passive spins even at optimal mixing times in maltose.

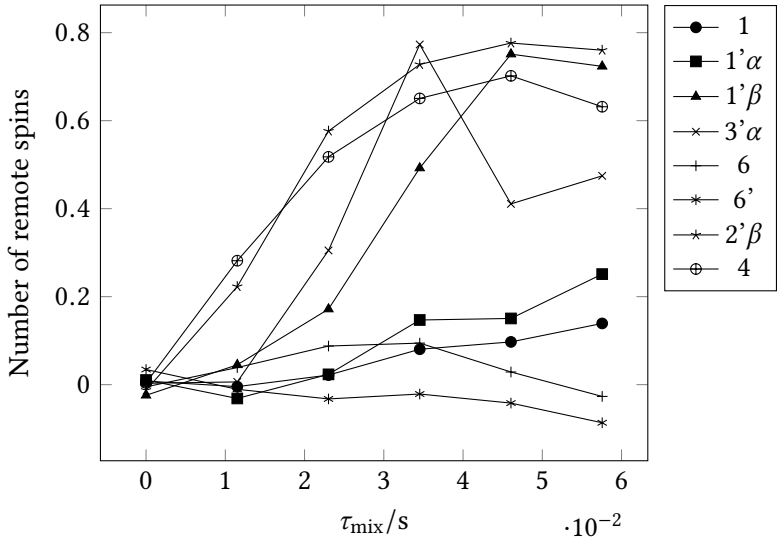

Figure 6.36: Theoretical number of remote spins per local spin of maltose reached by mixing versus mixing time in the ASAP-HSQC. Values obtained from the ASAP-HSQC model, using the number of spins as fitting parameter.

6.3 Optimal Excitation Angle

6.3.1 The Definition of the Ernst Angle

As seen before, the signal intensity of an experiment is created from polarization by pulses with a flip angle $\beta > 0$. The polarization of the steady state is reduced by high values of β, the signal intensity of a single scan, however, has its maximum at $\beta = 90°$. To find the best value of β, we go back to Equation (6.5) that describes the signal intensity, and calculate the derivative with respect to $\cos\beta$. As shown before in [76], the maximum signal intensity is achieved via the flip angle β_{opt} with

$$\cos\beta_{opt} = E_1 = \exp\left(-\frac{\tau_{rec}}{T_1}\right). \tag{6.24}$$

This flip angle is generally referred to as the *Ernst angle* and is commonly used in experiments when signal recovery is significantly slower than acceptable repetition times T_R or more precisely τ_{rec}, as for example in ^{13}C-1D experiments of small compounds, but also prevalent in medical imaging and other fields. The optimality of the Ernst angle solution has also been confirmed for a number of more complicated cases by optimal control theory [157].

6.3.2 The Ernst Angle for HSQC Experiments

An important contribution to rapid-acquisition heteronuclear experiments is excitation at an optimized angle. In the ALSOFAST- and the ASAP-HSQC, but not in the conventional HSQC, the amount of excitation can be tuned by changing the INEPT delay.

Moving on to Equation (6.10) for the ALSOFAST-HSQC, differentiating with respect to $\cos\beta$, to maximize the signal intensity, the condition for maximum steady-state intensity in the ALSOFAST-HSQC is

$$\cos\beta_{\text{opt}} = E_{\text{HSQC}}E_1. \tag{6.25}$$

This expression is very similar to the original Ernst angle formula.

The steady state polarization of the ASAP-HSQC is also dependent on the excitation angle. However, its influence is reduced when remote polarization can be included by mixing. Based on Equation (6.23), the coupling and mixing of k local spins and $n-k$ remote spins changes the optimal angle to

$$\cos\beta_{\text{opt}} = \frac{kE_{\text{HSQC}}E_{\text{mix}}E_1}{n-(n-k)E^{(\text{r})}_{\text{HSQC}}E^{(\text{r})}_{\text{mix}}E^{(\text{r})}_1}. \tag{6.26}$$

In most cases this is higher than the optimal angle in the ALSOFAST-HSQC. Assuming perfect HSQC and mixing efficiency by $E_{\text{mix}} = E_{\text{HSQC}} = 1$, and no remote spins by $n = k$, Equation (6.26) is identical to Equation (6.24), to the original Ernst angle equation.

A subset of the experiments above were repeated with initial transfer delays of the preparatory HSQC multiplied by 0.1 to 1. To make sure, the signal is not lost among the noise, the readout HSQC's transfer was still performed with the full delay. Effectively this allows measuring the steady state polarization. As shown in Figure 6.38A, when the recovery delay is short, lowering the excitation angle greatly increases the steady state polarization of the ALSOFAST-HSQC compared to the conventional sequence. The ASAP-HSQC's polarization is also increased, but the mixing sequence reduces the influence of the excitation angle. The mixing sequence, on the other hand, always suffers from pulse imperfections and saturation, lowering the available magnetization. As long as the recovery delay is short, the loss is easily compensated by the contribution from surrounding protons. The mixing is most effective when the difference between the active but depleted protons and the surrounding reservoir is large. When the recovery delay is increased, relaxation of the active protons increases polarization but at the same time reduces the difference between active and passive protons. At some point the loss to pulse imperfections outweighs the gains and the mixing can only reduce the polarization. In Figures 6.37 and 6.38, there are always three regions visible. Short recovery delays and full excitation favor the ASAP-HSQC. This region is most important, as it promises highest experimental signal intensity. Lowering the excitation angle reduces the advantages of the

ASAP-HSQC, but increases the ALSOFAST-HSQC polarization. Increasing the recovery delay favors the conventional sequence, due to the slightly faster T_1 relaxation. Reaching very long recovery delays, the conventional and the ALSOFAST-HSQC polarizations converge, while the ASAP-HSQC polarization is reduced from the mixing sequence.

Steady state polarization is an important property, however, ultimately everything depends on the steady state signal intensity and the signal-to-noise ratio that can be obtained per experiment duration. Schematically, polarization is transformed into coherence by an excitation pulse or a pulse sequence. Coherence is then measured and yields signal intensities in the spectrum. For perfect excitation, the signal intensity is related to the polarization by

$$S = P \cdot \sin \beta. \tag{6.27}$$

This allows calculating the expected steady state intensity from the available data. The angl β that was obtained previously and shown in Table 6.1 was used to reduce the signal intensity.

The best way to compare experiment intensities of experiments with different durations, is to estimate and compare the relative achievable signal-to-noise ratio per time, which is equivalent to intensity per square root of the experiment duration. The experiment duration was approximately 10 ms of unchanged pulse sequence plus the variable duration of mixing and recovery. This intensity per root of experiment duration is shown in Figures 6.39 and 6.40. The maximum intensity is achieved with the ASAP-HSQC with a recovery delay around 0.5 s with excitation angle close to 90°. While the disadvantages from the mixing sequence, additional time and pulse imperfections, disfavor the ASAP-HSQC, in this parameter region, the advantages dominate. The maximum of the ALSOFAST-HSQC is shifted towards reduced excitation angle, while the ASAP-HSQC can sustain high polarization with almost full excitation. The conventional HSQC is only advantageous when long recovery delays are used, but overall, a shorter recovery delay is favorable.

6.3.3 A Glimpse at the LowCost-HSQC

The LowCost-HSQC (or LowCost-ASAP-HSQC) is an advanced rapid-acquisition HSQC experiment [146, 158], closely related to the ASAP-HSQC experiment. An outline of the pulse sequence is shown in Figure 6.41. The LowCost-HSQC features an extended first transfer step in place of the regular INEPT, which is optimized to preserve remote ^{1}H polarization instead of ^{1}H coherence. The ^{1}H polarization is then unaffected by homonuclear coupling during the t_1 evolution time and remains undiminished even after long t_1 delays required for high-resolution experiments. The revised transfer also allows utilization of preservation of equivalent pathways (PEP) [159, 160], also called sensitivity improved or sensitivity enhanced

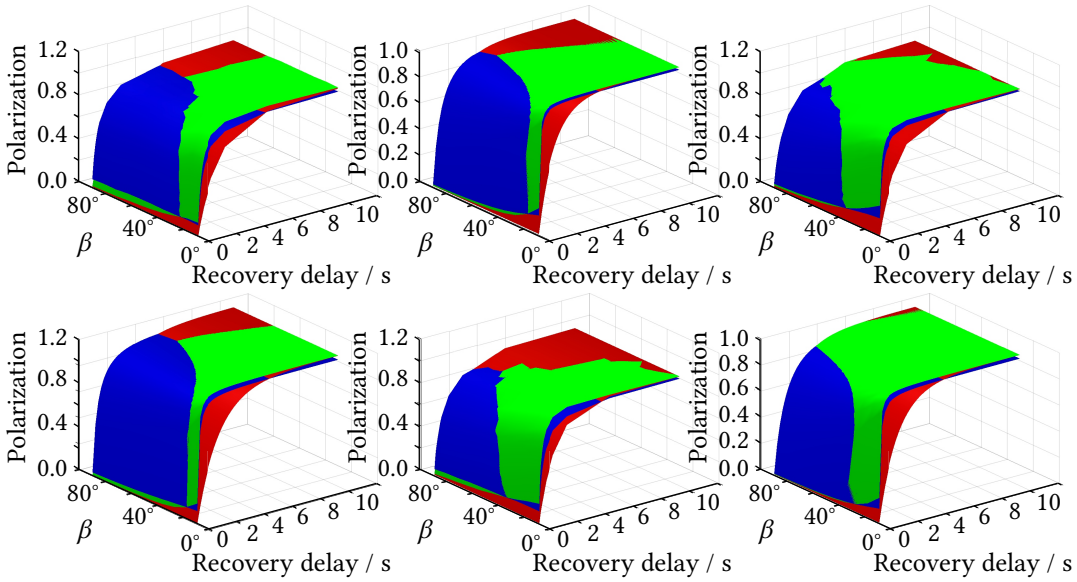

Figure 6.37: Experimental (top) and theoretical (bottom) steady state polarization of positions 1, 4 and 8+10 of menthol. Conventional HSQC in red, ALSOFAST-HSQC in green, ASAP-HSQC in blue.

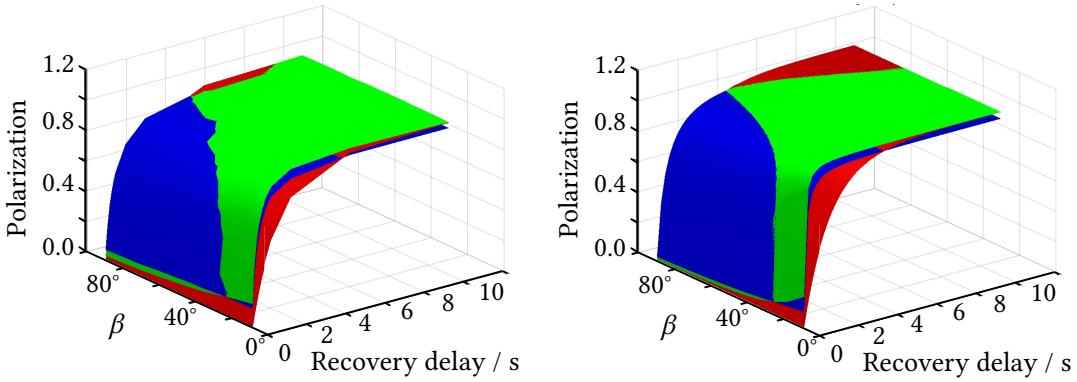

Figure 6.38: Experimental and theoretical mean steady state polarization of menthol. Conventional HSQC in red, ALSOFAST-HSQC in green, ASAP-HSQC in blue.

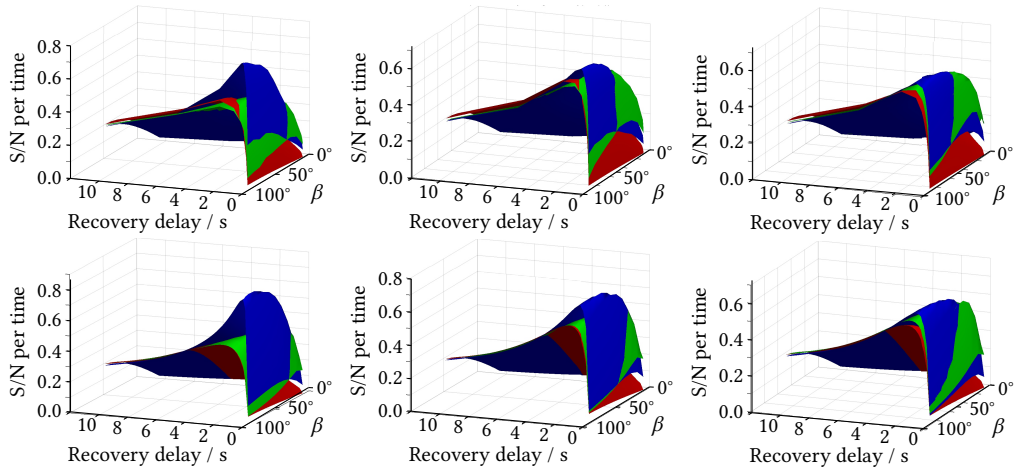

Figure 6.39: Experimental and theoretical steady state signal intensity of positions 1, 4 and 8+10 of menthol. Conventional HSQC in red, ALSOFAST-HSQC in green, ASAP-HSQC in blue.

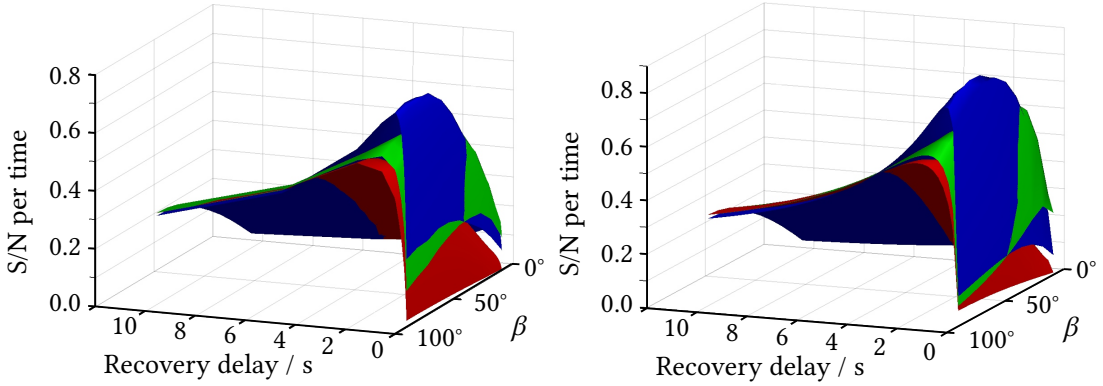

Figure 6.40: Experimental and theoretical mean steady state signal intensity of menthol. Conventional HSQC in red, ALSOFAST-HSQC in green, ASAP-HSQC in blue.

transfer, that can improve signal intensity by a factor of $\sqrt{2}$. It is incompatible with all other ASAP-HSQC sequences found so far.

These two advantages are significant in many applications, yet meaningless for this work. However, polarization of ^{1}H bound to ^{13}C is lost irrevocably, eliminating the possibility of β excitation. This allows a short look at the effect of proton mixing without preserving any local magnetization from ^{13}C-bound protons. The mean steady state polarization achieved with the

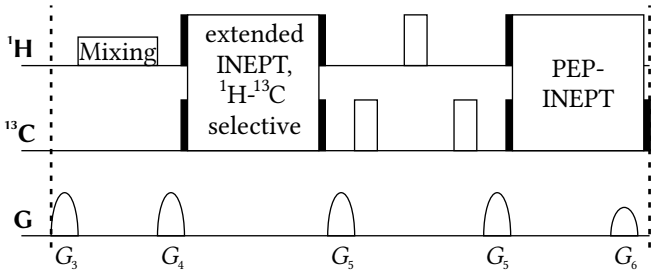

Figure 6.41: Scheme of the LowCost-HSQC sub-sequence used for the comparison. The sub-sequence is used as preparatory as well as readout block and combined with a recovery delay as shown in Figure 6.8.

LowCost-HSQC sequence is shown in Figure 6.42. Like with the ASAP-HSQC before, there is an increase in steady state polarization when the mixing is applied. Further evaluation shows the tight coupling network that contributes to the steady state polarization. In Figure 6.43, the number of remote spins that contribute per local spin is shown.

A different perspective of the LowCost experiment is, to interpret the reservoir-destructive excitation in combination with proton mixing as a more abstact form of β excitation. In Figure 6.43 this effective angle β is shown. It is easily seen, that in molecules with sufficient coupled hydrogen atoms, the interscan mixing of polarization from ^{1}H bound to ^{12}C and ^{13}C provides the benefits of incomplete excitation without sacrificing signal intensity. Given 2 adjacent protons, a LowCost scan with full excitation depletes only 50 % of the overall magnetization, corresponding to $\beta = 45°$ excitation, while providing the signal intesity of $\beta = 90°$ excitation.

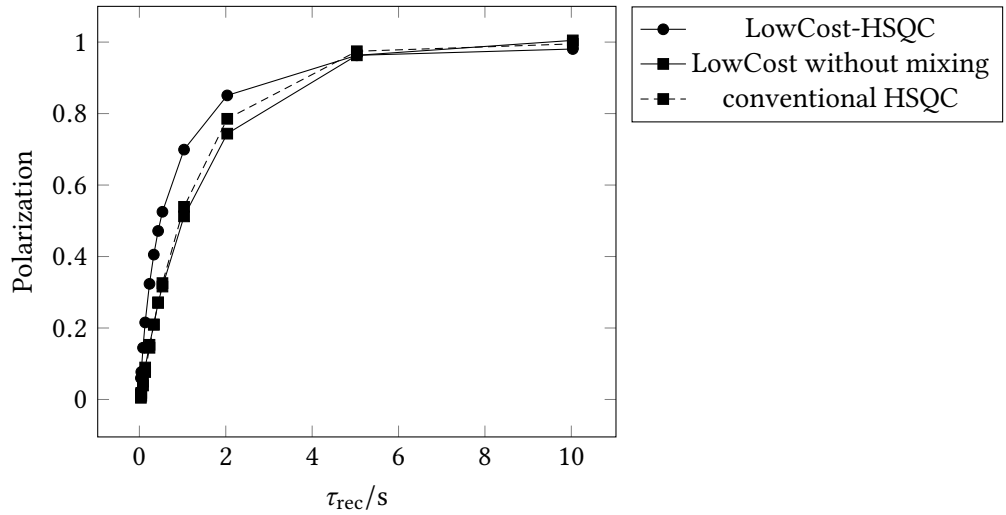

Figure 6.42: Mean experimental menthol steady state polarization from the LowCost-HSQC-recovery experiment. The reservoir is aligned along $+z$, mixing time is 34.5 ms when mixing is used. Without mixing, the polarization of the LowCost-HSQC is very close to the conventional HSQC. With mixing, the contribution of remote protons is significant.

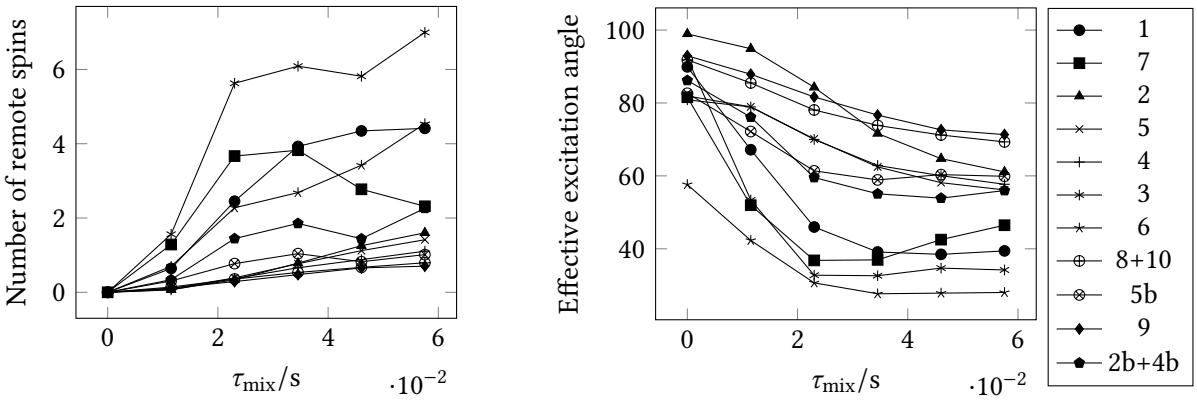

(a) Number of remote spins per local spin reached by mixing in the LowCost-HSQC.

(b) Effective β for all spins created by mixing with passive spins in the LowCost-HSQC.

Figure 6.43: Interpretations of the experimental LowCost-HSQC polarization. a) The number of spins reached by mixing is comparable to the number reached in the ASAP-HSQC, confirming the similarity between the two experiments and also their theoretical models. b) The effective excitation angle corresponding to the steady state polarization of the LowCost-HSQC for all spins of menthol. The effective excitation angle is created by the mixing with remote ^{1}H while the transfer step does not preserve any local reservoir magnetization.

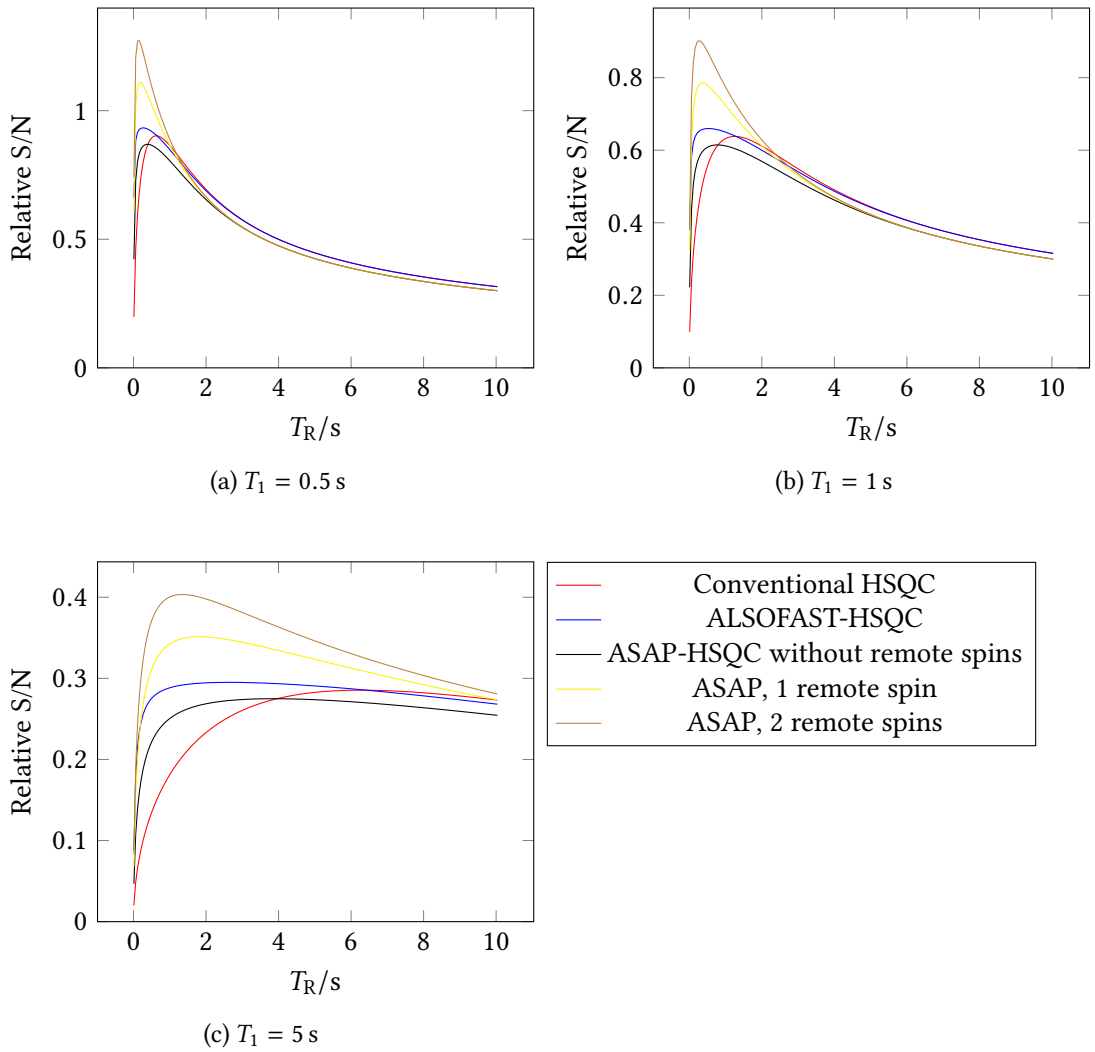

Figure 6.44: Estimate of the relative signal-to-noise ratio; steady state signal intensity per square root of duration, $\sqrt{T_R}$. This includes the time required for the mixing sequence of the ASAP-HSQC. The contribution of acquisition time and therefore spectral resolution is neglected in this estimation. Comparison of conventional HSQC, ALSOFAST-HSQC at optimal excitation angle, and ASAP-HSQC at optimal excitation angle with complete mixing of 0, 1 or 2 remote spins. In a real experiment, T_R must include the 10 to 30 ms duration of the sequence and the acquisition time, which is usually limited to 0.1 to 0.4 s by the decoupling hardware. a) $T_1 = 0.5$ s is in the order of the duration of a single scan. The difference between the experiments is most pronounced with repetition times too short to contain the desired acquisition time. b) $T_1 = 1$ s is larger than the duration of a single scan. The highest signal-to-noise ratio coincides with the optimal acquisition time and the ALSOFAST- and the ASAP-HSQC bring significant benefits. c) $T_1 = 5$ s corresponds to slow relaxation. Polarization hardly recovers at typical HSQC repetition delays. In this case, application of ALSOFAST- and ASAP-HSQC experiments still is advantageous.

6.4 Conclusion: When to Use Which Experiment?

In the former sections, many details that influence of polarization recovery and ultimately signal intensity per experiment time could be discovered. A simple mathematical model could be derived combining all the details.

Most important for ASAP experiments is of course the number of spins that can be reached by the mixing sequence. In Figure 6.44 the comparison of the ideal reachable signal intensity is shown with different spin systems and relaxation times.

To include the reduced relaxation, caused by the dipolar contribution, for this calculation, the ALSOFAST- and ASAP-HSQC have their T_1 relaxation time increased by 10 %, which seems to be a reasonable value. Both experiments are simulated at their optimal excitation angle, whereas complete excitation is used in the conventional experiment. It can be seen, that a single coupled spin contributes enough polarization to the steady state to achieve highest signal intensity in the time scale of 100 ms to 1 s which is highly relevant in HSQC applications. Shorter delays do not allow sufficient acquisition time for useful resolution, while the upper limit of acquisition is imposed by the energy deposition from decoupling. The ALSOFAST-HSQC also yields higher intensities than the conventional sequence in most cases when the recovery delay is shorter than T_1. The look at the LowCost-ASAP-HSQC confirms the high influence of the remote spins. In this experiment, no Ernst angle-like exitation is possible, still the steady state polarization and the signal intensity is increased by the mixing sequence. In real systems, the mixing will not be complete so several remote spins will be required to reach these theoretical curves. Simulation of the transfer during the mixing sequence on the spin state level could provide clarification.

Next to the number of reachable spins, the relaxation times of the molecules play a large role. For T_1 relaxation times below 1 s, a significant portion of the polarization is recovered before the next scan in any experiment. Short T_2 times reduce the reservoir polarization during the pulse sequence. Both relaxation processes are active during the mixing sequence and further decrease the available polarization.

Nonetheless, the model shows, ASAP experiments can be highly advantageous when applied to the right molecules.

Chapter 7

Progressive Excitation

7.1 Experiments that Never Reach Steady State

As seen in Chapter 6, a low effective excitation flip angle is beneficial to the steady state polarization. Choosing the right flip angle that balances relaxation and signal intensity, maximum spectral intensity can be achieved in multiscan experiments. For a single scan, however, a 90° pulse creates the maximum intensity in samples without nonlinear effects. Taking a closer look at the transition shows that in the first few scans, before reaching a steady state, the signal intensity undergoes additional fluctuations.

In a 1D experiment with multiple scans the fluctuations are averaged by addition of the following scans. This can reduce the comparability of individual signals but is not a serious problem. In 2D experiments, however, the intensity of every single F_1 point is evaluated by the Fourier transform. Any fluctuation will create additional artifact intensity or distort the shape of signals. As fluctuations of intensity do not change the frequency in the directly detected dimension, such artifact intensity remains confined to its F_2 frequency. In spectra this is often seen as columns of noise stretching over the whole spectrum at the frequency of signals with high intensity, therefore it is often called F_1 noise or multiplicative noise. To reduce fluctuations, therefore, in the beginning of an experiment a number of *dummy scans* is performed, running the same pulse sequence but without actually recording data to bring the system close to the steady state.

Depending on sample relaxation times, reaching the steady state takes significant time and the available polarization and intensity may not be as high as desired. Especially when the experiment itself is only acquired for a small number of scans, it may be beneficial not to aim for reaching the steady state and ensure constant signal amplitude by a different method. This is even more important when the initial state is significantly different from the equilibrium state, as is the case with hyperpolarized samples [161–163] where the initial magnetization is absurdly high but cannot be recovered within the 2D experiment by most hyperpolarization methods available to date.

One way to ensure constant amplitude without performing dummy scans and waiting for the steady state is to vary the excitation flip angle from scan to scan by a predetermined list. In general, the ideal excitation angle increases monotonically as polarization decreases, concluding with a full 90° pulse. The method, which we called progressive excitation, squeezes all the initial polarization from a molecule, taking along everything that recovers between the scans, leaving it completely without polarization after the last scan.

The method has been applied to MRI [164, 165], where varying flip angles over space and time is seen more often. It has also found initial applications in one-dimensional hyperpolarization experiments [166, 167]. So far only simple models without polarization recovery have been derived and not yet been applied to multidimensional NMR. In the following, a model for the ASAP-HSQC including T_1 relaxation will be presented.

7.2 Mathematical Model

The model described herein relies heavily on a Matlab program based on the equations. The code corresponding to the sections is included in the appendix on Page 258. The nomenclature from last chapter is used where possible and all terms are indexed by the scan number i. Figure 7.1 shows the sequence at scan number i that runs from 1 to ns. The polarization at the start of scan i is $P_i(0)$. When a pulse with flip angle φ_i and negligible pulse length 0_+ is applied to this polarization, transverse magnetization is created giving rise to the NMR signal

$$S_i = P_i(0) \cdot \sin(\varphi_i) \tag{7.1}$$

while the remaining polarization is

$$P_i(0_+) = P_i(0) \cdot \cos(\varphi_i). \tag{7.2}$$

This polarization then undergoes relaxation or other processes until the end of the experiment at $t = T_\mathrm{R}$, where

$$P_i(T_\mathrm{R}) = P_{i+1}(0). \tag{7.3}$$

To record constant signal intensity over all scans,

$$S_{i+1} = S_i \tag{7.4}$$

is required for all i, and to use all available magnetization, the last pulse is required to be

$$\varphi_{ns} = \frac{\pi}{2} = 90°. \tag{7.5}$$

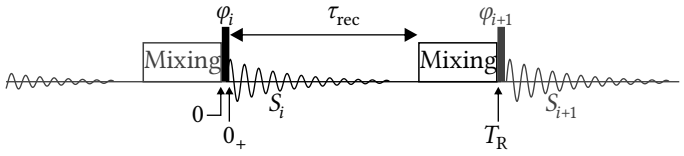

Figure 7.1: Pulse sequence and time delays of the model used for the progressive excitation calculation. The scan i is shown. The pulse with flip angle φ_i is applied on the polarization P_i to create the signal S_i. During τ_{rec}, T_1 relaxation can take place. Optional ASAP-style averaging of proton intensities is indicated by the mixing element. The polarization available to the next pulse is P_{i+1}.

The following sections describe different scenarios with different processes taking place between two pulses, from $t = 0_+$ to T_{R}. In the examples, $P_1(0) = P_{\mathrm{Eq}} = 1$ is used for initial polarization, while other values are possible, e. g.$P_1 \gg P_{\mathrm{Eq}}$ or $P_1 \ll P_{\mathrm{Eq}}$ in a hyperpolarization experiment. Where mixing between spins is concerned, $k = 1$ is the number of active ^{1}H, e. g. bound directly to a ^{13}C for ASAP experiments, with $n - k = 2$ remote ^{1}H in the vicinity.

7.2.1 Neglecting Relaxation

Without relaxation or other processes, when no change of magnetization between the pulses is taken into account,

$$P_i(0_+) = P_i(T_{\mathrm{R}}) = P_{i+1}(0). \tag{7.6}$$

Inserting Equation (7.6) into Equation (7.4) yields the recursive solution

$$\varphi_i = \arctan\left(\sin\left(\varphi_{i+1}\right)\right) \tag{7.7}$$

that allows calculating all φ_i. Examplary results for this case are shown in Figure 7.2.

7.2.2 Ideal ASAP-Style Mixing

ASAP experiments use an isotope-selective excitation scheme in combination a tunable flip angle. Ideally, the excitation affects only d protons bound directly to ^{13}C, leaving the remote polarization of r other protons untouched. After the acquisition of the FID, all proton polarization is averaged by an isotropic mixing sequence. After the mixing sequence, the polarization is

$$P_{i+1} = \frac{rP_i(0) + dP_i(0_+)}{r + d} = \frac{P_i(0)}{r + d} \cdot \left(d\cos\left(\varphi_i\right) + r\right), \tag{7.8}$$

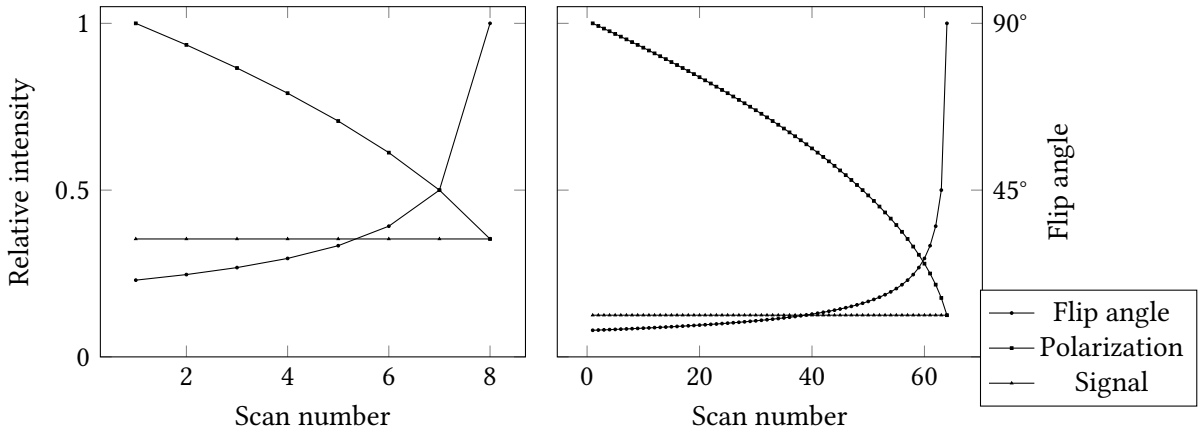

(a) 8 scans (b) 64 scans

Figure 7.2: Optimal flip angle for a scan (circles), Polarization after the pulse (squares), and signal intensity created by the pulse (triangles) for a) 8 and b) 64 scans without considering relaxation processes.

which leads to the equation

$$0 = (r + d)\sin(\varphi_i) - d\sin(\varphi_{i+1})\cos(\varphi_i) - r\sin(\varphi_{i+1}), \tag{7.9}$$

that was solved numerically, as no closed solution could be found. Results for this case are shown in Figure 7.3.

7.2.3 T_1 Relaxation

Polarization recovery via T_1 relaxation is described by

$$P_{i+1}(0) = 1 + (P_i(0_+) - 1) \cdot E_1, \tag{7.10}$$

using the abbreviation $E_1 = \exp(\tau_{\text{rec}}/T_1)$ introduced in Equation (6.4). Inserting Equation (7.10) into Equation (7.4) leads to the equation

$$0 = -\sin(\varphi_i) + \cos(\varphi_i) \cdot E_1 \cdot \sin(\varphi_{i+1}) + \frac{\sin(\varphi_{i+1})}{P_i(0)} \cdot (1 - E_1) \tag{7.11}$$

that has to be solved to obtain a recursive solution. Unfortunately, due to the occurrence of $P_i(0)$ in the equation, boundary conditions for the first and the last scan exist. A numerical solution can be found iteratively, guessing an initial set of $P_i(0)$, then for all φ_i and calculating a

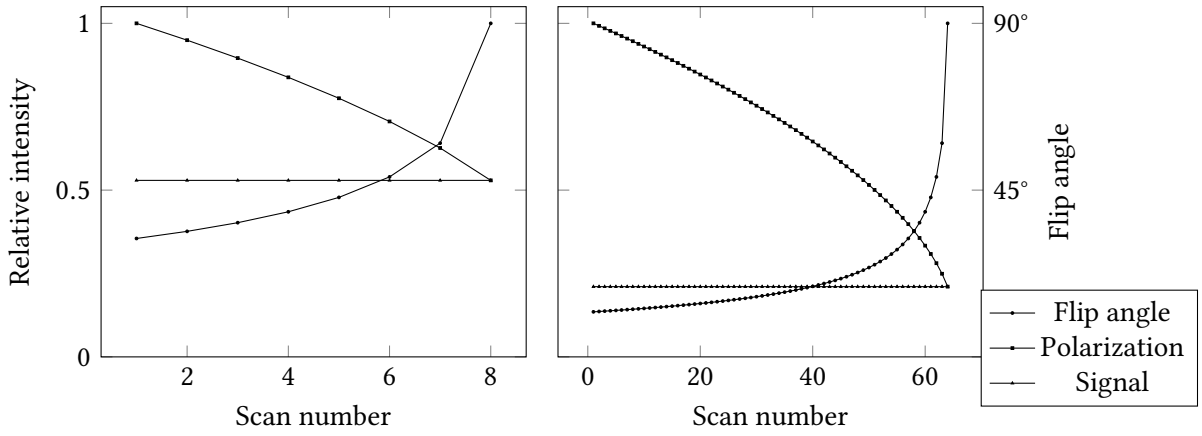

(a) 8 scans (b) 64 scans

Figure 7.3: Optimal flip angle for a scan (circles), Polarization after the pulse (squares), and signal intensity created by the pulse (triangles) for a) 8 and b) 64 scans without relaxation but with ASAP-like mixing between $d = 1$ observed and $r = 2$ neighboring protons.

more accurate set of P_i using the φ_i. This is repeated until sufficiently high and constant signal intensity is reached. Results for this case are shown in Figure 7.4.

Ernst Angle

In a system with a given T_1 and recovery time τ_{rec}, after a sufficient number of scans with constant flip angle, the polarization and signal intensity approach a constant value. The Ernst angle was derived from Equation (6.24) of the last chapter as

$$\beta_{\text{opt}} = \arccos\left(E_1\right). \tag{7.12}$$

Using the Ernst angle as constant excitation angle yields the highest signal intensity for the set of T_1 and recovery time τ_{rec} [76]. This is well-suited for comparison with progressive excitation, as illustrated in Figure 7.5.

For very long experiments, e. g. 1024 scans, a plateau region appears in the progressive excitation scheme, that is very similar to Ernst angle excitation, as is shown in Figure 7.6. Progressive excitation is not intended to be used in such long experiments, however, a generalized scheme could be devised:

- Starting with very low flip angle, the flip angle is increased until Ernst angle is reached.
- Ernst angle is used for constant excitation in the steady state-like phase of the experiment.

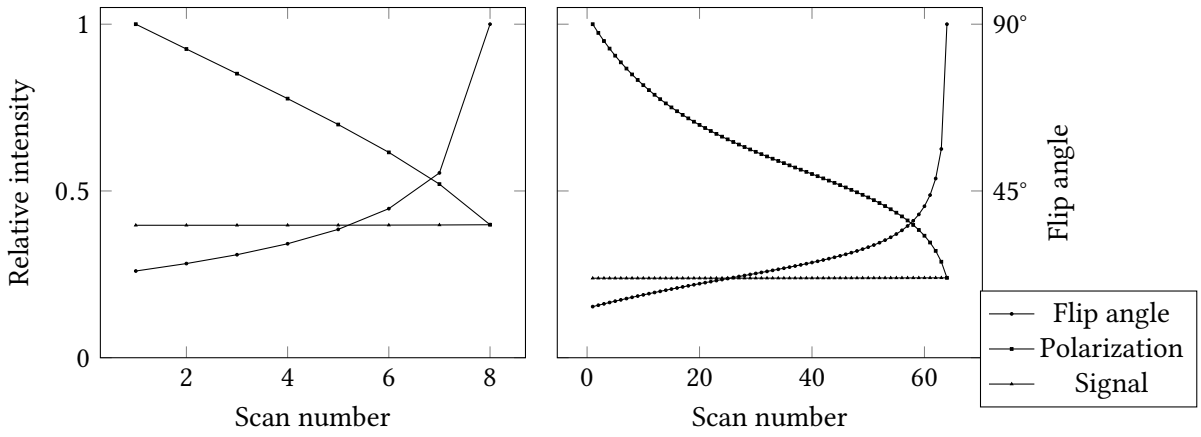

(a) 8 scans (b) 64 scans

Figure 7.4: Optimal flip angle for a scan (circles), Polarization after the pulse (squares), and signal intensity created by the pulse (triangles) for a) 8 and b) 64 scans with $T_1 = 10\,\mathrm{s}$ and repetition time $T_\mathrm{R} = 1\,\mathrm{s}$.

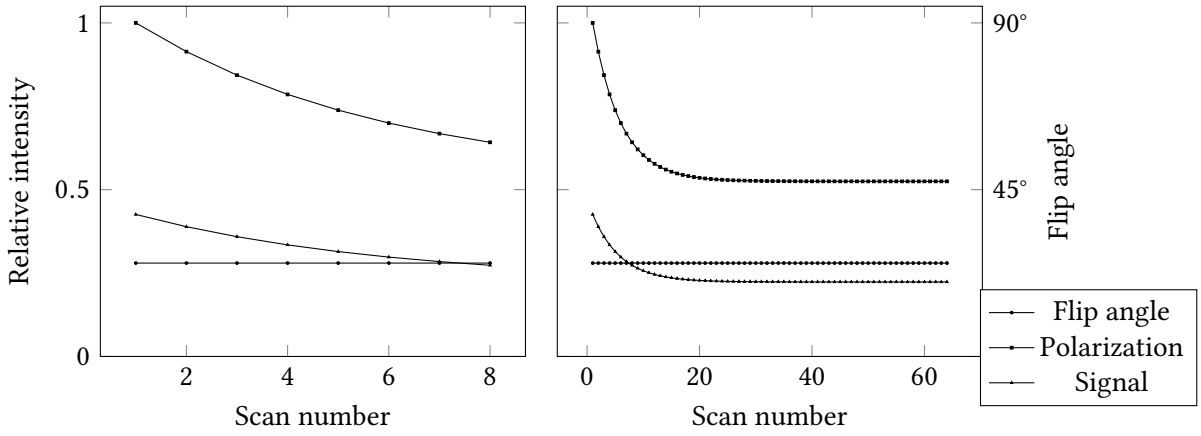

(a) 8 scans (b) 64 scans

Figure 7.5: Ernst angle exitation for comparison. Constant flip angle excitation (circles), Polarization after the pulse (squares), and signal intensity created by the pulse (triangles), with T_1 relaxation for a) 8 and b) 64 scans with $T_1 = 10\,\mathrm{s}$ and repetition time $T_\mathrm{R} = 1\,\mathrm{s}$.

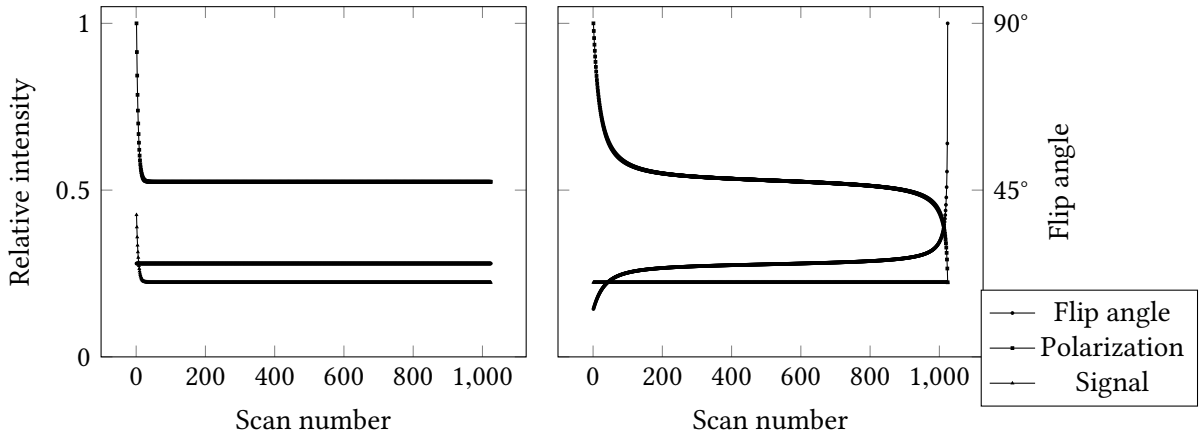

(a) Ernst angle (b) Progressive excitation matched to T_1 relaxation

Figure 7.6: Flip angle of a scan (circles), Polarization after the pulse (squares), and signal intensity created by the pulse (triangles) for a) Ernst angle excitation and b) progressive excitation. Both schemes are matched to $T_1 = 10\,\mathrm{s}$ and repetition time $T_R = 1\,\mathrm{s}$

- For the last few scans, the flip angle is increased again, until 90° is reached.

The direct gain in signal intensity is minimal, however, the experiment can then be run without dummy scans and applied very flexibly.

7.2.4 ASAP Mixing and T_1 Relaxation

Combining ASAP mixing with T_1 relaxation, the polarization is described by

$$P_{i+1}(0) = 1 + \left(\frac{P_i(0)}{r+d}\left(d\cos(\varphi_i) + r\right) - 1\right) \cdot E_1. \tag{7.13}$$

Inserting Equation (7.13) into Equation (7.4) leads to the equation

$$0 = -\sin(\varphi_i) + \cos(\varphi_i) \cdot E_1 \cdot \sin\left(\varphi_{i+1}\right) \frac{d}{r+d} + \left(1 - E_1 + P_i(0) E_1 \frac{r}{r+d}\right) \cdot \frac{\sin\left(\varphi_{i+1}\right)}{P_i(0)}, \tag{7.14}$$

that has to be solved to obtain a recursive solution. Again, the involvement of $P_i(0)$ prevents direct calculation. Again, iterative solving for all φ_i while guessing $P_i(0)$ can be performed to obtain results as shown in Figure 7.7.

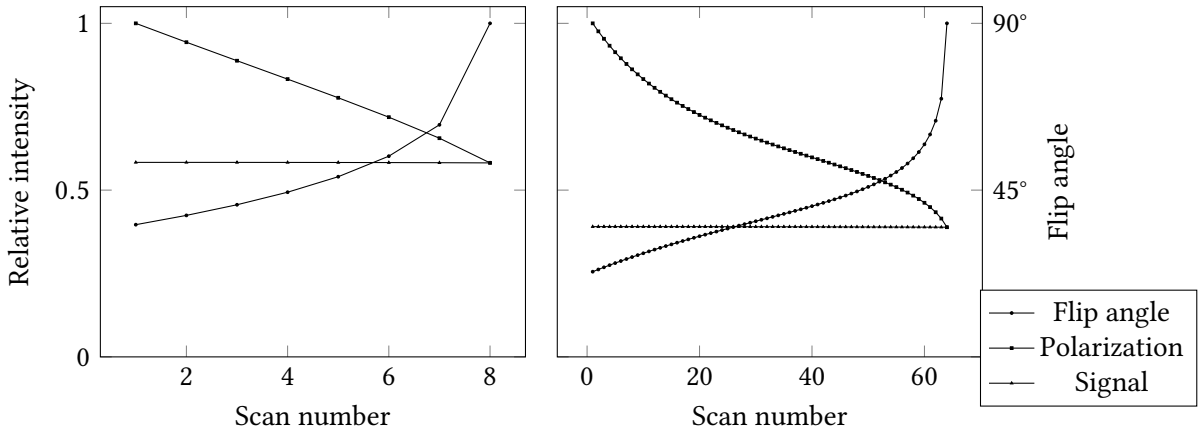

(a) 8 scans (b) 64 scans

Figure 7.7: Optimal flip angle for a scan (circles), Polarization after the pulse (squares), and signal intensity created by the pulse (triangles) for a) 8 and b) 64 scans with $T_1 = 10\,\mathrm{s}$ and repetition time $T_R = 1\,\mathrm{s}$ with ASAP-like mixing between $k = 1$ observed and $n - k = 2$ neighboring protons.

7.3 Experimental

In all applications it turned out that exact calibration of the pulse power is essential. In a similar way, offset effects will also interfere with the excitation scheme by causing deviations in the effective flip angle. In the simple example experiments, the focus was not on broadband application. The RADFA pulses presented in Section 3.5, however, will be of great help to compensate against offset effects and create a more robust excitation scheme.

7.3.1 1D Experiment Optimized for T_1 Relaxation

The theory of the T_1 relaxation-only case in Section 7.2.3 can be tested by recording a pulse-acquire spectrum repeatedly in pseudo-2D fashion.

The pulse program `zg2d` was modified to use a list of pulse lengths. It will be compared to a regular `zg2d` experiment where the excitation angle is set to the Ernst angle. Menthol in $CDCl_3$ was used as a test sample. The signal intensity of the H-C-Me signal of the proton next to the methyl group is plotted against the scan number in Figure 7.8. As expected, the constant-flip angle excitation yields rapidly decaying signal intensity. The progressive-excitation method provides more constant intensity, and yields higher overall intensity. However, the relaxation properties of the system are not matched exactly, and signal intensity slowly rises over the course of the experiment.

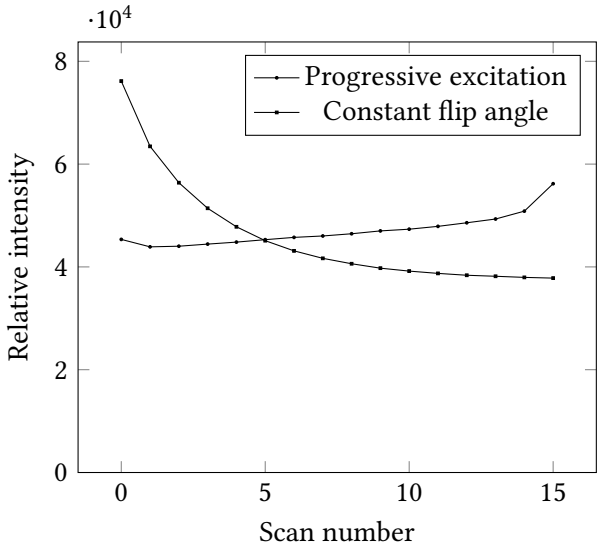

Figure 7.8: Experimental signal intensity of the position 3 of menthol in $CDCl_3$, the H-C-Me proton. τ_{rec} is 0.35 s and T_1 is approximately 2.3 s. 16 scans were recorded. $\tau_{rec} = 0.15 \cdot T_1$ was used for progressive excitation and $\beta = 35°$ was used for constant excitation.

7.3.2 Progressive Excitation HMQC

Technically, the ALSOFAST-HSQC as well as the ASAP-HSQC sequence can utilize the progressive-excitation scheme, i. e., it can be implemented in the pulse program by reading the INEPT delay from a list. The effective excitation angle, however, is created by heteronuclear coupling and therefore dependent on the value of $^1J_{CH}$, which, in most real samples featuring common organic chemistry molecules, varies from 120 to 180 Hz. Some parts of the molecule will inevitably emerge from the INEPT block at wrong excitation angles and the progressive-excitation scheme will fail to yield constant intensity. Until a robust method to achieve uniform excitation angles is found, it is reasonable to apply the excitation scheme to an experiment with more accurately and more reliably tunable flip angle. The HMQC, when implemented with minimal pulses as shown in Figure 7.9, fulfills this requirement.

In hyperpolarization experiments, the sample does not recover polarization but rather loses it by T_1 relaxation driving it towards equilibrium. To imitate a hyperpolarization experiment, the spectrum has to be acquired in very short time compared to the T_1 relaxation time. Lacking real hyperpolarization, the loss due to T_1 relaxation effect cannot be included experimentally in a realistic way.

In Figure 7.10, the comparison between a progressive excitation HMQC and a constant flip HMQC are illustrated. The spectra were acquired on the Bruker line shape sample, 1 % $CHCl_3$ in Acetone-d_6. 32 real points were acquired in the indirect dimension, corresponding

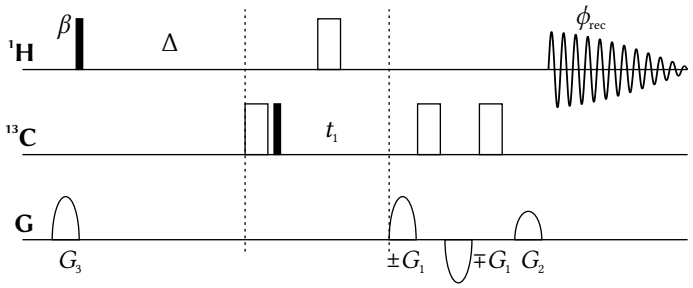

Figure 7.9: HMQC pulse sequence with only two pulses on ^{1}H and variable flip angle excitation. The Bruker pulse program `hmqcetgp` was modified to include a list of variable pulse lengths and a purge gradient before the first pulse. The flip angle of the pulse labeled with β is determined by the list. In the reference experiment, the same pulse length was used for all scans. The 180° pulse has to be considered when adjusting β by using $180° - \varphi_i$ for the list or the constant angle. All pulse phases in the sequence are x pulses, the first two pulses on ^{13}C are subjected to TPPI progression. Phase sensitivity in the indirect dimension is achieved via echo/antiecho coherence pathway selection using the gradients $G_1 = (80\,\%, -80\,\%)$ and $G_2 = (40.2\,\%, 40.2\,\%)$. Filled rectangles represent 90° pulses, open rectangles 180° pulses.

to 16 complex points. Repetition time of the experiment was 1.5 s, T_1 was not measured but estimated to be above 60 s. The FID in Figure 7.10a was obtained by calculating the absolute value of the hypercomplex spectrum, i. e., combining echo and antiecho FID. In comparison, progressive excitation achieves highest signal and constant signal intensity. While providing only slightlcy lower intensity, the constant flip angle experiment shows rapid signal intensity decline when run without dummy scans. This can cause line broadening and may introduce additional phase errors when the echo and antiecho FIDs that are acquired in sequence have different amplitude. Performing dummy scans before the acquisition sacrifices a large fraction of the initial polarization, but provides constant signal intensity. Figure 7.10b shows the F_2 trace of the same spectra. Best constant excitation results were achieved with $\beta = 180° - 1.6° = 178.4°$. All spectra have very low signal-to-noise ratio, originating from the short experiment duration. They were essentially acquired on equilibrium polarization without T_1 relaxation. Comparing the three peaks, progressive excitation yields higher intensity, reduced line width and improved line shape.

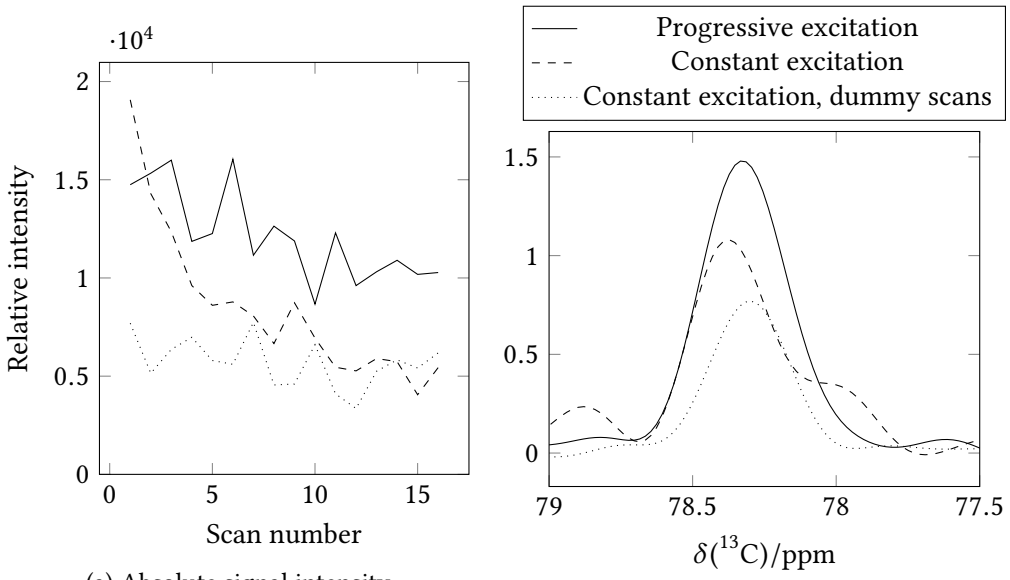

(a) Absolute signal intensity

(b) F_2 traces

Figure 7.10: HMQC spectrum acquired on 1 % $CHCl_3$ in Acetone-d_6; experimental comparison of progressive excitation (solid lines), constant excitation without dummy scans (dashed lines), and constant excitation with 16 dummy scans (dotted lines). 1536×32 real points were acquired without dummy scans in 5 s, or with dummy scans in 8 s. To prevent digitalization problems, the Fourier transform was performed at the high resolution of 4094×512 points. a) Absolute signal intensity of complex F_2 points, of the chloroform peak at 8.02 ppm. For each step, an echo and an antiecho FID were added, and the absolute value calculated. The fluctuating intensity is not an artifact frequency, but actual experimental noise caused by the low overall signal intensity. b) F_2 traces of HMQC spectra acquired in $CHCl_3$ extracted at the maximum intensity of the chloroform peak at 8.02 ppm. $\beta = 180° - 1.6°$ for constant excitation, $T_1 = \infty$ was used to calculate the progressive excitation steps.

7.4 Conclusion

Progressive excitation is a viable tool that enables small improvements already when room temperature polarized samples are measured in fast experiments. The additional effort is manageable, just like proper setup of Ernst angle excitation, it requires estimation of relaxation times. A set of progressive excitation list files covering common setups could be prepared in advance. Progressive excitation, however, is very sensible to proper estimation of the molecular parameters. Mismatched relaxation times, e. g., will quickly lead to varying signal intensities. For the experimental implementation, this is joined with more conventional problems like offset effects, wrongly calibrated RF amplitudes or mismatched coupling transfer delays, and the gains may be lost. At least for the offset effects, a possible solution is the use of RADFA pulses [21], that can achieve adjustable flip angles over large bandwidths, as shown in Section 3.5. The HMQC experiment presented as example, could further use the linear-phase RADFA pulses that provide increased performance.

The improvement by the progressive-excitation scheme is, of course, dependent on the difference between the thermal equilibrium polarization and the steady state polarization. Samples polarized above room temperature equilibrium may benefit from advanced excitation schemes.

An extension of the method that might prove valuable is to create an excitation profile, that is not constant but creates a desired line width, covering, in part, the effect of a window function. This will enable spending more polarization on scans that have high influence on spectral quality and less polarization on others.

Chapter 8

Anisotropy and Inhomogeneity of NMR Samples

The ^{2}H imaging of gels and liquid crystals was developed in cooperation with Christian Merle. It was extended to heteronuclear ^{1}H,^{13}C-3D experiments in cooperation with Malin Reller. Parts of this chapter are published in [168] and [169].

8.1 The Value of Anisotropic NMR Measurements

The fundamental difference between NMR active and inactive nuclei is the magnetic moment: all NMR active nuclei have non-zero magnetic moment, they have at least a dipolar magnetic field. And, as any pair of toy magnets will easily show, magnetic dipoles interact through space, with a force depending on their orientation and alignment. Nuclear dipole-dipole couplings are among the strongest interactions between spin-carrying nuclei, and solid state spectra are usually dominated by dipolar splittings instead of chemical shift dispersion. A wealth of structural information can be obtained from dipolar couplings, as they reveal details about the relative orientation between spins and their absolute orientation with respect to the external magnetic field direction. In liquid state NMR, molecules tumble and rotate, a process summarized as rotational diffusion, and spins experience all sorts of orientations over a timescale even smaller than characteristic coupling evolution times. Dipolar and quadrupolar couplings and all other orientation-dependent magnetic interactions, like chemical shift anisotropy (CSA), are therefore averaged to zero and many users of NMR spectroscopy are not even aware of their existence. On the upside, this makes it possible to obtain highly resolved NMR spectra with sub-Hertz line widths, free from dipolar multiplets hundreds of kilohertz wide. At the same time, most of the information is lost, only a glimpse of anisotropic parameters can be caught from their influence on relaxation, most notably in the NOESY experiment [4, 170].

In an anisotropic medium, molecular motion is hindered, which leads to an incomplete averaging of the anisotropic interactions. The anisotropic interactions are reintroduced as *residual* anisotropic magnetic interactions. NMR spectroscopy in partial alignment was first achieved

in a liquid crystal mesophase [171–173]. In these media, high resolution spectra showing intramolecular magnetic interactions can be obtained without perturbation by intermolecular interactions. Strained elastomeric gels possess a similar structure [174], and from molecules dissolved in these strained gels RDCs and other anisotropic parameters can be obtained [175–178]. RDCs can be used to determine constitution [179], relative configuration [180–182], and preferred conformation or conformational ensemble [183] of molecules where conventional NMR methods, such as nuclear Overhauser effect or ^3J coupling constant analysis, fail to provide a unique solution to the structural problem [184].

A challenging but common task in analytical chemistry is the distinction of enantiomers and the corresponding estimation of enantiomeric excess. It is most often addressed by chiral chromatography and optical measurements like optical rotatory dispersion or circular dichroism spectroscopy, but also different approaches based on NMR spectroscopy are being used. In the latter case, it is necessary to form diastereomers from the enantiomeric compounds, which is either achieved by chemical modification with, for example the Mosher ester [185] and related substances [186], by the formation of weak diastereomeric complexes with lanthanide shift reagents [187], or chiral alignment media [188, 189]. The diastereomeric entities can then in principle be distinguished either by differences in chemical shifts or by different residual dipolar couplings (RDC) and residual quadrupolar couplings (RQC) of partially aligned samples [188, 190].

8.1.1 Inhomogeneity Problems with Anisotropic Samples

In a 1D spectrum, RDCs occur as additional couplings, often visible between a greater number of spins than isotropic couplings. The additional splitting caused by these couplings can seriously interfere with spectral resolution. A well-prepared sample, therefore is essential for the successful measurement of residual anisotropic NMR parameters. Next to the magnetic field homogeneity that is always a critical point, especially the degree of alignment should be as homogeneously distributed as possible over the active sample volume. Both stretched gels and liquid crystalline phases as alignment media need to equilibrate which can be a time-consuming task, and it is very important to be able to monitor the actual status of a sample. Complicated spectra with barely interpretable lineshapes and sometimes several unexpected signals are observed frequently, probably due to not yet equilibrated alignment media, but also maybe because of a broken gel, an air bubble, or a concentration gradient in a liquid crystal.

The line shape encountered is caused to a large extent by spatial inhomogeneity. Due to the shape of the active sample volume, inhomogeneities along the z direction are most severe. Figure 8.2a schematically shows the composition of the overall lineshape from all the regions

of the sample. While the spatial distribution determines the line shape, the line shape does not allow to unambiguously infer the sample properties. The spectrum obtained by an imperfectly shimmed sample as illustrated in Figure 8.2b is indistinguishable from the spectrum of inhomogeneous splitting in a perfectly homogeneous magnetic field in Figure 8.2c. In realistic samples, contributions of both effects can be seen, in particular since a sample with inhomogeneous alignment properties is difficult to shim. Conventionally, 1D ^{2}H spectra of the deuterated solvent are used to characterize the homogeneity of alignment, but the lack of spatial information leaves the user with pure guesswork about the underlying reasons of inhomogeneities. The introduction of spatial resolution allows the interpretation of samples with respect to underlying homogeneity issues.

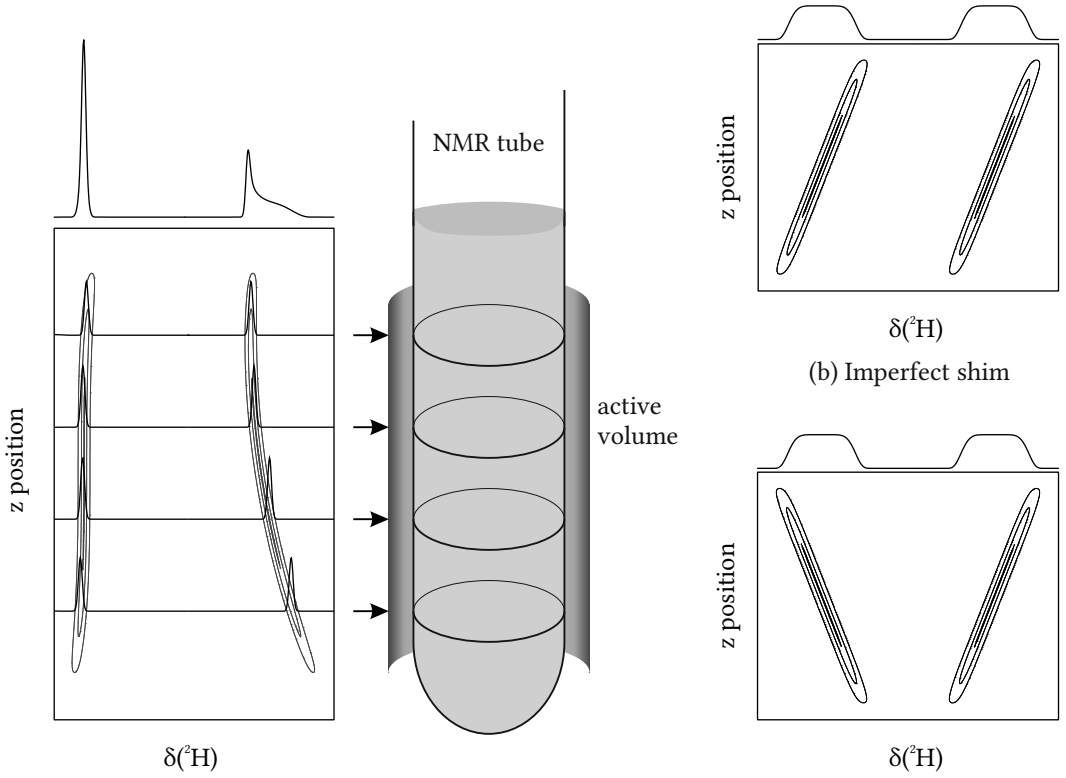

Figure 8.1: Schematic description of the expected results of ^{2}H imaging on partially aligned samples. a) Solvent peaks are split into doublets due to residual quadrupolar couplings, the alignment strength may vary within the sample. In addition, magnetic field inhomogeneity can introduce additional frequency deviations. The ^{2}H z profile allows distinction of broad lines due to b) imperfect shims, or c) inhomogenous alignment distribution, which cannot be distinguished based on the 1D experiment shown as projection on top.

8.1.2 Spatially Resolved NMR Spectroscopy

Magnetic resonance imaging (MRI) has a long tradition in medicinal applications. Contrast was usually derived from spin density or relaxation times, while spectral information often occurred as undesired chemical shift artifacts, caused by the different resonance frequencies of fat and water protons. Starting with separate images from the two media, chemical shift imaging arose [191, 192]. Applications are always limited by the experiment duration, especially with *in vivo* applications in mind. Adding a *J*-resolved dimension instead of chemical shift as source of chemical information is particularly interesting, as it can be sampled with far less points [193, 194], and several applications have been proposed [195, 196]. Based on echo-planar imaging (EPI) [87], echo-planar spectroscopic imaging (EPSI) provides simultaneous acquisition of a spectral and a spatial dimension [197, 198] that has been extended to COSY-type spectra (EPCOSI) [199]. In combination with non-uniform sampling techniques, it finally allows recording *J*-resolved spectra with chemical shift information and two or three spatial dimensions [200, 201]. Imaging is not limited to ^{1}H imaging, phosphorus in the form of the phosphate ion is required for all known forms of life, ^{31}P imaging gives insight in metabolic processes and allows imaging of bones [202, 203], while sodium ions play a role in many biological processes [204]. Even *in vivo* HMQC imaging has been reported to probe the distribution of a ^{13}C-labeled anticancer drug in tumor-bearing mice [205, 206].

Besides the generous use of pulsed magnetic fields gradients [207], the use of imaging methods in high-resolution NMR spectroscopy is quite rare. The ultrafast experiments [85, 89] already mentioned employ spatially resolved acquisition, the *z* filter actively creates spatial phase dispersion [90] and the G-SERF method simplifies coupling measurements [208]. Selective acquisition of 1D spectra from arbitrarily chosen volume elements to increase resolution [209] and parallel acquisition from a capillary bundle to improve the throughput in industrial applications [210] are among the few examples.

For imaging applications, usually slice-selective pulses, frequency encoding during acquisition and phase encoding gradient pulses are utilized, and more exotic schemes exist [211]. Of the possible methods, phase encoding is most conveniently combined with NMR spectroscopy. In contrast to slice selection and frequency encoding, it does not interfere with chemical shift evolution. In terms of 2D NMR spectroscopy it is also straightforwardly explained as an additional indirectly detected dimension. Like in a simple COSY experiment, the magnetization is excited and then let evolve for the duration of t_1 in the transverse plane. A magnetic field gradient is applied at the same time, changing the Larmor frequency of all spins. Instead of applying a mixing or transfer pulse, the gradient is simply switched off, whereupon the spins are returned to their natural frequency and an FID is recorded. While a COSY spectrum shows the

unperturbed chemical shift frequency in the indirect dimension after Fourier transformation, the indirect dimension of this experiment, additionally shows the frequency produced by the gradient. This frequency is proportional to the position of spins within the gradient. The phase encoding is further refined by using a constant delay instead of incremented t_1 and incrementing the gradient strength instead. The constant delay removes the chemical shift evolution from the imaging dimension.

Figure 8.3 shows the phase encoding sequence that was utilized to obtain NMR spectra with a spatial and a chemical shift dimension. The phase encoding step is similar to any other indirect dimension in multidimensional NMR. It can easily be combined with conventional encoding elements to create 3D experiments providing additional chemical information. In principle, phase encoding can also be extended to additional spatial dimensions, using multidirectional pulsed magnetic field gradients, which were, unfortunately, not available in our laboratory.

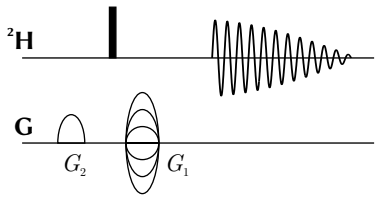

(a) ^{2}H Phase encoding sequence

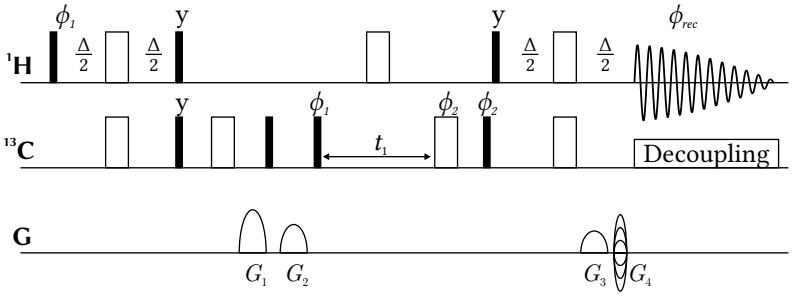

(b) HSQC-imaging

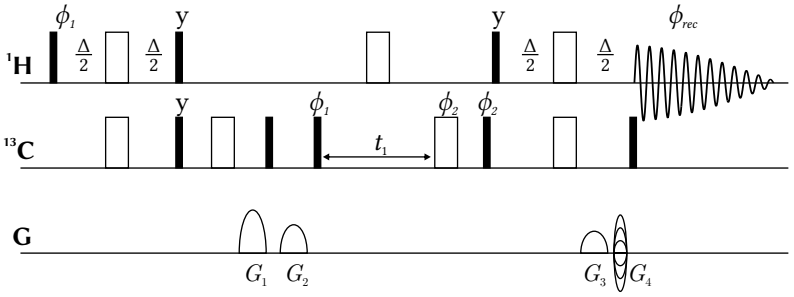

(c) CLIP-HSQC-imaging

Figure 8.3: Pulse sequences of a) the ^{2}H phase encoded experiment to obtain chemical shift-resolved z profiles. The phase encoding gradient length is usually in the ms range and incremented from −95 to 95 % gradient strength. To image a range of 30 mm with 256 points, the gradient length was 1.5 ms. An additional gradient pulse can be used to remove leftover coherence from previous scans. For ^{1}H imaging, due to the higher gyromagnetic ratio, the gradient length is in the 100 µs range. b) The 3D HSQC-imaging experiment and c) the 3D CLIP-HSQC-imaging experiment are based on the `hsqcgpph` pulse sequence included in TopSpin 3.2, used with default values for all pulses and gradient strengths. The spatial resolution is achieved by adding a phase encoding z gradient G_4 of 116.7 µs length and −47.5 to 47.5 % gradient strength in the last transfer delay. The phase ϕ_1 is used for States-TPPI progression and ϕ_2 = x, −x.

8.2 ^{2}H Imaging for Gels and Liquid Crystals

As already mentioned, one frequently observed difficulty with partially aligned samples are differential relative linewidths of ^{2}H multiplets, which, however, are unrelated to relaxation effects and appear to be shim-dependent. They can readily be explained by correlated inhomogeneities. Depending on the shim, either the left or the right doublet component of the 1D ^{2}H spectra show reduced linewidths or both lines are practically identical. Using ^{2}H imaging, the cause of the different linewidths can easily be derived as the interplay of a gradient in the alignment strength that is superimposed by a shift due to an additional magnetic field gradient. Figure 8.4a shows an inhomogeneously split PBLG sample, where the shim is optimized to minimize the linewidth of the left component. It should be noted that the shim is actually imperfect in this case, and only for this component the two effects cancel each other. The right part of the multiplet instead feels the broadening from the alignment gradient in addition to the imperfect shim. All signals acquired from the sample with this set of shims will be affected by the same combination of errors. Shimming to a homogeneous field leaves the broadening due to the alignment gradient, which affects both multiplet components in the same manner, as shown in Figure 8.4b for a different sample.

The imaging experiments also allow the detection of defects in the liquid crystalline phase. Figure 8.4c exhibits a PBLG/$CDCl_3$ sample with a central isotropic line for the deuterated solvent, indicating the coexistence of the oriented and isotropic phases in the different isosurfaces. Over a small region, the two phases even coexist within a single plane perpendicular to the z axis. Figure 8.4d, finally shows a nicely equilibrated lyotropic mesophase, in which even the dipolar coupling between the deuterium nuclei of CD_2Cl_2 is visible.

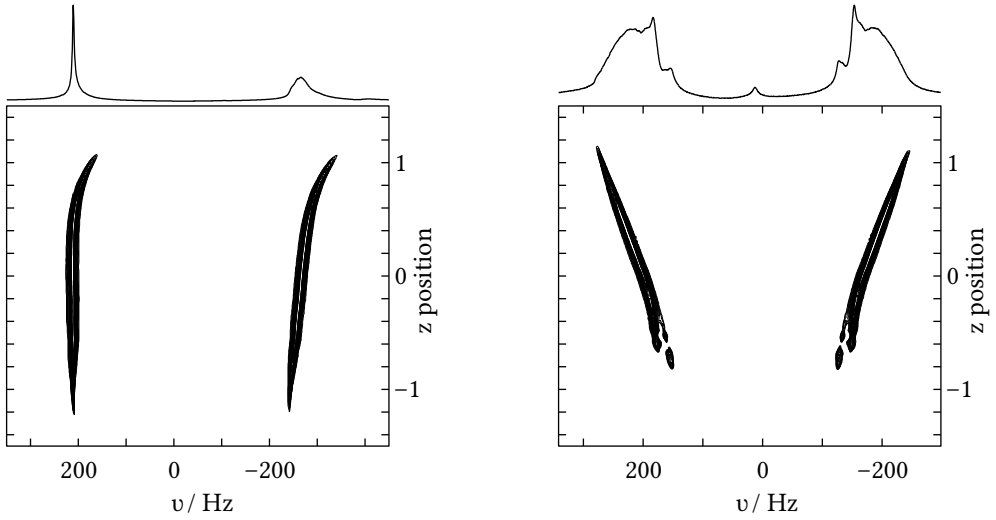

(a) Left part shimmed

(b) Close-to-ideal shim

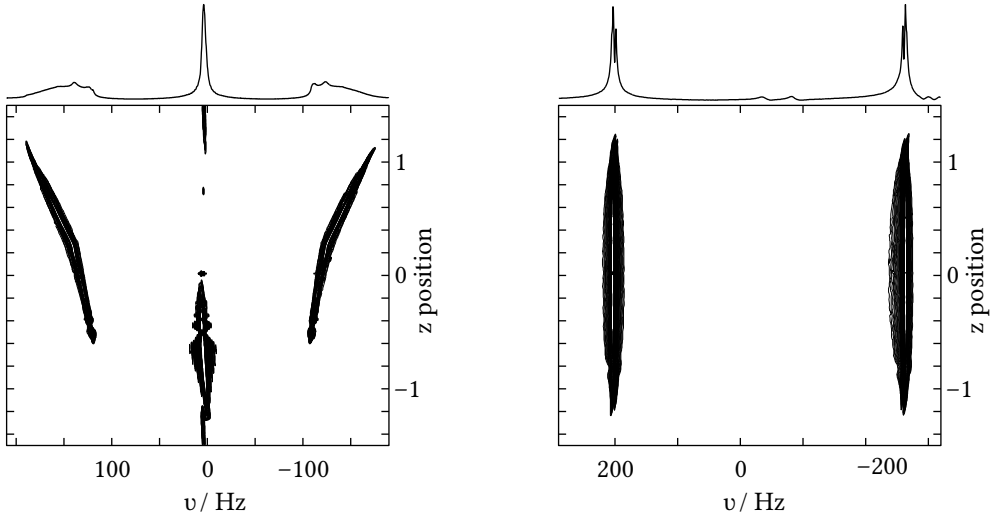

(c) Isotropic region

(d) Homogenous sample

Figure 8.4: ^{2}H profiles of liquid crystal samples encountered; a) Inhomogenous PBLG/$CDCl_3$ probably due to concentration gradient, shim optimized for the left peak, i. e.wrong z shim settings. b) Sample from a, PBLG/$CDCl_3$ shim close to ideal. c) PBLG/$CDCl_3$ the lower part of the sample is isotropic. d) CD_2Cl_2 multiplet of PBLG/CD_2Cl_2/$CDCl_3$ well equilibrated.

8.3 HSQC-Imaging

Deuterium spectra of samples where the solvent is the only deuterated compound naturally are quite empty. In contrast, proton spectra of mixtures provide ample chemical information but often contain overlapping peaks. Usually this problem is approached by the introduction of additional spectral dimensions, exploiting the high chemical shift dispersion of some nuclei like ^{13}C. Measuring coherence formed by connected ^{1}H-^{13}C groups in an HSQC is a convenient way to reduce spectral crowding. Fortunately, the phase encoding dimension that provides the spatial resolution in the ^{2}H imaging experiment is similar to any other indirect dimension in multidimensional NMR. It can be combined with conventional encoding elements to create experiments with a spatial and a chemical dimension. This gives access to the full range of spatial information. It allows, e. g., measuring sample homogeneity beyond alignment strength, detecting concentration gradients and temperature gradients, but also evaluation of regions of highest quality or correction of B_0 inhomogeneity along the direction of the spatial dimension.

One such sequence is the 3D HSQC-imaging sequence shown in Figure 8.3b. It was implemented on a 600 MHz Avance II+ NMR Spectrometer equipped with a BBI Probehead and TopSpin 3.2. For demonstration, it was applied to a two-phase sample containing a $CDCl_3$ phase below a D_2O phase. Sucrose and menthol were dissolved in the sample, their solubility confines the sucrose to the D_2O phase and the menthol to the $CDCl_3$ phase. A sketch of the sample is shown alongside an HSQC spectrum, a ^{2}H and a ^{1}H z profile in Figure 8.5.

Figure 8.6 shows the strength of the the 3D HSQC-imaging spectrum. An HSQC spectrum of each phase was created from a sum projection over the homogeneous regions only. Signals originating from the top and bottom of the sample or from the phase boundary are discarded and corresponding artifacts removed. The shim was optimized for the upper phase, so especially the signals from the lower part benefit from this evaluation.

To examine the spatial distribution of the molecules, a projection as shown in Figure 8.7 is advantageous. The high discriminatory power of the HSQC provides full information for each slice of the sample. This representation also makes chemical shift differences within the sample visible. These differences can occur when temperature gradients or concentration gradients are involved. Spatially resolved spectra give insight into the cause of inhomogeneities, turning artifacts into comprehensible information.

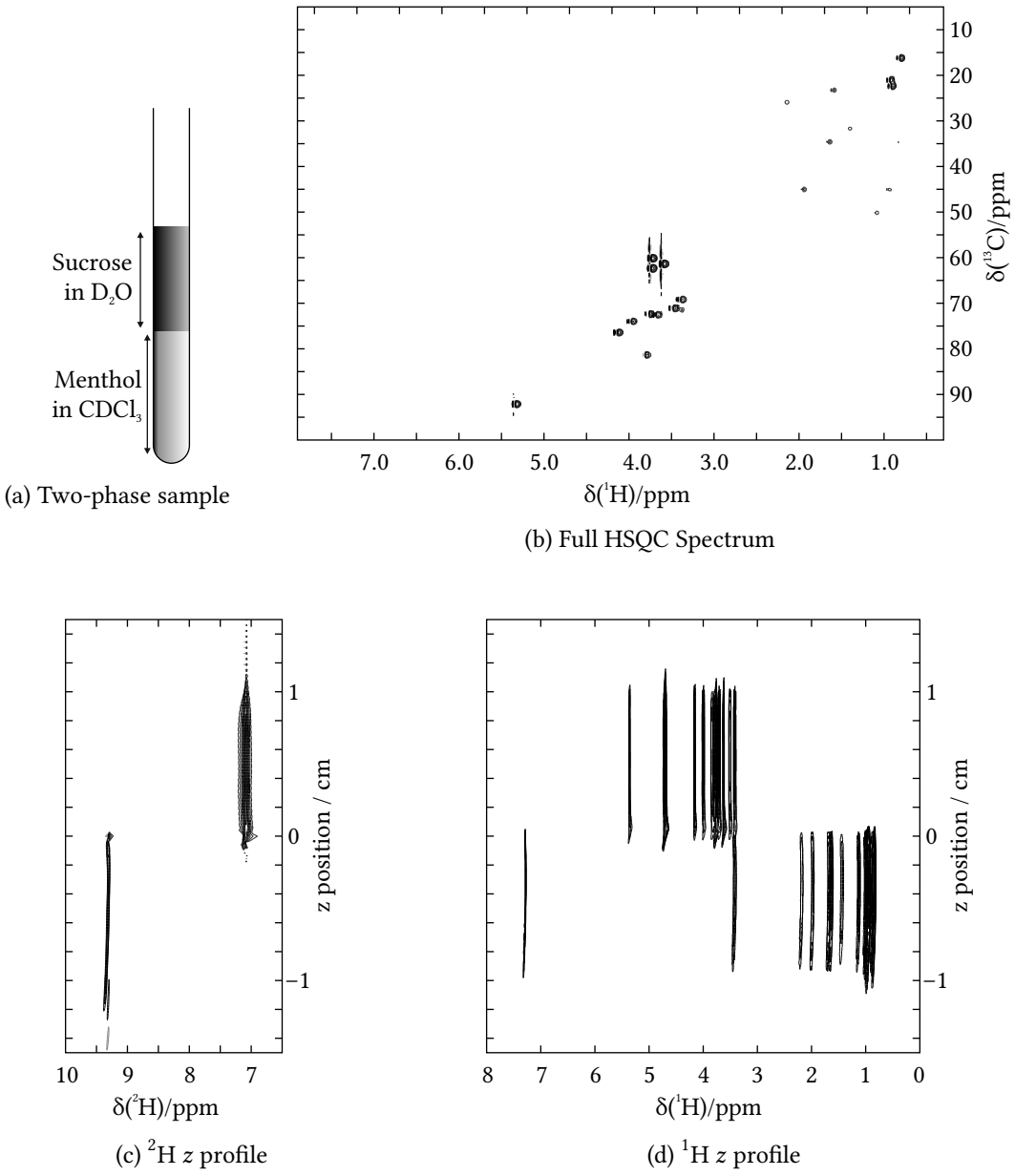

Figure 8.5: a) Sketch of the two-phase sample containing sucrose and menthol in D_2O and $CDCl_3$. b) regular HSQC spectrum without spatial resolution; 2048×128 real points acquired with 2 scans per increment and 16 dummy scans in 5 min 27 s with the pulse program `hsqcetgpsisp2.3` at default settings. c) The ^{2}H profile shows the solvent distribution following the phase separation. The solubility of the solvents in the respective other phase is very low. d) The ^{1}H profile shows the distribution of the analytes, sucrose is confined to the D_2O phase, menthol is confined to the $CDCl_3$ phase.

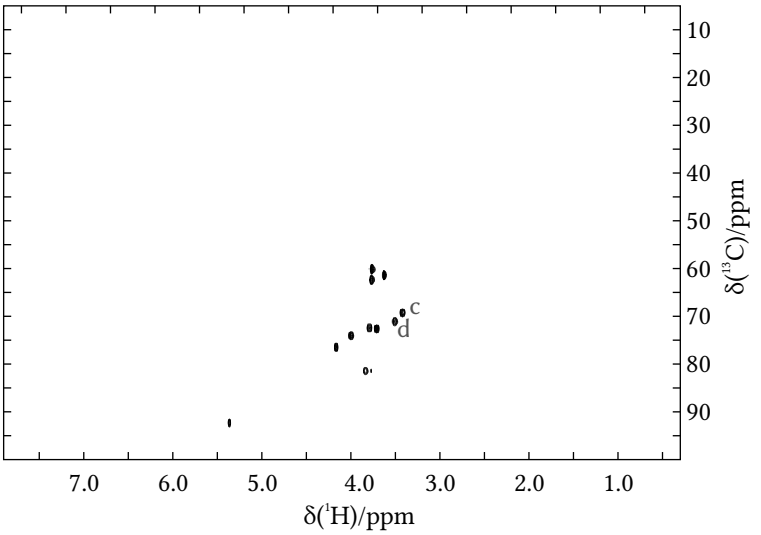

(a) Projection from upper phase

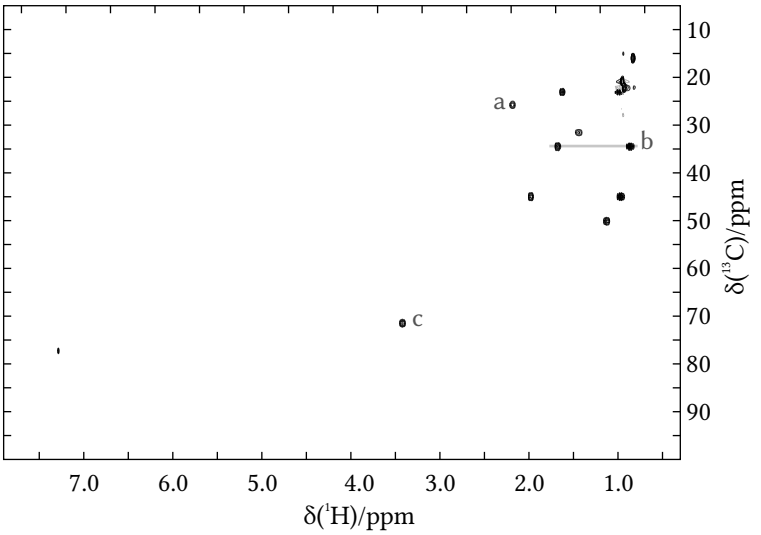

(b) Projection from lower phase

Figure 8.6: Sum projections from a 3D HSQC-imaging spectrum acquired on the two-phase sample containing sucrose and menthol in D_2O and $CDCl_3$. Spectrum of 2048×128 real HSQC points in combination with 64 points of phase encoding over a z range of 3 cm; acquired with 2 scans per increment and 16 dummy scans in 7 h 41 min. The z profiles of peaks marked with the letters a to d are shown in Figure 8.7. A separate HSQC spectrum can be extracted for the top and bottom part of the sample. a) Sum projection of the top part of a 3D HSQC-imaging spectrum, collected over the z range from 3.3 to 8.9 mm. The spectrum resembles an HSQC spectrum of sucrose in D_2O. b) Sum projection of the bottom part of a 3D HSQC-imaging spectrum, collected over the z range from -0.5 to -4.7 mm. The spectrum resembles an HSQC spectrum of menthol in $CDCl_3$. Figure 8.5 shows that B_0 of the $CDCl_3$ phase is not homogeneous, in other words, the shim is bad. The spatially resolved 3D spectrum allows selection of a sufficiently homogeneous region for further evaluation: the linewidth is reduced and the artifacts next to all peaks are removed.

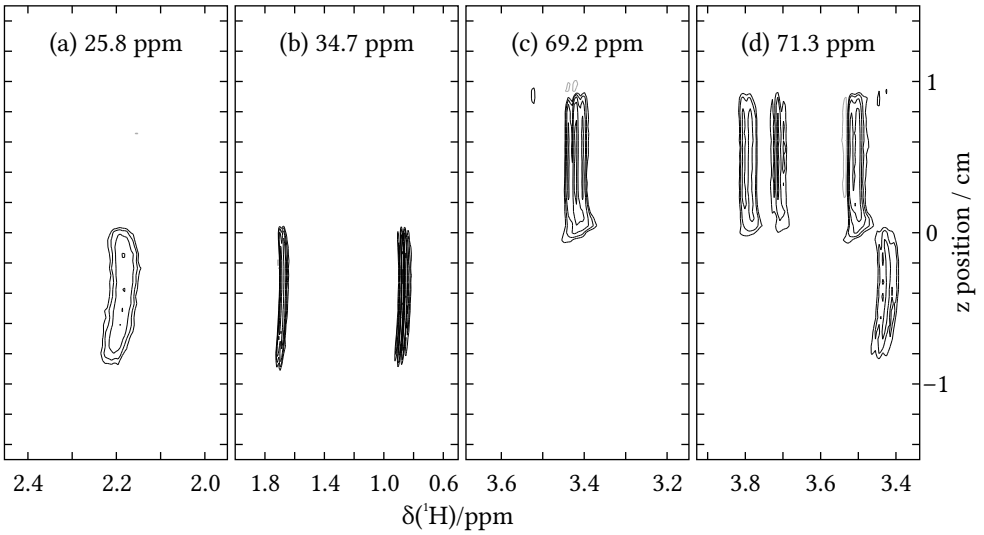

Figure 8.7: z profile of peaks at four ^{13}C frequencies from the 3D HSQC-imaging spectrum acquired on the two-phase sample containing sucrose in D_2O and menthol in $CDCl_3$ shown in Figure 8.6. Sum projections were collected from 3 to 5 planes of the ^{13}C-dimension (F_1) to include the region of highest intensity for each peak. a) Menthol peak at $\delta(^{13}C) = 25.8$ ppm. b) Menthol peak at $\delta(^{13}C) = 34.7$ ppm. c) Sucrose peak at $\delta(^{13}C) = 69.2$ ppm. d) Overlapping menthol and sucrose peaks at $\delta(^{13}C) = 71.3$ ppm.

8.4 CLIP-HSQC-Imaging

The 3D sequences can also be used to facilitate RDC measurements. The ^{2}H imaging presented in this chapter provides information about the spatial homogeneity of the alignment. This valuable information can be used to determine the equilibration state of the sample. Some samples, however, fail to become completely homogenous. RDCs are usually measured by their total coupling $T = J + D$, to obtain the dipolar coupling constant, the J coupling constant has to be known. This value is not highly sensitive, but may vary in different solvents, and careless interpretation can introduce errors in subsequent evaluation of RDC data. Therefore sometimes, inhomogeneity is even desired, since it allows parallel measurement of the different cases, i. e.parallel extraction of RDCs at different alignment strength and in isotropic surroundings, in the same environment.

In general, one important method to measure RDCs between ^{1}H and ^{13}C is the CLIP-HSQC [212]. The CLIP-HSQC utilizes no heteronuclear decoupling during acquisition of the FID, so the total coupling $^1T_{CH}$ is visible on all peaks. Combining the CLIP-HSQC with the z profile imaging yields the 3D CLIP-HSQC-imaging sequence displayed in Figure 8.3c.

To demonstrate the visualizing power of the CLIP-HSQC-imaging, it was applied to a liquid crystal sample of polyphenylisocyanide. Polyisocyanides are optically active helical polymers based on monomers derived from L-Alanine or D-Alanine. Their helix sense can be controlled during polymerization, and they self-assemble into lyotropic cholesteric liquid crystals [213]. Svenja Wesp from the Group of Prof. Dr. Reggelin at TU Darmstadt succeeded in preparation of a sample of polyphenylisocyanide in $CDCl_3$ that features two homogeneous phases. The quadrupolar splitting of $CDCl_3$ was 374 Hz in the anisotropic mesophase and 2 Hz in the other phase, a value low enough in comparison to be considered isotropic for further evaluation. (−)-Isopinocampheol (IPC) was dissolved in the liquid crystal solution. The sample composition is visualized in Figure 8.8 from proton and deuterium imaging experiments, obtained via the sequence from Figure 8.3a.

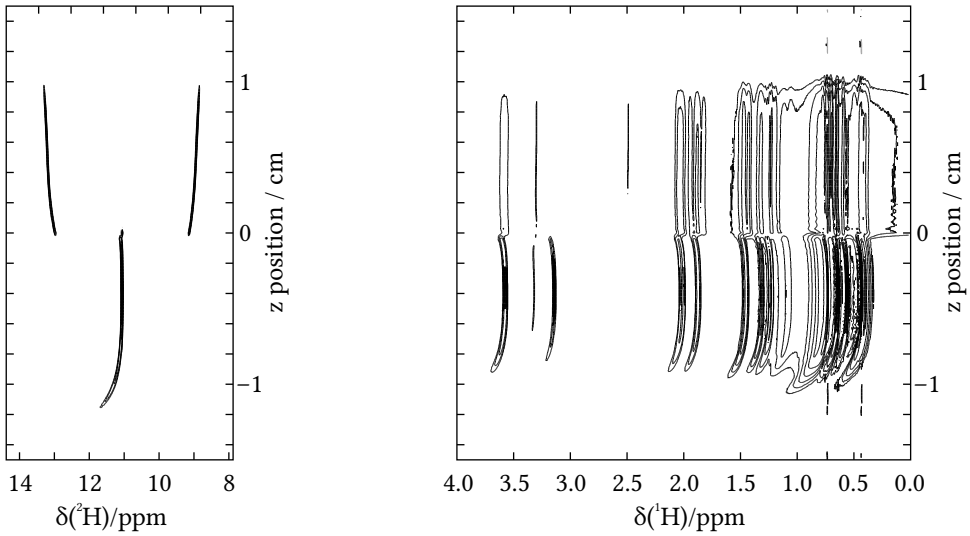

(a) ^{2}H z profile (b) ^{1}H z profile

Figure 8.8: 2D spectra obtained from the liquid crystal sample. Spatial resolution is achieved via phase encoding in the indirect dimension. a) ^{2}H profile of the liquid crystal sample. b) ^{1}H profile of the liquid crystal sample. The z direction shows the phase separation, two mostly homogeneous phases are present.

To extract RDC data from this sample, the 3D CLIP-HSQC-imaging sequence displayed in Figure 8.3c was utilized. Out of the 3D spectrum an HSQC spectrum can be created from projections of each plane of the z dimension. Adding several such projections of a homogeneous sample region yields high-resolution high-intensity HSQC spectra, of which the spectrum obtained from the anisotropic mesophase is shown in Figure 8.10a. Projections can also be calculated over different dimensions to reveal additional information. Figures 8.10b and 8.10c

show the z profile of individual ^{1}H-^{13}C signals. From this representation, the coupling constants can be derived at very high precision from both phases. If any residual inhomogeneity within a phase is present, the different scaling of J and dipolar coupling constant can even increase accuracy of the measurement.

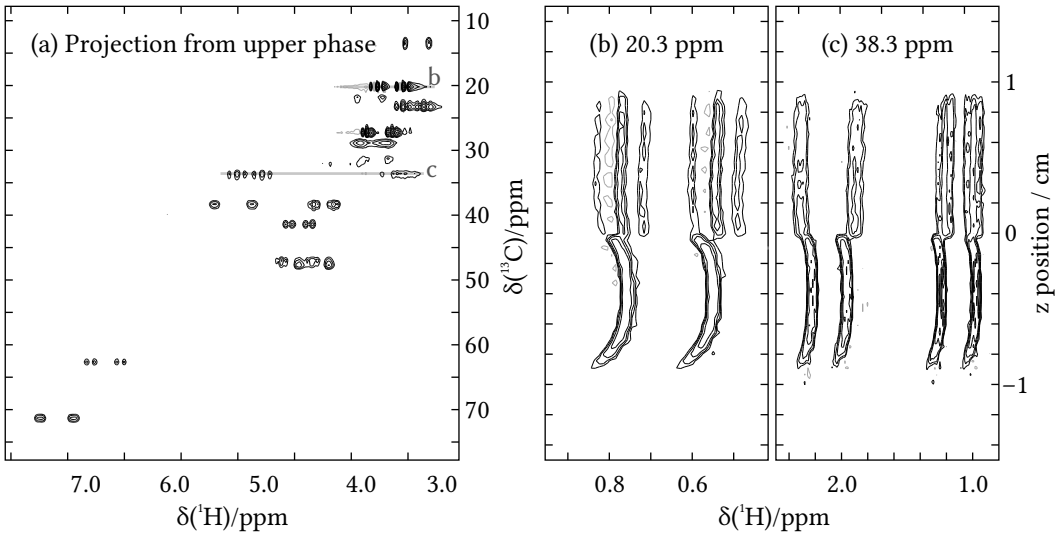

Figure 8.9: Sum projection from a 3D CLIP-HSQC-imaging spectrum and z profile of peaks at two ^{13}C frequencies from the same spectrum acquired on (−)-IPC in a liquid crystalline polyphenylisocyanide/$CDCl_3$ sample featuring an anisotropic and an isotropic phase. Spectrum of 8192×128 real HSQC points in combination with 64 points of phase encoding over a z range of 3 cm; acquired with 2 scans per increment and 16 dummy scans in 7 h 44 min. a) A separate HSQC spectrum can be extracted for the top and bottom part of the sample, the sum projection of the top part of a 3D HSQC-imaging spectrum was collected over the z range from 0.4 to 8.4 mm. The z profiles of peaks marked with letters b and c are shown on the right. b) Peak at $\delta(^{13}\mathrm{C}) = 20.3$ ppm. c) Peaks of the CH_2 group at $\delta(^{13}\mathrm{C}) = 38.3$ ppm.

8.5 Enantiomeric Differenciation at 1 T

8.5.1 Small Benchtop NMR Spectrometers

The ongoing miniaturization of NMR spectrometers and advances in magnet design have opened new venues for applications [214–216]. So-called medium-field benchtop NMR spectrometers utilize permanent magnets without the need of cryogenic cooling and feature low stray field. They typically operate at proton Larmor frequencies of 20 to 60 MHz and deliver sufficient homogeneity for spectroscopic application and will bring NMR spectroscopy directly into chemical laboratories. Immediate on the spot measurements of routine ^{1}H spectra for monitoring

syntheses become possible in research facilities as well as at production sites where desktop NMR spectroscopy will be a cost-effective, powerful tool for quality control and yield optimization. In this context, it is of great interest in how far challenging applications are accessible by medium-field, portable NMR spectrometers.

However, enantiomeric differentiation is still a challenging task, even on modern high-field NMR spectrometers. The differences between enantiomers are usually quite small, and it was not clear if the limitations in terms of resolution, sensitivity and technical issues like field stability allow such measurements at all.

In order to provide a proof of principle for enantiomeric distinction using medium-field NMR spectroscopy, we focused here on a general approach independent of the magnetic field strength and adapted it to the corresponding experimental setup on a medium-field 42.8 MHz Magritek/ACT prototype spectrometer [217]. Because the chemical shift resolution of the spectrometer is roughly one tenth of a ppm, differentiation based on chemical shift differences would only work in favorable cases with sufficient enantiomeric differentiation power so that we concentrated on differences in coupling constants, which do not depend on the strength of the magnetic field. Furthermore, as sensitivity and available probe heads on medium-field NMR spectrometers do not yet allow the measurement of either deuterium quadrupolar [218] or heteronuclear dipolar couplings [188], we focus on the distinction via homonuclear ^{1}H-^{1}H RDC [219, 220]. We have chosen the amino acid alanine as test molecule for which enantiomeric distinction has been extensively studied using high-field high-resolution NMR spectroscopy [184, 219, 221–223].

8.5.2 NMR Experiments

The simplest experiment, a 1D ^{1}H spectrum, is shown in Figure 8.11a in black for L-Alanine hosted in a 25 % gelatin gel. The spectrum of the unstretched state with a gelatin gel of length L_0 clearly shows the splittings as a result of $^{3}J_{\mathrm{HH}}$ couplings with the underlying coupling constant being measurable on both the H^{α} quartet as well as the $\mathrm{CH_3}$ doublet to be roughly 7 Hz. If the same sample is stretched to length L using a rubber-based stretching apparatus [221, 224, 225], the resulting total splitting changes because of the dipolar contribution to $^{3}T_{\mathrm{HH}} = {}^{3}J_{\mathrm{HH}} + {}^{3}D_{\mathrm{HH}}$. Also, the isochronous methyl protons split into a triplet of doublets because of the additional $^{2}J_{\mathrm{HH}}$ dipolar couplings [74]. The alignment strength is indicated by the strain or extension factor $\Xi = (L - L_0)/L_0$ [219], and the stronger the alignment, the larger the dipolar contribution to the multiplets. The multiplets obtained with increased alignment strength are visible in the gray spectra in Figure 8.11a.

Corresponding spectra for a 2 : 1 mixture of D-Alanine and L-Alanine in 25 % gelatin/$\mathrm{D_2O}$ are shown in Figure 8.11b. Again, the effect of RDCs is easily visible in the 1D spectra, and a closer

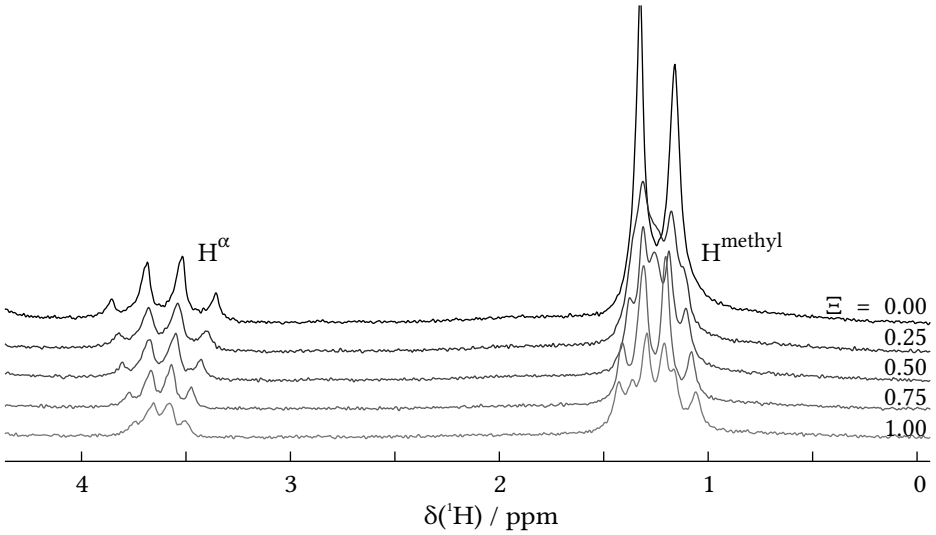

(a) L-Alanine sample

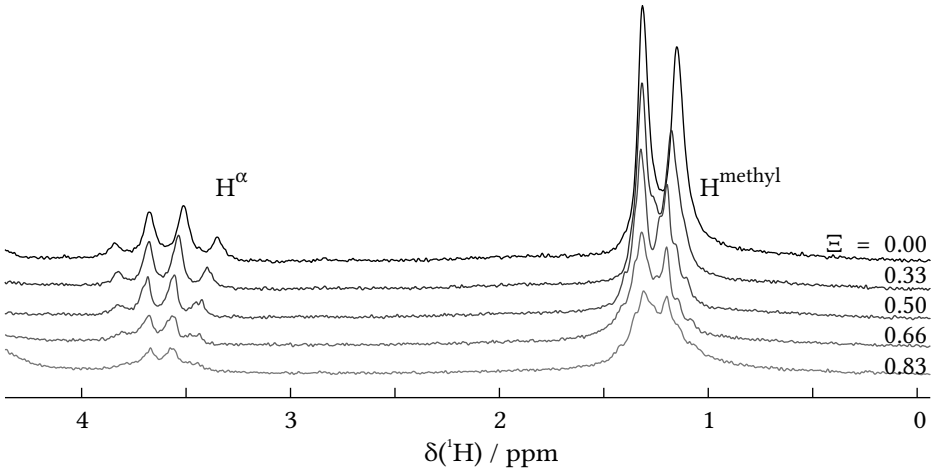

(b) D+L-Alanine sample

Figure 8.11: 1D ^{1}H spectra of a) 167 mM L-Alanine and b) a mixture of 111 mM D-Alanine and 56 mM L-Alanine each dispersed in 25 % gelatin/D_2O. Several spectra for the two samples with different degrees of stretching corresponding to extension factors Ξ are shown. The line width of the H^{methyl} peaks is approximately 4.5 Hz in the unstretched sample. With increasing alignment, multiplets change because of $^{2}D_{HH}$ and $^{3}D_{HH}$ residual dipolar couplings. Thirty-two scans were accumulated, acquiring 8192 points in 1.64 s each with a repetition time of 3 s.

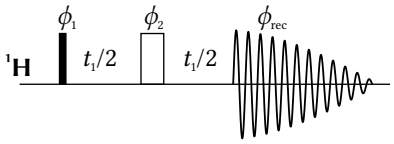

Figure 8.12: Pulse sequence of the 2D J-resolved experiment. The same experiment is included in the Bruker library as `jresqf`, pulse phases are $\phi_1 = 4(x), 4(y), 4(-x), 4(-y)$; $\phi_2 = y, x, y, -y, y, -y, -x, x, y, -y, -x, x, -x, x, -y, y$; $\phi_{rec} = x, x, -x, -x, y, y, -y, -y$. The 180° pulse in the middle of the t_1 delay ensures refocusing of B_1 inhomogenities in the indirect dimension, thus the F_1 linewidth can be reduced.

inspection reveals that the mixture results in multiplets that are different from the L-Alanine sample. A clear distinction of enantiomers as previously reported for similar samples [219], however, is not possible because of the limited resolution due to relatively broad lines. We therefore took the next step by implementing 2D J-resolved experiments [193, 194, 226, 227], which are well known to inherently compensate static magnetic field inhomogeneities in the indirectly acquired dimension by formation of Hahn echoes. The pulse sequence of a simple J-resolved experiment is displayed in Figure 8.12.

Indeed, corresponding spectra show significantly improved line widths in the J dimension of 1.8 Hz compared to approximately 4.5 Hz in the conventional 1D. Figure 8.13 shows the directly processed 2D spectra with the typical tilts of the multiplets together with the coupling contributions from the isotropic and partially aligned L-Alanine and D+L-Alanine samples. While especially the methyl group shows a well-recognizable multiplet structure for pure L-Alanine, the overlap of signals in the mixture leads to a complex pattern that is best addressed by modeling the spectra as shown in Figures 8.14 and 8.15. Multiplets were tilted and 1D slices along the J-dimension were extracted and compared with multiplets simulated using self-written Matlab code until satisfying agreement was achieved. For the L-Alanine sample, dipolar contributions of $^2D_{HH} = 5.65$ Hz and $^3D_{HH} = 3.05$ Hz could be identified, and for the enantiomeric mixture, corresponding couplings are $^2D_{HH} = 2.55$ Hz and $^3D_{HH} = 2.00$ Hz for D-Alanine and $^2D_{HH} = 7.35$ Hz and $^3D_{HH} = 3.97$ Hz for L-Alanine. All peaks but the outermost peaks of L-Alanine and the central peak of the D-Alanine multiplet consist of contributions from both molecules at the same ratio. This unfortunate combination of dipolar couplings leaves only three peaks for measuring the relative ratio D-Alanine versus L-Alanine. Using the intensities of the sum projection from Figure 8.15, the ratio can be estimated to 1.9, corresponding to an enantiomeric excess of 0.31, which is very close to the weighed-in ratio of 2.0 with $ee = 0.33$. Comparison of the multiplet intensity to a simple $1:3:6:4:6:3:1$ multiplet indicates an estimated maximum error of 15 % in the measurement of the enantiomeric ratio.

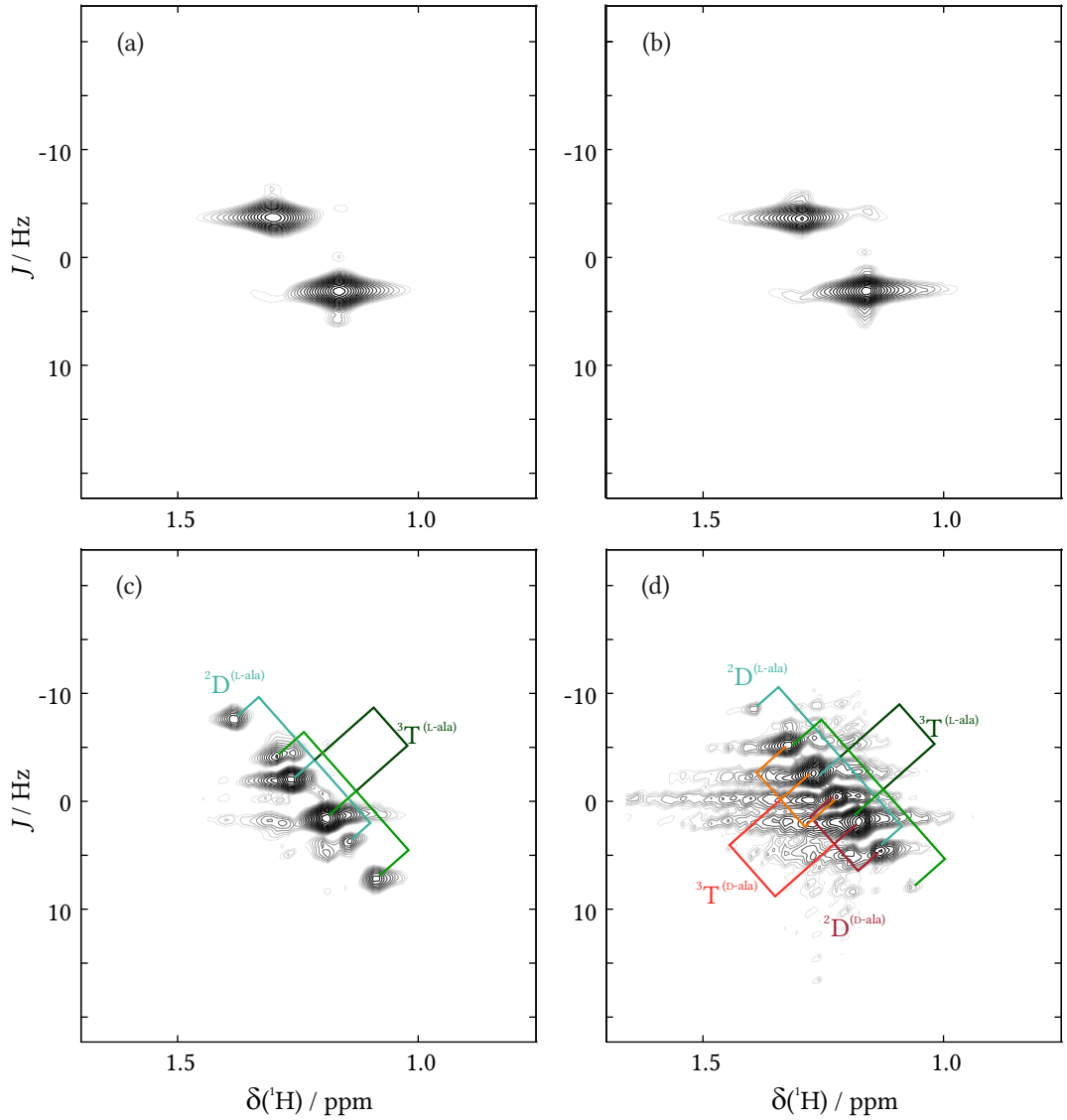

Figure 8.13: J-resolved spectra of the methyl groups of a,c) L-Alanine and b,d) D+L-Alanine (2 : 1) in gelatin/D_2O measured using a,b) the unstretched, isotropic samples with $\Xi = 0$ and c,d) the stretched samples with $\Xi \approx 1$. The splittings caused by the different couplings are identified. 4096×48 data points were recorded in 1 h 59 min with 819.2 ms acquisition time and eight scans per increment. The spectral width in the indirect dimension was 50 Hz. Individual scans were aligned, using the highest peak of the spectrum as a reference, to compensate for remaining B_0 instability. Spectra were tilted by 45° using standard procedures for J-resolved spectroscopy, to preserve information, no symmetrization was performed.

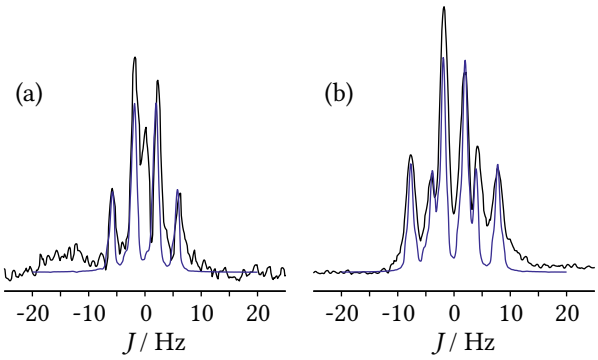

Figure 8.14: Sum projection of a) H^{α} and b) H^{methyl} multiplets of stretched L-Alanine with $\Xi \approx 1$ from 2D J-resolved spectra (black), overlaid with the simulated multiplet of L-Alanine in blue. The spectrum was integrated over a range of 5.5 Hz in the directly detected direction symmetrically around the center of the peak. The line intensities of the H^{methyl} multiplet roughly follow the expected $1:1:2:2:1:1$ multiplet of the weak coupling limit, slightly distorted by second-order artifacts. Simulations were performed using MATLAB R2012b and self-written code. The full homonuclear secular Hamiltonians for chemical shift, J coupling and D coupling was included.

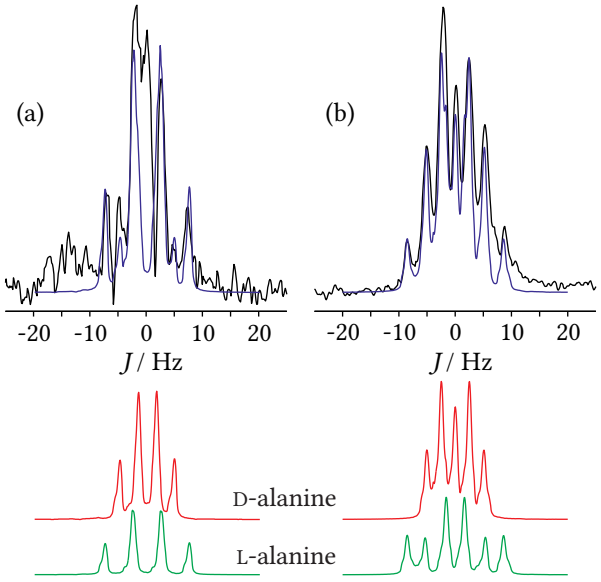

Figure 8.15: Sum projection of a) H^{α} and b) H^{methyl} multiplets of the stretched mixture sample of D+L-Alanine with $\Xi \approx 1$ from 2D J-resolved spectra (black), overlaid with the simulated peaks in blue. The spectrum was integrated over a range of 5.5 Hz in the directly detected direction symmetrically around the center of the peak. The individual multiplets of D-Alanine (red,top) and L-Alanine (green,bottom) that constitute the spectrum are displayed below. The D-Alanine H^{methyl} multiplet intensities (b, top) approach the ratio $1:2:(1:1):2:1$. From the intensities of the outer and central peaks, the fraction of D-Alanine can be estimated to be 1.9 while comparison of all peaks to a simplified $1:3:6:4:6:3:1$ multiplet model indicates an error of approximately 15 %. Simulations were performed using MATLAB R2012b and self-written code. The full homonuclear secular Hamiltonians for chemical shift, J coupling and D coupling was included.

8.6 Conclusion

For the successful measurement of anisotropic NMR parameters it is very important to ensure homogeneity of the sample. Conventionally, a simple 1D ^{2}H NMR spectrum is collected and if a clean and symmetric ^{2}H quadrupolar splitting is observed the sample is considered to be ready to use. In cases where the deuterium spectrum is not clean and symmetric, ^{2}H imaging of partially aligned samples is an effective tool for visualizing the homogeneity with respect to both magnetic field and alignment strength, and magnetic field inhomogeneity can easily be distinguished from inhomogeneity of the alignment strength. ^{2}H imaging, therefore, allows an unbiased evaluation of the quality of a given sample with respect to NMR measurements. With the distribution of alignment strength in hand, the explanation of frequently observed differential linewidths is straightforward.

The ^{2}H imaging can, in principle, be applied to any alignment medium and any quadrupolar nucleus. However, certain considerations should be taken into account. One of the most sensitive solvents with respect to quadrupolar interactions is $CDCl_3$ since it is an asymmetric molecule with a strong electric field gradient tensor. Other solvents like acetone-d_6 and DMSO-d_6 have been shown to be very poor for probing the degree of anisotropy based on $\Delta\nu_Q$ splittings. Although alignment media with the latter solvents can be used for ^{2}H imaging, resulting spectra will not be very indicative for inhomogeneity, and in such cases it might be a good idea to add $CDCl_3$ to the desired solvent and check its quadrupolar splitting. When using quadrupolar nuclei other than deuterium one should be aware that effective quadrupolar relaxation processes might prevent the successful detection of corresponding spectra. The acquisition of ^{23}Na spectra [221] and ^{7}Li 1D spectra [228] has been shown already, and corresponding imaging experiments should be easily applicable.

The extension of imaging experiments to ^{1}H detection shifts the scope from physical sample characterization towards detection of spatially dispersed chemical information. The inclusion of the ^{13}C chemical shift by the HSQC element provides excellent spectral separation of individual peaks. In combination, the 3D HSQC and 3D CLIP-HSQC experiments allow a variety of new ways to obtain information from samples with intentional and unintentional inhomogeneities. The imaging methods can even provide additional information from sample inhomogeneity, when each slice of the sample is evaluated individually. The different scaling of J and dipolar coupling constant can increase accuracy of the RDC measurement, or, as shown in the two-phase liquid crystalline sample, two completely different orientations can be measured in parallel in the same environment.

Apart from high-field high-resolution NMR, RDCs are becoming more and more accessible by benchtop spectrometers. The experimental results show that the distinction of enantiomers is

readily possible using low-field 43 MHz ^{1}H NMR spectroscopy and partial alignment in a chiral alignment medium. In contrast to chemical shift differences, for which resolution is limited by the homogeneity of the static magnetic field, differences in coupling constants are directly measured using *J*-resolved spectroscopy with a resolution that only depends on natural line width and overall spectrometer stability. Especially the latter aspect has been a serious issue with benchtop medium-field spectrometers so far, but spectrometer design during the last years improved considerably, and state-of-the-art spectrometers available today appear to fulfill the requirements for the acquisition of well-resolved 2D *J* spectra. As long as spin systems are fairly small, as in the case of alanine, the reduction of peak intensity as a result of the multiplet splitting can be tolerated. For larger spin systems, this decrease in intensity might become an issue using a simple, non-selective *J*-resolved pulse sequence, but a number of more sophisticated, selective experiments exist that have been designed to eliminate most homonuclear couplings [208, 220].

The distinction of enantiomers could be further enhanced by the applicability of heteronuclear experiments like BIRD-decoupled variants of an HSQC [221] or the direct acquisition of deuterium spectra [229]. The required ^{13}C, ^{19}F or ^{31}P coils are already available in first low-field spectrometers. Together with imaging-capable pulsed magnetic field gradient systems the foreseeable applications are manifold [194, 214, 216].

In the near future, medium-field NMR spectroscopy is expected to benefit from the use of advanced techniques for sensitivity enhancement such as the combination with hyperpolarization techniques [230]. Schemes like para-hydrogen NMR [231] that transfer spin order with chemical selectivity are of particular interest because they boost sensitivity and simplify the spectra at the same time.

Chapter 9

Summary

In the work at hand, pulse shape optimization and experiment development backed by new theoretical models were used to find novel methods for modern NMR spectroscopy. The results comprise a variety of different areas in magnetic resonance, from the study of principal physical limits towards imaging correlation with sample anisotropies, medium-field NMR, fast experiments for everyday applications, and the development of a detailed theory regarding their signal intensities.

The pulse shape optimization using optimal control theory (OCT) carried out in this work yielded three groups of versatile new pulse shapes. In a first study, the physical limits of broadband excitation and inversion pulses with restricted RF energy have been investigated in detail and an analytical formula for their performance bounds has been attempted. The results might guide future development of corresponding pulse shapes, which will become increasingly important for ^{1}H spectrometer frequencies beyond 1 GHz. The RADFA pulses with their adjustable effective flip angle, and the linear-phase RADFA pulses with greatly improved performance but limited field of application, are the second group of specialized pulse shapes. They are ready to replace rectangular pulses to enable broadband experiments, whenever scaling of RF amplitudes is necessary, like for example in widely used Ernst angle-type experiments. The research on pulses with maximum achievable quadratic phase dispersion during a pulse shape, the third group of pulse shapes, simultaneously provided the required knowledge and the pulse shapes to implement effective short z filter elements and the CLIP-COSY experiment.

The CLIP-COSY, as a novel, fast, and phase-sensitive COSY experiment has been developed, which has the potential to significantly speed up applications in routine NMR and the field of NMR metabolomics. It provides the same structural information about molecular connectivity as a conventional COSY, but the less complex line shape of the CLIP-COSY simplifies the cross peaks in spectra and experimental setup and processing is simplified simultaneously. Most importantly, spectra of high quality can be acquired with significantly reduced experiment duration – combined with non-uniform sampling, highly resolved CLIP-COSY spectra can be acquired in about three minutes. The pulse sequence of the CLIP-COSY also serves as basis for extended sequences. The CLIP-relayed-COSY experiment is highly useful in signal assignment.

It is especially helpful for signal assignment of crowded spectral regions, where the cross peaks of normal COSY-type spectra overlap with diagonal signals, and no molecular connectivity can be inferred. By reaching beyond these crowded regions, spectra of larger spin systems can be assigned with ease. Together with a possible but hitherto unpublished HSQC-CLIP-COSY, a set of experiments that are especially suited for the identification and assignment of sequences of coupled atoms, could be completed. The CLIP-relayed-COSY sequence can also be set up to include a high number of spins, approximating so-called planar mixing (PM) conditions. The resulting spectra are similar to spectra obtained using the well-known TOCSY experiment. The presented PM-TOCSY experiment, however, can create cross peaks over huge frequency distances, much larger than conventional TOCSY experiments using the DIPSI-2 or the FLOPSY sequence. It allows the acquisition of full spectral width ^{13}C or ^{19}F PM-TOCSY spectra, but might also be used with shaped pulses compensated for high RF field deviations encountered in toroidal cavity probes.

Two improved versions of the ASAP-HSQC, a symmetric and an antisymmetric one with a minimum number of pulses on the heteronucleus channel, have been developed and characterized in detail. The new sequences provide increased spectral quality, and can be adapted for different situations to reduce the effects of diffusion or provide increased artifact suppression. They can also be modified to create experiments like the ^{1}H,^{13}C-multiplicity-edited ASAP-HSQC, an experiment that allows the determination of the number of ^{1}H attached to a ^{13}C and greatly simplifies the assignment of signals from CH_2 groups. The reduced experiment duration will allow routine NMR laboratories to acquire an ASAP-HSQC and a multiplicity-edited ASAP-HSQC spectrum in far less than the time a single conventional HSQC requires. Adding this to the time saved by recording CLIP-COSY instead of conventional COSY spectra, the standard set of routine experiments could be expanded to include additional 2D experiments, that had to be excluded due to limited measurement time. The ASAP-HSQC may, in principle, be combined with other experiments, like the DOSY, to obtain an ASAP-HSQC-DOSY for highly resolved diffusion measurements. The 3D HSQC-imaging experiments would also benefit from the reduced experiment duration provided by a conceivable ASAP-HSQC-imaging experiment.

The expected signal intensity of ASAP and related experiments has not been possible to describe adequately with existing tools. Therefore, two models for the relevant types of experiments were derived and confirmed. Especially the model for the ASAP scheme and relaxation behavior is highly relevant in the current rush for shorter experiments. It shows good agreement with experimental data, and allows optimizing experimental parameters for ASAP-HSQC or ALSOFAST-HSQC from a few characteristic molecular parameters. Together with the novel ASAP-HSQC sequences, well-rounded progress could be achieved.

In the final chapter of the thesis, RDC relate experiments are presented. Using imaging techniques in combination with deuterium quadrupolar splitting, an experiment was developed, that allows thorough characterization of alignment within liquid crystalline and stretched polymer samples. While imaging methods have long been available, the new method probes the local anisotropy of the alignment medium, which is of vital importance for all RDC measurements. In several laboratories world wide this method is now used routinely to characterize every partially aligned sample for RDC-based structure determination.

When examined at the microscopic level, alignment inhomogeneities are created from contributions of locally homogeneous regions. When the spatial distribution of local alignment strengths in a partially aligned sample is revealed by ^{2}H quadrupolar imaging, the regions can be evaluated individually with high precision. It is therefore possible, to apply the imaging experiment to ^{1}H nuclei and shift the focus from sample characterization to RDC determination. For this purpose, the 3D HSQC-imaging and 3D CLIP-HSQC-imaging sequences were developed. The spectra obtained with these experiments allow selective evaluation from arbitrary layers of the sample, in which the effect of inhomogeneous alignment and magnetic field inhomogeneity, i. e. imperfect shim, is reduced. Spectra obtained from these smaller volumes, therefore can have significantly improved resolution. For the evaluation of the RDC data, it has to be combined with isotropic coupling constants. Consequently, usually two measurements on two separate samples are required. If these measurements are performed under different conditions, the two datasets may correspond to different conformations, introducing a systematic error. Applying the 3D CLIP-HSQC-imaging experiment to a sample containing an aligned and an isotropic phase, all couplings can be obtained simultaneously and under equal conditions. This will increase the accuracy that can be reached using RDC-based structure determination.

A striking development that opens up many new fields of NMR applications, are novel benchtop NMR spectrometers operating with medium-field permanent magnets. They might soon be available in every chemistry laboratory. Here we provided the first distinction of enantiomers on a benchtop NMR spectrometer using ^{1}H,^{1}H-RDCs. As more and more hardware features become available, permanent-magnet spectrometers will soon catch up with high-field spectrometers in many aspects except for the main magnetic field strength, and many applications of RDC measurements will follow this early example.

Zusammenfassung

In der vorliegenden Arbeit wurden Pulsoptimierungen und Experimentenentwicklung, gestützt durch neue theoretische Überlegungen, eingesetzt um der modernen NMR-Spektroskopie neue Methoden zur Verfügung zu stellen. Die Ergebnisse beziehen sich auf viele verschiedene Bereiche der NMR-Methode. Sie reichen von Untersuchungen der grundlegenden physikalischen Zusammenhänge über ortsaufgelöste Anisotropiemessungen und Nieder- oder Mittelfeld-NMR, bis hin zu schnellen Experimenten für Routine-NMR-Anwendungen und die Entwicklung einer detaillierten Theorie über die damit erreichbaren Signalintensitäten.

Die im Rahmen dieser Arbeit mittels optimaler Steruerungstheorie (OCT) durchgeführten Pulsoptimierungen lieferten drei Gruppen neuer Pulse. In einer erste Optimierungsreihe wurden die die physikalischen Grenzen von Breitbandinversions- und Breitbandanregungspulsen mit limitierter RF-Energie untersucht und analytische Formeln über die maximal erreichbare Pulsqualität konnten aufgestellt werden. Die Resultate könnten als Richtlinie für zukünftige Entwicklungen solcher Pulse dienen, die für Spektrometerfrequenzen jenseits von 1 GHz zunehmend wichtiger werden. Die RADFA Pulse bieten einen variabel einstellbaren Anregungswinkel und können viele Experimenten, die solche variable Anregungswinkel voraussetzen, zu Breitbandexperimenten machen. Die RADFA-Pulse mit linearer Phasenentwicklung bieten noch deutlich höhere Pulsqualität sind aber nicht ganz so flexibel einsetzbar. Aus den Untersuchungen von Pulsen mit maximaler Phasenverteilung, der dritten Gruppe neuer Pulsformen, konnte sogar gleichzeitig das entscheidende Wissen und die nötigen Pulse gewonnen werden, effiziente z-Filter-Elemente und das CLIP-COSY-Experiment zu realisieren.

Mit dem CLIP-COSY wurde, ein neuartiges, schnelles, phasensenempfindliches COSY-artiges Experiment entwickelt. Es hat das Potential, Messungen in der Routine-NMR, aber auch in NMR-Metabolomics-Studien enorm zu beschleunigen oder qualitativ zu erweitern. Es liefert die gleichen Strukturinformationen wie das konventionelle COSY, mit denen benachbarte Protonen im Spektrum gefunden werden können. Die Form der Signale ist aber wesentlich unkomplizierter, und erleichtert die experimentelle Feineinstellung und Auswertung. Der größte Vorteil ist die stark reduzierte minimale Experimentdauer gegenüber dem DQF-COSY – in Kombination mit unregelmäßigem Abtasten (NUS) kann ein hochaufgelöstes CLIP-COSY-Spektrum bereits in etwa drei Minuten aufgenommen werden. Die Pulssequenz des CLIP-COSY dient auch als

Grundlage für erweiterte Sequenzen. In spektralen Bereichen mit vielen Signalen, überlappen oft die Diagonal- und Kreuzsignale einfacher COSY-Experimente, und die Zuordnung ist unterbrochen. Das CLIP-relayed-COSY-Experiment ist dann sehr nützlich zur Signalzuordnung, da es die Identifizierung von Positionen über die überlappenden Bereiche hinaus ermöglicht. Größere Spinsysteme können, von einem bekannten Signal ausgehend, Schritt für Schritt zugeordnet werden. Zusammen mit einem noch fertigzustellenden HSQC-CLIP-COSY könnte eine Sammlung von Experimenten zur sequenziellen Zuordnung benachbarter Atome vervollständigt werden. Das CLIP-relayed-COSY-Experiment kann auch für maximale Reichweite eingestellt werden, um möglichst viele Spins in einem Experiment zu korrelieren. Dabei werden näherungsweise die Bedingungen des planaren Mischens (PM) erzeugt, eine Technik die mit dem TOCSY-Experiment verwandt ist. Die Spektren eines PM-TOCSY-Experiments ähneln daher auch gewöhnlichen TOCSY-Spektren. Im Gegensatz zum TOCSY, kann das PM-TOCSY aber sehr leicht durch geformte Pulse erweitert werden und mit Breitbandpulsen können Kopplungen über immense Frequenzabstände hinweg nachgewiesen werden. Die Bandbreite übersteigt die der verbreiteten DIPSI-2- oder FLOPSY-Sequenzen bei weitem. Es können beispielsweise ^{13}C- oder ^{19}F-PM-TOCSY-Spektren über quasi die volle chemische Verschiebungsbandbreite aufgenommen werden. Mit Pulsen, die für die großen RF-Feldabweichungen solcher Systeme optimiert sind, könnte das Experiment auch an toroidalen Hohlraumresonatoren mit extremer B_1-Inhomogenität durchgeführt werden und damit ganz neue Anwendungsbereiche erschließen.

Zwei verbesserte Versionen des ASAP-HSQC, eine symmetrische und eine asymmetrische mit besonders wenig Pulsen auf dem Heterokernkanal, wurden entwickelt und im Detail untersucht. Die neuen Sequenzen erhöhen die Spektrenqualität und können je nach Situation angepasst werden, um etwa Verluste durch Relaxation klein zu halten oder Artefakte möglichst gut zu unterdrücken. Sie können auch zu anderern Experimenten erweitert werden, etwa zum ^{1}H,X-multiplizitätseditierten ASAP-HSQC. Dieses Experiment ermöglicht die Bestimmung der Anzahl von ^{1}H, die an ein ^{13}C gebunden sind und macht es sehr leicht, CH_2-Gruppen im Spektrum zu finden. Die reduzierte Messzeit macht es möglich, im Service-NMR-Bereich ein ASAP-HSQC und ein multiplizitätseditiertes ASAP-HSQC in weniger als der Zeit eines konventionellen HSQC aufzunehmen. Zusammen mit der Zeitersparnis durch das CLIP-COSY, könnte der Standardsatz von Experimenten um ein oder mehrere beliebige 2D-Experimente, die sonst aus Zeitgründen nicht durchgeführt werden können, erweitert werden. Es sollte auch möglich sein, das ASAP-HSQC mit anderern Experimenten zu verbinden, etwa mit dem DOSY-Experiment, um ein 3D-ASAP-HSQC-DOSY für hochaufgelöste Diffusionsmessungen zu erhalten. Die ortsaufgelösten 3D-HSQC-Experimente wären nach der Beschleunigung durch die ASAP-Methode deutlich attraktiver.

Die zu erwartende Signalintensität von ASAP- und ähnlichen Experimenten konnte mit verfügbaren Mitteln noch nicht beschrieben werden. Daher wurden zwei mathematische Modelle für die relevanten Experimente aufgestellt und bestätigt. Vor allem das Modell für ASAP-Experimente und ihre Relaxationseigenschaften ist bei der aktuellen Entwicklung kürzerer Experimente hochrelevant. Es zeigt gute Übereinstimmung mit experimentellen Daten und erlaubt die Bestimmung optimaler Einstellungen für das Experiment für das ASAP- oder ALSOFAST-HSQC aus wenigen charakteristischen Moleküleigenschaften. Zusammen mit den neuen ASAP-HSQC-Sequenzen konnte ein Fortschritt auf ganzer Linie erzielt werden.

Im letzten Kapitel der Arbeit wurden Experimente mit zu dipolaren Restkopplungen (RDCs) vorgestellt. Aus bildgebende Verfahren in Kombination mit der quadrupolaren Aufspaltung von Deuteriumkernen wurde ein Experiment entwickelt, das es ermöglicht, die Orientierungsbedingungen von Flüssigkristallproben und gestreckten Polymergelproben exakt zu bestimmen. Es ist nun möglich, inhomogene Anisotropie, eine sehr wichtige Probeneigenschaft für RDC-Messungen, ortsaufgelöst zu untersuchen. In vielen NMR-Einrichtungen auf der ganzen Welt wird diese Methode mittlerweile an jeder partiell orientierten Probe durchgeführt, die in der RDC-Strukturaufklärung verwendet werden soll.

Auf mikroskopischer Ebene entsteht inhomogene Orientierung aus dem Beitrag vieler in sich homogener Regionen. Wenn diese räumliche Verteilung der unterschiedlichen Orientierungen bekannt ist, können die einzelnen Regionen individuell mit hoher Genauigkeit ausgewertet werden. Es ist deshalb möglich, die ortaufgelösten Messungen mit ^{1}H als detektiertem Kern durchzuführen und so den Fokus von der Probencharakterisierung zu RDC-Messungen zu verschieben. Hierfür wurden die ortsaufgelösten 3D-HSQC- und 3D-CLIP-HSQC-Experimente entwickelt. Aus den Spektren dieser Experimente können einzelne Schichten der Probe gezielt ausgewertet werden. Der Effekt inhomogener Orientierung aber auch Magnetfeldinhomogenität, d. h. suboptimale Shimeinstellungen, ist in einzelnen Schichten reduziert. Spektren, die daraus extrahiert werden, können deshalb deutlich besser aufgelöst sein, als Spektren der gesamten Probe. Für die Auswertung von RDC-Daten sind auch Kopplungskonstanten aus isotroper Umgebung durchzuführen. Mit dem 3D-CLIP-HSQC-Experiment und einer zweiphasigen Probe mit einer isotropen und einer anisotropen Phase, können alle Kopplungen gleichzeitig unter identischen Bedingungen gemessen werden. Die erreichbare Genauigkeit der auf RDCs basierenden Strukturbestimmung kann dadurch erhöht werden.

Neuartige Tischspektrometer, die mit Permanentmagneten Feldstärken von ein bis zwei Tesla erreichen, sind eine spannende aktuelle Entwicklung, mit der die NMR-Spektroskopie in viele neue Anwendungsbereiche vordringen kann. Diese Geräte könnten bald in jedem größeren Labor direkt vorhanden sein. Im Rahmen dieser Arbeit wurde die erste Enantiomerenunterscheidung in einem solchen Tischspektrometer mithilfe von RDCs durchgeführt und

vorgestellt. Es ist zu erwarten, dass für Permanentmagnetspektrometer schnell viele Errungenschaften von Hochfeldspektrometern nachgeholt werden, und diesem ersten Beispiel viele weitere RDC-Anwendungen folgen.

Danksagung

Ich danke Burkhard erneut für die Aufnahme in den Arbeitskreis, die Einführung in die NMR-Theorie, die unzähligen Ideen und Gespräche, und für die Möglichkeit, diese Arbeit in seiner Arbeitsgruppe durchzuführen.

Ich danke meinen Bürokollegen aus den verschiedenen Büros für die angenehme Arbeitsatmosphäre, die gute Zusammenarbeit, und die Hilfs- aber auch Diskussionsbereitschaft. Vor allem Johanna und David, mit denen ich die längste Zeit, die schönste Musik und den besten Kaffee genießen konnte. Mein Dank gilt natürlich dem ganzen AK-Bulu. Ihr seid der beste Lieblingsarbeitskreis. Ich danke den coolen Leuten bei BIF-Paff-POF, (Ihr wisst, wenn Ihr gemeint seid.) Daniel gebührt darüberhinaus Dank für das LaTeX-Rumgenerde. Ich danke meinen Eltern von ganzem Herzen: Seht, was Ihr mir ermöglicht habt; was Ihr aus mir gemacht habt.

Ella, Dir danke ich besonders; für die Unterstützung, den Zuspruch, das Vertrauen und die Liebe. Danke, dass Du mir immer zugehört hast, wenn ich erzählt habe.

Diese Arbeit wäre nicht möglich gewesen ohne den Kontakt zu vielen lieben Menschen, von denen hier nicht alle aufgeführt sind, die mich innerhalb aber vor allem auch außerhalb der Universität begleitet und geprägt haben. Ich danke Euch; die Zeit wäre ohne Euch wesentlich weniger angenehm gewesen.

Appendix

List of Figures

CLIP-COSY Pulse Programs

CLIP-COSY

```
;CLIPCOSY
;avance-version (10/02/12)
;Clean In-phase COSY
;2D H-1/H-1 correlation using in-
    phase transfer
;phase sensitive using states
    processing
;using shaped pulses for z-filter
    blocks
;
;$CLASS=HighRes
;$DIM=2D
;$TYPE=
;$SUBTYPE=
;$COMMENT=

#include <Avance.incl>
#include <Grad.incl>
#include <Delay.incl>

"p2=p1*2"
"d4=1s/(cnst2*4)"
"d11=30m"
"in0=inf1"
"d0=in0/2-p1*4/3.1416"
"acqt0=-p1*2/3.1416"

1 ze
2 d11 pl1:f1
  d1

;begin experiment
  p1 ph1 UNBLKGRAD ;excitation,
     ph10 cycled for states
  d0

;first filter block
  p1 ph10
  4u gron1 pl0:f1
  (p23:sp23 ph8):f1
  4u groff
  d16 pl1:f1
  p1 ph2

;in-phase transfer block, planar
    mixing
  d4
  p2 ph20
  d4
  p1 ph20
  d4
  p2 ph3
  d4

;second filter block
  p1 ph21
  4u gron2 pl0:f1
  (p24:sp24 ph9):f1
  40u groff
  p16:gp3
  d16 pl1:f1 BLKGRAD
  p1 ph4 ;pulse cycled with ph31

  go=2 ph31
  d11 mc #0 to 2
     F1PH(calph(ph1, +90), caldel(
         d0, +in0))
exit

;excitation, states, TPPI
ph1 = 0 0 0 0 2 2 2 2 2 2 2 2 0 0
    0 0
ph10= 0
;shape pulse phase (z-filter)
ph8 = 0 1 0 1 1 0 1 0 3 2 3 2 2 3
    2 3
ph9 = 2 3 2 3 3 2 3 2 1 0 1 0 0 1
    0 1
;transfer block phases
ph2 = 0
ph20= 1 3 3 1
ph3 = 3 2 3 2; any phase
ph21= 0 0 2 2
;readout/receiver phase
ph4 = 0 ; any phase
ph31= 0 2 2 0 2 0 0 2 2 0 0 2 0 2
    2 0


#ifdef PCYCLE0
;excitation, states, TPPI
ph1 = 0
ph10= 0
```

```
;shape pulse phase (z-filter)
ph8 = 0
ph9 = 2
;transfer block phases
ph2 = 0
ph20= 1
ph3 = 3; any phase
ph21= 0
;readout/receiver phase
ph4 = 0 ; any phase
ph31= 0
#endif

#ifdef PCYCLE1
;excitation, states, TPPI
ph1 = 0
ph10= 0
;shape pulse phase (z-filter)
ph8 = 0 1 3 2
ph9 = 2 3 0 1
;transfer block phases
ph2 = 0
ph20= 1 3 3 1
ph3 = 3 2 3 2; any phase
ph21= 0 0 2 2
;readout/receiver phase
ph4 = 0 ; any phase
ph31=0 2 2 0
#endif

#ifdef PCYCLE2
;excitation, states, TPPI
ph1 = 0 2 2 0
ph10= 0
;shape pulse phase (z-filter)
ph8 = 0 1 3 2
ph9 = 2 3 0 1
;transfer block phases
ph2 = 0
ph20= 1
ph3 = 3; any phase
ph21= 0
;readout/receiver phase
ph4 = 0 ; any phase
ph31=0 2 2 0
#endif

#ifdef PCYCLE3
;excitation, states, TPPI
ph1 = 0
ph10= 0 2 2 0
;shape pulse phase (z-filter)
ph8 = 0 1 3 2
ph9 = 2 3 0 1
;transfer block phases
ph2 = 0
ph20= 1
ph3 = 3; any phase
ph21= 0 2 0 2
;readout/receiver phase
ph4 = 0 ; any phase
ph31= 0 0 2 2
#endif

#ifdef PCYCLE4
;excitation, states, TPPI
ph1 = 0
ph10= 0
;shape pulse phase (z-filter)
ph8 = 0 1 3 2
ph9 = 2 3 0 1
;transfer block phases
ph2 = 0
ph20= 1
ph3 = 3; any phase
ph21= 0
;readout/receiver phase
ph4 = 0 2 2 0 1 3 3 1; any phase
ph31= 0 2 2 0 1 3 3 1
#endif

#ifdef PCYCLE5
;excitation, states, TPPI
ph1 = 0 0 0 0 2 2 2 2
ph10= 0 0 0 0 0 0 0 0 2 2 2 2 2 2 2
    2 2
;shape pulse phase (z-filter)
ph8 = 0 1 3 2
ph9 = 2 3 0 1
;transfer block phases
ph2 = 0
ph20= 1 3 3 1
ph3 = 3 2 3 2; any phase
ph21= 0 0 2 2
;readout/receiver phase
ph4 = 0; any phase
ph31= 0 2 2 0 2 0 0 2 2 0 0 2 0 2
    2 0
```

```
#endif

#ifdef PCYCLE6
;excitation, states, TPPI
ph1 = 0 0 0 0 2 2 2 2
ph10= 0 0 0 0 0 0 0 0 2 2 2 2 2 2
    2 2
;shape pulse phase (z-filter)
ph8 = 0 1 3 2
ph9 = 2 3 0 1
;transfer block phases
ph2 = 0
ph20= 1 3 3 1
ph3 = 3 2 3 2; any phase
ph21= 0 0 2 2
;readout/receiver phase
ph4 = 0 0 0 0 1 1 1 1; any phase
ph31= 0 2 2 0 3 1 1 3 2 0 0 2 1 3
    3 1
#endif

#ifdef PCYCLE7
;excitation, states, TPPI
ph1 = 0 0 0 0 2 2 2 2 2 2 2 2 0 0
    0 0
ph10= 0
;shape pulse phase (z-filter)
ph8 = 0 1 0 1 1 0 1 0 3 2 3 2 2 3
    2 3
ph9 = 2 3 2 3 3 2 3 2 1 0 1 0 0 1
    0 1
;transfer block phases
ph2 = 0
ph20= 1 3 3 1
ph3 = 3 2 3 2; any phase
ph21= 0 0 2 2
;readout/receiver phase
ph4 = 0 ; any phase
ph31= 0 2 2 0 2 0 0 2 2 0 0 2 0 2
    2 0
#endif

;pl0 : 0W
;pl1 : power level for pulse (
    default)
;sp23: shaped dephasing pulse
;p1 : 90 degree high power pulse
;p2 : 180 degree high power pulse
;p23: 180 degree shaped pulse for
    dephasing
;p16: homospoil/gradient pulse
                                [1 msec
    ]

;p23: 1st inversion pulse for
    dephasing (z-filter)
;p24: 2nd inversion pulse for
    dephasing (z-filter)
;spnam23: 1st inversion pulse for
    dephasing (z-filter)
;spnam24: 2nd inversion pulse for
    dephasing (z-filter)
;sp23: Power level for dephasing
    pulse (z-filter)
;sp24: Power level for dephasing
    pulse (z-filter)

;d0 : incremented delay (2D)
                                    [3
    usec]
;d1 : relaxation delay; 1-5 * T1
;d4 : 1/(4J(HH))
;d11: delay for disk I/O

    [30 msec]
;d16: delay for homospoil/gradient
     recovery
;cnst2: > J(HH); 30 Hz
;inf1: 1/SW(X) = 2 * DW(X)
;in0: 1/(2 * SW(X)) = DW(X)
;nd0: 2
;NS: 2 * n
;DS: 16
;td1: number of experiments
;FnMODE: States-TPPI, TPPI, States
     or QSEQ

;for z-only gradients:
;gpz1: 7.2%
;gpz2: -7.5%
;gpz3: -17.9%

;use gradient files:
;gpnam3: SMSQ10.100

;Processing
```

```
;PHC0(F1): 0
;PHC1(F1): -180
;FCOR(F1): 1

;$Id: clipcosy,v 0.9 2015/07/20
    16:34:17 mk Exp $
```

CLIP-COSY with Shaped Pulses

```
;CLIPCOSYSP
;avance-version (10/02/12)
;Clean In-phase COSY
;2D H-1/H-1 correlation using in-
    phase transfer
;phase sensitive using states
    processing
;using shaped pulses for all
    pulses
;
;$CLASS=HighRes
;$DIM=2D
;$TYPE=
;$SUBTYPE=
;$COMMENT=

#include <Avance.incl>
#include <Grad.incl>
#include <Delay.incl>

"d4=1s/(cnst2*4)"
"d11=30m"
"in0=inf1"
"d0=in0/2"
"acqt0=0"

1 ze
2 d11
  d1 pl0:f1

;begin experiment
  (p13:sp13 ph1):f1 ;BEBOP
  d0 UNBLKGRAD

;first filter block
  (p13:sp16 ph10):f1  ;BEBOP
  4u
  4u gron1
  (p23:sp23 ph8):f1
  4u groff
  d16
  (p13:sp13 ph2):f1 ;BEBOP

;in-phase transfer block, planar
    mixing
  d4
  (p14:sp14 ph20):f1 ;UR180
  d4
  (p15:sp15 ph20):f1 ;UR90
  d4
  (p14:sp14 ph3):f1 ;UR180
  d4

;second filter block
  (p13:sp16 ph21):f1 ;tr BEBOP
  4u gron2
  (p24:sp24 ph9):f1
  40u groff
  p16:gp3 ;gradient to prevent
     complete refocusing
  d16
  1m BLKGRAD
  (p13:sp13 ph4):f1 ;BEBOP

;acquisition
  go=2 ph31
  d11 mc #0 to 2
     F1PH(calph(ph1, +90), caldel(
        d0, +in0))
exit


;excitation, states, TPPI
ph1 = 0 0 0 0 2 2 2 2 2 2 2 2 0 0
    0 0
ph10= 0
;shape pulse phase (z-filter)
ph8 = 0 1 0 1 1 0 1 0 3 2 3 2 2 3
    2 3
ph9 = 2 3 2 3 3 2 3 2 1 0 1 0 0 1
    0 1
;transfer block phases
ph2 = 0
ph20= 1 3 3 1
ph3 = 3 2 3 2; any phase
ph21= 0 0 2 2
;readout/receiver phase
ph4 = 0 ; any phase
```

```
ph31= 0 2 2 0 2 0 0 2 2 0 0 2 0 2
    2 0




;PHASEN WURDEN AN DIE OCT-
    PULSOPTIMIERUNG ANGEPASST!
;ph2 und 21 wurde um 1 verringert,
     um die effektive Drehachse
    beim BEBOP ;zu korrigieren (
    BEBOP z->x ph0 ist so ähnlich
    wie 90ŕy-Puls)

#ifdef PCYCLE0
;excitation, states, TPPI
ph1 = 0
ph10= 0
;shape pulse phase (z-filter)
ph8 = 0
ph9 = 2
;transfer block phases
ph2 = 0
ph20= 1
ph3 = 3; any phase
ph21= 0
;readout/receiver phase
ph4 = 0 ; any phase
ph31= 0
#endif

#ifdef PCYCLE1
;excitation, states, TPPI
ph1 = 0
ph10= 0
;shape pulse phase (z-filter)
ph8 = 0 1 3 2
ph9 = 2 3 0 1
;transfer block phases
ph2 = 0
ph20= 1 3 3 1
ph3 = 3 2 3 2; any phase
ph21= 0 0 2 2
;readout/receiver phase
ph4 = 0 ; any phase
ph31=0 2 2 0
#endif

#ifdef PCYCLE2
;excitation, states, TPPI
ph1 = 0 2 2 0
ph10= 0
;shape pulse phase (z-filter)
ph8 = 0 1 3 2
ph9 = 2 3 0 1
;transfer block phases
ph2 = 0
ph20= 1
ph3 = 3; any phase
ph21= 0
;readout/receiver phase
ph4 = 0 ; any phase
ph31=0 2 2 0
#endif

#ifdef PCYCLE3
;excitation, states, TPPI
ph1 = 0
ph10= 0 2 2 0
;shape pulse phase (z-filter)
ph8 = 0 1 3 2
ph9 = 2 3 0 1
;transfer block phases
ph2 = 0
ph20= 1
ph3 = 3; any phase
ph21= 0 2 0 2
;readout/receiver phase
ph4 = 0 ; any phase
ph31= 0 0 2 2
#endif

#ifdef PCYCLE4
;excitation, states, TPPI
ph1 = 0
ph10= 0
;shape pulse phase (z-filter)
ph8 = 0 1 3 2
ph9 = 2 3 0 1
;transfer block phases
ph2 = 0
ph20= 1
ph3 = 3; any phase
ph21= 0
;readout/receiver phase
ph4 = 0 2 2 0 1 3 3 1; any phase
ph31= 0 2 2 0 1 3 3 1
#endif
```

```
#ifdef PCYCLE5
;excitation, states, TPPI
ph1 = 0 0 0 0 2 2 2 2
ph10= 0 0 0 0 0 0 0 0 2 2 2 2 2 2
    2 2
;shape pulse phase (z-filter)
ph8 = 0 1 3 2
ph9 = 2 3 0 1
;transfer block phases
ph2 = 0
ph20= 1 3 3 1
ph3 = 3 2 3 2; any phase
ph21= 0 0 2 2
;readout/receiver phase
ph4 = 0; any phase
ph31= 0 2 2 0 2 0 0 2 2 0 0 2 0 2
    2 0
#endif

#ifdef PCYCLE6
;excitation, states, TPPI
ph1 = 0 0 0 0 2 2 2 2
ph10= 0 0 0 0 0 0 0 0 2 2 2 2 2 2
    2 2
;shape pulse phase (z-filter)
ph8 = 0 1 3 2
ph9 = 2 3 0 1
;transfer block phases
ph2 = 0
ph20= 1 3 3 1
ph3 = 3 2 3 2; any phase
ph21= 0 0 2 2
;readout/receiver phase
ph4 = 0 0 0 0 1 1 1 1; any phase
ph31= 0 2 2 0 3 1 1 3 2 0 0 2 1 3
    3 1
#endif

#ifdef PCYCLE7
;excitation, states, TPPI
ph1 = 0 0 0 0 2 2 2 2 2 2 2 2 0 0
    0 0
ph10= 0
;shape pulse phase (z-filter)
ph8 = 0 1 0 1 1 0 1 0 3 2 3 2 2 3
    2 3
ph9 = 2 3 2 3 3 2 3 2 1 0 1 0 0 1
    0 1
;transfer block phases
ph2 = 0
ph20= 1 3 3 1
ph3 = 3 2 3 2; any phase
ph21= 0 0 2 2
;readout/receiver phase
ph4 = 0 ; any phase
ph31= 0 2 2 0 2 0 0 2 2 0 0 2 0 2
    2 0
#endif

;pl0 : 0W
;pl1 : power level for pulse (
    default)
;p11: 190u
;p13: 550u
;p14: 200u
;p15: 200u
;p23: 1st inversion pulse for
    dephasing (z-filter)
;p24: 2nd inversion pulse for
    dephasing (z-filter)
;spnam11: xy-BEBOP_190u_RF10kHz...
;spnam12: xy-BEBOP_tr_190u_RF10kHz
    ...
;spnam13: jc08_BEBOP_z-y_550u_BW10
    ...
;spnam14: URx180_200_0.5u_BW10...
;spnam15: jc20_BURBOP_x90.0deg...
;spnam16: jc04_BEBOP_yz_550u...
;spnam23: 1st inversion pulse for
    dephasing (z-filter)
;spnam24: 2nd inversion pulse for
    dephasing (z-filter)
;sp11: 10 kHz: Power level for 25
    us 90ř pulse
;sp12: 10 kHz: Power level for 25
    us 90ř pulse
;sp13: 20 kHz: Power level for
    12.5us 90ř pulse
;sp14: 20 kHz: Power level for
    12.5us 90ř pulse
;sp15: 20 kHz: Power level for
    12.5us 90ř pulse
;sp16: 20 kHz: Power level for
    12.5us 90ř pulse
;sp23: Power level for dephasing
    pulse (z-filter)
```

```
;sp24: Power level for dephasing
    pulse (z-filter)

;p16: homospoil/gradient pulse
                              [1
    msec]
;d0 : incremented delay (2D)
                                 [3
    usec]
;d1 : relaxation delay; 1-5 * T1
;d4 : 1/(4J(HH))
;d11: delay for disk I/O

    [30 msec]
;d16: delay for homospoil/gradient
     recovery
;cnst2: > J(HH); 30 Hz
;inf1: 1/SW(X) = 2 * DW(X)
;in0: 1/(2 * SW(X)) = DW(X)
;nd0: 2
;NS: 2 * n
;DS: 16
;td1: number of experiments
;FnMODE: States-TPPI, TPPI, States
     or QSEQ

;for z-only gradients:
;gpz1: 7.2% z-filter gradient
;gpz2: -7.5% z-filter gradient
;gpz3: -17.9% purge gradient

;use gradient files:
;gpnam3: SMSQ10.100

;Processing

;PHC0(F1): 0
;PHC1(F1): -180
;FCOR(F1): 1

;$Id: clipcosysp,v 0.9 2015/07/20
    16:34:17 mk Exp $
```

CLIP-COSY for Water Supression/Proteins

```
;mk_cosyclip
;watergate 3-9-19
;2nd z-filter removed
;avance-version (10/02/12)
;CLIP COSY
;2D H-1/H-1 correlation using in-
    phase transfer
;phase sensitive using states
    procession
;using shaped pulses for z-filter
    blocks
;
;$CLASS=HighRes
;$DIM=2D
;$TYPE=
;$SUBTYPE=
;$COMMENT=


#include <Avance.incl>
#include <Grad.incl>
#include <Delay.incl>


"p2=p1*2"

"d11=30m"

"p2=p1*2"
"DELTA = 1m" ;delay after 3-9-19
"DELTA2 = ( 2* (2*(p16+d16)+p27
    *4.539+d19*10+p0*.231)  +DELTA
    *2)" ;length of 3-9-19
"d4=1s/(cnst2*4)-p17-d16"
"d2=1s/(cnst3*4)-p17-d16 - 0.5*
    DELTA2"

"d11=30m"
"in0=inf1"
"d0=in0/2-p1*4/3.1416"
"acqt0=-p1*2/3.1416"


1 ze
2 d1 pl1:f1
  d11 UNBLKGRAD
3 p1 ph1 ;excitation, ph10 cycled
    for states
  d0

  p1 ph10 ;first z-filter-block,
  d12 pl0:f1 gron1
```

```
  (p23:sp23 ph8):f1
  d17
  d16 pl1:f1 groff
  p1 ph2

;in-phase transfer block, planar
   mixing
p17:gp2
d16
  d4
  p2 ph20
  d4
p17:gp2
d16

  p1 ph20

p17:gp3
d16
  d2
  p2 ph3
  d2

  DELTA*0.25
  p17:gp3
  d16

; watergate

  p16:gp5
  d16 pl18:f1
  p27*0.231 ph4
  d19*2
  p27*0.692 ph4
  d19*2
  p27*1.462 ph4
  d19*2
  p27*1.462 ph5
  d19*2
  p27*0.692 ph5
  d19*2
  p27*0.231 ph5
  p16:gp5
  d16
DELTA*0.25
DELTA*0.25
  p16:gp6
  d16 pl18:f1
  p27*0.231 ph6
  d19*2
  p27*0.692 ph6
  d19*2
  p27*1.462 ph6
  d19*2
  p27*1.462 ph7
  d19*2
  p27*0.692 ph7
  d19*2
  p0*0.231 ph7
  p16:gp6
  d16

  DELTA*0.25 BLKGRAD


  go=2 ph31
  d1 mc #0 to 2
     F1PH(calph(ph1, +90), caldel(
        d0, +in0))
exit

;excitation, states, TPPI
ph1 = 0
ph10= 0
;shape pulse phase (z-filter)
ph8 = 0
;transfer block phases
ph2 = 0 0 0 0 2 2 2 2
ph20= 1
ph3 = 3 3 3 3 3 3 3 3  0 0 0 0 0 0 0
     0 0 1 1 1 1 1 1 1 1  2 2 2 2
    2 2 2 2; any phase

;watergate phase
ph4 = 0 0 1 1 2 2 3 3
ph5 = 2 2 3 3 0 0 1 1
ph6 = 0 2 1 3
ph7 = 2 0 3 1
;readout/receiver phase
ph31= 0 0 0 0 2 2 2 2  2 2 2 2  0
    0 0 0

; ph2: +-1 verdrehen?
; ph56/78 +-1 gegeneinandern?
; erst ph2 oder erst watergate
    cyclen?
; phasenänderungen zu _ws3 und
    _gron propagieren
```

```
#ifdef working
;excitation, states, TPPI
ph1 = 0
ph10= 0
;shape pulse phase (z-filter)
ph8 = 0
;transfer block phases
ph2 = 0 0 0 0 2 2 2 2
ph20= 1
ph3 = 3 3 3 3 3 3 3 3 0 0 0 0 0 0
   0 0 1 1 1 1 1 1 1 1 2 2 2 2 2 2
   2 2 2; any phase
;watergate phase
ph5 = 0 1 2 3
ph6 = 2 3 0 1
;readout/receiver phase
ph31= 0 2 0 2 2 0 2 0  2 0 2 0 0 2
    0 2
#endif


;pl0 : 0W
;pl1 : power level for pulse (
   default)
;pl18: f1 channel - power level
   for 3-9-19-pulse (watergate)
;sp23: shaped dephasing pulse
;p1 : 90 degree high power pulse
;p2 : 180 degree high power pulse
;p0 : f1 channel -  90 degree
   pulse at pl18
;                       use for
   fine adjustment
;p27: f1 channel -  90 degree
   pulse at pl18
;p23: 180 degree shaped pulse for
   dephasing
;p16: homospoil/gradient pulse
                              [1
   msec]
;d0 : incremented delay (2D)
                                 [3
   usec]
;d1 : relaxation delay; 1-5 * T1
;d2 : 1/(4J(HH))
;d11: delay for disk I/O

   [30 msec]
;d16: delay for homospoil/gradient
    recovery
;d19: delay for binomial water
   suppression
;     d19 = (1/(2*d)), d =
   distance of next null (in Hz)
;cnst2: > J(HH)
;inf1: 1/SW(X) = 2 * DW(X)
;in0: 1/(2 * SW(X)) = DW(X)
;nd0: 2
;NS: 2 * n
;DS: 16
;td1: number of experiments
;FnMODE: States

;for z-only gradients:
;gpz1: 10%
;gpz2: -10%
;gpz5: ~40%
;gpz6: ~40%

;use gradient files:
;gpnam3: SMSQ10.100
;gpnam4: SMSQ10.100
;gpnam5: SMSQ10.100


;$Id: mk_cosyclip,v 0.9 2012/07/25
    16:34:17 ber Exp $
```

CLIP-relay-COSY

```
;CLIPCOSY
;avance-version (10/02/12)
;Clean In-phase COSY
;2D H-1/H-1 correlation using in-
   phase transfer
;phase sensitive using states
   processing
;using shaped pulses for z-filter
   blocks
;
;$CLASS=HighRes
;$DIM=2D
;$TYPE=
;$SUBTYPE=
;$COMMENT=

#include <Avance.incl>
```

```
#include <Grad.incl>
#include <Delay.incl>

"p2=p1*2"
"d4=1s/(cnst2*4)"
"d11=30m"
"in0=inf1"
"d0=in0/2-p1*4/3.1416"
"acqt0=-p1*2/3.1416"

"l2=l1-1"
"d5=d4 * 4 * (l2 + 1)"

1 ze
2 d11 pl1:f1
  d1

;begin experiment
  p1 ph1 UNBLKGRAD ;excitation,
     ph10 cycled for states
  d0

;first filter block
  p1 ph10
  4u gron1 pl0:f1
  (p23:sp23 ph8):f1
  4u groff
  d16 pl1:f1
  p1 ph2

;in-phase transfer block, planar
    mixing
  d4
  p2 ph20
  d4
  p1 ph20

5 d4
  d4
  p2 ph20
  d4
  d4
  p1 ph20
lo to 5 times l2

  d4
  p2 ph3
  d4

;second filter block
  p1 ph21
  4u gron2 pl0:f1
  (p24:sp24 ph9):f1
  40u groff
  p16:gp3
  d16 pl1:f1 BLKGRAD
  p1 ph4 ;pulse cycled with ph31

  go=2 ph31
  d11 mc #0 to 2
     F1PH(calph(ph1, +90), caldel(
        d0, +in0))
exit

;excitation, states, TPPI
ph1 = 0 0 0 0 2 2 2 2 2 2 2 2 0 0
    0 0
ph10= 0
;shape pulse phase (z-filter)
ph8 = 0 1 0 1 1 0 1 0 3 2 3 2 2 3
    2 3
ph9 = 2 3 2 3 3 2 3 2 1 0 1 0 0 1
    0 1
;transfer block phases
ph2 = 0
ph20= 1 3 3 1
ph3 = 3 2 3 2; any phase
ph21= 0 0 2 2
;readout/receiver phase
ph4 = 0 ; any phase
ph31= 0 2 2 0 2 0 0 2 2 0 0 2 0 2
    2 0



#ifdef PCYCLE0
;excitation, states, TPPI
ph1 = 0
ph10= 0
;shape pulse phase (z-filter)
ph8 = 0
ph9 = 2
;transfer block phases
ph2 = 0
ph20= 1
ph3 = 3; any phase
ph21= 0
;readout/receiver phase
ph4 = 0 ; any phase
```

```
ph31= 0
#endif

#ifdef PCYCLE1
;excitation, states, TPPI
ph1 = 0
ph10= 0
;shape pulse phase (z-filter)
ph8 = 0 1 3 2
ph9 = 2 3 0 1
;transfer block phases
ph2 = 0
ph20= 1 3 3 1
ph3 = 3 2 3 2; any phase
ph21= 0 0 2 2
;readout/receiver phase
ph4 = 0 ; any phase
ph31=0 2 2 0
#endif

#ifdef PCYCLE2
;excitation, states, TPPI
ph1 = 0 2 2 0
ph10= 0
;shape pulse phase (z-filter)
ph8 = 0 1 3 2
ph9 = 2 3 0 1
;transfer block phases
ph2 = 0
ph20= 1
ph3 = 3; any phase
ph21= 0
;readout/receiver phase
ph4 = 0 ; any phase
ph31=0 2 2 0
#endif

#ifdef PCYCLE3
;excitation, states, TPPI
ph1 = 0
ph10= 0 2 2 0
;shape pulse phase (z-filter)
ph8 = 0 1 3 2
ph9 = 2 3 0 1
;transfer block phases
ph2 = 0
ph20= 1
ph3 = 3; any phase
ph21= 0 2 0 2
;readout/receiver phase
ph4 = 0 ; any phase
ph31= 0 0 2 2
#endif

#ifdef PCYCLE4
;excitation, states, TPPI
ph1 = 0
ph10= 0
;shape pulse phase (z-filter)
ph8 = 0 1 3 2
ph9 = 2 3 0 1
;transfer block phases
ph2 = 0
ph20= 1
ph3 = 3; any phase
ph21= 0
;readout/receiver phase
ph4 = 0 2 2 0 1 3 3 1; any phase
ph31= 0 2 2 0 1 3 3 1
#endif

#ifdef PCYCLE5
;excitation, states, TPPI
ph1 = 0 0 0 0 2 2 2 2
ph10= 0 0 0 0 0 0 0 0 2 2 2 2 2 2
    2 2
;shape pulse phase (z-filter)
ph8 = 0 1 3 2
ph9 = 2 3 0 1
;transfer block phases
ph2 = 0
ph20= 1 3 3 1
ph3 = 3 2 3 2; any phase
ph21= 0 0 2 2
;readout/receiver phase
ph4 = 0; any phase
ph31= 0 2 2 0 2 0 0 2 2 0 0 2 0 2
    2 0
#endif

#ifdef PCYCLE6
;excitation, states, TPPI
ph1 = 0 0 0 0 2 2 2 2
ph10= 0 0 0 0 0 0 0 0 2 2 2 2 2 2
    2 2
;shape pulse phase (z-filter)
ph8 = 0 1 3 2
ph9 = 2 3 0 1
```

```
;transfer block phases
ph2 = 0
ph20= 1 3 3 1
ph3 = 3 2 3 2; any phase
ph21= 0 0 2 2
;readout/receiver phase
ph4 = 0 0 0 0 1 1 1 1; any phase
ph31= 0 2 2 0 3 1 1 3 2 0 0 2 1 3
    3 1
#endif

#ifdef PCYCLE7
;excitation, states, TPPI
ph1 = 0 0 0 0 2 2 2 2 2 2 2 2 0 0
    0 0
ph10= 0
;shape pulse phase (z-filter)
ph8 = 0 1 0 1 1 0 1 0 3 2 3 2 2 3
    2 3
ph9 = 2 3 2 3 3 2 3 2 1 0 1 0 0 1
    0 1
;transfer block phases
ph2 = 0
ph20= 1 3 3 1
ph3 = 3 2 3 2; any phase
ph21= 0 0 2 2
;readout/receiver phase
ph4 = 0 ; any phase
ph31= 0 2 2 0 2 0 0 2 2 0 0 2 0 2
    2 0
#endif

;pl0 : 0W
;pl1 : power level for pulse (
    default)
;sp23: shaped dephasing pulse
;p1 : 90 degree high power pulse
;p2 : 180 degree high power pulse
;p23: 180 degree shaped pulse for
    dephasing
;p16: homospoil/gradient pulse
                              [1 msec
    ]

;p23: 1st inversion pulse for
    dephasing (z-filter)
;p24: 2nd inversion pulse for
    dephasing (z-filter)
;spnam23: 1st inversion pulse for
    dephasing (z-filter)
;spnam24: 2nd inversion pulse for
    dephasing (z-filter)
;sp23: Power level for dephasing
    pulse (z-filter)
;sp24: Power level for dephasing
    pulse (z-filter)

;d0 : incremented delay (2D)
                                  [3
    usec]
;d1 : relaxation delay; 1-5 * T1
;d4 : 1/(4J(HH))
;d11: delay for disk I/O

    [30 msec]
;d16: delay for homospoil/gradient
     recovery
;cnst2: > J(HH); 30 Hz
;inf1: 1/SW(X) = 2 * DW(X)
;in0: 1/(2 * SW(X)) = DW(X)
;nd0: 2
;NS: 2 * n
;DS: 16
;td1: number of experiments
;FnMODE: States-TPPI, TPPI, States
     or QSEQ

;for z-only gradients:
;gpz1: 7.2%
;gpz2: -7.5%
;gpz3: -17.9%

;use gradient files:
;gpnam3: SMSQ10.100

;Processing

;PHC0(F1): 0
;PHC1(F1): -180
;FCOR(F1): 1

;$Id: clipcosy,v 0.9 2015/07/20
    16:34:17 mk Exp $
```

ASAP-HSQC-Related Pulse Programs

Symmetric ASAP-HSQC

```
;ASAP!hsqcetgp
;avance-version (09/04/17)
;ASAP!HSQC
;2D H-1/X correlation via double
    inept transfer
;phase sensitive using Echo/
    Antiecho-TPPI gradient
    selection
;with decoupling during
    acquisition
;with DIPSI mixing after
    acquisition for ASAP
;       (Johanna Becker, David
    Schulze Sünninghausen, Martin
    Koos; 2013)
;$CLASS=HighRes
;$DIM=2D
;$TYPE=
;$SUBTYPE=
;$COMMENT=

#include <Avance.incl>
#include <Grad.incl>
#include <Delay.incl>

"d3=1s/(cnst1*4)" ; reduced INEPT
    delay (1st transfer)
"d4=1s/(cnst2*4)" ; general INEPT
    delay (2nd transfer)

"d11=30m"
"p2=p1*2"
"p4=p3*2"
"d0=3u"
"in0=inf1/2"

"acqt0=0"

"DELTA4=d4-p16-d16-de+p1*2/PI-4u"
                  ; d4 reduced
    for EA gradient pulse
"DELTA =p16+d16+d0+p2*0.5"
                              ;
    gradient pulse length,
    refocusing of first d0

"FACTOR1=(d9/(p6*115.112))/2" ;
    DISPI parameters
"l1=FACTOR1*2"

1 ze
  d11 pl12:f2
2 d1 do:f2
  4u UNBLKGRAD
  p16:gp3
  d16 pl10:f1
;begin DIPSI-2
3 p6*3.556 ph23
  p6*4.556 ph25
  p6*3.222 ph23
  p6*3.167 ph25
  p6*0.333 ph23
  p6*2.722 ph25
  p6*4.167 ph23
  p6*2.944 ph25
  p6*4.111 ph23

  p6*3.556 ph25
  p6*4.556 ph23
  p6*3.222 ph25
  p6*3.167 ph23
  p6*0.333 ph25
  p6*2.722 ph23
  p6*4.167 ph25
  p6*2.944 ph23
  p6*4.111 ph25

  p6*3.556 ph25
  p6*4.556 ph23
  p6*3.222 ph25
  p6*3.167 ph23
  p6*0.333 ph25
  p6*2.722 ph23
  p6*4.167 ph25
  p6*2.944 ph23
  p6*4.111 ph25

  p6*3.556 ph23
  p6*4.556 ph25
  p6*3.222 ph23
  p6*3.167 ph25
  p6*0.333 ph23
```

```
  p6*2.722 ph25
  p6*4.167 ph23
  p6*2.944 ph25
  p6*4.111 ph23
 lo to 3 times l1
;end DIPSI-2
  4u
  p16:gp4
  d16 pl1:f1 pl2:f2

;inept, reduced delay
4 (p1 ph1)
  d3
  (center (p2 ph1) (p4 ph6):f2 )
  d3
  (p1 ph2) (p3 ph3):f2

;coherence pathway selection 1
  4u
  DELTA
  (p4 ph4):f2
  4u
  p16:gp1*0.5*EA
  d16
;t1
  d0
  (p2 ph5)
  d0
;coherence pathway selection 2
  4u
  p16:gp1*0.5*EA
  d16
  (p4 ph14):f2
  4u
  DELTA

;inept
  (ralign (p1 ph1) (p3 ph7):f2 )
  d4
  (center (p2 ph1) (p4 ph1):f2 )
  4u
  p16:gp2
  d16 pl12:f2
  DELTA4 BLKGRAD

;acquisition
  go=2 ph31 cpd2:f2
  d1 do:f2 mc #0 to 2
      F1EA(calgrad(EA), caldel(d0,
          +in0) & calph(ph3, +180)
          & calph(ph6, +180) &
          calph(ph31, +180))
exit

ph1=0
ph2=1
ph3=0 2
ph4 =0 0 0 0 2 2 2 2
ph14=2 2 2 2 0 0 0 0
ph5=0 0 2 2
ph6=0
ph7=0 0 0 0 2 2 2 2
ph23=3
ph25=1
ph31=0 2 0 2 2 0 2 0

;pl1 : f1 channel - power level
    for pulse (default)
;pl2 : f2 channel - power level
    for pulse (default)
;pl10 : f1 channel - power level
    for mixing sequence
;pl12: f2 channel - power level
    for CPD/BB decoupling
;p1 : f1 channel -  90 degree high
     power pulse
;p2 : f1 channel - 180 degree high
     power pulse
;p3 : f2 channel -  90 degree high
     power pulse
;p4 : f2 channel - 180 degree high
     power pulse
;p6 : f1 channel - 90 degree pulse
     for mixing sequence
;p16: homospoil/gradient pulse

;d0 : incremented delay (2D)
                      [3 usec]
;d1 : relaxation delay; 1-5 * T1
;d4 : 1/(4J)XH
;d3 : reduced d4
;d11: delay for disk I/O

    [30 msec]
;d16: delay for homospoil/gradient
     recovery
;cnst2: = J(XH)
```

```
;cnst1: reduced cnst2 ('ernst
   angle')
;inf1: 1/SW(X) = 2 * DW(X)
;in0: 1/(2 * SW(X)) = DW(X)
;nd0: 2
;NS: 1 * n
;DS: >= 16
;td1: number of experiments
;FnMODE: echo-antiecho
;cpd2: decoupling according to
   sequence defined by cpdprg2
;pcpd2: f2 channel - 90 degree
   pulse for decoupling sequence

;use gradient ratio:    gp 1 : gp
   2 : gp 3 : gp 4
;                          80 :
   20.1 : 33 : 44  for C-13

;for z-only gradients:
;gpz1: 80%
;gpz2: 20.1% for C-13
;gpz3: 33% ; gradient before
   mixing
;gpz4: 43% ; gradient after mixing

;use gradient files:
;gpnam1: SMSQ10.100
;gpnam2: SMSQ10.100
;gpnam3: SMSQ10.100
;gpnam4: SMSQ10.100

;$Id: asap!hsqcetgp,v 1.5.2.1
   2011/02/24 17:27:48 ber Exp $
```

Symmetric ASAP-HSQC with Shaped Pulses

```
;ASAP!hsqcetgp
;avance-version (09/04/17)
;ASAP!HSQC
;2D H-1/X correlation via double
   inept transfer
;phase sensitive using Echo/
   Antiecho-TPPI gradient
   selection
;with decoupling during
   acquisition
;with DIPSI mixing after
   acquisition for ASAP
;using shape pulses on f1 and f2.

;$CLASS=HighRes
;$DIM=2D
;$TYPE=
;$SUBTYPE=
;$COMMENT=

#include <Avance.incl>
#include <Grad.incl>
#include <Delay.incl>

"d3=(d4+4u)*cnst3-4u" ; reduced
   INEPT delay (1st transfer)
"d4=1s/(cnst2*4) -4u" ; general
   INEPT delay (2nd transfer)
"DELTA4=d4-p16-d16-de+p1*2/PI"; d4
    reduced for EA gradient pulse
"DELTA =p16+d16+d0+p22*0.5"
           ; gradient pulse
   length, refocusing of first d0
"d11=30m"
"d0=3u"
"in0=inf1/2"
"acqt0=0"
"FACTOR1=(d9/(p6*115.112))/2" ;
   DISPI parameters
"l1=FACTOR1*2"

1 ze
  d11
2 d1  do:f2
  4u UNBLKGRAD
  p16:gp3
  d16 pl10:f1
;begin DIPSI-2
3 p6*3.556 ph23
  p6*4.556 ph25
  p6*3.222 ph23
  p6*3.167 ph25
  p6*0.333 ph23
  p6*2.722 ph25
  p6*4.167 ph23
  p6*2.944 ph25
  p6*4.111 ph23

  p6*3.556 ph25
```

```
  p6*4.556 ph23
  p6*3.222 ph25
  p6*3.167 ph23
  p6*0.333 ph25
  p6*2.722 ph23
  p6*4.167 ph25
  p6*2.944 ph23
  p6*4.111 ph25

  p6*3.556 ph25
  p6*4.556 ph23
  p6*3.222 ph25
  p6*3.167 ph23
  p6*0.333 ph25
  p6*2.722 ph23
  p6*4.167 ph25
  p6*2.944 ph23
  p6*4.111 ph25

  p6*3.556 ph23
  p6*4.556 ph25
  p6*3.222 ph23
  p6*3.167 ph25
  p6*0.333 ph23
  p6*2.722 ph25
  p6*4.167 ph23
  p6*2.944 ph25
  p6*4.111 ph23
 lo to 3 times l1
;end DIPSI-2
  4u
  p16:gp4
  d16 pl0:f1 pl0:f2 ; power level
     for shape pulses

;inept, reduced delay
4 (p21:sp21 ph1):f1
           ;BEBOP:f1, [zx]
  d3
  4u
  (p22:sp22 ph1):f1 (p22:sp23 ph1)
     :f2    ;BUBI( URx180:f1,
     BIBOP:f2 [z-z])
  d3
  4u pl1:f1
  (p1 ph1):f1 (p21:sp24 ph4):f2
             ;p1, BEBOP:f2 [zy]

;coherence pathway selection 1
  4u
  DELTA
  (p22:sp23 ph7):f2
  4u
  p16:gp1*0.5*EA
  d16 pl0:f1

;t1
  d0
  (p22:sp22 ph5):f1
             ;URx180 F1
  d0

;coherence pathway selection 2
  4u
  p16:gp1*0.5*EA
  d16
  (p22:sp23 ph8):f2
  4u
  DELTA pl1:f1

;inept
  (ralign (p1 ph2):f1 (p21:sp26
     ph3):f2);p1, BEBOP:f2 [yz]
  4u
  d4 pl0:f1
  (p22:sp22 ph1):f1 (p22:sp23 ph6)
     :f2    ;BUBI( URx180:f1,
     BIBOP:f2 [z-z] )
  4u
  p16:gp2
  d16 pl12:f2 pl1:f1
  DELTA4 BLKGRAD

  go=2 ph31 cpd2:f2
  d1 do:f2 mc #0 to 2
     F1EA(calgrad(EA), caldel(d0,
        +in0) & calph(ph3, +180)
        & calph(ph6, +180) &
        calph(ph31, +180))
exit

#ifdef NOPHASECYCLE
ph1=0
ph2=1
ph3=0
ph4 =0
ph5=3
ph14=2
```

```
ph5=0
ph6=0
ph7=1
ph8=3
ph23=3
ph25=1
ph31=0
#else
ph1=0
ph2=1
ph3=0 2
ph4 =0 0 0 0 2 2 2 2
ph14=2 2 2 2 0 0 0 0
ph5=0 0 2 2
ph6=0
ph7=1 1 1 1 3 3 3 3
ph8=3 3 3 3 1 1 1 1
ph23=3
ph25=1
ph31=0 2 0 2 2 0 2 0
#endif /*nophasecycle*/

;pl1 : f1 channel - power level
   for pulse (default)
;pl2 : f2 channel - power level
   for pulse (default)
;pl10 : f1 channel - power level
   for mixing sequence
;pl12: f2 channel - power level
   for CPD/BB decoupling
;p1 : f1 channel -  90 degree high
    power pulse
;p3 : f2 channel -  90 degree high
    power pulse
;p6 : f1 channel - 90 degree pulse
    for mixing sequence
;p16: homospoil/gradient pulse

;p21 : 550u excitation pulses
;p22 : 600u UR and Inversion
   pulses
;p25 : 1100u 13C refocusing pulse
;spnam21 :
   jc01_BEBOP_zx_550u_BW10_RF20_pm20_Hc2
   .99997119.pul
;spnam22 :
   jc02_BURBOP_x_600u_BW10_RF20_pm20_matched
   .pul
;spnam23 : jc03_BIBOP_600u_BW37.5
   _RF10_pm5_matched.pul
;spnam24 : jc05_BEBOP_zy_550u_BW37
   .5_RF10_pm5_matched.pul
;spnam25 :
   jc07_BURBOP_y_1100u_BW37.5
   _RF10_pm5_Hc0.999876221.pul
;spnam26 : jc09_BEBOP_-
   yz_550u_BW37.5
   _RF10_pm5_matched.pul
;sp21 : 20 kHz Rf Amplitude
;sp22 : 20 kHz Rf Amplitude
;sp23 : 10 kHz Rf Amplitude
;sp24 : 10 kHz Rf Amplitude
;sp25 : 10 kHz Rf Amplitude
;sp26 : 10 kHz Rf Amplitude

;d0 : incremented delay (2D)
                      [3 usec]
;d1 : relaxation delay; 1-5 * T1
;d4 : 1/(4J)XH
;d3 : reduced d4
;d11: delay for disk I/O

   [30 msec]
;d16: delay for homospoil/gradient
    recovery
;cnst2: = J(XH)
;cnst1: reduced cnst2 ('ernst
   angle')
;inf1: 1/SW(X) = 2 * DW(X)
;in0: 1/(2 * SW(X)) = DW(X)
;nd0: 2
;NS: 1 * n
;DS: >= 16
;td1: number of experiments
;FnMODE: echo-antiecho
;cpd2: decoupling according to
   sequence defined by cpdprg2
;pcpd2: f2 channel - 90 degree
   pulse for decoupling sequence

;use gradient ratio:    gp 1 : gp
   2 : gp 3 : gp 4
;                         80 :
   20.1 : 33 : 44  for C-13
;for z-only gradients:
;gpz1: 80%
```

```
;gpz2: 20.1% for C-13
;gpz3: 33% ; gradient before
    mixing
;gpz4: 43% ; gradient after mixing

;use gradient files:
;gpnam1: SMSQ10.100
;gpnam2: SMSQ10.100
;gpnam3: SMSQ10.100
;gpnam4: SMSQ10.100

;$Id: asap!hsqcetgp_sp,v 1.5.2.1
    2011/02/24 17:27:48 ber Exp $
```

Asymmetric ASAP-HSQC

```
;ASAP!hsqcetgp
;avance-version (09/04/17)
;ASAP!HSQC
;2D H-1/X correlation via double
    inept transfer
;phase sensitive using Echo/
    Antiecho-TPPI gradient
    selection
;with decoupling during
    acquisition
;$CLASS=HighRes
;$DIM=2D
;$TYPE=
;$SUBTYPE=
;$COMMENT=

#include <Avance.incl>
#include <Grad.incl>
#include <Delay.incl>

"p2=p1*2"
"p4=p3*2"

"d4=1s/(cnst2*4) -4u"
"d5=1s/(cnst1*4) -4u"
"d11=30m"
"d0=3u"
"in0=inf1/2"
"acqt0=0"
"DELTA4=d4-p16-d16-de+p1*2/PI"
"DELTA =p16+d16"
"DELTA1=d0"
"DELTA2=p4/2-p3+p1" ;balances last
    inept pulse (UR90, exc)

"FACTOR1=(d9/(p6*115.112))/2"
"l1=FACTOR1*2"

1 ze
2 d11
  d1 do:f2
  4u UNBLKGRAD
  p16:gp6
  d16 pl10:f1
;begin DIPSI-2
3 p6*3.556 ph23
  p6*4.556 ph25
  p6*3.222 ph23
  p6*3.167 ph25
  p6*0.333 ph23
  p6*2.722 ph25
  p6*4.167 ph23
  p6*2.944 ph25
  p6*4.111 ph23

  p6*3.556 ph25
  p6*4.556 ph23
  p6*3.222 ph25
  p6*3.167 ph23
  p6*0.333 ph25
  p6*2.722 ph23
  p6*4.167 ph25
  p6*2.944 ph23
  p6*4.111 ph25

  p6*3.556 ph25
  p6*4.556 ph23
  p6*3.222 ph25
  p6*3.167 ph23
  p6*0.333 ph25
  p6*2.722 ph23
  p6*4.167 ph25
  p6*2.944 ph23
  p6*4.111 ph25

  p6*3.556 ph23
  p6*4.556 ph25
  p6*3.222 ph23
  p6*3.167 ph25
  p6*0.333 ph23
  p6*2.722 ph25
```

```
  p6*4.167 ph23
  p6*2.944 ph25
  p6*4.111 ph23
 lo to 3 times l1
;end DIPSI-2
  4u
  p16:gp7
  d16 pl1:f1 pl2:f2

;inept
4 (p1 ph1):f1                    ;
   BEBOP f1, zx
  d5
  4u
  (center (p2 ph1):f1 (p4 ph6):f2)
           ;BUBI: URx180, BIBOP
  d5
  4u
  (p1 ph2):f1 (p3 ph3):f2        ;
     p1, BEBOP zy

;gradient delay
  DELTA2
  4u
  p16:gp1
  d16

;t1
  d0
  (p2 ph5):f1                    ;
     URx180 F1
  d0

;gradient delay
  4u
  p16:gp2
  d16

;180 pulses and balancing delays
  (p4 ph4):f2                    ;
     URx180 f2

  4u
  p16:gp3
  d16
  DELTA1

  (p2 ph15):f1                   ;
     URx180 F1

  DELTA1
  4u
  p16:gp4
  d16

  DELTA2

;inept
  (ralign (p1 ph10):f1 (p3 ph4):f2
      )      ;p1, BEBOPyz
  4u
  d4
  (center (p2 ph1):f1 (p4 ph1):f2)
           ;BUBI: URx180, BIBOP
  4u
  p16:gp5*EA
  d16 pl12:f2
  DELTA4 BLKGRAD
#                ifdef HC12 /*flip
   12C magnetization back to -y*/
  p1 ph1
#                endif /*12C*/

  go=2 ph31 cpd2:f2
  d11 do:f2 mc #0 to 2
     F1EA(calgrad(EA), caldel(d0,
        +in0) & calph(ph3, +180)
        & calph(ph6, +180) &
        calph(ph31, +180))
exit

#  ifdef NOPHASECYCLE
ph1=0
ph10=2
ph2=1
ph3=0 ;2
ph4 =0; 0 0 0 2 2 2 2
ph14=2; 2 2 2 0 0 0 0
ph5=0 ;0 2 2
ph15 = 2
ph6=0
ph23=3
ph25=1
ph31=0 ;2 0 2 2 0 2 0
#  else
ph1=0
ph10=2
ph2=1
```

```
ph3=0 2
ph4 =0 0 0 0 2 2 2 2
ph5 =0 0 2 2
ph15=2 2 0 0
ph6=0
ph23=3
ph25=1
ph31=0 2 0 2 2 0 2 0
#  endif

;pl1 : f1 channel - power level
   for pulse (default)
;pl12: f2 channel - power level
   for CPD/BB decoupling
;p1 : f1 channel -  90 degree high
    power pulse
;p3 : f2 channel -  90 degree high
    power pulse
;p16: homospoil/gradient pulse

;p21 : 550u excitation pulses
;p22 : 600u UR and Inversion
   pulses
;p25 : 1100u 13C refocusing pulse
;spnam21 :
   jc01_BEBOP_zx_550u_BW10_RF20_pm20_Hc0
   .99997119.pul
;spnam22 :
   jc02_BURBOP_x_600u_BW10_RF20_pm20_matched
   .pul
;spnam23 : jc03_BIBOP_600u_BW37.5
   _RF10_pm5_matched.pul
;spnam24 : jc05_BEBOP_zy_550u_BW37
   .5_RF10_pm5_matched.pul
;spnam25 :
   jc07_BURBOP_y_1100u_BW37.5
   _RF10_pm5_Hc0.999876221.pul
;spnam26 : jc09_BEBOP_-
   yz_550u_BW37.5
   _RF10_pm5_matched.pul
;sp21 : 20 kHz Rf Amplitude
;sp22 : 20 kHz Rf Amplitude
;sp23 : 10 kHz Rf Amplitude
;sp24 : 10 kHz Rf Amplitude
;sp25 : 10 kHz Rf Amplitude
;sp26 : 10 kHz Rf Amplitude

;d0 : incremented delay (2D)
                    [3 usec]
;d1 : relaxation delay; 1-5 * T1
;d4 : 1/(4J)XH
;d11: delay for disk I/O

   [30 msec]
;d16: delay for homospoil/gradient
    recovery
;cnst2: = J(XH)
;cnst1: reduced cnst2
;inf1: 1/SW(X) = 2 * DW(X)
;in0: 1/(2 * SW(X)) = DW(X)
;nd0: 2
;NS: 1 * n
;DS: >= 16
;td1: number of experiments
;FnMODE: echo-antiecho
;cpd2: decoupling according to
   sequence defined by cpdprg2
;pcpd2: f2 channel - 90 degree
   pulse for decoupling sequence

;use gradient ratio:    gp 1 : gp
   2 : gp 3
;                         40 : 40
   : 20.1   for C-13
;for z-only gradients:
;gpz1: 40%
;gpz2: 40%
;gpz3: 20.1% for C-13

;use gradient files:
;gpnam1: SMSQ10.100
;gpnam2: SMSQ10.100
;gpnam3: SMSQ10.100

;$Id: asap!hsqcetgp,v 1.5.2.1
   2011/02/24 17:27:48 ber Exp $
```

Asymmetric ASAP-HSQC with Shaped Pulses

```
;ASAP!hsqcetgp
;avance-version (09/04/17)
;ASAP!HSQC
;2D H-1/X correlation via double
   inept transfer
```

```
;phase sensitive using Echo/
    Antiecho-TPPI gradient
    selection
;with decoupling during
    acquisition
;$CLASS=HighRes
;$DIM=2D
;$TYPE=
;$SUBTYPE=
;$COMMENT=

#include <Avance.incl>
#include <Grad.incl>
#include <Delay.incl>

"d4=1s/(cnst2*4) -4u"
"d5=1s/(cnst1*4) -4u"
"d11=30m"
"d0=3u"
"in0=inf1/2"
"acqt0=0"
"DELTA4=d4-p16-d16-de+p1*2/PI"
"DELTA =p16+d16"
"DELTA1=d0"
"DELTA2=p25/2-p21+p1" ;balances
    last inept pulse (UR90, exc)

"FACTOR1=(d9/(p6*115.112))/2"
"l1=FACTOR1*2"

1 ze
2 d11
  d1 do:f2
  4u UNBLKGRAD
  p16:gp6*EA*-1
  d16 pl10:f1
;begin DIPSI-2
3 p6*3.556 ph23
  p6*4.556 ph25
  p6*3.222 ph23
  p6*3.167 ph25
  p6*0.333 ph23
  p6*2.722 ph25
  p6*4.167 ph23
  p6*2.944 ph25
  p6*4.111 ph23

  p6*3.556 ph25
  p6*4.556 ph23
  p6*3.222 ph25
  p6*3.167 ph23
  p6*0.333 ph25
  p6*2.722 ph23
  p6*4.167 ph25
  p6*2.944 ph23
  p6*4.111 ph25

  p6*3.556 ph25
  p6*4.556 ph23
  p6*3.222 ph25
  p6*3.167 ph23
  p6*0.333 ph25
  p6*2.722 ph23
  p6*4.167 ph25
  p6*2.944 ph23
  p6*4.111 ph25

  p6*3.556 ph23
  p6*4.556 ph25
  p6*3.222 ph23
  p6*3.167 ph25
  p6*0.333 ph23
  p6*2.722 ph25
  p6*4.167 ph23
  p6*2.944 ph25
  p6*4.111 ph23
  lo to 3 times l1
;end DIPSI-2
  4u
  p16:gp7
  d16 pl0:f1 pl0:f2

;inept
4 (p21:sp21 ph1):f1
            ;BEBOP f1, zx
  d5
  4u
  (p22:sp22 ph1):f1 (p22:sp23 ph6)
     :f2    ;BUBI: URx180, BIBOP
  d5
  4u pl1:f1
  (p1 ph1):f1 (p21:sp24 ph3):f2
              ;p1, BEBOP zy

;gradient delay
  DELTA2
  4u
  p16:gp1
```

```
  d16 pl0:f1

;t1
  d0
  (p22:sp22 ph5):f1
              ;URx180 F1
  d0

;gradient delay
  4u
  p16:gp2
  d16

;180 pulses and balancing delays
  (p25:sp25 ph4):f2
              ;URx180 f2

  4u
  p16:gp3
  d16
  DELTA1

  (p22:sp22 ph15):f1
              ;URx180 F1

  DELTA1
  4u
  p16:gp4
  d16

  DELTA2

;inept
  (ralign (p1 ph2):f1 (p21:sp26
     ph4):f2);p1, BEBOPyz
  4u
  d4 pl0:f1
  (p22:sp22 ph1):f1 (p22:sp23 ph1)
     :f2    ;BUBI: URx180, BIBOP
  4u
  p16:gp5*EA
  d16 pl12:f2
#                ifdef HC12 /*flip
    12C magnetization back to -y*/
  DELTA4 pl1:f1 BLKGRAD
  p1 ph1
#                else /* regular
    hsqc */
  DELTA4 BLKGRAD
#                endif /*12C*/

  go=2 ph31 cpd2:f2
  d11 do:f2 mc #0 to 2
     F1EA(calgrad(EA), caldel(d0,
        +in0) & calph(ph3, +180)
        & calph(ph6, +180) &
        calph(ph31, +180))
exit

#  ifdef NOPHASECYCLE
ph1=0
ph2=1
ph3=0 ;2
ph4 =0; 0 0 0 2 2 2 2
ph14=2; 2 2 2 0 0 0 0
ph5=0 ;0 2 2
ph6=0
ph23=3
ph25=1
ph31=0 ;2 0 2 2 0 2 0
#  else
ph1=0
ph2=1
ph3=0 2
ph4 =0 0 0 0 2 2 2 2
ph5 =0 0 2 2
ph15=2 2 0 0
ph6=0
ph23=3
ph25=1
ph31=0 2 0 2 2 0 2 0
#  endif

;pl1 : f1 channel - power level
    for pulse (default)
;pl12: f2 channel - power level
    for CPD/BB decoupling
;p1 : f1 channel -  90 degree high
     power pulse
;p3 : f2 channel -  90 degree high
     power pulse
;p16: homospoil/gradient pulse

;p21 : 550u excitation pulses
;p22 : 600u UR and Inversion
    pulses
;p25 : 1100u 13C refocusing pulse
```

```
;spnam21 :
   jc01_BEBOP_zx_550u_BW10_RF20_pm20_Hc0
   .99997119.pul
;spnam22 :
   jc02_BURBOP_x_600u_BW10_RF20_pm20_matched
   .pul
;spnam23 : jc03_BIBOP_600u_BW37.5
   _RF10_pm5_matched.pul
;spnam24 : jc05_BEBOP_zy_550u_BW37
   .5_RF10_pm5_matched.pul
;spnam25 :
   jc07_BURBOP_y_1100u_BW37.5
   _RF10_pm5_Hc0.999876221.pul
;spnam26 : jc09_BEBOP_-
   yz_550u_BW37.5
   _RF10_pm5_matched.pul
;sp21 : 20 kHz Rf Amplitude
;sp22 : 20 kHz Rf Amplitude
;sp23 : 10 kHz Rf Amplitude
;sp24 : 10 kHz Rf Amplitude
;sp25 : 10 kHz Rf Amplitude
;sp26 : 10 kHz Rf Amplitude

;d0 : incremented delay (2D)
                    [3 usec]
;d1 : relaxation delay; 1-5 * T1
;d4 : 1/(4J)XH
;d11: delay for disk I/O

   [30 msec]
;d16: delay for homospoil/gradient
    recovery
;cnst2: = J(XH)
;cnst1: reduced cnst2
;inf1: 1/SW(X) = 2 * DW(X)
;in0: 1/(2 * SW(X)) = DW(X)
;nd0: 2
;NS: 1 * n
;DS: >= 16
;td1: number of experiments
;FnMODE: echo-antiecho
;cpd2: decoupling according to
   sequence defined by cpdprg2
;pcpd2: f2 channel - 90 degree
   pulse for decoupling sequence

;use gradient ratio:    gp 1 : gp
   2 : gp 3
;                          40 : 40
   for C-13

;for z-only gradients:
;gpz1: 40%
;gpz2: 40%
;gpz3: 20.1% for C-13

;use gradient files:
;gpnam1: SMSQ10.100
;gpnam2: SMSQ10.100
;gpnam3: SMSQ10.100

;$Id: asap!hsqcetgp,v 1.5.2.1
   2011/02/24 17:27:48 ber Exp $
```

Edited ASAP-HSQC

```
;ASAP!hsqcetgp
;avance-version (09/04/17)
;ASAP!HSQC
;2D H-1/X correlation via double
   inept transfer
;phase sensitive using Echo/
   Antiecho-TPPI gradient
   selection
;with decoupling during
   acquisition
;$CLASS=HighRes
;$DIM=2D
;$TYPE=
;$SUBTYPE=
;$COMMENT=

#include <Avance.incl>
#include <Grad.incl>
#include <Delay.incl>

"p2=2*p1"
"p4=2*p3"

"d4=1s/(cnst2*4) -4u"
"d5=1s/(cnst1*4) -4u"
"d11=30m"
"d0=3u"
"in0=inf1/2"
"acqt0=0"
"DELTA4=d4-p16-d16-de+p1*2/PI"
"DELTA =p16+d16"
```

```
"DELTA1=d0"
"DELTA2=p4/2-p3+p1" ;balances last
    inept pulse (UR90, exc)

"FACTOR1=(d9/(p6*115.112))/2"
"l1=FACTOR1*2"

1 ze
2 d11
  d1 do:f2
  4u UNBLKGRAD
  p16:gp6*EA*-1
  d16 pl10:f1
;begin DIPSI-2
3 p6*3.556 ph23
  p6*4.556 ph25
  p6*3.222 ph23
  p6*3.167 ph25
  p6*0.333 ph23
  p6*2.722 ph25
  p6*4.167 ph23
  p6*2.944 ph25
  p6*4.111 ph23

  p6*3.556 ph25
  p6*4.556 ph23
  p6*3.222 ph25
  p6*3.167 ph23
  p6*0.333 ph25
  p6*2.722 ph23
  p6*4.167 ph25
  p6*2.944 ph23
  p6*4.111 ph25

  p6*3.556 ph25
  p6*4.556 ph23
  p6*3.222 ph25
  p6*3.167 ph23
  p6*0.333 ph25
  p6*2.722 ph23
  p6*4.167 ph25
  p6*2.944 ph23
  p6*4.111 ph25

  p6*3.556 ph23
  p6*4.556 ph25
  p6*3.222 ph23
  p6*3.167 ph25
  p6*0.333 ph23
  p6*2.722 ph25
  p6*4.167 ph23
  p6*2.944 ph25
  p6*4.111 ph23
 lo to 3 times l1
;end DIPSI-2
  4u
  p16:gp7
  d16 pl1:f1 pl2:f2

;inept
4 (p1 ph1):f1                          ;
   BEBOP f1, zx
  d5
  4u
  (center (p2 ph1):f1 (p4 ph6):f2)
            ;BUBI: URx180, BIBOP
  d5
  4u
  (p1 ph2):f1 (p3 ph3):f2              ;
     p1, BEBOP zy

;gradient delay
  DELTA2
  4u
  p16:gp1
  d16

;t1
  d0
  (p2 ph5):f1                          ;
     URx180 F1
  d0

;gradient delay
  4u
  p16:gp2
  d16

; editing delay
  8u
  d4
  d4

;180 pulses and balancing delays
  (p4 ph4):f2                          ;
     URx180 f2

  4u
```

```
  p16:gp3
  d16
  DELTA1

  (p2 ph15):f1                    ;
     URx180 F1

; editing delay
  8u
  d4
  d4

; gradient and balancing delays
  DELTA1
  4u
  p16:gp4
  d16

  DELTA2

;inept
  (ralign (p1 ph1):f1 (p3 ph4):f2)
           ;p1, BEBOPyz
  4u
  d4
  (center (p2 ph1):f1 (p4 ph1):f2)
           ;BUBI: URx180, BIBOP
  4u
  p16:gp5*EA
  d16 pl12:f2
  DELTA4 BLKGRAD
#                 ifdef HC12 /*flip
    12C magnetization back to -y*/
  p1 ph1
#                 endif /*12C*/

  go=2 ph31 cpd2:f2
  d11 do:f2 mc #0 to 2
     F1EA(calgrad(EA), caldel(d0,
         +in0) & calph(ph3, +180)
         & calph(ph6, +180) &
         calph(ph31, +180))
exit

#  ifdef NOPHASECYCLE
ph1=0
ph2=1
ph3=0 ;2
ph4 =0; 0 0 0 2 2 2 2
ph14=2; 2 2 2 0 0 0 0
ph5=0 ;0 2 2
ph6=0
ph23=3
ph25=1
ph31=0 ;2 0 2 2 0 2 0
#  else
ph1=0
ph2=1
ph3=0 2
ph4 =0 0 0 0 2 2 2 2
ph5 =0 0 2 2
ph15=2 2 0 0
ph6=0
ph23=3
ph25=1
ph31=0 2 0 2 2 0 2 0
#  endif

;pl1 : f1 channel - power level
    for pulse (default)
;pl12: f2 channel - power level
    for CPD/BB decoupling
;p1 : f1 channel -  90 degree high
     power pulse
;p3 : f2 channel -  90 degree high
     power pulse
;p16: homospoil/gradient pulse

;p21 : 550u excitation pulses
;p22 : 600u UR and Inversion
    pulses
;p25 : 1100u 13C refocusing pulse
;spnam21 :
    jc01_BEBOP_zx_550u_BW10_RF20_pm20_Hc0
    .99997119.pul
;spnam22 :
    jc02_BURBOP_x_600u_BW10_RF20_pm20_matched
    .pul
;spnam23 : jc03_BIBOP_600u_BW37.5
    _RF10_pm5_matched.pul
;spnam24 : jc05_BEBOP_zy_550u_BW37
    .5_RF10_pm5_matched.pul
;spnam25 :
    jc07_BURBOP_y_1100u_BW37.5
    _RF10_pm5_Hc0.999876221.pul
;spnam26 : jc09_BEBOP_-
    yz_550u_BW37.5
    _RF10_pm5_matched.pul
```

```
;sp21 : 20 kHz Rf Amplitude
;sp22 : 20 kHz Rf Amplitude
;sp23 : 10 kHz Rf Amplitude
;sp24 : 10 kHz Rf Amplitude
;sp25 : 10 kHz Rf Amplitude
;sp26 : 10 kHz Rf Amplitude

;d0 : incremented delay (2D)
                    [3 usec]
;d1 : relaxation delay; 1-5 * T1
;d4 : 1/(4J)XH
;d11: delay for disk I/O

   [30 msec]
;d16: delay for homospoil/gradient
    recovery
;cnst2: = J(XH)
;cnst1: reduced cnst2
;inf1: 1/SW(X) = 2 * DW(X)
;in0: 1/(2 * SW(X)) = DW(X)
;nd0: 2
;NS: 1 * n
;DS: >= 16
;td1: number of experiments
;FnMODE: echo-antiecho
;cpd2: decoupling according to
   sequence defined by cpdprg2
;pcpd2: f2 channel - 90 degree
   pulse for decoupling sequence

;use gradient ratio:    gp 1 : gp
   2 : gp 3
;                          40 : 40
   : 20.1    for C-13

;for z-only gradients:
;gpz1: 40%
;gpz2: 40%
;gpz3: 20.1% for C-13

;use gradient files:
;gpnam1: SMSQ10.100
;gpnam2: SMSQ10.100
;gpnam3: SMSQ10.100

;$Id: asap!hsqcetgp,v 1.5.2.1
   2011/02/24 17:27:48 ber Exp $
```

HSQC-Recovery Experiment

```
;hsqc-recovery
;avance-version (09/04/17)
;
;Experiment to measure signal
   recovery at the different
   states after
;HSQC-experiments:
; 1H-12C dephased (regular hsqc)
; 1H-12C aligned along +z (asap/
   alsofast-hsqc)
;signal recovery can be measured
; without DIPSI mixing (regular/
   alsofast hsqc)
; with DIPSI mixing (asap hasqc)
;readout is done by another HSQC.
;With CLIP pulse (no decoupling
   during acquisition)
;Using shape pulses on f1 and f2.
;
;run with DS=0, NS=1 or 2 and long
    D1 (20-60s)
;zgflags change some things...

;-DC12DEPHASE dephase protons at
   12C in first hsqc
;-DC12REVERSE reverses protons at
   12C to -z in first hsqc
;removed flags:
;  READOUTTEST runs only the
   readout-hsqc, replaced by l2 =
    0
;  NODIPSI to remove DISPI mixing,
    replaced by d9 = 0
;
;$CLASS=HighRes
;$DIM=2D
;$TYPE=
;$SUBTYPE=
;$COMMENT=

#include <Avance.incl>
#include <Grad.incl>
#include <Delay.incl>

;"d3=1s/(cnst1*4) -4u" ; reduced
   INEPT delay (1st transfer)
"d4=1s/(cnst2*4) -4u" ; general
   INEPT delay (2nd transfer)
```

```
;"cnst3=1" ; single scan, maximum
    intensity desired
"d3=(d4+4u)*cnst3-4u"; reduced
    INEPT delay (1st transfer)

"d11=30m"
"d0=3u"
"in0=inf1/2"
"acqt0=0"

"DELTA4=d4-p16-d16-de+p1*2/PI"; d4
     reduced for EA gradient pulse
"DELTA5=DELTA4-p3"; d4 reduced for
     EA gradient pulse and CLIP
    pulse
"DELTA =p16+d16+d0+p22*0.5"
            ; gradient pulse
    length, refocusing of first d0

"FACTOR1=(d9/(p6*115.112))/2" ;
    DISPI parameters
"l1=FACTOR1*2"
"d19=l1*p6*115.112" ; real DISPI
    length

1 ze
  d1
;-----------------------------
; SATURATION HSQC
;-----------------------------


;inept, reduced delay
2 d11
  d1 pl0:f1 pl0:f2

3 d11
  (p21:sp21 ph1):f1
              ;BEBOP:f1, [zx]
  d3
  4u
  (p22:sp22 ph1):f1 (p22:sp23 ph1)
      :f2    ;BUBI( URx180:f1,
     BIBOP:f2 [z-z])
  d3
  4u pl1:f1
  (p1 ph1):f1 (p21:sp24 ph4):f2
              ;p1, BEBOP:f2 [zy]

;coherence pathway selection 1
  4u
  DELTA UNBLKGRAD
  (p25:sp25 ph4):f2
              ;URx180 f2
  4u
  p16:gp1*0.5*1.1234
  d16 pl0:f1

;t1
  d0

;reversing protons bound to C12 (
    which are transveral at this
    moment)
;causes them to end up along -z
    after the final inept
#ifdef C12REVERSE
  (p22:sp22 ph2):f1
#else
  (p22:sp22 ph5):f1
              ;URx180 F1
#endif
  d0

;coherence pathway selection 2
  4u
  p16:gp1*0.5*1.1234
  d16
  (p25:sp25 ph14):f2
              ;URx180 f2
  4u
  DELTA pl1:f1

;inept

;this controls the orientation of
    the protons bound to 12C (and
    the
;inphase 1H13C part). use the
    zgflags to switch
#ifdef C12DEPHASE
  (ralign (p1 ph1):f1 (p21:sp26
      ph3):f2);p1, BEBOP:f2 [yz]
#else
    (ralign (p1 ph2):f1 (p21:sp26
       ph3):f2);p1, BEBOP:f2 [yz]
#endif
```

```
  4u
  d4 pl0:f1
  (p22:sp22 ph1):f1 (p22:sp23 ph6)
      :f2    ;BUBI( URx180:f1,
      BIBOP:f2 [z-z] )
  4u
  p16:gp2*1.1234
  d16
  DELTA4 pl0:f1 pl0:f2 BLKGRAD

;-----------------------------
; RECOVERY DELAY / DIPSI MIXING
;-----------------------------

;first run some delay...
  vd
  4u UNBLKGRAD
  p17:gp3
  d16 pl10:f1

;then follow me DIPSI, baby!

;begin DIPSI-2
4 p6*3.556 ph23
  p6*4.556 ph25
  p6*3.222 ph23
  p6*3.167 ph25
  p6*0.333 ph23
  p6*2.722 ph25
  p6*4.167 ph23
  p6*2.944 ph25
  p6*4.111 ph23

  p6*3.556 ph25
  p6*4.556 ph23
  p6*3.222 ph25
  p6*3.167 ph23
  p6*0.333 ph25
  p6*2.722 ph23
  p6*4.167 ph25
  p6*2.944 ph23
  p6*4.111 ph25

  p6*3.556 ph25
  p6*4.556 ph23
  p6*3.222 ph25
  p6*3.167 ph23
  p6*0.333 ph25
  p6*2.722 ph23
  p6*4.167 ph25
  p6*2.944 ph23
  p6*4.111 ph25

  p6*3.556 ph23
  p6*4.556 ph25
  p6*3.222 ph23
  p6*3.167 ph25
  p6*0.333 ph23
  p6*2.722 ph25
  p6*4.167 ph23
  p6*2.944 ph25
  p6*4.111 ph23
 lo to 4 times l1
;end DIPSI-2
  4u
  p16:gp4
  d16  pl0:f1
 lo to 3 times l2

;-----------------------------
; READOUT HSQC
;-----------------------------

;inept, reduced delay
5 (p21:sp21 ph1):f1
            ;BEBOP:f1, [zx]
  d4
  4u
  (p22:sp22 ph1):f1 (p22:sp23 ph1)
      :f2    ;BUBI( URx180:f1,
      BIBOP:f2 [z-z])
  d4
  4u pl1:f1
  (p1 ph1):f1 (p21:sp24 ph4):f2
              ;p1, BEBOP:f2 [zy]

;coherence pathway selection 1
  4u
  DELTA UNBLKGRAD
  (p25:sp25 ph4):f2
              ;URx180 f2
  4u
  p16:gp1*0.5
  d16 pl0:f1

;t1
  d0
```

```
  (p22:sp22 ph5):f1
              ;URx180 F1
  d0

;coherence pathway selection 2
  4u
  p16:gp1*0.5
  d16
  (p25:sp25 ph14):f2
              ;URx180 f2
  4u
  DELTA pl1:f1

;inept
  (ralign (p1 ph2):f1 (p21:sp26
     ph3):f2);p1, BEBOP:f2 [yz]
  4u
  d4 pl0:f1
  (p22:sp22 ph1):f1 (p22:sp23 ph6)
     :f2    ;BUBI( URx180:f1,
     BIBOP:f2 [z-z] )
  4u
  p16:gp2
  d16 pl2:f2
  DELTA5 BLKGRAD
  (p3 ph1):f2

  go=2 ph31
  d11 mc #0 to 2
     F1QF(ivd)
exit

; phase cycle is 'broken' for the
    first hsqc
; should work for readout hsqc
    anyways...
; not optimized for artifacts from
     first hsqc, though.
ph1=0
ph2=1
ph3=0 2
ph4 =0 0; 0 0 2 2 2 2
ph14=2 2; 2 2 0 0 0 0
ph5=0 0; 2 2
ph6=0
ph23=3
ph25=1
ph31=0 2; 0 2 2 0 2 0
```

```
;pl1 : f1 channel - power level
    for pulse (default)
;pl2 : f2 channel - power level
    for pulse (default)
;pl10 : f1 channel - power level
    for mixing sequence
;pl12: f2 channel - power level
    for CPD/BB decoupling
;p1 : f1 channel -  90 degree high
     power pulse
;p3 : f2 channel -  90 degree high
     power pulse
;p6 : f1 channel - 90 degree pulse
     for mixing sequence
;p16: homospoil/gradient pulse

;p21 : 550u excitation pulses
;p22 : 600u UR and Inversion
    pulses
;p25 : 1100u 13C refocusing pulse
;spnam21 :
    jc01_BEBOP_zx_550u_BW10_RF20_pm20_Hc0
    .99997119.pul
;spnam22 :
    jc02_BURBOP_x_600u_BW10_RF20_pm20_matched
    .pul
;spnam23 : jc03_BIBOP_600u_BW37.5
    _RF10_pm5_matched.pul
;spnam24 : jc05_BEBOP_zy_550u_BW37
    .5_RF10_pm5_matched.pul
;spnam25 :
    jc07_BURBOP_y_1100u_BW37.5
    _RF10_pm5_Hc0.999876221.pul
;spnam26 : jc09_BEBOP_-
    yz_550u_BW37.5
    _RF10_pm5_matched.pul
;sp21 : 20 kHz Rf Amplitude
;sp22 : 20 kHz Rf Amplitude
;sp23 : 10 kHz Rf Amplitude
;sp24 : 10 kHz Rf Amplitude
;sp25 : 10 kHz Rf Amplitude
;sp26 : 10 kHz Rf Amplitude

;d0 : incremented delay (2D)
                    [3 usec]
;d1 : relaxation delay; 1-5 * T1
;d4 : 1/(4J)XH
;d3 : reduced d4
```

```
;d11: delay for disk I/O

    [30 msec]
;d16: delay for homospoil/gradient
     recovery
;cnst2: = J(XH)
;cnst3: 1 ('ernst angle' around
    0.3-0.8)
;inf1: 1/SW(X) = 2 * DW(X)
;in0: 1/(2 * SW(X)) = DW(X)
;nd0: 2
;NS: 1 * n
;DS: >= 16
;td1: number of experiments
;FnMODE: echo-antiecho
;cpd2: decoupling according to
    sequence defined by cpdprg2
;pcpd2: f2 channel - 90 degree
    pulse for decoupling sequence

;use gradient ratio:    gp 1 : gp
    2 : gp 3 : gp 4
;                          80 :
    20.1 : 33 : 44  for C-13

;for z-only gradients:
;gpz1: 80%
;gpz2: 20.1% for C-13
;gpz3: 33% ; gradient before
    mixing
;gpz4: 43% ; gradient after mixing

;use gradient files:
;gpnam1: SMSQ10.100
;gpnam2: SMSQ10.100
;gpnam3: SMSQ10.100
;gpnam4: SMSQ10.100

;$Id: asap!hsqcetgp_sp,v 1.5.2.1
    2011/02/24 17:27:48 ber Exp $
```

Imaging-Related Pulse Programs

Deuterium Imaging

```
;2D sequence for z-imaging
    preserving chemical shift
;using a phase encoding gradient
; mc, mk
; 2H-Version
;$CLASS=HighRes
;$DIM=2D
;$TYPE=
;$SUBTYPE=
;$COMMENT=


#include <Avance.incl>
#include <Grad.incl>
#include <Delay.incl>

"cnst1=50.71736*0.95*0.8914027" ;
    gradient*integralfactor Gs/cm
"cnst2=41.07" ; gamma2H MTs
"p30=(td1/cnst0) * (1/cnst1) * (1/
    cnst2) *(2*3.14159265/100)*
    0.5 s"

"l1=td1-1"
lgrad r1d = l1


"acqt0=-d21-p30-p1*2/3.1416"


1 ze
  30m LOCKDEC_ON          ;this
     allows for 2h decoupling...?
  30m H2_PULSE            ;switch
     off lock
  30m H2_LOCK             ;switch on
      lock during d1
2 30m H2_LOCK             ;switch on
    lock during d1
3 d1

  50u H2_PULSE UNBLKGRAD ;lock off
      for whole experiment
  p1 ph1
  p30:gp6*r1d*0.95
  5u
  d21 BLKGRAD
  go=2 ph31
  30m H2_LOCK             ;switch on
      lock during d1
  d1 wr #0 if #0 igrad r1d zd
  lo to 3 times l1
```

```
  goto 5
; dumme gradientenfunktion läuft
    nicht bis 1
; also noch einmal durchlaufen
    lassen mit r1d=1

4 30m H2_LOCK              ;switch on
    lock during d1
  d1

5 50u H2_PULSE UNBLKGRAD ;lock off
    for whole experiment
  p1 ph1
  p30:gp6*r1d*0.95
  5u
  d21 BLKGRAD
  go=4 ph31

  30m H2_LOCK
  d1 wr #0 if #0 zd
  30m LOCKDEC_OFF
exit


ph1= 0 2 1 3
ph31=0 2 1 3


;cnst0 : z-Range in cm
;pl1 : f1 channel - power level
    for pulse (default)
;p1  : f1 channel -  90 degree
    high power pulse
;gpz6: 100% phase encoding
    gradient
;d1  : relaxation delay; 1-5 * T1
;d21: eddy current delay (Te)
                    [5 ms]
;NS: 1 * n
;DS: 1 * m
;td1: number of experiments
;FnMODE: QF

;use gradient files:
;gpnam6: SMSQ10.32

;$Id: ledbpgp2s,v 1.7 2009/07/02
    16:40:45 ber Exp $
```

Proton Imaging

```
;2D sequence for z-imaging
    preserving chemical shift
;using a phase encoding gradient
; mc, mk
;
;$CLASS=HighRes
;$DIM=2D
;$TYPE=
;$SUBTYPE=
;$COMMENT=


#include <Avance.incl>
#include <Grad.incl>
#include <Delay.incl>

"cnst1=50.71736*0.95*0.8914027" ;
    gradient*integralfactor Gs/cm
"cnst2=267.5" ; gammaH MTs
"p30=(td1/cnst0) * (1/cnst1) * (1/
    cnst2) *(2*3.14159265/100)*
    0.5 s"

"l1=td1-1"
lgrad r1d = l1

"acqt0=-d21-p30-p1*2/3.1416"

1 ze
2 d1
3 50u UNBLKGRAD
  p30:gp6*r1d*0.95*-1 ;additional
      gradient to destroy
      remaining magnetization
  d21
  p1 ph1
  p30:gp6*r1d*0.95
  d21 BLKGRAD
```

```
  go=2 ph31

;  d1 mc #0 to 2 F1QF(igrad r1d)
  d1 wr #0 if #0 zd igrad r1d
  lo to 3 times l1

; dumme gradientenfunktion läuft
    nicht bis 1
; also noch einmal durchlaufen
    lassen mit r1d=1
  goto 5
4 d1

5 50u UNBLKGRAD
  p30:gp6*1*0.95*-1 ;additional
      gradient to destroy
      remaining magnetization

  p1 ph1
  p30:gp6*1*0.95
  d21 BLKGRAD
  go=4 ph31
  d1 wr #0 if #0 zd
exit


ph1= 0 2 1 3
ph31=0 2 1 3

;cnst0 : z-Range in cm
;pl1 : f1 channel - power level
    for pulse (default)
;p1  : f1 channel -  90 degree
    high power pulse
;gpz6: 100% phase encoding
    gradient
;d1  : relaxation delay; 1-5 * T1
;d21: eddy current delay (Te)
                    [100 us]
;NS: 1 * n
;DS: 1 * m
;td1: number of experiments
;FnMODE: QF

;use gradient files:
;gpnam6: SMSQ10.32

;use phase PHC1:F1
;1 phc1 360*td1/2

;$Id: ledbpgp2s,v 1.7 2009/07/02
    16:40:45 ber Exp $
```

3D-HSQC-Imaging

```
;hsqcgpph
;avance-version (13/09/11)
;HSQC
;2D H-1/X correlation via double
    inept transfer
;phase sensitive
;with decoupling during
    acquisition
;peak type selection using
    gradient pulses with coherence
     selection
;    step before t1
;use pulseprogram 'hsqcgpnd1d' for
     setup
;
;$CLASS=HighRes
;$DIM=2D
;$TYPE=
;$SUBTYPE=
;$COMMENT=


#include <Avance.incl>
#include <Grad.incl>
#include <Delay.incl>


"p2=p1*2"
"p4=p3*2"
"d4=1s/(cnst2*4)"
"d11=30m"


"d0=3u"
```

```
"in0=inf1/2"


"DELTA=d0*2+p2"
"DELTA1=p16+d16+4u"
"DELTA2=d4-p16-d16-de+p1*2/PI-8u -
    d21 -p30"

;imaging calculations
"cnst11=50.71736*0.95*0.8914027" ;
     gradient*integralfactor Gs/cm
"cnst12=267.5" ; gammaH MTs
"p30=(td2/cnst10) * (1/cnst11) *
    (1/cnst12) *(2*3.14159265/100)
    * 0.5 s"

"l1=td2-1"
lgrad r1d = l1
;end of imaging calc

"acqt0=0"
baseopt_echo


1  ze
   d11 pl12:f2
2  d1 do:f2
3  (p1 ph1)
   d4 pl2:f2
   (center (p2 ph2) (p4 ph6):f2 )
   d4
   (p1 ph3) (p3 ph7):f2
   DELTA1 UNBLKGRAD
   (p4 ph8):f2
   4u
   p16:gp1
   d16
   (p3 ph9):f2
   4u
   p16:gp2
   d16
   (p3 ph10):f2
   d0
   (p2 ph4)
   d0
   (p4 ph11):f2
   DELTA
   (p3 ph11):f2
   (p1 ph3)
   d4
   (center (p2 ph5) (p4 ph12):f2 )
   4u
   p16:gp3
   d16
;IMAGING GRADIENT
p30:gp6*r1d*0.95
  d21
;IMAGING GRADIENT
   DELTA2 pl12:f2 BLKGRAD
   4u
   go=2 ph31 cpd2:f2
        d1 do:f2 mc #0 to 2
                          F2QF(
                             calgrad
                             (r1d))
                          F1PH(calph
                             (ph10,
                              +90),

                             caldel
                             (d0, +
                             in0))
exit


ph1=0
ph2=0
ph3=1
ph4=0 0 2 2
ph5=0
ph6=0
ph7=1 1 1 1 3 3 3 3
ph8=0
ph9=3
ph10=0
ph11=0 2
ph12=0
ph31=0 2 0 2 2 0 2 0


;pl1 : f1 channel - power level
    for pulse (default)
;pl2 : f2 channel - power level
    for pulse (default)
;pl12: f2 channel - power level
    for CPD/BB decoupling
;p1 : f1 channel -  90 degree high
     power pulse
```

```
;p2 : f1 channel - 180 degree high
    power pulse
;p3 : f2 channel -  90 degree high
    power pulse
;p4 : f2 channel - 180 degree high
    power pulse
;p16: homospoil/gradient pulse
;d0 : incremented delay (2D)
                    [3 usec]
;d1 : relaxation delay; 1-5 * T1
;d4 : 1/(4J)XH
;d11: delay for disk I/O

   [30 msec]
;d16: delay for homospoil/gradient
    recovery
;cnst10 : z-Range in cm
;cnst2: = J(XH)
;inf1: 1/SW(X) = 2 * DW(X)
;in0: 1/(2 * SW(X)) = DW(X)
;nd0: 2
;ns: 1 * n
;ds: 16
;td1: number of experiments
;FnMODE: States-TPPI, TPPI, States
    or QSEQ
;cpd2: decoupling according to
   sequence defined by cpdprg2
;pcpd2: f2 channel - 90 degree
   pulse for decoupling sequence


;use gradient ratio:    gp 1 : gp
   2 : gp 3
;                          80 :
   30 : 20.1    for C-13
;                          80 :
   30 :  8.1    for N-15

;for z-only gradients:
;gpz1: 80%
;gpz2: 30%
;gpz3: 20.1% for C-13, 8.1% for N
   -15

;use gradient files:
;gpnam1: SMSQ10.100
;gpnam2: SMSQ10.100
;gpnam3: SMSQ10.100

;$Id: hsqcgpph,v 1.5.4.1.4.3
   2014/01/17 15:19:37 ber Exp $
```

3D-CLIP-HSQC-Imaging

```
;hsqcgpph
;avance-version (13/09/11)
;HSQC
;2D H-1/X correlation via double
   inept transfer
;phase sensitive
;with decoupling during
   acquisition
;peak type selection using
   gradient pulses with coherence
    selection
;   step before t1
;use pulseprogram 'hsqcgpnd1d' for
    setup
;
;$CLASS=HighRes
;$DIM=2D
;$TYPE=
;$SUBTYPE=
;$COMMENT=


#include <Avance.incl>
#include <Grad.incl>
#include <Delay.incl>


"p2=p1*2"
"p4=p3*2"
"d4=1s/(cnst2*4)"
"d11=30m"


"d0=3u"

"in0=inf1/2"


"DELTA=d0*2+p2"
"DELTA1=p16+d16+4u"
```

```
"DELTA2=d4-p16-d16-de+p1*2/PI-4u -
    d21 -p30 -p3" ; one '-4u'
    changed to '-p3' for clip-
    pulse

;imaging calculations
"cnst11=50.71736*0.95*0.8914027" ;
     gradient*integralfactor Gs/cm
"cnst12=267.5" ; gammaH MTs
"p30=(td2/cnst10) * (1/cnst11) *
    (1/cnst12) *(2*3.14159265/100)
    * 0.5 s"

"l1=td2-1"
lgrad r1d = l1
;end of imaging calc

"acqt0=0"
baseopt_echo


1  ze
   d11 ;pl12:f2
2  d1 do:f2
3  (p1 ph1)
   d4 pl2:f2
   (center (p2 ph2) (p4 ph6):f2 )
   d4
   (p1 ph3) (p3 ph7):f2
   DELTA1 UNBLKGRAD
   (p4 ph8):f2
   4u
   p16:gp1
   d16
   (p3 ph9):f2
   4u
   p16:gp2
   d16
   (p3 ph10):f2
   d0
   (p2 ph4)
   d0
   (p4 ph11):f2
   DELTA
   (p3 ph11):f2
   (p1 ph3)
   d4
   (center (p2 ph5) (p4 ph12):f2 )
   4u
   p16:gp3
   d16
;IMAGING GRADIENT
p30:gp6*r1d*0.95
  d21
;IMAGING GRADIENT
   DELTA2 BLKGRAD ;pl12:f2
  (p3 ph1):f2
   go=2 ph31 ;cpd2:f2
        d1 do:f2 mc #0 to 2
                          F2QF(
                             calgrad
                             (r1d))
                          F1PH(calph
                             (ph10,
                              +90),

                             caldel
                             (d0, +
                             in0))
exit


ph1=0
ph2=0
ph3=1
ph4=0 0 2 2
ph5=0
ph6=0
ph7=1 1 1 1 3 3 3 3
ph8=0
ph9=3
ph10=0
ph11=0 2
ph12=0
ph31=0 2 0 2 2 0 2 0


;pl1 : f1 channel - power level
    for pulse (default)
;pl2 : f2 channel - power level
    for pulse (default)
;pl12: f2 channel - power level
    for CPD/BB decoupling
;p1 : f1 channel -  90 degree high
     power pulse
;p2 : f1 channel - 180 degree high
     power pulse
```

```
;p3 : f2 channel - 90 degree high
    power pulse
;p4 : f2 channel - 180 degree high
    power pulse
;p16: homospoil/gradient pulse
;d0 : incremented delay (2D)
                    [3 usec]
;d1 : relaxation delay; 1-5 * T1
;d4 : 1/(4J)XH
;d11: delay for disk I/O

   [30 msec]
;d16: delay for homospoil/gradient
    recovery
;cnst10 : z-Range in cm
;cnst2: = J(XH)
;inf1: 1/SW(X) = 2 * DW(X)
;in0: 1/(2 * SW(X)) = DW(X)
;nd0: 2
;ns: 1 * n
;ds: 16
;td1: number of experiments
;FnMODE: States-TPPI, TPPI, States
    or QSEQ
;cpd2: decoupling according to
   sequence defined by cpdprg2
;pcpd2: f2 channel - 90 degree
   pulse for decoupling sequence


;use gradient ratio:    gp 1 : gp
   2 : gp 3
;                          80 :
   30 : 20.1    for C-13
;                          80 :
   30 :  8.1    for N-15

;for z-only gradients:
;gpz1: 80%
;gpz2: 30%
;gpz3: 20.1% for C-13, 8.1% for N
   -15

;use gradient files:
;gpnam1: SMSQ10.100
;gpnam2: SMSQ10.100
;gpnam3: SMSQ10.100

;$Id: hsqcgpph,v 1.5.4.1.4.3
   2014/01/17 15:19:37 ber Exp $
```

Matlab Scripts

ReadWritePulses

A collection of Matlab functions that read, write, convert and display Bruker and Octopussi pulse shape files. Written for Matlab 2015 ± 5. Input format will be detected automatically (most of the time), and the header will be parsed for expected keywords. The `pars_header.m` script is probably the weak point. Whenever the Octopussi format is changed, some values will be missing from the header variable after parsing. *Somebody* should rewrite that. A shortcut to convert Octopussi files to Bruker format is `oct2bru`. Basic usage examples are

```
[shape, header] = read_pulse(
   filename);
write_pulse(outputfilename, shape,
    header);
oct2bru(inputfilename,
   outputfilename);
```

read_pulse.m

```
% READ_PULSE Reads Bruker and
    octopussi (and maybe some
    other) ascii shape
% pulse files. Lines starting with
    # or $ will be interpreted as
    header.
% Data should follow after the
    header, one line per increment
% seperated by comma, semicolon,
    space or tab.
%
% [shape, header] =
%     read_pulse(string:filename[,
    int:verbose])
%
% filename: string; path to pulse
    file, sole required argument.
```

```
% verbose: int; control amount of
    output, 0=quiet, 2=max.
%
% shape is a struct containing .
    data=the shape itself in
    cartesian form
% and some additional information.
% header contains as many
    parameters as could be
    extracted as well as
%   the whole header (without #, $
    ) in header.text.

function [shape, header] =
    read_pulse(filename, verbose)
%% set to 1 for debuging /
    debugging statements...
% if 0
%     clear;
%     verbose = 2;
%
%     %example filenames:
%     %filename = 'C:\Program
    Files\MATLAB\R2010b\etc\wave\
    jc05_BEBOP_z-y_550u_BW37.5
    _RF10_pm5_matched.pul';
%     %filename = 'C:\Program
    Files\MATLAB\R2010b\etc\wave\
    quadratpuls';
%     filename = 'C:\Bruker\
    TopSpin3.0\exp\stan\nmr\lists\
    wave\Crp60,0.5,20.1';
%     %filename = 'C:\Program
    Files\MATLAB\R2010b\etc\wave\
    gaussian_256 - Kopie.pk';
% end
%%check matlab version
versionn = version;
versionn = str2double(versionn(1))
    ;

%% check arguments
if nargin < 1  %is any filename
    available
    error('read_pulse: no filename
        supplied.');
end
if nargin > 2 %display status
    information?
    if ~isnumeric(verbose)
        if verbose < 0
            verbose = 0;
    end
    elseif verbose > 2
        verbose = 2;
    end
else
    verbose = 0;
end

if versionn>6
%% Open the file and verify
% Correct the slashes to match the
    system architecture. doesn't
    work on matlab6
if ispc
    filename=regexprep(filename,'/
        ','\');
else
    filename=regexprep(filename,'\
        ','/');
end
end

wavefile = fopen(filename, 'r');

if wavefile < 0
    error([mfilename ': ' filename
        ' does not exist or could
       not be opened']);
else
    if verbose > 1
        disp([mfilename ': opened
            file ' filename]);
    end
end

% read header from open file
header = parse_header(wavefile,
    verbose);
% read rest of file, hopefully the
    real data
shape = parse_data(wavefile,
    verbose);
fclose(wavefile);

header.filename = filename;
shape.filename = filename;
```

```
%% check what''s been read.
%there must be data in file
if shape.npoints <= 0
    error([mfilename ': no data in
        file ' filename]);
end

%if ~isfield(header,'text')
    header.fileformat =
        guess_format(shape);
%end

if strcmp(header.fileformat, '
    bruker')
    shape = transform_shape(shape)
        ;
end

    %else: check for NaN in data
        ...
if any(any(isnan([shape.data{:}]))
    )
    warning([mfilename ': data
        contains NaN']);
end
if any(any(isinf([shape.data{:}]))
    )
    warning([mfilename ': data
        contains Inf']);
end

%create header or check [header
    <-> data] consistency
[tempnull, header] =
    confirm_header(shape, header);
clear('tempnull');

shape.maxampl = max(sqrt(shape.
    data{1}.^2+shape.data{2}.^2) )
    ;
```

guess_format.m

```
function fileformat = guess_format
    (shape)

%fileformat
shape_max(1) = max(shape.data{1});
shape_max(2) = max(shape.data{2});
shape_min(1) = min(shape.data{1});
shape_min(2) = min(shape.data{2});

cguess= 0;
%cguess will be incremented for
    octopussi,
%   decremented for bruker
% final value positiv -> oct,
    negativ -> bru
cguess = cguess + shape_max(1)>
    101 -0.5;
cguess = cguess + shape_max(2)>
    360*2 -0.5;
cguess = cguess + 0.7* ((shape_min
    (1)< -1) -0.5);
cguess = cguess + 0.3* ((shape_min
    (1)< -101) -0.5);
cguess = cguess + 0.7* ((shape_min
    (2)< -1)-0.5);
cguess = cguess + 0.3* ((shape_min
    (2)< -360*2) -0.5);
%amplitudes and angles could be
    negative after conversion

%max_x \approx max_y in octopussi
% -> max 2 <101 -> octo IF max 2 <
    101, too (and max(x^2+y^2) <
    101^2)

if cguess > 0
    fileformat = 'octopussi';
elseif cguess <0
    fileformat = 'bruker';
else
    fileformat = 'unknown';
end
```

parse_data.m

```
% PARSE_DATA parses pulse-file
    data using textscan
% shape = parse_shape(fileID:
    wavefile[, int:verbose])
%
% wavefile is the fileID of an
    open file
% verbose level 0-2 controls the
    amount of output
```

```
% (currently the only 0 and 1 have
    an effect)
%
% shape is a struct-variable
    containing .data={columns} of
    the file
% and some other data

function shape=parse_data(wavefile
    , verbose)

%% read the rest of the file
if nargin <1
    error([mfilename ': no fileID
        supplied']);
elseif nargin <2
    verbose = 0;
end

versionn = version;
versionn = str2double(versionn(1))
    ;
if versionn>6
[columns, fposition] = ...
    textscan(wavefile, '%f%f%f%f%f
        ', 'Delimiter', ', ;\t', '
        MultipleDelimsAsOne', true
        );
else

end

ncolumns = 0;

%% create output
for n = 1:length(columns)
    if ~all(isnan(columns{n}))
        ncolumns = ncolumns+1;
    end

%another way assigns array in the
    loop,
%that''s not how it should be done
    but
%shouldn''t really matter for 2-3
    columns
%     if ~all(isnan(columns{n}))
%       shape.data{n} = columns{n
    };
%     shape.ncolumns =
%     end
end

if ncolumns > 0
    shape.data = cell(1, ncolumns)
        ;
    shape.data = columns(1:
        ncolumns);
    shape.npoints = length(columns
        {1});
    shape.ncolumns = ncolumns;
    if verbose > 0
    disp([mfilename ': finished
        reading ' num2str(ncolumns
        ) ' columns x ' ...
         num2str(shape.npoints) '
            points of data.']);
    end
else
    shape.npoints = 0;
    shape.npoints = 0;
    warning([mfilename ': no
        readable data in file,
        position ' num2str(
        fposition) '.']);
end

end
```

parse_header.m

```
% PARSE_HEADER parses pulse-file
    header linewise,
% looking for #, ##, ##$ or $$ at
    beginning-of-line
% header = parse_header(fileID:
    wavefile[, int:verbose])
%
% wavefile is the fileID of an
    open file
% verbose level 0-2 controls the
    amount of output
% (currently the only 0 and 1 have
    an effect)
%
% header is a struct-variable full
    of parameters and
```

```
% header.text is the full header
    stripped of #, $
%
% final position in file is
    beginning of first non-header-
    line

function header=parse_header(
    wavefile, verbose)

versionn = version;
versionn = str2double(versionn(1))
    ;

if nargin <1
    error([mfilename ': no fileID
        supplied.']);
elseif nargin <2
    verbose = 0;
end


%filecounter starts at 0, is
    incremented
%after reading a line and
    identifying it as header
file_line = 0;
end_of_header = 0;
fposition = ftell(wavefile);
curline = '';
fileformat = 'unknown';

while ~end_of_header==1 && ~feof(
    wavefile)
    %% read one line, check
        leading chars

    %save current position, then
        read one line
    fposition = ftell(wavefile);
    curline = fgetl(wavefile);


    %add current line to header.
        text, if it is still
        header
    %header is identified by # or
        $ at BOL
    if curline(1) == '#' | curline
        (1) == '$'
        %increment linecounter
        file_line = file_line+1;

        %header.text should not
            contain # or $ at BOL
        %will be stripped now: (
            not in matlab6)
        if versionn>6
            header.text{file_line}
                = regexprep(
                curline,'^[#$]+',
                '');
        end
    else
        %if a line without #/$
            occures, this marks
            the beginning of data
        %strange characters in
            header could result in
             early termination
        %of the header
        end_of_header = 1;
    end

    %% identify format

    %to detect file format, the
        first line is searched for
         the
    %jcamp-conform '##title=' line
        .

    if file_line == 1 && length(
        curline)>8 && ~isempty(
        strfind(lower(curline(1:8)
        ), '##title='))
            fileformat = 'bruker';
    end

    %this is a bit guessy for the
        octopussi format,
    %but there seems to be no good
         way to determine it from
        first line
    %check again at second line,
        should contain '#' and '
        cost'.
```

```
if file_line == 2 && strcmp(
    fileformat, 'unknown') &&
    curline(1) == '#'
     if ~isempty(strfind(lower(
         curline), 'cost' ))
          fileformat = '
              octopussi';
     elseif ~isempty(strfind(
         lower(curline), '
         bruker' ))
          fileformat = 'bruker';
          %if the ##title= is
              not present, a '
              bruker' in the
              second line
          %would indicate a
              bruker shape file.
     else
          fileformat = 'unknown'
              ;
          %this will apply both
              bruker and
              octopussi keyword
              matching
          %in hope to get
              anything at all...
     end
end
%after whole header has been
    read, the 'jcamp-dx' line
    could help
%further to determine file
    format if more complicated
     cases arise.

%octopussi: last line is
    something like x-ampl... y
    -ampl...

header.fileformat = fileformat
    ;

%% parse contents of header
    for usable variables
%parsing the header is really
    annoying...
%-use strfind to find specific
     strings.
%-use textscan on the curline-
    string with fancy format
    to
% extract entry as cell.
%-turn cell into array=string.

%bruker:
% thinking about those strings
    , it should be fine to
    remove
% the ##$= from the strfind
    and match some more cases
if strcmp(fileformat,'bruker')
     || strcmp(fileformat,'
    unknown')
     if ~isempty(strfind(lower(
         curline), '##title='))
          header.title =
              textscan(curline,
              '%s', '
              CommentStyle', {'#
              ', '='}, '
              Delimiter','\r\n')
              ;
          header.title =
              cell2mat(header.
              title{1});
     elseif ~isempty(strfind(
         lower(curline), '##
         npoints='))
          header.npoints =
              textscan(curline,
              '%s', '
              CommentStyle', {'#
              ', '='}, '
              Delimiter','\r\n')
              ;
          header.npoints =
              str2double(
              cell2mat(header.
              npoints{1}));
     elseif ~isempty(strfind(
         lower(curline), '##
         jcamp-dx='))
          header.jcampdx =
              textscan(curline,
              '%s', '
              CommentStyle', {'#
              ', '='}, '
```

```
            Delimiter','\r\n')
            ;
        header.jcampdx =
            cell2mat(header.
            jcampdx{1});
    elseif ~isempty(strfind(
        lower(curline), '##
        $bandwidth='))
        header.bandwidth =
            textscan(curline,
            '%s', '
            CommentStyle', {'#
            ', '='}, '
            Delimiter','\r\n')
            ;
        header.bandwidth =
            str2double(
            cell2mat(header.
            bandwidth{1}));
    elseif ~isempty(strfind(
        lower(curline), '##
        $inputfile='))
        header.inputfile =
            textscan(curline,
            '%s', '
            CommentStyle', {'#
            ', '='}, '
            Delimiter','\r\n')
            ;
        header.inputfile =
            cell2mat(header.
            inputfile{1});
    elseif ~isempty(strfind(
        lower(curline), '##
        $rfampl='))
        header.rfampl =
            textscan(curline,
            '%s', '
            CommentStyle', {'#
            ', '='}, '
            Delimiter','\r\n')
            ;
        header.rfampl =
            str2double(
            cell2mat(header.
            rfampl{1}));
    elseif ~isempty(strfind(
        lower(curline), '##
        $cost='))
        header.cost = textscan
            (curline, '%s', '
            CommentStyle', {'#
            ', '='}, '
            Delimiter','\r\n')
            ;
        header.cost =
            str2double(
            cell2mat(header.
            cost{1}));
    elseif ~isempty(strfind(
        lower(curline), '##
        $pulseclass='))
        header.pulseclass =
            textscan(curline,
            '%s', '
            CommentStyle', {'#
            ', '='}, '
            Delimiter','\r\n')
            ;
        header.pulseclass =
            cell2mat(header.
            pulseclass{1});
    elseif ~isempty(strfind(
        lower(curline), '##
        $pulselength='))
        header.pulselength =
            textscan(curline,
            '%s', '
            CommentStyle', {'#
            ', '='}, '
            Delimiter','\r\n')
            ;
        header.pulselength =
            str2double(
            cell2mat(header.
            pulselength{1}));
    elseif ~isempty(strfind(
        lower(curline), '##
        $pulsedig='))
        header.pulsedig =
            textscan(curline,
            '%s', '
            CommentStyle', {'#
            ', '='}, '
            Delimiter','\r\n')
            ;
        header.pulsedig =
            str2double(
```

```
            cell2mat(header.
            pulsedig{1}));
        elseif ~isempty(strfind(
            lower(curline), '##
            $rfcomp='))
            header.rfcomp =
            textscan(curline,
            '%s', '
            CommentStyle', {'#
            ', '='}, '
            Delimiter','\r\n')
            ;
            header.rfcomp =
            str2double(
            cell2mat(header.
            rfcomp{1}));
        elseif ~isempty(strfind(
            lower(curline), '##
            $transfer='))
            header.transfer =
            textscan(curline,
            '%s', '
            CommentStyle', {'#
            ', '='}, '
            Delimiter','\r\n')
            ;
            header.transfer =
            cell2mat(header.
            transfer{1});
        elseif ~isempty(strfind(
            lower(curline), '##
            $selectivity='))
            header.selectivity =
            textscan(curline,
            '%s', '
            CommentStyle', {'#
            ', '='}, '
            Delimiter','\r\n')
            ;
            header.selectivity =
            str2double(
            cell2mat(header.
            selectivity{1}));
    end
end

%octopussi:

if strcmp(fileformat, '
    octopussi') || strcmp(
    fileformat,'unknown')
    if ~isempty(strfind(lower(
        curline), 'cost␣␣'))
        header.cost = textscan
            (curline, '#%s%s')
            ;
        header.cost=
            str2double(
            cell2mat(header.
            cost{2}));
    elseif ~isempty(strfind(
        lower(curline), '
        npulses'))
        header.npoints =
            textscan(curline,
            '#%s%s');
        header.npoints=
            str2double(
            cell2mat(header.
            npoints{2}));
    elseif ~isempty(strfind(
        lower(curline), '
        plength/us'))
        header.pulselength =
            textscan(curline,
            '#%s%s');
        header.pulselength=
            str2double([
            cell2mat(header.
            pulselength{2}) 'E
            -06']);
    elseif ~isempty(strfind(
        lower(curline), 'bw_i'
        ))
        header.bandwidth =
            textscan(curline,
            '#%s%s%s');
        header.bandwidth=
            str2double(
            cell2mat(header.
            bandwidth{3}));
    elseif ~isempty(strfind(
        lower(curline), '
        maxrf_'))
        header.rfampl =
            textscan(curline,
            '#%s%s%s');
```

```
            header.rfampl=
                str2double(
                cell2mat(header.
                rfampl{3}));
        elseif ~isempty(strfind(
            lower(curline), 'b1␣
            dev'))
            header.rfcomp =
                textscan(curline
                (21:end), '%s');
            header.rfcomp=
                str2double(
                cell2mat(header.
                rfcomp{1}));
        elseif ~isempty(strfind(
            lower(curline), '
            scalecs'))
            header.scalecs =
                textscan(curline,
                '#%s%s');
            header.scalecs=
                str2double(
                cell2mat(header.
                scalecs{2}));
        end
    end
end

%% rewind to beginning of data,
    final output
%rewind file to beginning of
    current line
fseek(wavefile, fposition, -1);

%linecounter was 0 in the
    beginning, if it was never
    incremented
%the header is empty or couldn''t
    be read.
if file_line < 1
    warning([mfilename ':␣no␣
        header␣could␣be␣read.']);
    header.lines = 0;
else
    header.lines = length(header.
        text);
    if verbose > 1 %if requested,
        state what happened...
        disp([mfilename ':␣
            finished␣reading␣'
            num2str(header.lines)
            ...
            '␣lines␣of␣header,␣
                format␣is␣' header
                .fileformat '.']);
    end
end
```

confirm_header.m

```
function [conflicts, header] =
    confirm_header(shape, header)
%shape should always be cartesian
    at this point
if nargin<1
    error([mfilename ':␣no␣shape␣
        supplied.']);
end
if nargout == 2
    %if header is requested for
        output
    keep_header = false;
    %header will be overwritten to
        match the shape data
else
    keep_header = true;
end
if nargin <2
    header = struct;
    keep_header = false;
end

conflicts=0;
%in some cases '==' comparison
    might fail
%this tolerance will be used in an
    inequality:
num_tolerance = 0.000000001;

%npoints
if isfield(header,'npoints') &&
    shape.npoints ~= header.
    npoints
    warning([mfilename ':␣npoints␣
        in␣header␣(' num2str(
        header.npoints) ...
```

```
        ') conflicts with number
            of lines in data ('
            num2str(shape.npoints)
             ').']);
    conflicts = conflicts+1;

    if ~keep_header
        header.npoints = shape.
            npoints;
    end
elseif ~keep_header
    header.npoints = shape.npoints
        ;
end

%rflimit
% rf must not exceed header.rfampl
    - count occurences and warn
if isfield(header,'rfampl')
    rfexceeds = sum((shape.data
        {1}.^2+shape.data{2}.^2) /
         header.rfampl^2 - 1 >
        num_tolerance);
    if rfexceeds > 0
        warning([mfilename '
            Maximum amplitude ('
            num2str(header.rfampl)
             ' kHz) exceeded '
            num2str(rfexceeds) ...
             ' times, maximum is '
                num2str(sqrt(max(
                shape.data{1}.^2+
                shape.data{2}.^2))
                ) '.']);
        conflicts = conflicts+1;
    end
elseif ~keep_header
    rfmax = round(sqrt(max(shape.
        data{1}.^2 + shape.data
        {2}.^2 )));
    round_value = 100+ 400*(rfmax
        > 101) ; %für bruker wird
        100 benutzt, sonst wird
        auf 500er gerundet
    rfmax = ceil(rfmax/round_value
        )*round_value;
    header.rfampl = rfmax;
end

%pulselength and time
    digitalization
%first condition: enough columns
%2nd condition: (sum of tdig)/
    plength = 1
% (due to numerical errors this is
     an inequality)
%pulselength in octopussi output
    is in us
if length(shape.data) > 2 &&
    isfield(header,'pulselength')
    ...
        && abs(sum(shape.data{3}/
            header.pulselength)-1)
             > num_tolerance
    warning([mfilename ': '
        pulselength from header
        conflicts with sum of
        increments']);
    conflicts = conflicts+1;

elseif ~keep_header
    if length(shape.data) == 3 &&
        min(shape.data{3}) > 0
        plength = sum(shape.data
            {3});
        if plength < 100
            header.pulselength =
                plength;
        end
    elseif length(shape.data) == 4
        && min(shape.data{4}) > 0
        plength = sum(shape.data
            {4});
        if plength < 100
            header.pulselength =
                plength;
        end
    end
end
```

transform_shape.m

```
function shape=transform_shape(
    shape, rfampl, direction)
%default direction is polar to
    cartesian (octopussi to bruker
    )
%reverse with 'reverse'
```

```
%    shape=transform_shape(shape)
%    shape=transform_shape(shape,
    rfampl, 'reverse');
if nargin<2 || ~isnumeric(rfampl)
    rfampl=100;
end

if nargin<3 || ~strcmp(direction,
    'reverse')
    %normal way

    %direct conversion using
        matlab's pol2cart(theta, r
        ),
    %bruker-angle is in degree ->
        radians
    [shape.data{1}, shape.data{2}]
         = pol2cart(pi/180*shape.
        data{2}, shape.data{1}*
        rfampl/100);


else
    %reverse calculation
    [shape.data{2}, shape.data{1}]
         = cart2pol(shape.data{1},
         shape.data{2});

    %conversion to bruker-like
        format needs:
    %-turning negative to positive
         angles (adding 2pi) using
         mod, the sign
    %  of mod(x,y) equals the sign
         of y, so no further
        calculations.
    %-conversion to degree.
    shape.data{2} = mod(shape.data
        {2}, 2*pi)*180/pi;

    shape.data{1} = shape.data{1}
        / rfampl * 100;
end
```

write_bruker.m

```
% WRITE_BRUKER writes cartesian
    pulse shape to bruker file
% write_bruker(string:filename,
    struct:shape, struct:header[,
    int:verbose])
%
% existing file will be
    overwritten.


function writeerror = write_bruker
    (filename, shape, header,
    verbose)
%check arguments
if nargin < 2
    error([mfilename ': string:
        filename and struct:shape
        are required arguments.'])
        ;
end
if nargin < 3
    [~,header] = confirm_header(
        shape);
else
    [~, header] = confirm_header(
        shape, header);
end
if nargin <4 || ~isnumeric(verbose
    ) || verbose <0
    verbose = 0;
end

%check for varying timestep length
    ...
%this is currently not supported
    :(
if length(shape.data) > 2 && not(
    all(shape.data{3}==shape.data
    {3}(1)))
    disp([mfilename ': Irregular
        pulse interval lengths,
        splitting integrals
        currently not supported.'
        ]);
end

%make sure shape.data is a column
    vector

for n=1:length(shape.data)
    %this means column:
```

```
    if all([size(shape.data{n})>1]
        == [1 zeros((ndims(shape.
        data{n}))-1)])
        %do nothing, mentioned for
            readability...

        %this means line vector:
    elseif all([size(shape.data{n
        })>1] == [0 1 zeros((ndims
        (shape.data{n}))-2)])
        %flip the vector
        shape.data{n} = shape.data
            {n}.';

    else
        error([mfilename ': shape.
            data has unrecognized
            format.'])
    end
end

shape = transform_shape(shape,
    header.rfampl, 'reverse');

%% Open the file and verify
% Correct the slashes to match the
    system architecture
if ispc
    filename=regexprep(filename,'/
        ','\');
else
    filename=regexprep(filename,'\
        ','/');
end

if exist(filename, 'file')==2
    if verbose > 0
    disp([mfilename ': file exists
        , will be renamed to .
        write_pulse_backup.']);
    end
    movefile(filename, [filename '
        .write_pulse_backup']);
end

wavefile = fopen(filename, 'w');

if wavefile < 0
    error([mfilename ': ' filename
        ' could not be opened']);
else
    if verbose > 1
        disp([mfilename ': opened
            file ' filename]);
    end
end

%% write file
bytecount=0;
%write header, moved to own
    function because of
    annoyingness...
bytecount = bytecount+
    write_bruker_header(wavefile,
    header);

%write full header as comment
if isfield(header, 'text')
    bytecount = bytecount +
        fprintf(wavefile,'##=%s\r\
        n', header.text{:});
end

%this is the opening of the data
    part
bytecount = bytecount + fprintf(
    wavefile,'##%s= %s\r\n', '
    XYPOINTS', '(XY..XY)');

if bytecount <= 0
    warning([mfilename ': No
        header could be written to
        ' filename]);
elseif verbose >1
    disp([mfilename ': ' num2str(
        bytecount) ' bytes of
        header written to file.'])
        ;
end



%write shape, this line does it:
bytecount = fprintf(wavefile, '
    %9.9f,\t %9.9f\r\n', [shape.
    data{1}.'; shape.data{2}.']);
```

```
if bytecount <= 0
    error([mfilename ': No data
        could be written to '
        filename]);
elseif verbose >1
    disp([mfilename ': ' num2str(
        bytecount) ' bytes of data
        written to file.']);
end

%this ends the file
fprintf(wavefile, '##%s=\r\n', '
    END');

fclose(wavefile);
if bytecount > 0
    writeerror = 0;
else
    writeerror = 1;
end

if verbose > 0
disp(['pulseshape written to file
    ' filename]);
end
```

write_bruker_header.m

```
function bytecount =
    write_bruker_header(wavefile,
    header)
bytecount = 0;


if isfield(header, 'title')
    bytecount = bytecount +
        fprintf(wavefile,'##%s= %s
        \r\n', 'TITLE', header.
        title);
else
    bytecount = bytecount +
        fprintf(wavefile,'##%s=\r\
        n', 'TITLE');
end
bytecount = bytecount + fprintf(
    wavefile,'##%s= %s\r\n', '
    jcamp-dx', '5.00 Bruker JCAMP
    library');
bytecount = bytecount + fprintf(
    wavefile,'##%s= %s\r\n', '
    owner', [getenv('username')
    getenv('USER')]);
bytecount = bytecount + fprintf(
    wavefile,'##%s= %s\r\n', '
    origin', 'ioc/ibg2/kit');
bytecount = bytecount + fprintf(
    wavefile,'##%s= %s\r\n', '
    data_type', 'shape data');

bytecount = bytecount + fprintf(
    wavefile,'##$%s= \r\n', '
    SHAPE_PARAMETERS');
bytecount = bytecount + fprintf(
    wavefile,'##$%s= \r\n', '
    SHAPE_BWFAC');
bytecount = bytecount + fprintf(
    wavefile,'##$%s= \r\n', '
    SHAPE_INTEGFAC');
bytecount = bytecount + fprintf(
    wavefile,'##$%s= \r\n', '
    SHAPE_MODE');
bytecount = bytecount + fprintf(
    wavefile,'##%s= %s\r\n', 'MINX
    ', '0.0E00');
bytecount = bytecount + fprintf(
    wavefile,'##%s= %s\r\n', 'MAXX
    ', '1.0E02');

if isfield(header, 'pulseclass')
    bytecount = bytecount +
        fprintf(wavefile,'##$%s= %
        s\r\n', 'pulseclass',
        header.pulseclass);
end
if isfield(header, 'cost')
    bytecount = bytecount +
        fprintf(wavefile,'##$%s= %
        G\r\n', 'cost', header.
        cost);
end
if isfield(header, 'inputfile')
    bytecount = bytecount +
        fprintf(wavefile,'##$%s= %
        s\r\n', 'inputfile',
        header.inputfile);
end
if isfield(header, 'filename')
```

```
    bytecount = bytecount +
        fprintf(wavefile,'##$%s= %
        s\r\n', 'filename', header
        .filename);
end
if isfield(header, 'bandwidth')
    bytecount = bytecount +
        fprintf(wavefile,'##$%s= %
        G\r\n', 'bandwidth',
        header.bandwidth);
else
    bytecount = bytecount +
        fprintf(wavefile,'##$%s=\r
        \n', 'bandwidth');
end
if isfield(header, 'rfampl')
    bytecount = bytecount +
        fprintf(wavefile,'##$%s= %
        G\r\n', 'rfampl', header.
        rfampl);
else
    bytecount = bytecount +
        fprintf(wavefile,'##$%s=\r
        \n', 'rfampl');
end
if isfield(header, 'rfcomp')
    bytecount = bytecount +
        fprintf(wavefile,'##$%s= %
        G\r\n', 'rfcomp', header.
        rfcomp);
else
    bytecount = bytecount +
        fprintf(wavefile,'##$%s=\r
        \n', 'rfcomp');
end
if isfield(header, 'pulselength')
    bytecount = bytecount +
        fprintf(wavefile,'##$%s= %
        G\r\n', 'pulselength',
        header.pulselength);
else
    bytecount = bytecount +
        fprintf(wavefile,'##$%s=\r
        \n', 'pulselength');
end
if isfield(header, 'pulsedig')
    bytecount = bytecount +
        fprintf(wavefile,'##$%s= %
        G\r\n', 'pulsedig', header
        .pulsedig);
else
    bytecount = bytecount +
        fprintf(wavefile,'##$%s=\r
        \n', 'pulsedig');
end
if isfield(header, 'selectivity')
    bytecount = bytecount +
        fprintf(wavefile,'##$%s= %
        G\r\n', 'selectivity',
        header.selectivity);
end

if isfield(header, 'npoints')
    bytecount = bytecount +
        fprintf(wavefile,'##%s= %u
        \r\n', 'NPOINTS', header.
        npoints);
else
    bytecount = bytecount +
        fprintf(wavefile,'##%s=\r\
        n', 'NPOINTS');
    warning([mfilename ': npoints
        not set in header.']);
end

if isfield(header, 'scalecs')
    bytecount = bytecount +
        fprintf(wavefile,'##$%s= %
        G\r\n', 'scalecs', header.
        scalecs);
end
```

write_octopussi.m

```
% WRITE_OCTOPUSSI writes cartesian
    pulse shape to octopussi
% file (e.g. for further
    optimizations).
% write_bruker(string:filename,
    struct:shape, struct:header[,
    int:verbose])
%
% existing file will be
    overwritten.
```

```
function writeerror =
    write_octopussi(filename,
    shape, header, verbose)
%check arguments
if nargin < 2
    error([mfilename ': string:
        filename and struct:shape
        are required arguments.'])
        ;
end
if nargin < 3
    [~,header] = confirm_header(
        shape);
else
    [~, header] = confirm_header(
        shape, header);
end
if nargin <4 || ~isnumeric(verbose
    ) || verbose <0
    verbose = 0;
end


%% Open the file and verify
% Correct the slashes to match the
     system architecture
if ispc
    filename=regexprep(filename,'/
        ','\');
else
    filename=regexprep(filename,'\
        ','/');
end

if exist(filename, 'file')==2
    if verbose > 0
    disp([mfilename ': file exists
        , will be renamed to .
        write_pulse_backup.']);
    end
    movefile(filename, [filename '
        .write_pulse_backup']);
end

wavefile = fopen(filename, 'w');

if wavefile < 0
    error([mfilename ': ' filename
         ' could not be opened']);
else
    if verbose > 1
        disp([mfilename ': opened
            file ' filename]);
    end
end

%% write file
bytecount=0;
%write header, moved to own
    function because of
    annoyingness...
%this does not exist: the header
    is ignored by octopussi
    anyways.
%bytecount =
    write_octopussi_header(
    wavefile, header);

%write full header as comment
%whatever is available of the
    original header will be
    written again
if isfield(header, 'text')
    bytecount = bytecount +
        fprintf(wavefile,'#   %s\r
        \n', header.text{:});
end

if bytecount <= 0
    warning([mfilename ': No
        header could be written to
        ' filename]);
elseif verbose >1
    disp([mfilename ': ' num2str(
        bytecount) ' bytes of
        header written to file.'])
        ;
end

%check for varying timestep length
    ...
%this is currently not supported
    :(
%but no problem for octopussi
    files :)
% if length(shape.data) > 2 && not
    (all(shape.data{3}==shape.data
    {3}(1)))
```

```
%     disp([mfilename ': Irregular
    pulse interval lengths,
    splitting integrals currently
    not supported.']);
% end

%write shape, this line does it:
%bytecount = fprintf(wavefile,
    '%9.9f\t %9.9f\t %9.9f\r\n', [
    shape.data{1}.'; shape.data
    {2}.'; shape.data{3}.']);
bytecount = fprintf(wavefile, '
    %9.9f\t %9.9f\t %9.9f\r\n', [
    shape.data{1}.' shape.data
    {2}.' shape.data{3}.'].');

if bytecount <= 0
    error([mfilename ': No data
        could be written to '
        filename]);
elseif verbose >1
    disp([mfilename ': ' num2str(
        bytecount) ' bytes of data
        written to file.']);
end

fclose(wavefile);
if bytecount > 0
    writeerror = 0;
else
    writeerror = 1;
end

if verbose > 0
disp(['pulseshape written to file
    ' filename]);
end
```

display_shape.m

```
function display_shape(shape,
    header)

%get pulselength...

maxrf=max(max(abs([shape.data{:}])
    ));

subplot(2,1,1)
plot(shape.data{1}/maxrf,'b');
hold on
plot(shape.data{2}/maxrf,'r');
hold off
legend('x','y');
title('x- and y-amplitude');

shape=transform_shape(shape, maxrf
    , 'reverse');

subplot(2,1,2)
plot(shape.data{1}/100,'r');
hold on
plot(shape.data{2}/360,'b');
hold off
legend('ampl','phase');
title('amplitude and phase');
```

split_pulse.m

```
function shape = split_pulse(shape
    , number)

if exist('number','var') && 0==mod
    (number,1) && number>1
    multiplylist = number*ones(1,
        shape.npoints);
else
    number = 1;
    multiplylist = shape.data{3}/
        min(shape.data{3});

    %check for non-multiple steps
    while any(multiplylist*number
        ~= double(uint64(
        multiplylist*number)))
        number=number+1;
    end
    multiplylist=multiplylist*
        number;
    disp([mfilename ': Trying to
        get equal steps for all
        increments.']);
end
disp([mfilename ': Number of steps
    multiplied by ' num2str(
    number) '.' ]);
% alternative method:
```

```
% mod(shape.data{3}/min(shape.data
    {3}),1);


for old_pos = 1:length(shape.data
    {3})
    new_pos = sum(multiplylist(1:
        old_pos-1));
    for splitindex = 1:
        multiplylist(old_pos)
        for n=1:2
            newshape.data{n}(
                new_pos+splitindex
                ) = shape.data{n}(
                old_pos);
        end
    end
end

shape.npoints=sum(multiplylist);
newshape.data{3}=ones(1,shape.
    npoints)*min(shape.data{3}/
    number);

% % length(shape.data{3})
% % length(newshape.data{3})
% % min(shape.data{3})
% % max(shape.data{3})
% % min(newshape.data{3})
% % max(newshape.data{3})
% % sum(shape.data{3})
% % sum(newshape.data{3})

shape.data=newshape.data;
end
```

oct2bru.m

```
% OCT2BRU reads a pulse-shape-file
    and converts it to bruker-
    format.
% If no output filename is given,
    .bru will be attended to
    filename.
%   oct2bru(string:infilename[,
    string:outfilename])

function oct2bru(infilename,
    outfilename)

if nargin<1 %check arguments
    error([mfilename ':␣no␣
        filename␣given']);
elseif nargin<2
    outfilename = [infilename '.
        bruker'];
end

[shape, header]=read_pulse(
    infilename); %read pulse
write_bruker(outfilename, shape,
    header); %write pulse
```

Progressive Excitation

Declarations

```
    td1 = 512; %number of scans
    flip = zeros(1,td1); %initial
        flip angles
    flip(td1) = pi/2; %last flip
        angle
    pola = ones(1,td1+1); %
        magnetisierung vor dem
        scan i, (direkt vor dem
        puls)
    signal = zeros(1,td1); %signal
         beim scan i (direkt nach
        dem puls)
    %magnetisierung nach dem puls
        ist pola(i+1)
    %   == magnetisierung vor dem
        scan i+1
    d = 1; %13C-protonen
    r = 2; %remote protonen
         tau = 1; %recovery time
    t1 = 10; %t_1 relaxation time
```

Without Relaxation

```
% initialize final flip angle
flip(td) = pi/2;
% recursive calculation of all
    other flip angles
for itd = td-1:-1:1
  flip(itd) = atan(sin(flip(itd+1)
      ));
end
```

```
% simulating the experiment
for itd = 1:td
  pola(itd+1) = pola(itd)*cos(flip
      (itd));
  signal(itd) = pola(itd)*sin(flip
      (itd));
end
```

Ideal ASAP-Style Mixing

```
% initialize final flip angle
flip(td) = pi/2;
% recursive calculation of all
    other flip angles
for itd = td-1:-1:1
  % temporary variables for easier
      reading
  sin2 = sin(real(flip(itd+1)));
  a = (r+d);
  b = -d*sin2;
  c = -r*sin2;
  % solving the equation for flip
      angle
  flip(itd)=fzero(@(x)(a*sin(x)+b*
      cos(x)+c), flip(itd));
end
% simulating the experiment
for itd = 1:td
  pola(itd+1) = pola(itd)*(d*cos(
      flip(itd))+r)/(r+d);
  signal(itd) = pola(itd)*sin(flip
      (itd));
end
```

T_1 relaxation

```
% initialize final flip angle
flip(td) = pi/2;
% initial guess for polarization
    over experiment
pola = ones(1,td+1);
% loop until calculation converges
while min(signal)/max(signal) <
    0.995
  % recursive calculation of all
      flip angles
  for itd = td-1:-1:1
    % temporary variables for
        easier reading
    sin2 = sin(flip(itd+1));
    expt = exp(-tau/t1);
    % solving the equation for
        flip angle
    flip(itd) = fzero(@(x) -sin(x)
        +cos(x)*expt*sin2 ...
        +sin2/pola(itd)*(1-expt),
            flip(itd));
  end
  % simulating the experiment
  for itd = 1:td
    pola(itd+1) = 1-(1-pola(itd)*
        cos(flip(itd)))*exp(-tau/
        t1);
    signal(itd) = pola(itd)*sin(
        flip(itd));
  end
end
```

Ernst angle

```
% constant flip angle for all
    scans
flip = ones(1,td1)*acos(exp(-tau/
    t1));
for itd = 1:td1
  pola(itd+1) = 1-(1-pola(itd)*cos
      (flip(itd)))*exp(-tau/t1);
  signal(itd) = pola(itd)*sin(flip
      (itd));
end
```

Ideal ASAP-style mixing and T_1 relaxation

```
% initialize final flip angle
flip(td) = pi/2;
% initial guess for polarization
    over experiment
pola = ones(1,td+1);
% loop until calculation converges
while min(signal)/max(signal) <
    0.995
  % recursive calculation of all
      flip angles
  for itd = td-1:-1:1
```

```
    % temporary variables for
        easier reading
    sin2 = sin(flip(itd+1));
    expt = exp(-tau/t1);
    % solving the equation for
        flip angle
    flip(itd) = fzero( @(x)-sin(x)
       +cos(x)*expt*sin2*d/(r+d)
       ...
        +(1-expt+pola(itd)*expt*r
           /(r+d))*sin2/pola(itd)
           , flip(itd));
  end
  % simulating the experiment
  for itd = 1:td
    pola(itd+1) = 1-exp(-tau/t1)+
       pola(itd)*exp(-tau/t1)...
        *(d*cos(flip(itd))+r)/(r+d
           );
    signal(itd) = pola(itd)*sin(
       flip(itd));
  end
end
```

Extensions of the Octopussi Program

Extensions of the Octopussi Program

Calculation for the Quadratic Phase Pulses

Fortran code to calculate the cost function in the file OCTcost.f.

```
c 1spin xy                 unitÃďrer,
    te, quadratic rotation axis
    as function of offset
c                          t
    symmetric BURBOP), 2010.07.22
    SE, Martin Koos
c phi3 quadratic axis
c rechenweg uf: = expm( -ii * pi (
    Ix cos Phase + Iy sin Phase))
c                          !konstante
    =1d-5 !in 1/grad, damit
    phasenwinkel in grad ist
c
    PARALLELproofed
 ================================
      phase = w(1)**2 * offsconst
          !in grad
      call cmul(cos(phase *pi
         /180),ctrlham(1),work1)
      call cmul(sin(phase *pi
         /180),ctrlham(2),work2)
      call madd(work1,work2,
         unitary)
      call czmul(-pi,ii,unitary,
         unitary)
      call expm(1d0,unitary,
         unitary)
         !input: expm(a,H) U=expm
             (a*H), a=real.
             output: work1=U
      call geteye(work1)
      do k=1,npulses
        call gethami(k)
        call expm(duration(k),
           pham(k),work4)   !expm
           (t,Hj,work4)
        call mmul(work4,work1,
           work2)           !(Uj
           +1*Uj...U1)
        call mcopy(work2,work1)
      enddo
      call dagger(unitary,work2)
                !Uf+
      call mmul(work2,work1,work2
         )      !(Uf+ * Uj...U1)
      call trace(work2,ttcost2)
                 !Re(Tr{(Uf+ * Uj
         ...U1)})
      ttcost1=ttcost1-ttcost2/
         normuni
```

Fortran code to calculate the gradient in the file OCTgrad.f.

```
! 2 spins xy    exact   new
    unitary exact grad from
    eigenbasis
! (not symmetric BURBOP),
    2010.07.22
! phi3 quadratic          quadratic
    rotation axis as function of
    offset,
!                          SE, Martin
     Koos
```

```
!                          exat grad
   for universal rotations
   without s-compensation
!
   PARALLELproof SE
 ================================
         phase = w(1)**2 *
            offsconst !in grad
         call cmul(cos(phase *pi
            /180),Ix(1),work1)
         call cmul(sin(phase *pi
            /180),Iy(1),work2)
          call madd(work1,work2,
             unitary)
          call czmul(-pi,ii,
             unitary,unitary)
         call expm(1d0,unitary,
            unitary)
               !input: expm(a,H)
                  U=expm(a*H), a
                  =real. output:
                   work1=U
               !get single U,
                  same U as with
                   expm(-iH),
                  even with full
                   H (+Sctrl)
            call geteye(work1)
            call mdiv(work1,2d0,
               work1)
            do k=1,npulses

                        !einzeln
                alle, voller H
              call geteigenhami(k
                 )
               !VORSICHT: kein -i
                  *... H= 2pi (
                  Vctrl*sum(Ik)
                  + Vz*Iz + Vz*
                  Sz + Vj*Iz*Sz)
              call VDe(pham(k),k)

                           !V=
                 work2, D=wor9,
                 e=work8

              call mcopy(work2,
                 optV(k))
              call mcopy(work9,
                 optD(k))
              call mcopy(work8,
                 opte(k))

              call dagger(work2,
                 work3)
              call mmul(work8,
                 work3,work4)
                                  !
                U = V*e*V'
              call mmul(work2,
                 work4,optG(k))
                           ! G
                 = nicht
                aufmultiplizierte
                 U
            enddo

            ! -------------
               vorwÃ¤rts:
               multiply U
            call geteye(work1)
            call mdiv(work1,2d0,
               prho(1))
                        !DANGER:
                goes til npulses
               +1
            do k=1,npulses

                        ! Ueff,
               U_ISeff = Uj...U1
               *1
              call mmul(optG(k),
                 prho(k),prho(k
                 +1))
            enddo
            call dagger(unitary,
               work2)
                        ! U_IF+
            call mdiv(work2,2d0,
               work2)
                        ! norm

            ! -------------
               rÃ¼ckwÃ¤rts:
               multiply from
               U_IF+
```

```
call dagger(unitary,
    work1)
call mdiv(work1,2d0,
    work1)
! -------------or:
    multiplay from
    U_IF+*U_Seff+

call mcopy(work1,
    plambda(npulses
    +1))          !
    DANGER: comes
    from npulses+1
do k=npulses,1,-1

              !
    rÃ¼ckwÃ¤rts
    aufmultplizieren
    von U
  call mmul(plambda(k
      +1),optG(k),
      plambda(k)) !
      LD (lambda
      dagger)
enddo

! ------------- grad
do ictrl=1,nctrl
  call cmul(pii,
      ctrlham(ictrl),
      workg1(ictrl))
enddo
do k=1,npulses

            ! calc
    grad                !
  call mmul(prho(k),
      plambda(k+1),
      work1)            !
          ! UiUf (
              vorwÃ¤rts
              - mal    !
              rÃ¼ckwÃ¤rts
              -
              multiplikate
              )
  call dagger(optV(k)
      ,work2)

call mmul(work1,
    optV(k),work1)
call mmul(work2,
    work1,work1)
                        !
     V'*UiUf*V,
    checkpoint
    exact
call mtrans(work1,
    work1)
              ! (V'*
    UiUf*V).'
do ictrl=1,2
  call mmul(workg1(
      ictrl),optV(k
      ),workg2(
      ictrl))  ! I*
      V
  call mmul(work2,
      workg2(ictrl)
      ,workg2(ictrl
      ))     ! V'*I*
      V
  call mpstern(
      workg2(ictrl)
      ,optD(k),
      workg2(ictrl)
      )       ! (V
      '*I*V).*D


call mpstern(workg2
    (ictrl),work1,
    workg2(ictrl))
    ! (V'*I*V).*D.*
     (V'*UiUf*V).'
call sumsumim(workg2
(ictrl),gradg(ictrl))       !
imag(sum(sum(" )))
    gradg(ictrl)=gradg(
ictrl)*duration(k)          !
imag(sum(sum("  )))*timestep
    grad(ictrl,k)=grad(
ictrl,k)+gradg(ictrl)
call sumsumim(workg2
    (ictrl),ttcost)
              ! imag(
    sum(sum(" )))
ttcost=ttcost*
    duration(k)*(3-
```

```
                nspins)       !
                imag(sum(sum(  ")
                ))*timestep
              grad2(ictrl,k)=grad2
                (ictrl,k)+ttcost
            enddo
          enddo
```

Spline Interpolated Inital Shapes

Generation of the initial shape in file genctrl.f.

```
c--------> Initialazing starting
    random points
        magnitude=magn
        if (reiseed .eq. 1) then
                              !single
            initialization of
           srand
          call srand(iseed)
        endif

        if (hardpulse(1) .eq. 0)
            then
        do 10 i=1,npulses
          duration(i)=timestep
 10     continue
        endif
        i=1

        u = 0.0
        if (npulses.le.10) then
          n = npulses
        elseif (npulses.lt.1000)
            then
          n = 10
        else
          n = 100
        endif

        do 11 i=1,n
c         dummyx(i)=2*dble(rand(0)
    )-1
c         dummyy(i)=2*dble(rand(0)
    )-1
c         dummyz(i)=2*dble(rand(0)
    )-1
          xw(i) = 2*dble(rand(0))
              -1
          yw(i) = 2*dble(rand(0))
              -1
          zpulse(ispins,i) = 2*
              dble(rand(0))-1
          u(i) = real( ((i-1)*(
              npulses-1)/(n-1))+1
              )

 11     continue

        call spline(u, xw, n, 0.0,
            -0.0, dx2)
        call spline(u, yw, n, 1.0,
            -1.0, dy2)


        do 12 i=1,npulses
          call splint(u, xw, dx2,
              n, dble(i), xpulse(
              ispins,i))
          call splint(u, yw, dy2,
              n, dble(i), ypulse(
              ispins,i))

 12     continue
```

RF Power Limit

File OCT2frprmn.f.

```
c
    ------------------------------------------------

        subroutine cg_rflimit(pvec
            )
c
    ------------------------------------------------

c       calcs rf-limit out of pvec
     (and not out of ctrl)
c       for n spins. each must
    have xy-control

        include 'octopussi.cmn
!\$omp␣THREADPRIVATE(/basics/)dd
␣␣␣␣␣␣␣␣integer␣i,ctrlPerSpin,k
␣␣␣␣␣␣␣␣real*8␣pvec(nctrl*npulses)
    ,gdur,scaledur
```

```
c␣␣␣␣␣␣␣if␣(hardpulse(1)␣.gt.␣0)␣
    goto␣111

␣␣␣␣␣␣␣␣ampl(1)=0.0d0
␣␣␣␣␣␣␣␣if(sctrl(1)␣.eq.␣2)␣then
␣␣␣␣␣␣␣␣␣␣ctrlPerSpin=2␣␣␣␣␣␣␣␣␣␣
    ␣␣␣␣␣␣␣␣␣␣␣␣␣␣␣␣␣␣␣␣␣␣␣␣␣␣␣␣␣
    !␣fr␣alle␣spins␣dieselbe␣ctrl-
    anzahl
␣␣␣␣␣␣␣␣elseif(sctrl(1)␣.eq.␣3)␣
    then
␣␣␣␣␣␣␣␣␣␣ctrlPerSpin=3
␣␣␣␣␣␣␣␣endif

␣␣␣␣␣␣␣␣do␣i=1,npulses
␣␣␣␣␣␣␣␣␣␣do␣ictrl=1,nctrl,
    ctrlPerSpin␣␣␣␣␣␣␣␣␣␣␣␣␣␣␣␣␣␣
    ␣␣␣␣␣␣␣␣␣␣␣␣␣␣␣!␣2␣spins␣xy␣
    oder␣xy(z)
␣␣␣␣␣␣␣␣␣␣␣␣ampl(ictrl)=ampl(1)+(
    pvec(nctrl*i-nctrl+ictrl)**2+␣
    ␣␣␣␣␣␣␣␣␣␣!␣ampl=sqrt(x<B2>+y<
    B2>)
␣␣␣␣␣/pvec(nctrl*i-nctrl+ictrl+1)
    **2)
␣␣␣␣␣␣␣␣␣␣enddo
␣␣␣␣␣␣␣␣enddo
␣␣␣␣␣␣␣␣␣␣ampl(1)=sqrt(ampl(1)/
    npulses)
␣␣␣␣␣␣␣␣do␣i=1,npulses
␣␣␣␣␣␣␣␣␣␣do␣ictrl=1,nctrl,
    ctrlPerSpin
␣␣␣␣␣␣␣␣␣␣␣␣if␣(ictrl␣.lt.␣
    ctrlPerSpin)␣then␣␣␣␣␣␣␣␣␣␣␣␣␣
    ␣␣␣␣␣␣␣␣␣␣␣␣␣␣␣!␣shrink␣ctrl␣
    zu␣spin1␣f<FC>r␣xy␣oder␣xy(z)␣
    ctrl
␣␣␣␣␣␣␣␣␣␣␣␣␣␣if␣(constantPhase␣.
    eq.␣1)␣then
␣␣␣␣␣␣␣␣␣␣␣␣␣␣␣␣pvec(nctrl*i-nctrl
    +ictrl)=pvec(nctrl*i-nctrl+
    ictrl)*␣␣␣␣!␣ctrl*␣%␣von␣
    maxampl
␣␣␣␣␣/maxampl/ampl(1)
␣␣␣␣␣␣␣␣␣␣␣␣␣␣␣␣pvec(nctrl*i-nctrl
    +ictrl+1)=pvec(nctrl*i-nctrl+
    ictrl+1)*
␣␣␣␣␣/maxampl/ampl(1)
␣␣␣␣␣␣␣␣␣␣␣␣␣␣elseif␣(ampl(1)␣.gt.
    ␣maxampl)␣then
␣␣␣␣␣␣␣␣␣␣␣␣␣␣␣␣pvec(nctrl*i-nctrl
    +ictrl)=pvec(nctrl*i-nctrl+
    ictrl)*␣␣␣␣!␣ctrl*␣%␣von␣
    maxampl
␣␣␣␣␣/maxampl/ampl(1)
␣␣␣␣␣␣␣␣␣␣␣␣␣␣␣␣pvec(nctrl*i-nctrl
    +ictrl+1)=pvec(nctrl*i-nctrl+
    ictrl+1)*
␣␣␣␣␣/maxampl/ampl(1)
␣␣␣␣␣␣␣␣␣␣␣␣␣␣endif
␣␣␣␣␣␣␣␣␣␣␣␣else␣␣␣␣␣␣␣␣␣␣␣␣␣␣␣␣␣␣
    ␣␣␣␣␣␣␣␣␣␣␣␣␣␣␣␣␣␣␣␣␣␣␣␣␣␣␣␣␣
    ␣␣␣␣␣␣␣␣!␣spin2␣xy␣oder␣xy/z)
␣␣␣␣␣␣␣␣␣␣␣␣␣if␣(constantPhase␣.eq
    .␣1)␣then
␣␣␣␣␣␣␣␣␣␣␣␣␣␣␣pvec(nctrl*i-nctrl+
    ictrl)=pvec(nctrl*i-nctrl+
    ictrl)*
␣␣␣␣␣/maxampls/ampl(1)
␣␣␣␣␣␣␣␣␣␣␣␣␣␣␣pvec(nctrl*i-nctrl+
    ictrl+1)=pvec(nctrl*i-nctrl+
    ictrl+1)*
␣␣␣␣␣/maxampls/ampl(1)
␣␣␣␣␣␣␣␣␣␣␣␣␣elseif␣(ampl(1)␣.gt.␣
    maxampls)␣then␣␣␣␣␣␣␣␣␣␣␣␣␣␣␣
    ␣␣␣␣␣␣␣␣!␣shrink␣ctrl␣zu␣spin2
␣␣␣␣␣␣␣␣␣␣␣␣␣␣␣pvec(nctrl*i-nctrl+
    ictrl)=pvec(nctrl*i-nctrl+
    ictrl)*
␣␣␣␣␣/maxampls/ampl(1)
␣␣␣␣␣␣␣␣␣␣␣␣␣␣␣pvec(nctrl*i-nctrl+
    ictrl+1)=pvec(nctrl*i-nctrl+
    ictrl+1)*
␣␣␣␣␣/maxampls/ampl(1)
␣␣␣␣␣␣␣␣␣␣␣␣␣endif
␣␣␣␣␣␣␣␣␣␣␣endif
␣␣␣␣␣␣␣␣␣enddo
␣␣␣␣␣enddo
```

Calculations for RADFA

File OCTcost.f.

```
        if (costtype(1,1) .eq.
            120)then
```

```
c 1spins xy                point 2
    point (BEBOP,BIBOP),
    2014.04.01 MK
c variable flip angle pulse,
    dependent on B1. martin
c ================================
      ttcost=0
      call mcopy(initialrho,rho)
      do k=1,npulses

         !vorwï£¡rts bis prho(k
         +1)
       call getham(k)

          !2pi*i(w(1)Iz+WxIx+
          WyIy) in bestehendes
          pham
       call propagate(duration(k)
          ,pham(k))
       call mcopy(rhoout,rho)
      enddo
      call dagger(rhoout,rhoout)
                                  !
         macht aus i- i+
c      martin: hier targetrho
    berechnen...
          call cmul(cos(
             flipa_list(iB1)),
             initialrho, work1)
          call cmul(sin(
             flipa_list(iB1)),
             ix, work2)
          call madd(work1, work2
             , targetrho)
       call mscalp(targetrho,
          rhoout,ttcost2)
                     !trace{
          rhoout,i*t*[Ix,rho]}
c       write(*,*)flipa_list(iB1)
c       write(*,*)'initialrho'
c       call dmx(initialrho)
c       write(*,*)'ix'
c       call dmx(ix)
c       write(*,*)'targetrho'
c       call dmx(targetrho)
      ttcost1=ttcost1+ttcost2/
         normrho
       endif
```

Calculation of the gradient, file OCTgrad.f.

```
        if (costtype(1,1) .eq.
           120)then
c 1 spins xyz   approx
c phi0                     point 2
    point (BEBOP,BIBOP),
    2010.09.29 SE
c ================================

            call geteye(work1)
            call mdiv(work1,2d0,
               work1)
            do k=1,npulses

               !einzeln alle,
               voller H
              call geteigenhami(k
                 )
                !VORSICHT: kein
                 -i*... H= 2pi
                (Vctrl*sum(Ik)
                + Vz*Iz + Vz*Sz
                 + Vj*Iz*Sz)
              call VDe(pham(k),k)


                !V=work2, D=
                wor9, e=work8

              call mcopy(work2,
                 optV(k))
              call mcopy(work9,
                 optD(k))
              call mcopy(work8,
                 opte(k))

              call dagger(work2,
                 work3)
              call mmul(work8,
                 work3,work4)
                                !
                 G = U = V*e*V'
              call mmul(work2,
                 work4,optG(k))
                           ! G
                 = nicht
                 aufmultiplizierte
                  U
```

```
            enddo

! ---       initialrho propagieren
            call mcopy(initialrho,
               prho(1))
            do k=1,npulses

               !
               Aufmultiplizieren,
                von rho
              call dagger(optG(k),
                 work2)
              call mmul(prho(k),
                 work2,prho(k+1))
              call mmul(optG(k),
                 prho(k+1),prho(k
                 +1))
            enddo
c       martin: targetrho
    berechnen. funktion?
            call cmul(cos(
               flipa_list(iB1)),
               initialrho, work1)
            call cmul(sin(
               flipa_list(iB1)),
               ix, work2)
            call madd(work1, work2
               , targetrho)

c       write(*,*)flipa_list(iB1)
c       write(*,*)'initialrho'
c       call dmx(initialrho)
c       write(*,*)'ix'
c       call dmx(ix)
c       write(*,*)'targetrho'
c       call dmx(targetrho)




c       write(*,*)'targetrho'
c       call dmx(targetrho)

! ---       targetrho
    rï£¡ckwï£¡rts propagieren
            call mcopy(targetrho,
               plambda(npulses+1)
               )      ! DANGER:
                  comes from npulses
                  +1
            do k=npulses,1,-1

               ! rï£¡ckwï£¡rts
               aufmultplizieren
               von U
              call dagger(optG(k),
                 work2)
              call mmul(plambda(k
                 +1),optG(k),
                 work3)
              call mmul(work2,
                 work3,plambda(k)
                 )
            enddo
```

Modification for linear-phase RADFA in file OCTcost.f. Same modification required in OCTgrad.f.

```
         if (costtype(1,1) .eq.
            120)then
c 1spins xy              point 2
    point (BEBOP,BIBOP),
    2014.04.01 MK
c variable flip angle pulse,
    dependent on B1. martin
c ================================
         ttcost=0
         call mcopy(initialrho,rho)
         do k=1,npulses

            !vorwï£¡rts bis prho(k
            +1)
          call getham(k)

             !2pi*i(w(1)Iz+WxIx+
             WyIy) in bestehendes
             pham
          call propagate(duration(k)
             ,pham(k))
          call mcopy(rhoout,rho)
         enddo
         call dagger(rhoout,rhoout)
                                   !
            macht aus i- i+


c        martin: hier targetrho
    berechnen...
```

```
            call cmul(cos(
                flipa_list(iB1)),
                initialrho, work1)
          call cmul(sin(flipa_list(
              iB1))*sin(2*pi*plength
              *
     /(1.0e-6)*offsconst*w(1)),iy,
              work2)
          call cmul(sin(flipa_list(
              iB1))*cos(2*pi*plength
              *
     /(1.0e-6)*offsconst*w(1)),ix,
              work3)
            call madd(work1, work2
                , targetrho)
            call madd(work3,
                targetrho,
                targetrho)
        call mscalp(targetrho,
            rhoout,ttcost2)
                        !trace{
            rhoout,i*t*[Ix,rho]}
c       write(*,*)flipa_list(iB1)
c       write(*,*)'initialrho'
c       call dmx(initialrho)
c       write(*,*)'ix'
c       call dmx(ix)
c       write(*,*)'targetrho'
c       call dmx(targetrho)
       ttcost1=ttcost1+ttcost2/
           normrho
        endif
```

Bibliography

[1] G. Bodenhausen and D. J. Ruben, "Natural abundance nitrogen-15 NMR by enhanced heteronuclear spectroscopy", *Chem. Phys. Lett.*, vol. 69, no. 1, pp. 185–189, 1980.

[2] S. G. Levine, "A Short History of the Chemical Shift", *J. Chem. Educ.*, vol. 78, no. 1, p. 133, 2001.

[3] M. Karplus, "Vicinal Proton Coupling in Nuclear Magnetic Resonance", *J. Am. Chem. Soc.*, vol. 85, no. 18, pp. 2870–2871, 1963.

[4] J. Stonehouse, P. Adell, J. Keeler, and A. J. Shaka, "Ultrahigh-Quality NOE Spectra", *J. Am. Chem. Soc.*, vol. 116, no. 13, pp. 6037–6038, 1994.

[5] R. R. Ernst and W. A. Anderson, "Application of Fourier Transform Spectroscopy to Magnetic Resonance", *Rev. Sci. Instrum.*, vol. 37, no. 1, pp. 93–102, 1966.

[6] H. Kovacs, D. Moskau, and M. Spraul, "Cryogenically cooled probes–a leap in NMR technology", *Prog. Nucl. Magn. Reson. Spectrosc.*, vol. 46, no. 2-3, pp. 131–155, 2005.

[7] H. G. Niessen, P. Trautner, S. Wiemann, J. Bargon, and K. Woelk, "The toroid cavity autoclave for high-pressure and variable-temperature *in situ* nuclear magnetic resonance studies", *Rev. Sci. Instrum.*, vol. 73, no. 3, pp. 1259–1266, 2002.

[8] C. Bauer, R. Freeman, T. Frenkiel, J. Keeler, and A. J. Shaka, "Gaussian pulses", *Journal of Magnetic Resonance (1969)*, vol. 58, no. 3, pp. 442–457, 1984.

[9] W. S. Warren, "Effects of arbitrary laser or NMR pulse shapes on population inversion and coherence", *The Journal of Chemical Physics*, vol. 81, no. 12, pp. 5437–5448, 1984.

[10] J. Baum, R. Tycko, and A. Pines, "Broadband and adiabatic inversion of a two-level system by phase-modulated pulses", *Phys. Rev. A*, vol. 32, pp. 3435–3447, 6 1985.

[11] M. S. Silver, R. I. Joseph, and D. I. Hoult, "Selective spin inversion in nuclear magnetic resonance and coherent optics through an exact solution of the bloch-riccati equation", *Phys. Rev. A*, vol. 31, pp. 2753–2755, 4 1985.

[12] M. H. Levitt, "Composite Pulses", *Progress in NMR Spectroscopy*, vol. 18, pp. 62–122, 1986.

[13] N. Khaneja, T. Reiss, C. Kehlet, T. Schulte-Herbrüggen, and S. J. Glaser, "Optimal control of coupled spin dynamics: Design of NMR pulse sequences by gradient ascent algorithms", *J. Magn. Reson.*, vol. 172, no. 2, pp. 296–305, 2005.

[14] A. Bhattacharya, "Chemistry: Breaking the billion-hertz barrier", *Nature*, vol. 463, no. 7281, pp. 605–606, 2010.

[15] A. Bax, R. H. Griffey, and B. L. Hawkins, "Correlation of proton and nitrogen-15 chemical shifts by multiple quantum NMR", *Journal of Magnetic Resonance (1969)*, vol. 55, no. 2, pp. 301–315, 1983.

[16] W. P. Aue, E. Bartholdi, and R. R. Ernst, "Two-dimensional spectroscopy. Application to nuclear magnetic resonance ", *J. Chem. Phys.*, vol. 64, no. 5, pp. 2229–2246, 1976.

[17] M. Mobli and J. C. Hoch, "Nonuniform sampling and non-Fourier signal processing methods in multidimensional NMR", *Prog. Nucl. Magn. Reson. Spectrosc.*, vol. 83, pp. 21–41, 2014.

[18] M. R. M. Koos, G. Kummerlöwe, L. Kaltschnee, C. M. Thiele, and B. Luy, "CLIP-COSY: A Clean In-Phase Experiment for the Rapid Acquisition of COSY-type Correlations", *Angew. Chem. Int. Ed.*, vol. 55, no. 27, pp. 7655–7659, 2016.

[19] Ē. Kupče and R. Freeman, "Fast multidimensional NMR by polarization sharing", *Magn. Reson. Chem.*, vol. 45, no. 1, pp. 2–4, 2007.

[20] D. Schulze-Sünninghausen, J. Becker, and B. Luy, "Rapid Heteronuclear Single Quantum Correlation NMR Spectra at Natural Abundance", *J. Am. Chem. Soc.*, vol. 136, no. 4, pp. 1242–1245, 2014.

[21] M. R. M. Koos, H. Feyrer, and B. Luy, "Broadband excitation pulses with variable RF amplitude-dependent flip angle (RADFA)", *Magn. Reson. Chem.*, vol. 53, no. 11, pp. 886–893, 2015.

[22] F. Bloch, "Nuclear Induction", *Phys. Rev.*, vol. 70, pp. 460–474, 7-8 1946.

[23] F. Bloch and I. I. Rabi, "Atoms in Variable Magnetic Fields", *Rev. Mod. Phys.*, vol. 17, pp. 237–244, 2-3 1945.

[24] S. McDonald and W. S. Warren, "Uses of shaped pulses in NMR: A primer", *Concepts in Magnetic Resonance*, vol. 3, no. 2, pp. 55–81, 1991.

[25] P. Zeeman, "The Effect of Magnetisation on the Nature of Light Emitted by a Substance", *Nature*, vol. 55, p. 347, 1897.

[26] A. Bryson, *Applied Optimal Control: Optimization, Estimation and Control*, ser. Halsted Press Book. Taylor & Francis, 1975.

[27] E. Pinch, *Optimal Control and the Calculus of Variations*. Oxford University Press, UK, 1993.

[28] A. E. Bryson, "Optimal control – 1950 to 1985", *IEEE Control Systems*, vol. 16, no. 3, pp. 26–33, 1996.

[29] R. Dorfman, "An Economic Interpretation of Optimal Control Theory", *Am. Econ. Rev.*, vol. 59, no. 5, pp. 817–831, 1969.

[30] E. S. Armstrong and J. H. Suddath, "Application of Pontryagin's Maximum Principle to the Lunar Orbit Rendezvous Problem", in *Guidance and Control Conference*, ser. Guidance, Navigation, and Control and Co-located Conferences. American Institute of Aeronautics and Astronautics, 1963.

[31] T. E. Skinner, T. O. Reiss, B. Luy, N. Khaneja, and S. J. Glaser, "Application of optimal control theory to the design of broadband excitation pulses for high-resolution NMR", *J. Magn. Reson.*, vol. 163, no. 1, pp. 8–15, 2003.

[32] J. L. Neves, B. Heitmann, N. Khaneja, and S. J. Glaser, "Heteronuclear decoupling by optimal tracking", *J. Magn. Reson.*, vol. 201, no. 1, pp. 7–17, 2009.

[33] T. Reinsperger, "Optimal control-enhanced deconvolution of NMR spectra: homo- and heteronuclear decoupling", PhD thesis, Karlsruhe Institute of Technology, Karlsruhe, Karlsruhe, 2016.

[34] J. Mao, T. Mareci, K. Scott, and E. Andrew, "Selective inversion radiofrequency pulses by optimal control", *Journal of Magnetic Resonance (1969)*, vol. 70, no. 2, pp. 310–318, 1986.

[35] D. Rosenfeld and Y. Zur, "Design of adiabatic selective pulses using optimal control theory", *Magn. Reson. Med.*, vol. 36, no. 3, pp. 401–409, 1996.

[36] V. F. Krotov, "Global methods in optimal control theory", in *Advances in Nonlinear Dynamics and Control: A Report from Russia*, A. B. Kurzhanski, Ed. Boston, MA: Birkhäuser Boston, 1993, pp. 74–121.

[37] M. S. Vinding, I. I. Maximov, Z. Tošner, and N. C. Nielsen, "Fast numerical design of spatial-selective rf pulses in MRI using Krotov and quasi-Newton based optimal control methods", *The Journal of Chemical Physics*, vol. 137, no. 5, 054203, 2012.

[38] D. M. Reich, M. Ndong, and C. P. Koch, "Monotonically convergent optimization in quantum control using krotov's method", *The Journal of Chemical Physics*, vol. 136, no. 10, 104103, 2012.

[39] N. C. Nielsen, C. Kehlet, S. J. Glaser, and N. Khaneja, "Optimal Control Methods in NMR Spectroscopy", in *eMagRes*. John Wiley & Sons, Ltd, 2007.

[40] M. Ndong, M. Lapert, C. P. Koch, and D. Sugny, "Comparative study of monotonically convergent optimization algorithms for the control of molecular rotation", *Phys. Rev. A*, vol. 87, p. 043 416, 4 2013.

[41] S. Machnes, U. Sander, S. J. Glaser, P. de Fouquières, A. Gruslys, S. Schirmer, and T. Schulte-Herbrüggen, "Comparing, optimizing, and benchmarking quantum-control algorithms in a unifying programming framework", *Phys. Rev. A*, vol. 84, p. 022 305, 2 2011.

[42] T. Levante, T. Bremi, and R. Ernst, "Pulse-Sequence Optimization with Analytical Derivatives. Application to Deuterium Decoupling in Oriented Phases", *Journal of Magnetic Resonance, Series A*, vol. 121, no. 2, pp. 167–177, 1996.

[43] I. Kuprov and C. T. Rodgers, "Derivatives of spin dynamics simulations", *The Journal of Chemical Physics*, vol. 131, no. 23, 234108, 2009.

[44] S. Ehni, "Optimal Control in the High Resolution NMR-Spectroscopy: Transfer Elements and their Application for Structure Elucidation", PhD thesis, Karlsruhe Institute of Technology, Karlsruhe, 2013.

[45] P. de Fouquieres, S. Schirmer, S. Glaser, and I. Kuprov, "Second order gradient ascent pulse engineering", *J. Magn. Reson.*, vol. 212, no. 2, pp. 412–417, 2011.

[46] D. L. Goodwin and I. Kuprov, "Modified Newton-Raphson GRAPE methods for optimal control of spin systems", *The Journal of Chemical Physics*, vol. 144, no. 20, 204107, 2016.

[47] T. W. Borneman, M. D. Huerlimann, and D. G. Cory, "Application of optimal control to CPMG refocusing pulse design", *J. Magn. Reson.*, vol. 207, no. 2, pp. 220–233, 2010.

[48] T. E. Skinner, N. I. Gershenzon, M. Nimbalkar, W. Bermel, B. Luy, and S. J. Glaser, "New strategies for designing robust universal rotation pulses: Application to broadband refocusing at low power", *J. Magn. Reson.*, vol. 216, pp. 78–87, 2012.

[49] M. Nimbalkar, B. Luy, T. E. Skinner, J. L. Neves, N. I. Gershenzon, K. Kobzar, W. Bermel, and S. J. Glaser, "The Fantastic Four: A plug 'n' play set of optimal control pulses for enhancing NMR spectroscopy", *J. Magn. Reson.*, vol. 228, pp. 16–31, 2013.

[50] B. Luy, K. Kobzar, T. E. Skinner, N. Khaneja, and S. J. Glaser, "Construction of universal rotations from point-to-point transformations", *J. Magn. Reson.*, vol. 176, no. 2, pp. 179–186, 2005.

[51] K. Kobzar, S. Ehni, T. E. Skinner, S. J. Glaser, and B. Luy, "Exploring the limits of broadband 90° and 180° universal rotation pulses", *J. Magn. Reson.*, vol. 225, pp. 142–160, 2012.

[52] T. E. Skinner, T. O. Reiss, B. Luy, N. Khaneja, and S. J. Glaser, "Reducing the duration of broadband excitation pulses using optimal control with limited RF amplitude", *J. Magn. Reson.*, vol. 167, no. 1, pp. 68–74, 2004.

[53] T. E. Skinner, K. Kobzar, B. Luy, M. R. Bendall, W. Bermel, N. Khaneja, and S. J. Glaser, "Optimal control design of constant amplitude phase-modulated pulses: Application to calibration-free broadband excitation", *J. Magn. Reson.*, vol. 179, no. 2, pp. 241–249, 2006.

[54] T. E. Skinner, T. O. Reiss, B. Luy, N. Khaneja, and S. J. Glaser, "Tailoring the optimal control cost function to a desired output: Application to minimizing phase errors in short broadband excitation pulses", *J. Magn. Reson.*, vol. 172, no. 1, pp. 17–23, 2005.

[55] N. I. Gershenzon, K. Kobzar, B. Luy, S. J. Glaser, and T. E. Skinner, "Optimal control design of excitation pulses that accommodate relaxation", *J. Magn. Reson.*, vol. 188, no. 2, pp. 330–336, 2007.

[56] N. Khaneja, T. Reiss, B. Luy, and S. J. Glaser, "Optimal control of spin dynamics in the presence of relaxation", *J. Magn. Reson.*, vol. 162, no. 2, pp. 311–319, 2003.

[57] N. Khaneja, J.-S. Li, C. Kehlet, B. Luy, and S. J. Glaser, "Broadband Relaxation-Optimized Polarization Transfer in Magnetic Resonance", *Proceedings of the National Academy of Sciences*, vol. 101, p. 21, 2007.

[58] N. I. Gershenzon, T. E. Skinner, B. Brutscher, N. Khaneja, M. Nimbalkar, B. Luy, and S. J. Glaser, "Linear phase slope in pulse design: Application to coherence transfer", *J. Magn. Reson.*, vol. 192, no. 2, pp. 235–243, 2008.

[59] M. Braun and S. J. Glaser, "Cooperative pulses", *J. Magn. Reson.*, vol. 207, no. 1, pp. 114–123, 2010.

[60] S. Ehni and B. Luy, "BEBEtr and BUBI: *J*-compensated concurrent shaped pulses for ^{1}H-^{13}C experiments", *J. Magn. Reson.*, vol. 232, pp. 7–17, 2013.

[61] S. Ehni and B. Luy, "A systematic approach for optimizing the robustness of pulse sequence elements with respect to couplings, offsets, and B_1-field inhomogeneities (COB)", *Magn. Reson. Chem.*, vol. 50, pp. 63–72, 2012.

[62] S. Ehni and B. Luy, "Robust INEPT and refocused INEPT transfer with compensation of a wide range of couplings, offsets, and B_1-field inhomogeneities (COB3)", *J. Magn. Reson.*, vol. 247, pp. 111–117, 2014.

[63] K. Kobzar, T. E. Skinner, N. Khaneja, S. J. Glaser, and B. Luy, "Exploring the limits of broadband excitation and inversion pulses", *J. Magn. Reson.*, vol. 170, no. 2, pp. 236–243, 2004.

[64] K. Kobzar, T. E. Skinner, N. Khaneja, S. J. Glaser, and B. Luy, "Exploring the limits of broadband excitation and inversion: II. Rf-power optimized pulses", *J. Magn. Reson.*, vol. 194, no. 1, pp. 58–66, 2008.

[65] A. Bax and R. Freeman, "Relative signs of NMR spin coupling constants by two-dimensional Fourier transform spectroscopy", *Journal of Magnetic Resonance (1969)*, vol. 45, no. 1, pp. 177–181, 1981.

[66] A. Bax and R. Freeman, "Investigation of complex networks of spin-spin coupling by two-dimensional NMR", *J. Magn. Reson.*, vol. 44, no. 3, pp. 542–561, 1981.

[67] G. Bodenhausen, G. Wagner, M. Rance, O. W. Sørensen, K. Wüthrich, and R. R. Ernst, "Longitudinal two-spin order in 2D exchange spectroscopy (NOESY)", *Journal of Magnetic Resonance (1969)*, vol. 59, no. 3, pp. 542–550, 1984.

[68] G. Wagner, G. Bodenhausen, N. Müller, M. Rance, O. W. Sørensen, R. R. Ernst, and K. Wuethrich, "Exchange of two-spin order in nuclear magnetic resonance: Separation of exchange and cross-relaxation processes", *J. Am. Chem. Soc.*, vol. 107, no. 23, pp. 6440–6446, 1985.

[69] E. R. Zuiderweg, "Complete NMR fingerprints of proteins in H_2O solution without solvent presaturation. An application of two-dimensional longitudinal two-spin-order spectroscopy", *Journal of Magnetic Resonance (1969)*, vol. 71, no. 2, pp. 283–293, 1987.

[70] H. Oschkinat, A. Pastore, and G. Bodenhausen, "Determination of relaxation pathways in coupled spin systems by two-dimensional NMR exchange spectroscopy with small flip angles", *J. Am. Chem. Soc.*, vol. 109, no. 13, pp. 4110–4111, 1987.

[71] H. Oschkinat, A. Pastore, P. Pfändler, and G. Bodenhausen, "Two-dimensional correlation of directly and remotely connected transitions by zeta-filtered COSY", *J. Magn. Reson.*, vol. 69, no. 3, pp. 559–566, 1986.

[72] A. J. Pell, R. A. E. Edden, and J. Keeler, "Broadband proton-decoupled proton spectra", *Magn. Reson. Chem.*, vol. 45, no. 4, pp. 296–316, 2007.

[73] L. Mueller, "PE-COSY, a simple alternative to E-COSY", *J. Magn. Reson.*, vol. 72, no. 1, pp. 191–196, 1987.

[74] P. Tzvetkova, S. Simova, and B. Luy, "PEHSQC: A simple experiment for simultaneous and sign-sensitive measurement of $(^1J_{CH} + D_{CH})$ and $(^2J_{HH} + D_{HH})$ couplings", *J. Magn. Reson.*, vol. 186, no. 2, pp. 193–200, 2007.

[75] J. Sauri, P. Nolis, L. Castañar, A. Virgili, and T. Parella, "PEHSQMBC: Simultaneous measurement of proton-proton and proton-carbon coupling constants", *J. Magn. Reson.*, vol. 224, pp. 101–106, 2012.

[76] R. Ernst, G. Bodenhausen, and A. Wokaun, *Principles of Nuclear Magnetic Resonance in One and Two Dimensions*, ser. International series of monographs on chemistry. Clarendon Press, 1990.

[77] P. Schanda, Ē. Kupče, and B. Brutscher, "SOFAST-HMQC Experiments for Recording Two-dimensional Heteronuclear Correlation Spectra of Proteins within a Few Seconds", *J. Biomol. NMR*, vol. 33, no. 4, pp. 199–211, 2005.

[78] P. Schanda and B. Brutscher, "Very Fast Two-Dimensional NMR Spectroscopy for Real-Time Investigation of Dynamic Events in Proteins on the Time Scale of Seconds", *J. Am. Chem. Soc.*, vol. 127, no. 22, pp. 8014–8015, 2005.

[79] T. Kern, P. Schanda, and B. Brutscher, "Sensitivity-enhanced IPAP-SOFAST-HMQC for fast-pulsing 2D NMR with reduced radiofrequency load", *J. Magn. Reson.*, vol. 190, no. 2, pp. 333–338, 2008.

[80] B. Sathyamoorthy, J. Lee, I. Kimsey, L. R. Ganser, and H. Al-Hashimi, "Development and application of aromatic [^{13}C, ^{1}H] SOFAST-HMQC NMR experiment for nucleic acids", *J. Biomol. NMR*, vol. 60, no. 2, pp. 77–83, 2014.

[81] Ē. Kupče and R. Freeman, "Wideband Excitation with Polychromatic Pulses", *Journal of Magnetic Resonance, Series A*, vol. 108, no. 2, pp. 268–273, 1994.

[82] Ē. Kupče and R. Freeman, "Optimized Adiabatic Pulses for Wideband Spin Inversion", *Journal of Magnetic Resonance, Series A*, vol. 118, no. 2, pp. 299–303, 1996.

[83] C. Hardy, W. Edelstein, and D. Vatis, "Efficient adiabatic fast passage for NMR population inversion in the presence of radiofrequency field inhomogeneity and frequency offsets", *Journal of Magnetic Resonance (1969)*, vol. 66, no. 3, pp. 470–482, 1986.

[84] M. A. Smith, H. Hu, and A. J. Shaka, "Improved broadband inversion performance for nmr in liquids", *J. Magn. Reson.*, vol. 151, no. 2, pp. 269–283, 2001.

[85] L. Frydman, T. Scherf, and A. Lupulescu, "The acquisition of multidimensional NMR spectra within a single scan", *Proceedings of the National Academy of Sciences*, vol. 99, no. 25, pp. 15 858–15 862, 2002.

[86] P. Pelupessy, "Adiabatic Single Scan Two-Dimensional NMR Spectrocopy", *J. Am. Chem. Soc.*, vol. 125, no. 40, pp. 12 345–12 350, 2003.

[87] P. Mansfield and P. K. Grannell, "'diffraction" and microscopy in solids and liquids by NMR", *Phys. Rev. B*, vol. 12, pp. 3618–3634, 9 1975.

[88] A. Tal and L. Frydman, "Single-scan multidimensional magnetic resonance", *Prog. Nucl. Magn. Reson. Spectrosc.*, vol. 57, no. 3, pp. 241–292, 2010.

[89] P. Giraudeau and L. Frydman, "Ultrafast 2D NMR: An Emerging Tool in Analytical Spectroscopy", *Annu. Rev. Anal. Chem.*, vol. 7, no. 1, pp. 129–161, 2014.

[90] M. J. Thrippleton and J. Keeler, "Elimination of zero-quantum interference in two-dimensional NMR spectra", *Angew. Chem. Int. Ed.*, vol. 42, no. 33, pp. 3938–3941, 2003.

[91] K. E. Cano, M. J. Thrippleton, J. Keeler, and A. J. Shaka, "Cascaded z-filters for efficient single-scan suppression of zero-quantum coherence", *J. Magn. Reson.*, vol. 167, no. 2, pp. 291–297, 2004.

[92] J. Assländer, S. J. Glaser, and J. Hennig, "Spin echoes in the regime of weak dephasing", *Magn. Reson. Med.*, vol. 75, no. 1, pp. 150–160, 2016.

[93] M. Braun and S. J. Glaser, "Concurrently optimized cooperative pulses in robust quantum control: application to broadband Ramsey-type pulse sequence elements", *New J. Phys.*, vol. 16, no. 11, p. 115 002, 2014.

[94] I. Kuprov, "Spin system trajectory analysis under optimal control pulses", *J. Magn. Reson.*, vol. 233, pp. 107–112, 2013.

[95] U. Piantini, O. W. Sørensen, and R. R. Ernst, "Multiple quantum filters for elucidating NMR coupling networks", *J. Am. Chem. Soc.*, vol. 104, no. 24, pp. 6800–6801, 1982.

[96] D. Marion and A. Bax, "P-COSY, a sensitive alternative for double-quantum-filtered COSY", *J. Magn. Reson.*, vol. 80, no. 3, pp. 528–533, 1988.

[97] M. Rance, O. W. Sørensen, G. Bodenhausen, G. Wagner, R. R. Ernst, and K. Wüthrich, "Improved spectral resolution in COSY H-1-NMR spectra of proteins via double quantum filtering", *Biochem. Biophys. Res. Commun.*, vol. 117, no. 2, pp. 479–485, 1983.

[98] C. Griesinger, O. W. Sørensen, and R. R. Ernst, "Practical aspects of the E-COSY technique - measurement of scalar spin spin coupling-constants in peptides", *J. Magn. Reson.*, vol. 75, no. 3, pp. 474–492, 1987.

[99] C. Griesinger, O. W. Sørensen, and R. R. Ernst, "Correlation of connected transitions by two-dimensional NMR-spectroscopy", *J. Chem. Phys.*, vol. 85, no. 12, pp. 6837–6852, 1986.

[100] C. Griesinger, O. W. Sørensen, and R. R. Ernst, "Two-dimensional correlation of connected NMR transitions", *J. Am. Chem. Soc.*, vol. 107, no. 22, pp. 6394–6396, 1985.

[101] S. Berger, "Gradient selected constant time COSY", *Spectrosc. Lett.*, vol. 33, no. 1, pp. 1–8, 2000.

[102] M. E. Girvin, "Increased sensitivity of COSY spectra by use of constant-time t_1 periods (CT COSY)", *J. Magn. Reson., Ser. A*, vol. 108, no. 1, pp. 99–102, 1994.

[103] M. Rance, G. Wagner, O. W. Sørensen, K. Wüthrich, and R. R. Ernst, "Application of omega-1-decoupled 2D correlation spectra to the study of proteins", *J. Magn. Reson.*, vol. 59, no. 2, pp. 250–261, 1984.

[104] J. A. Aguilar, A. A. Colbourne, J. Cassani, M. Nilsson, and G. A. Morris, "Decoupling Two-Dimensional NMR Spectroscopy in Both Dimensions: Pure Shift NOESY and COSY", *Angew. Chem. Int. Ed.*, vol. 51, no. 26, pp. 6460–6463, 2012.

[105] G. Eich, G. Bodenhausen, and R. R. Ernst, "Exploring nuclear-spin systems by relayed magnetization transfer", *J. Am. Chem. Soc.*, vol. 104, no. 13, pp. 3731–3732, 1982.

[106] A. Kumar, R. V. Hosur, and K. Chandrasekhar, "A superior pulse scheme for homonuclear two-dimensional correlated spectroscopy", *J. Magn. Reson.*, vol. 60, no. 1, pp. 143–148, 1984.

[107] S. Talluri and H. A. Scheraga, "COSY with in-phase cross peaks", *J. Magn. Reson.*, vol. 86, no. 1, pp. 1–10, 1990.

[108] Y. L. Xia, G. Legge, K. Y. Jun, Y. L. Qi, H. Lee, and X. L. Gao, "IP-COSY, a totally in-phase and sensitive COSY experiment", *Magn. Reson. Chem.*, vol. 43, no. 5, pp. 372–379, 2005.

[109] L. Kaltschnee, A. Kolmer, I. Timári, V. Schmidts, R. W. Adams, M. Nilsson, K. E. Kövér, G. A. Morris, and C. M. Thiele, "'perfecting" pure shift HSQC: Full homodecoupling for accurate and precise determination of heteronuclear couplings", *Chem. Commun.*, vol. 50, no. 99, pp. 15 702–15 705, 2014.

[110] A. M. Torres, G. Zheng, and W. S. Price, "*J*-compensated PGSE: an improved NMR diffusion experiment with fewer phase distortions", *Magn. Reson. Chem.*, vol. 48, no. 2, pp. 129–133, 2010.

[111] P. C. M. van Zijl, C. T. W. Moonen, and M. von Kienlin, "Homonuclear-*J* refocusing in echo spectroscopy", *J. Magn. Reson.*, vol. 89, no. 1, pp. 28–40, 1990.

[112] K. Takegoshi, K. Ogura, and K. Hikichi, "A perfect spin-echo in a weakly homonuclear *J*-coupled 2 spin-1/2 system", *J. Magn. Reson.*, vol. 84, no. 3, pp. 611–615, 1989.

[113] M. Piotto, V. Saudek, and V. Sklenar, "Gradient-tailored excitation for single-quantum NMR-spectroscopy of aqueous-solutions", *J. Biomol. NMR*, vol. 2, no. 6, pp. 661–665, 1992.

[114] M. L. Liu, X. A. Mao, C. H. Ye, H. Huang, J. K. Nicholson, and J. C. Lindon, "Improved WATERGATE pulse sequences for solvent suppression in NMR spectroscopy", *J. Magn. Reson.*, vol. 132, no. 1, pp. 125–129, 1998.

[115] T. L. Hwang and A. J. Shaka, "Water suppression that works - excitation sculpting using arbitrary wave-forms and pulsed-field gradients", *J. Magn. Reson., Ser. A*, vol. 112, no. 2, pp. 275–279, 1995.

[116] R. W. Adams, C. M. Holroyd, J. A. Aguilar, M. Nilsson, and G. A. Morris, ""Perfecting" WATERGATE: clean proton NMR spectra from aqueous solution", *Chem. Commun.*, vol. 49, no. 4, pp. 358–360, 2013.

[117] M. Mayzel, J. Rosenlöw, L. Isaksson, and V. Y. Orekhov, "Time-resolved multidimensional NMR with non-uniform sampling", *Journal of Biomolecular NMR*, vol. 58, no. 2, pp. 129–139, 2014.

[118] O. W. Sørensen, G. W. Eich, M. H. Levitt, G. Bodenhausen, and R. R. Ernst, "Product operator formalism for the description of NMR pulse experiments", *Progress in NMR Spectroscopy*, vol. 16, p. 30, 1983.

[119] J. M. Böhlen, I. Burghardt, M. Rey, and G. Bodenhausen, "Frequency-modulated chirp pulses for broad-band inversion recovery in magnetic-resonance", *J. Magn. Reson.*, vol. 90, no. 1, pp. 183–191, 1990.

[120] J. M. Böhlen, M. Rey, and G. Bodenhausen, "Refocusing with chirped pulses for broadband excitation without phase dispersion", *J. Magn. Reson.*, vol. 84, no. 1, pp. 191–197, 1989.

[121] N. H. Meyer and K. Zangger, "Simplifying proton NMR spectra by instant homonuclear broadband decoupling", *Angew. Chem. Int. Ed.*, vol. 52, no. 28, pp. 7143–7146, 2013.

[122] M. Foroozandeh, R. W. Adams, N. J. Meharry, D. Jeannerat, M. Nilsson, and G. A. Morris, "Ultrahigh-Resolution NMR Spectroscopy", *Angew. Chem. Int. Ed.*, vol. 53, no. 27, pp. 6990–6992, 2014.

[123] K. Zangger and H. Sterk, "Homonuclear broadband-decoupled NMR spectra", *J. Magn. Reson.*, vol. 124, no. 2, pp. 486–489, 1997.

[124] J. R. Garbow, D. P. Weitekamp, and A. Pines, "Bilinear rotation decoupling of homonuclear scalar interactions", *Chem. Phys. Lett.*, vol. 93, no. 5, pp. 504–509, 1982.

[125] T. Reinsperger and B. Luy, "Homonuclear BIRD-decoupled spectra for measuring one-bond couplings with highest resolution: CLIP/CLAP-RESET and constant-time-CLIP/CLAP-RESET", *J. Magn. Reson.*, vol. 239, pp. 110–120, 2014.

[126] I. Timári, L. Kaltschnee, A. Kolmer, R. W. Adams, M. Nilsson, C. M. Thiele, G. A. Morris, and K. E. Kövér, "Accurate determination of one-bond heteronuclear coupling constants with "pure shift" broadband proton-decoupled CLIP/CLAP-HSQC experiments", *J. Magn. Reson.*, vol. 239, pp. 130–138, 2014.

[127] T. Schulte-Herbrüggen, Z. Mádi, O. Sørensen, and R. Ernst, "Reduction of multiplet complexity in COSY-type NMR spectra", *Mol. Phys.*, vol. 72, no. 4, pp. 847–871, 1991.

[128] S. R. Hartmann and E. L. Hahn, "Nuclear Double Resonance in the Rotating Frame", *Phys. Rev.*, vol. 128, no. 5, p. 12, 1962.

[129] D. G. Davis and A. Bax, "Assignment of complex proton NMR spectra via two-dimensional homonuclear Hartmann-Hahn spectroscopy", *J. Am. Chem. Soc.*, vol. 107, no. 9, pp. 2820–2821, 1985.

[130] S. J. Glaser and J. J. Quant, "Homonuclear and Heteronuclear Hartmann-Hahn Transfer in Isotropic Liquids", in *Advances in Magnetic and Optical Resonance*. Academic Press, Inc., 1996, vol. 19, p. 196.

[131] A. J. Shaka, C. J. Lee, and A. Pines, "Iterative schemes for bilinear operators; application to spin decoupling", *Journal of Magnetic Resonance (1969)*, vol. 77, no. 2, pp. 274–293, 1988.

[132] M. Kadkhodaie, O. Rivas, M. Tan, A. Mohebbi, and A. J. Shaka, "Broadband homonuclear cross polarization using flip-flop spectroscopy", *Journal of Magnetic Resonance (1969)*, vol. 91, no. 2, pp. 437–443, 1991.

[133] J. Furrer, F. Kramer, J. P. Marino, S. J. Glaser, and B. Luy, "Homonuclear Hartmann-Hahn transfer with reduced relaxation losses by use of the MOCCA-XY16 multiple pulse sequence", *J. Magn. Reson.*, vol. 166, no. 1, pp. 39–46, 2004.

[134] G. A. Morris, J. A. Aguilar, R. Evans, S. Haiber, and M. Nilsson, "True Chemical Shift Correlation Maps: A TOCSY Experiment with Pure Shifts in Both Dimensions", *J. Am. Chem. Soc.*, vol. 132, no. 37, pp. 12 770–12 772, 2010.

[135] J. J. Koivisto, "Zero-quantum filtered pure shift TOCSY", *Chem. Commun.*, vol. 49, no. 1, pp. 96–98, 2013.

[136] M. Foroozandeh, R. W. Adams, M. Nilsson, and G. A. Morris, "Ultrahigh-resolution total correlation nmr spectroscopy", *J. Am. Chem. Soc.*, vol. 136, no. 34, pp. 11 867–11 869, 2014.

[137] L. Castañar, P. Nolis, A. Virgili, and T. Parella, "Full sensitivity and enhanced resolution in homodecoupled band-selective nmr experiments", *Chemistry – A European Journal*, vol. 19, no. 51, pp. 17 283–17 286, 2013.

[138] Y. Shrot and L. Frydman, "Single-Scan NMR Spectroscopy at Arbitrary Dimensions", *J. Am. Chem. Soc.*, vol. 125, no. 37, pp. 11 385–11 396, 2003.

[139] B. Gouilleux, L. Rouger, and P. Giraudeau, "Ultrafast Multi-dimensional NMR: Principles and Recent Applications", in *eMagRes*. John Wiley & Sons, Ltd, 2007.

[140] R. E. Hurd and B. K. John, "Gradient-enhanced proton-detected heteronuclear multiple-quantum coherence spectroscopy", *Journal of Magnetic Resonance (1969)*, vol. 91, no. 3, pp. 648–653, 1991.

[141] L. Mueller, "Alternate HMQC experiments for recording HN and HC-correlation spectra in proteins at high throughput", *J. Biomol. NMR*, vol. 42, no. 2, pp. 129–137, 2008.

[142] J. Furrer, "A robust, sensitive, and versatile HMBC experiment for rapid structure elucidation by NMR: IMPACT-HMBC", *Chem. Commun.*, vol. 46, pp. 3396–3398, 19 2010.

[143] A. Bax, M. Ikura, L. E. Kay, D. A. Torchia, and R. Tschudin, "Comparison of different modes of two-dimensional reverse-correlation NMR for the study of proteins", *Journal of Magnetic Resonance (1969)*, vol. 86, no. 2, pp. 304–318, 1990.

[144] A. J. Shaka, P. B. Barker, and R. Freeman, "Computer-optimized decoupling scheme for wideband applications and low-level operation", *Journal of Magnetic Resonance (1969)*, vol. 64, no. 3, pp. 547–552, 1985.

[145] D. Schulze-Sünninghausen, J. Becker, M. R. Koos, and B. Luy, "Improvements, extensions, and practical aspects of rapid asap-hsqc and alsofast-hsqc pulse sequences for studying small molecules at natural abundance", *J. Magn. Reson.*, vol. 281, no. Supplement C, pp. 151–161, 2017.

[146] D. Schulze-Sünninghausen, "Entwicklung und Optimierung schneller mehrdimensionaler NMR-Experimente", PhD thesis, Karlsruhe Institute of Technology, Karlsruhe, Karlsruhe, 2016.

[147] D. Doddrell, D. Pegg, and M. Bendall, "Distortionless enhancement of NMR signals by polarization transfer", *Journal of Magnetic Resonance (1969)*, vol. 48, no. 2, pp. 323–327, 1982.

[148] L. E. Kay and A. Bax, "Separation of NH and NH_2 resonances in ^{1}H-detected heteronuclear multiple-quantum correlation spectra", *Journal of Magnetic Resonance (1969)*, vol. 84, no. 3, pp. 598–603, 1989.

[149] X. Zhang and C. Wang, "^{1}H-Detected editable heteronuclear multiple-quantum correlation experiment at natural abundance", *Journal of Magnetic Resonance (1969)*, vol. 91, no. 3, pp. 618–623, 1991.

[150] D. G. Davis, "Improved multiplet editing of proton-detected, heteronuclear shift-correlation spectra", *Journal of Magnetic Resonance (1969)*, vol. 91, no. 3, pp. 665–672, 1991.

[151] W. Willker, D. Leibfritz, R. Kerssebaum, and W. Bermel, "Gradient selection in inverse heteronuclear correlation spectroscopy", *Magn. Reson. Chem.*, vol. 31, no. 3, pp. 287–292, 1993.

[152] G. A. Morris and R. Freeman, "Enhancement of nuclear magnetic resonance signals by polarization transfer", *J. Am. Chem. Soc.*, vol. 101, no. 3, pp. 760–762, 1979.

[153] N. Niccolai, M. de la P. Leon de Miles, S. P. Hehir, and W. A. Gibbons, "Correlation time measurements of amino acid side chains from proton selective spin-lattice relaxation rates", *J. Am. Chem. Soc.*, vol. 100, no. 20, pp. 6528–6529, 1978.

[154] A. W. Overhauser, "Polarization of nuclei in metals", *Phys. Rev.*, vol. 92, pp. 411–415, 2 1953.

[155] F. A. L. Anet and A. J. R. Bourn, "Nuclear Magnetic Resonance Spectral Assignments from Nuclear Overhauser Effects", *J. Am. Chem. Soc.*, vol. 87, no. 22, pp. 5250–5251, 1965.

[156] R. Freeman, H. D. W. Hill, B. L. Tomlinson, and L. D. Hall, "Dipolar contribution to NMR spin-lattice relaxation of protons", *The Journal of Chemical Physics*, vol. 61, no. 11, pp. 4466–4473, 1974.

[157] M. Lapert, E. Assémat, S. J. Glaser, and D. Sugny, "Optimal control of the signal-to-noise ratio per unit time of a spin 1/2 particle: The crusher gradient and the radiation damping cases", *The Journal of Chemical Physics*, vol. 142, no. 4, 044202, 2015.

[158] J. Becker, M. R. M. Koos, D. Schulze-Sünninghausen, and B. Luy, 2016, in preparation.

[159] A. G. Palmer, J. Cavanagh, P. E. Wright, and M. Rance, "Sensitivity improvement in proton-detected two-dimensional heteronuclear correlation NMR spectroscopy", *Journal of Magnetic Resonance (1969)*, vol. 93, no. 1, pp. 151–170, 1991.

[160] L. E. Kay, P. Keifer, and T. Saarinen, "Pure absorption gradient enhanced heteronuclear single quantum correlation spectroscopy with improved sensitivity", *J. Am. Chem. Soc.*, vol. 114, no. 26, pp. 10 663–10 665, 1992.

[161] M. S. Albert, G. D. Cates, B. Driehuys, W. Happer, B. Saam, C. S. Springer, and A. Wishnia, "Biological magnetic resonance imaging using laser-polarized ^{129}Xe", *Nature*, vol. 370, no. 6486, pp. 199–201, 1994.

[162] J. H. Ardenkjær-Larsen, B. Fridlund, A. Gram, G. Hansson, L. Hansson, M. H. Lerche, R. Servin, M. Thaning, and K. Golman, "Increase in signal-to-noise ratio of > 10,000 times in liquid-state NMR", *Proceedings of the National Academy of Sciences*, vol. 100, no. 18, pp. 10 158–10 163, 2003.

[163] A. Bornet, R. Melzi, A. J. P. Linde, P. Hautle, B. van den Brandt, S. Jannin, and G. Bodenhausen, "Boosting Dissolution Dynamic Nuclear Polarization by Cross Polarization", *The Journal of Physical Chemistry Letters*, vol. 4, no. 1, pp. 111–114, 2013.

[164] J. P. Mugler, F. H. Epstein, and J. R. Brookeman, "Shaping the Signal Response during the Approach to Steady State in Three-Dimensional Magnetization-Prepared Rapid Gradient-Echo Imaging Using Variable Flip Angles", *Magn. Reson. Med.*, vol. 28, no. 2, pp. 165–185, 1992.

[165] M. K. Stehling, "Improved signal in "snapshot" FLASH by variable flip angles", *Magn. Reson. Imaging*, vol. 10, no. 1, pp. 165–167, 1992.

[166] K. Nagashima, "Optimum pulse flip angles for multi-scan acquisition of hyperpolarized NMR and MRI", *J. Magn. Reson.*, vol. 190, no. 2, pp. 183–188, 2008.

[167] Y. Xing, G. D. Reed, J. M. Pauly, A. B. Kerr, and P. E. Z. Larson, "Optimal variable flip angle schemes for dynamic acquisition of exchanging hyperpolarized substrates", *J. Magn. Reson.*, vol. 234, no. 0, pp. 75–81, 2013.

[168] P. Trigo-Mouriño, C. Merle, M. R. M. Koos, B. Luy, and R. R. Gil, "Probing Spatial Distribution of Alignment by Deuterium NMR Imaging", *Chemistry – A European Journal*, vol. 19, no. 22, pp. 7013–7019, 2013.

[169] M. R. M. Koos, E. Danieli, F. Casanova, B. Blümich, and B. Luy, "Differentiation of enantiomers by 2D NMR spectroscopy at 1 T using residual dipolar couplings", *Magn. Reson. Chem.*, vol. 54, no. 6, pp. 527–530, 2016.

[170] J. Jeener, B. H. Meier, P. Bachmann, and R. R. Ernst, "Investigation of exchange processes by two-dimensional NMR spectroscopy", *The Journal of Chemical Physics*, vol. 71, no. 11, pp. 4546–4553, 1979.

[171] A. Saupe and G. Englert, "High-Resolution Nuclear Magnetic Resonance Spectra of Orientated Molecules", *Phys. Rev. Lett.*, vol. 11, pp. 462–464, 10 1963.

[172] A. Saupe, "Kernresonanzen in kristallinen Flüssigkeiten und in Kristallinflüssigen Lösungen. Teil I", *Zeitschrift für Naturforschung A*, vol. 19, pp. 161–171, 1964.

[173] L. C. Snyder, "Analysis of Nuclear Magnetic Resonance Spectra of Molecules in Liquid-Crystal Solvents", *The Journal of Chemical Physics*, vol. 43, no. 11, pp. 4041–4050, 1965.

[174] B. Deloche and E. T. Samulski, "Short-range nematic-like orientational order in strained elastomers: A deuterium magnetic resonance study", *Macromolecules*, vol. 14, no. 3, pp. 575–581, 1981.

[175] H.-J. Sass, G. Musco, S. J. Stahl, P. T. Wingfield, and S. Grzesiek, "Solution NMR of proteins within polyacrylamide gels: Diffusional properties and residual alignment by mechanical stress or embedding of oriented purple membranes", *J. Biomol. NMR*, vol. 18, no. 4, pp. 303–309, 2000.

[176] R. Tycko, F. J. Blanco, and Y. Ishii, "Alignment of Biopolymers in Strained Gels: A New Way To Create Detectable Dipole-Dipole Couplings in High-Resolution Biomolecular NMR", *J. Am. Chem. Soc.*, vol. 122, no. 38, pp. 9340–9341, 2000.

[177] B. Luy, K. Kobzar, and H. Kessler, "An Easy and Scalable Method for the Partial Alignment of Organic Molecules for Measuring Residual Dipolar Couplings", *Angew. Chem. Int. Ed.*, vol. 43, no. 9, pp. 1092–1094, 2004.

[178] E. Brunner, "Residual dipolar couplings in protein NMR", *Concepts in Magnetic Resonance*, vol. 13, no. 4, pp. 238–259, 2001.

[179] G. Kummerlöwe, B. Crone, M. Kretschmer, S. F. Kirsch, and B. Luy, "Residual Dipolar Couplings as a Powerful Tool for Constitutional Analysis: The Unexpected Formation of Tricyclic Compounds", *Angew. Chem. Int. Ed.*, vol. 50, no. 11, pp. 2643–2645, 2011.

[180] G. Kummerlöwe and B. Luy, "Residual Dipolar Couplings for the Configurational and Conformational Analysis of Organic Molecules", in *Annual Reports on NMR Spectroscopy, Vol 68*, ser. Annual Reports on NMR Spectroscopy, Webb, GA, Ed., vol. 68, 2009, pp. 193–230.

[181] C. M. Thiele, "Residual Dipolar Couplings (RDCs) in Organic Structure Determination", *Eur. J. Org. Chem.*, no. 34, pp. 5673–5685, 2008.

[182] D. Intelmann, G. Kummerlöwe, G. Haseleu, N. Desmer, K. Schulze, R. Fröhlich, O. Frank, B. Luy, and T. Hofmann, "Structures of Storage-Induced Transformation Products of the Beer's Bitter Principles, Revealed by Sophisticated NMR Spectroscopic and LC-MS Techniques", *Chemistry – A European Journal*, vol. 15, no. 47, pp. 13 047–13 058, 2009.

[183] A. Schuetz, T. Murakami, N. Takada, J. Junker, M. Hashimoto, and C. Griesinger, "RDC-Enhanced NMR Spectroscopy in Structure Elucidation of Sucro-Neolambertellin", *Angew. Chem. Int. Ed.*, vol. 47, no. 11, pp. 2032–2034, 2008.

[184] K. Kobzar, H. Kessler, and B. Luy, "Stretched Gelatin Gels as Chiral Alignment Media for the Discrimination of Enantiomers by NMR Spectroscopy", *Angewandte Chemie International Edition*, vol. 44, no. 20, pp. 3145–3147, 2005.

[185] J. A. Dale and H. S. Mosher, "Nuclear magnetic resonance enantiomer reagents. Configurational correlations via nuclear magnetic resonance chemical shifts of diastereomeric mandelate, *O*-methylmandelate, and α-methoxy-α-trifluoromethylphenylacetate (MTPA) esters", *J. Am. Chem. Soc.*, vol. 95, no. 2, pp. 512–519, 1973.

[186] J. M. Seco, E. Quiñoá, and R. Riguera, "The Assignment of Absolute Configuration by NMR", *Chem. Rev.*, vol. 104, no. 1, pp. 17–118, 2004.

[187] T. Morrill, *Lanthanide Shift Reagents for Stereochemical Analysis*. John Wiley & Sons, 1987.

[188] M. Sarfati, P. Lesot, D. Merlet, and J. Courtieu, "Theoretical and experimental aspects of enantiomeric differentiation using natural abundance multinuclear NMR spectroscopy in chiral polypeptide liquid crystals", *Chem. Commun.*, pp. 2069–2081, 21 2000.

[189] I. Canet, J. Courtieu, A. Loewenstein, A. Meddour, and J. M. Pechine, "Enantiomeric analysis in a polypeptide lyotropic liquid crystal by deuterium NMR", *J. Am. Chem. Soc.*, vol. 117, no. 24, pp. 6520–6526, 1995.

[190] B. Luy, "Distinction of enantiomers by NMR spectroscopy using chiral orienting media", *J. Indian Inst. Sci.*, vol. 90, no. 1, pp. 119–132, 2010.

[191] L. Brateman, "Chemical Shift Imaging: A Review", *Am. J. Roentgenol.*, vol. 146, no. 5, pp. 971–980, 1986.

[192] T. R. Brown, B. M. Kincaid, and K. Ugurbil, "NMR chemical shift imaging in three dimensions", *Proceedings of the National Academy of Sciences*, vol. 79, no. 11, pp. 3523–3526, 1982.

[193] R. Freeman and H. D. W. Hill, "High-Resolution Study of NMR Spin Echoes: "*J* Spectra"", *The Journal of Chemical Physics*, vol. 54, no. 1, pp. 301–313, 1971.

[194] W. P. Aue, J. Karhan, and R. R. Ernst, "Homonuclear broad band decoupling and two-dimensional *J*-resolved NMR spectroscopy", *The Journal of Chemical Physics*, vol. 64, no. 10, pp. 4226–4227, 1976.

[195] E. Adalsteinsson and D. M. Spielman, "Spatially resolved two-dimensional spectroscopy", *Magn. Reson. Med.*, vol. 41, no. 1, pp. 8–12, 1999.

[196] L. N. Ryner, J. A. Sorenson, and M. Thomas, "Localized 2D *J*-resolved ^{1}H MR spectroscopy: Strong coupling effects *in vitro* and *in vivo*", *Magn. Reson. Imaging*, vol. 13, no. 6, pp. 853–869, 1995.

[197] S. Posse, C. DeCarli, and D. Le Bihan, "Three-dimensional echo-planar MR spectroscopic imaging at short echo times in the human brain.", *Radiology*, vol. 192, no. 3, pp. 733–738, 1994.

[198] R. V. Mulkern and L. P. Panych, "Echo planar spectroscopic imaging", *Concepts in Magnetic Resonance*, vol. 13, no. 4, pp. 213–237, 2001.

[199] S. Lipnick, G. Verma, S. Ramadan, J. Furuyama, and M. A. Thomas, "Echo planar correlated spectroscopic imaging: Implementation and pilot evaluation in human calf in vivo", *Magn. Reson. Med.*, vol. 64, no. 4, pp. 947–956, 2010.

[200] M. Sarma, R. Nagarajan, P. Macey, R. Kumar, J. Villablanca, J. Furuyama, and M. Thomas, "Accelerated Echo-Planar *J*-Resolved Spectroscopic Imaging in the Human Brain Using Compressed Sensing: A Pilot Validation in Obstructive Sleep Apnea", *American Journal of Neuroradiology*, vol. 35, no. 6 suppl, pp. 81–89, 2014.

[201] N. E. Wilson, Z. Iqbal, B. L. Burns, M. Keller, and M. A. Thomas, "Accelerated five-dimensional echo planar *J*-resolved spectroscopic imaging: Implementation and pilot validation in human brain", *Magn. Reson. Med.*, vol. 75, no. 1, pp. 42–51, 2016.

[202] M. F. Schocke, H. Zoller, W. Vogel, C. Wolf, C. Kremser, P. Steinboeck, G. Poelzl, O. Pachinger, W. R. Jaschke, and B. Metzler, "Cardiac phosphorus-31 two-dimensional chemical shift imaging in patients with hereditary hemochromatosis", *Magn. Reson. Imaging*, vol. 22, no. 4, pp. 515–521, 2004.

[203] M. A. Frey, M. Michaud, J. N. VanHouten, K. L. Insogna, J. A. Madri, and S. E. Barrett, "Phosphorus-31 MRI of hard and soft solids using quadratic echo line-narrowing", *Proceedings of the National Academy of Sciences*, vol. 109, no. 14, pp. 5190–5195, 2012.

[204] R. Ouwerkerk, "Sodium MRI", in *Magnetic Resonance Neuroimaging: Methods and Protocols*, M. Modo and W. J. Bulte, Eds. Totowa, N. J.: Humana Press, 2011, pp. 175–201.

[205] Y. Kato, B. Okollie, and D. Artemov, "Noninvasive ^{1}H/^{13}C magnetic resonance spectroscopic imaging of the intratumoral distribution of temozolomide", *Magn. Reson. Med.*, vol. 55, no. 4, pp. 755–761, 2006.

[206] Y. Kato, D. A. Holm, B. Okollie, and D. Artemov, "Noninvasive detection of temozolomide in brain tumor xenografts by magnetic resonance spectroscopy", *Neuro-oncol.*, vol. 12, no. 1, pp. 71–79, 2010.

[207] R. E. Hurd, "Gradient-enhanced spectroscopy", *Journal of Magnetic Resonance (1969)*, vol. 87, no. 2, pp. 422–428, 1990.

[208] N. Giraud, L. Biéguin, J. Courtieu, and D. Merlet, "Nuclear Magnetic Resonance Using a Spatial Frequency Encoding: Application to *J*-Edited Spectroscopy along the Sample", *Angew. Chem. Int. Ed.*, vol. 49, no. 20, pp. 3481–3484, 2010.

[209] W. Kozminski, "Application of spatially resolved NMR spectroscopy for high resolution spectra of heterogeneous samples", *Pol. J. Chem.*, vol. 74, no. 8, pp. 1185–1189, 2000.

[210] A. Ross, G. Schlotterbeck, H. Senn, and M. von Kienlin, "Application of Chemical Shift Imaging for Simultaneous and Fast Acquisition of NMR Spectra on Multiple Samples", *Angew. Chem. Int. Ed.*, vol. 40, no. 17, pp. 3243–3245, 2001.

[211] J.-N. Dumez and L. Frydman, "Multidimensional excitation pulses based on spatiotemporal encoding concepts", *J. Magn. Reson.*, vol. 226, pp. 22–34, 2013.

[212] A. Enthart, J. C. Freudenberger, J. Furrer, H. Kessler, and B. Luy, "The CLIP/CLAP-HSQC: Pure absorptive spectra for the measurement of one-bond couplings", *J. Magn. Reson.*, vol. 192, no. 2, pp. 314–322, 2008.

[213] T. Kajitani, K. Okoshi, S. Sakurai, J. Kumaki, and E. Yashima, "Helix-Sense Controlled Polymerization of a Single Phenyl Isocyanide Enantiomer Leading to Diastereomeric Helical Polyisocyanides with Opposite Helix-Sense and Cholesteric Liquid Crystals with Opposite Twist-Sense", *J. Am. Chem. Soc.*, vol. 128, no. 3, pp. 708–709, 2006.

[214] B. Blümich, F. Casanova, and S. Appelt, "NMR at low magnetic fields", *Chem. Phys. Lett.*, vol. 477, no. 4-6, pp. 231–240, 2009.

[215] M. Cudaj, G. Guthausen, T. Hofe, and M. Wilhelm, "SEC-MR-NMR: Online Coupling of Size Exclusion Chromatography and Medium Resolution NMR Spectroscopy", *Macromol. Rapid Commun.*, vol. 32, no. 8, pp. 665–670, 2011.

[216] B. Luy, "Towards Portable High-Resolution NMR Spectroscopy", *Angew. Chem. Int. Ed.*, vol. 50, no. 2, pp. 354–356, 2011.

[217] E. Danieli, J. Perlo, B. Blümich, and F. Casanova, "Small Magnets for Portable NMR Spectrometers", *Angew. Chem. Int. Ed.*, vol. 49, no. 24, pp. 4133–4135, 2010.

[218] P. Lesot, D. Merlet, A. Loewenstein, and J. Courtieu, "Enantiomeric visualization using proton-decoupled natural abundance deuterium NMR in poly(γ-benzyl-L-glutamate) liquid crystalline solutions", *Tetrahedron: Asymmetry*, vol. 9, no. 11, pp. 1871–1881, 1998.

[219] C. Naumann, W. A. Bubb, B. E. Chapman, and P. W. Kuchel, "Tunable-Alignment Chiral System Based on Gelatin for NMR Spectroscopy", *J. Am. Chem. Soc.*, vol. 129, no. 17, pp. 5340–5341, 2007.

[220] J. Farjon, D. Merlet, P. Lesot, and J. Courtieu, "Enantiomeric excess measurements in weakly oriented chiral liquid crystal solvents through 2D ^{1}H selective refocusing experiments", *J. Magn. Reson.*, vol. 158, no. 1–2, pp. 169–172, 2002.

[221] P. W. Kuchel, B. E. Chapman, N. Müller, W. A. Bubb, D. J. Philp, and A. M. Torres, "Apparatus for rapid adjustment of the degree of alignment of NMR samples in aqueous media: Verification with residual quadrupolar splittings in ^{23}Na and ^{133}Cs spectra", *Journal of Magnetic Resonance*, vol. 180, no. 2, pp. 256–265, 2006.

[222] U. Eliav and G. Navon, "Collagen Fibers as a Chiral Agent: A Demonstration of Stereochemistry Effects", *J. Am. Chem. Soc.*, vol. 128, no. 50, pp. 15 956–15 957, 2006.

[223] G. Kummerlöwe, M. U. Kiran, and B. Luy, "Covalently Cross-linked Gelatin Allows Chiral Distinction at Elevated Temperatures and in DMSO", *Chemistry – A European Journal*, vol. 15, no. 45, pp. 12 192–12 195, 2009.

[224] G. Kummerlöwe, E. F. McCord, S. F. Cheatham, S. Niss, R. W. Schnell, and B. Luy, "Tunable Alignment for All Polymer Gel/Solvent Combinations for the Measurement of Anisotropic NMR Parameters", *Chemistry – A European Journal*, vol. 16, no. 24, pp. 7087–7089, 2010.

[225] G. Kummerlöwe, F. Halbach, B. Laufer, and B. Luy, "Precise measurement of RDCs in water and DMSO based gels using a silicone rubber tube for tunable stretching", *The Open Spectroscopy Journal*, vol. 2, pp. 29–33, 2008.

[226] R. L. Vold and S. O. Chan, "Modulated Spin Echo Trains from Liquid Crystals", *The Journal of Chemical Physics*, vol. 53, no. 1, pp. 449–451, 1970.

[227] G. Bodenhausen, R. Freeman, and D. L. Turner, "Two-dimensional *J* spectroscopy: Proton-coupled carbon-13 NMR", *The Journal of Chemical Physics*, vol. 65, no. 2, pp. 839–840, 1976.

[228] A.-C. Pöppler, H. Keil, D. Stalke, and M. John, "^{7}Li Residual Quadrupolar Couplings as a Powerful Tool To Identify the Degree of Organolithium Aggregation", *Angew. Chem. Int. Ed.*, vol. 51, no. 31, pp. 7843–7846, 2012.

[229] J. P. Bayle, J. Courtieu, E. Gabetty, A. Loewenstein, and J. M. Pechine, "Enantiomeric analysis in a polypeptide lyotropic liquid-crystal through proton decoupled deuterium NMR", *New J. Chem.*, vol. 16, no. 8-9, pp. 837–838, 1992.

[230] H. W. Spiess, "NMR Spectroscopy: Pushing the Limits of Sensitivity", *Angew. Chem. Int. Ed.*, vol. 47, no. 4, pp. 639–642, 2008.

[231] R. A. Green, R. W. Adams, S. B. Duckett, R. E. Mewis, D. C. Williamson, and G. G. Green, "The theory and practice of hyperpolarization in magnetic resonance using *para*hydrogen", *Prog. Nucl. Magn. Reson. Spectrosc.*, vol. 67, pp. 1–48, 2012.